



INSTITUT  
POLYTECHNIQUE  
DE PARIS

NNT : 2021IPPAX125

Thèse de doctorat



# Inter-Calibration Aéroportée des Télescopes H.E.S.S. et Emission Gamma Diffuse Interstellaire de Très Haute Energie du Grand Nuage de Magellan

Thèse de doctorat de l'Institut Polytechnique de Paris  
préparée à l'École Polytechnique

École doctorale n°626 École Doctorale de l'Institut Polytechnique de Paris (ED IP  
Paris)

Spécialité de doctorat : Astrophysique

Thèse présentée et soutenue à Palaiseau, le 17 décembre 2021, par

**JACQUES MULLER**

Composition du Jury :

Régis Terrier Directeur de recherche, Université Paris Diderot (APC), Paris, France	Président
Isabelle Grenier Professeur, Université de Paris (AIM), Gif-sur-Yvette, France	Rapporteur
Oscar Blanch Bigas Directeur de recherche, The Barcelona Institute of Science and Technology (IFAE), Bellaterra, Spain	Rapporteur
Nukri Komin Professeur associé, University of Witwatersrand, Braamfontein, South Africa	Examineur
Pierrick Martin Chargé de recherche, Université de Toulouse (IRAP), Toulouse, France	Examineur
Gernot Maier Chargé de recherche, Deutsches Elektronen-Synchrotron (DESY), Zeuthen, Germany	Examineur
Anthony Brown Professeur assistant, Durham University, Durham, United Kingdom	Examineur
Mathieu de Naurois Directeur de recherche, École Polytechnique (LLR), Palaiseau, France	Directeur de thèse







*Science is a wonderful thing if one does not have to earn a living at it. One should earn one's living by work of which one is sure one is capable. Only when we do not have to be accountable to anyone can we find joy in scientific endeavor.*

*A. Einstein*



# Contents

<b>1</b>	<b>Very-high-energy gamma-ray astronomy</b>	<b>1</b>
1.1	Cosmic rays . . . . .	2
1.2	Acceleration mechanisms of cosmic rays . . . . .	7
1.2.1	Second order Fermi acceleration . . . . .	7
1.2.2	First order Fermi acceleration . . . . .	8
1.2.3	Maximum Energy . . . . .	9
1.2.4	Beyond the test-particle regime: Modern Diffuse Shock Acceleration (DSA) . . . . .	10
1.3	Production of gamma rays . . . . .	11
1.3.1	Synchrotron radiation . . . . .	11
1.3.2	Bremsstrahlung . . . . .	12
1.3.3	Inverse Compton Scattering . . . . .	13
1.3.4	Curvature radiation . . . . .	14
1.3.5	Pion Decay . . . . .	14
1.3.6	Resolving the different radiative processes . . . . .	15
1.4	Gamma-ray sources . . . . .	15
1.4.1	Supernova Remnants . . . . .	16
1.4.2	Pulsar Wind Nebula . . . . .	19
1.4.3	Binary Systems . . . . .	20
1.4.4	Active Galactic Nuclei . . . . .	20
1.4.5	Gamma-Ray Bursts . . . . .	22
1.4.6	Other gamma-ray sources . . . . .	22
1.5	Detection of gamma rays . . . . .	22
1.5.1	Satellite-based gamma-ray experiments . . . . .	23
1.5.2	Imaging atmospheric Cherenkov telescope arrays . . . . .	25
1.5.3	Other ground-based gamma-ray detectors . . . . .	34
<b>2</b>	<b>The H.E.S.S. Experiment</b>	<b>37</b>
2.1	Cameras . . . . .	38
2.1.1	CT1-4 . . . . .	38
2.1.2	CT5 . . . . .	38

2.2	Readout & Trigger . . . . .	40
2.3	Calibration . . . . .	41
2.3.1	Pedestal calibration . . . . .	41
2.3.2	Gain calibration . . . . .	42
2.3.3	Cross-calibration of gain channels . . . . .	43
2.3.4	Flat-field calibration . . . . .	43
2.3.5	Optical efficiency . . . . .	43
2.3.6	Pointing corrections . . . . .	47
2.4	Separation & Reconstruction . . . . .	48
2.4.1	Image cleaning . . . . .	49
2.4.2	Hillas reconstruction . . . . .	49
2.4.3	Semi-analytic model reconstruction . . . . .	51
2.5	Analysis . . . . .	53
2.5.1	Background subtraction . . . . .	53
2.5.2	Acceptance calculation . . . . .	57
2.5.3	Statistical significance . . . . .	59
2.5.4	Energy spectrum determination . . . . .	60
2.6	Performance . . . . .	62
<b>3</b>	<b>Improved calibration of optical efficiency at large zenith angle</b>	<b>65</b>
3.1	Zenith angle dependence in the muon optical efficiency . . . . .	65
3.2	Revisiting the event selection . . . . .	66
3.3	Cure of zenith angle dependence . . . . .	70
3.4	Revisiting the muon optical efficiencies of the UAV calibration runs	71
<b>4</b>	<b>UAV calibration</b>	<b>75</b>
4.1	Limitations of the muon-based optical efficiency calibration . . . . .	75
4.2	UAV calibration concept . . . . .	76
4.3	Setup . . . . .	78
4.4	Calibration of the UAV data . . . . .	80
4.5	Monte-Carlo Simulation . . . . .	81
4.5.1	Working principle of the Monte-Carlo simulation . . . . .	82
4.5.2	Simulating the general behaviour of the setup . . . . .	84
4.6	Analysis procedure . . . . .	88
4.6.1	Event selection . . . . .	89
4.6.2	Determination of the UAV position . . . . .	95
4.6.3	Inter-calibration of the telescopes . . . . .	100
4.7	UAV data and pointing corrections . . . . .	102
4.8	Pulse duration problem . . . . .	103
4.9	Results on remaining successful runs . . . . .	106
4.10	Comparison with muon optical efficiency calibration . . . . .	110

4.11	Pointing Correction . . . . .	112
4.12	Timing . . . . .	116
4.13	Conclusions . . . . .	120
<b>5</b>	<b>Introduction to interstellar diffuse emission and a novel detection method</b>	<b>123</b>
5.1	Interstellar diffuse emission . . . . .	124
5.2	The Large Magellanic Cloud and its interstellar diffuse emission . .	127
5.3	Why the standard analysis underestimates emission from very extended sources . . . . .	138
5.4	Run-wise simulations . . . . .	140
5.5	Generating Instrument Response Functions and Background Models from run-wise simulations . . . . .	143
5.6	Analysis procedure . . . . .	150
5.7	The advantage of the run-wise method for the analysis of extended sources . . . . .	155
<b>6</b>	<b>Interstellar diffuse emission in the Large Magellanic Cloud</b>	<b>157</b>
6.1	Characterization and particularities of the used datasets . . . . .	157
6.2	Systematics study on sources without any expected extended emission	167
6.3	Analysis results . . . . .	181
6.3.1	LMC . . . . .	181
6.3.2	SMC . . . . .	202
6.4	Physical interpretation of the excess seen in the Large Magellanic Cloud . . . . .	211
6.4.1	Position . . . . .	211
6.4.2	Flux . . . . .	221
6.5	Conclusion . . . . .	233
<b>7</b>	<b>Perspectives</b>	<b>235</b>
<b>A</b>	<b>Side-by-side comparison of residual maps and best-fit Gaussians</b>	<b>241</b>
<b>B</b>	<b>LMC results for standard analysis</b>	<b>245</b>



# Résumé

Le Système Stéréoscopique à Haute Energie H.E.S.S. est l'un des trois grands réseaux de Télescopes à Imagerie Tcherenkov Atmosphérique (IACT) opérationnels et est situé en Namibie à une altitude de 1800 m. Ces réseaux sont conçus pour détecter indirectement des photons aux énergies les plus hautes couramment observables, appelés rayons gamma, créés par les phénomènes cosmiques les plus violents comme des supernovæ, des pulsars, des trous noirs accrétants et des sursauts gamma. Pour des particules avec de telles énergies, l'atmosphère constitue un calorimètre, ce qui signifie qu'une particule dépose son énergie dans l'atmosphère et qu'on peut la mesurer. Les rayons gamma entrant dans l'atmosphère créent donc des gerbes de particules constituées de milliards de particules secondaires. Celles qui sont chargées émettent du rayonnement Tcherenkov qui peut être enregistrée par les IACTs. H.E.S.S. est constitué de cinq télescopes, dont quatre avec un miroir segmenté de forme hexagonale de 12 m de diamètre et un avec une forme presque rectangulaire avec un diamètre de 28 m. Pour pouvoir mesurer précisément l'énergie des photons gamma, il est indispensable de calibrer les télescopes individuellement, mais aussi de les inter-calibrer.

La première partie de cette thèse propose une nouvelle méthode pour déterminer les efficacités optiques relatives des télescopes du réseau H.E.S.S. Celle-ci est basée sur un drone volant au-dessus du réseau et éclairant les télescopes avec une source de lumière pulsée. Cette méthode permet, contrairement à celle utilisée jusqu'alors, de mesurer la dépendance à la longueur d'onde des efficacités. Ce point sera important pour les réseaux futurs comme CTA constitués de plusieurs types de télescopes et qui devraient avoir une précision et sensibilité sans précédent. Cette thèse discute les résultats d'une première campagne d'inter-calibration et démontre que cette méthode permet d'inter-calibrer les télescopes de H.E.S.S. Additionnellement, elle montre qu'il est possible d'utiliser les mêmes données des observations avec un drone pour vérifier l'horodatage et les corrections de pointé de H.E.S.S., qui sont nécessaires car le pointé est imparfait à cause de la déformation du sol et de la structure du télescope sous son propre poids.

La seconde partie de cette thèse discute la recherche d'émission gamma diffuse en provenance du Grand Nuage de Magellan. Il s'agit d'une galaxie naine

qui, à l'instar de la Voie Lactée, contient non seulement des étoiles mais également des rayons cosmique (protons et électrons principalement) et de la matière interstellaire. Outre les sources astrophysiques, on attend également une émission diffuse interstellaire produite par les interactions de ces particules avec le gaz interstellaire et les champs de rayonnement. Cette émission diffuse interstellaire constitue d'ailleurs le signal principal détecté par des satellites gamma sensibles à la partie basse énergie du spectre gamma (énergies GeV). L'étude de cette émission diffuse interstellaire est particulièrement intéressante, car elle permet de caractériser tous les processus reliés à sa production et nous ouvre ainsi une voie supplémentaire vers le spectre des rayons cosmiques, la distribution de gaz dans les galaxies et la population d'électrons accélérés proche de sources potentiellement non-découvertes, mais aussi parce qu'elle constitue un fond pour toutes les détections de sources. J'utilise une nouvelle méthode de soustraction de fond, initialement développé pour la détection d'émission diffuse interstellaire dans la Voie Lactée, et basée sur des simulations Monte Carlo observation-par-observation incluant tous les paramètres et conditions d'observations pertinents (simulations «*run-wise* ») du fond attendu. Ensuite, je soustrais ce fond entièrement simulé des données observées après avoir ajusté sa normalization avec un maximum de vraisemblance. Enfin, j'ajuste l'émission résiduelle sur les données en utilisant un maximum de vraisemblance (en gardant les sources connues masquées). Ceci mène à l'émergence d'une composante d'émission étendue près de N 157B qui pourrait être due à l'émission diffuse interstellaire, et constituer ainsi sa première détection avec un IACT. Une autre raison possible serait la contribution de sources non-résolues.

# Preface

The origin of the term astronomy comes from ancient greek and literally means the study of the stars, which is what has been mostly observed by astronomers for millennia beside a few objects in our local solar system. However, quite recently compared to the millennia of astronomical observations, new techniques to gather astronomical information, beside the human eye, were developed. This has led to a drastic increase of available information and to the discovery of numerous new objects and the scope of astronomy started to extend beyond stars. Indeed, these new detection techniques allowed the spectral range of available information to be extended beyond visible light to the whole range extending from the radio band to gamma rays. Detectors of new messengers, beside photons (i.e., the quanta of the light), carrying astronomical information, such as charged particles and more recently neutrinos and gravitational waves became available. I obtained the findings presented in this thesis using very-high-energy photons called gamma rays detected with H.E.S.S., an Imaging Atmospheric Cherenkov Telescope, a type of instrument which will be described later on.

These Imaging Atmospheric Cherenkov Telescopes have so far mostly detected individual, localized sources, similar to the stars observed for millennia. However, beside their emission, one also expects very extended interstellar diffuse emission, which is produced by the interaction of very-high-energy particles in the interstellar medium producing photons. This diffuse emission has been detected at lower energies, but so far not with Imaging Atmospheric Cherenkov Telescopes. The search for diffuse emission is one of the main focuses of this work. A second focus is on a novel calibration method to inter-calibrate the telescopes of a Cherenkov Telescope array with the help of an unmanned aerial vehicle (UAV). A good inter-calibration becomes more and more crucial as bigger arrays containing more telescopes are designed in order to increase sensitivity, energy and angular resolution.

In order to present my two projects, the first chapter of this thesis gives a general introduction on gamma-ray astronomy to describe the physics involved. I start by describing cosmic rays, their production and then the production of gamma rays, which is what is detected by Imaging Atmospheric Cherenkov Tele-

scopes, from these cosmic rays. Then, I introduce some of the observed sources and the detection of gamma rays, focusing on Cherenkov Telescopes, but also discussing other detection techniques. In the second chapter, I describe the H.E.S.S. telescope, its calibration and the analysis of H.E.S.S. data in order to have a solid basis to discuss a novel calibration technique and a novel detection technique used in the search of diffuse emission. In the third chapter, I discuss the optimization of the conventional muon-based optical efficiency calibration method at high zenith angles. During the test of the novel UAV-based optical efficiency calibration method, an anomalous zenith angle dependence has been discovered in this muon-based method which I have solved. Chapter four then discusses my work on the UAV calibration method in detail, i.e., the calibration of the UAV data, the Monte Carlo simulation I wrote for the UAV calibration, and finally the analysis procedure of the UAV data. Then, it discusses further uses of the UAV calibration data, namely the verification of the pointing corrections and the time stamping of H.E.S.S. Finally, I present and discuss the results of the successful UAV calibration campaign. In chapter five, I first give a general introduction on interstellar diffuse emission and present the novel analysis method I use for my work on diffuse emission in the Large Magellanic Cloud. This analysis method, developed recently within the H.E.S.S. collaboration, is based on the run-wise simulation method and the generation of instrument response functions and background models from these run-wise simulations. In chapter six, I present my work on diffuse emission in the Large Magellanic Cloud and apply this novel analysis method to Large Magellanic Cloud data. First, I characterize the used datasets. Finally, I present and discuss the obtained results and their physical interpretation. In chapter seven, I shortly describe the perspectives of this work.

Chapter one and two are a general introduction to the topic of gamma-ray astronomy and H.E.S.S. and chapter five constitutes an introduction to interstellar diffuse emission and the run-wise analysis method, whereas the other chapters focus on my work. For chapter three, I discovered the zenith angle dependence, its implications, the difference in the zenith angle distribution for high and low zenith angle runs and the necessity to over-work the events selection. In chapter four, I took care of the data analysis of the UAV calibration data which were taken by my collaborators. I presented my work on this at the 37<sup>th</sup> International Cosmic Ray Conference and submitted a paper to *Astroparticle Physics* which describes the same analysis as described in chapter four of this thesis and is content-wise very similar. In chapter six, I applied the novel analysis method to the Large and Small Magellanic Cloud dataset and performed the systematic studies on the Centaurus A and NGC 253 datasets.

# Chapter 1

## Very-high-energy gamma-ray astronomy

Humans have made astronomical observations for more than ten thousands of years; references to stellar constellations can already be found in the oldest cave paintings from stone age. However, until less than 250 years ago, researchers used only their eyes as detectors for cosmic radiation and were thus limited to observing photons in the very limited spectral range of visible light (approx. 1.65 eV - 3.26 eV). Only in 1800, did William Herschel discovered the first radiation of a celestial body in the non-visible spectrum, namely infrared light from the sun, with the help of a prism and a thermometer [1]. It then took another 130 years until observations extended further into the non-visible wavelengths, with the advent of radio-telescopes. With the advent of balloons and satellites, observations could be extended to electromagnetic radiation to which the earth atmosphere is opaque (which is the case for most spectral ranges as illustrated in figure 1.1) and so more and more spectral regions could be covered until gamma-ray energies were reached ( $>50$  MeV) in 1967 with the OSO-3 satellite [2].

The visible light emitted by the sun and the stars, which has been (beside the reflection of this light by other objects) the only source of information about the objects in the sky for almost all human history, is thermal radiation. To a first approximation, it follows a black-body spectrum which is continuous and only depends on the temperature of the emitting object. The peak energy of this spectrum increases with temperature. Gamma rays do not arise from thermal radiation, since there are no objects hot enough to produce light at such high energies in our Universe. Indeed, temperatures of  $1 \times 10^{15}$  K would be needed to reach a peak energy of about 1 TeV, and even to reach peak energies of 1 MeV, temperatures of  $1 \times 10^{12}$  K would already be necessary. This is about  $1 \times 10^{12}$  respectively  $1 \times 10^9$  times the temperature of the sun which has a peak energy in the eV range and follows from Wien's displacement law according to which

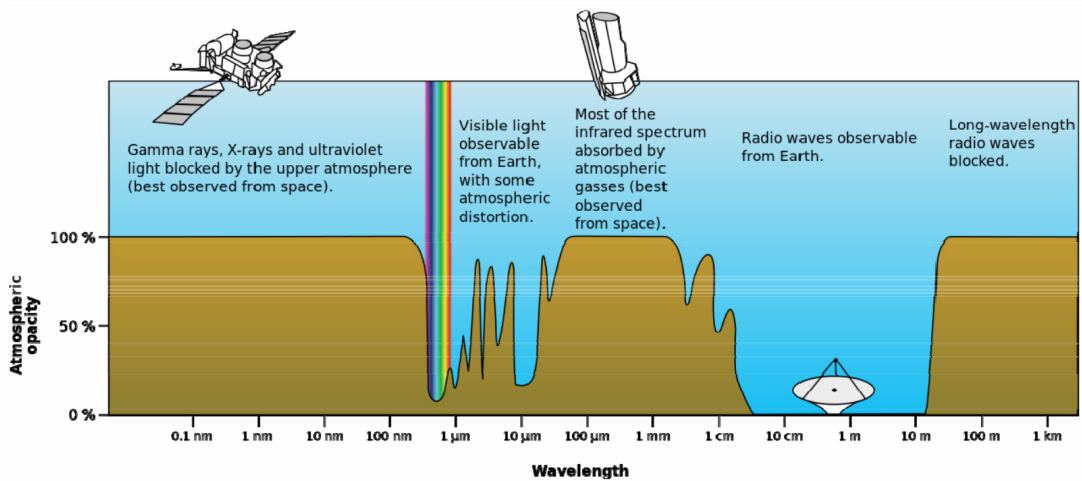


Figure 1.1: Atmospheric absorption as a function of wavelength. The atmosphere is only transparent to very limited wavelength range, making the use of balloons and satellites necessary for numerous astronomical observations. Reproduced from [4]

the peak energy is proportional to the temperature [3]. Instead, gamma rays are produced in non-thermal processes due to interactions of extremely high energy particles and so provide information about their acceleration mechanisms. These interactions can happen either at the source or in the interstellar medium, in which case the particles are called cosmic rays.

This chapter first introduces the history of the discovery of cosmic rays and discusses the main observational evidences for their presence, then the mechanisms which accelerate cosmic rays to such high energies so that they can produce gamma rays and produce gamma rays. Then, it introduces the most important cosmic sources of gamma rays and discuss the detection techniques for gamma rays.

## 1.1 Cosmic rays

In 1900, Charles Thomson Rees Wilson designed the first cloud chamber when trying to understand the formation of clouds [5]. Cloud chambers are sealed boxes filled with a supersaturated vapour. When an energetic charged particle passes through such a cloud chamber, it ionizes the gas and vapour condenses around the so formed ions leading to a visible particle trail. Thus, cloud chambers allow charged particles passing them to be visualized. What he did not know at that time, was that cloud chambers not only allow charged particles from radioactive sources to be recorded when they are brought close enough, but that they are also well suited to observe cosmic rays coming from astronomical sources. The presence

of these cosmic rays was only discovered in 1912 by Victor Hess in a balloon experiment in which he ascended to 5330 m in altitude [6]. He showed that the number of charged particles (which he detected by the spontaneous discharge of an electroscope) increases with altitude and so that they are very likely from extra-terrestrial origin, a discovery for which he was awarded the physics Nobel prize in 1936. In 1932, Carl David Anderson discovered the positron in cosmic rays [7]. He used an improved version of the cloud chamber developed by Wilson in which a magnetic field allowed the charge of the measured particles to be determined by the bending of the tracks they leave in the cloud chamber. In 1936, he discovered, together with Seth Neddermeyer, a negatively charged particle 200 times heavier than the electron which is nowadays known as muon [8]. In 1952, the first artificial accelerators reaching GeV energies were built [9] leading to particle physics and new particle discoveries being mostly undertaken in these facilities and allowing cosmic ray physicists to focus on astronomical questions.

Nowadays, cosmic rays have been well studied. They are constituted of charged particles. Due to turbulent galactic magnetic fields, they reach the Earth almost uniformly from all directions, except possibly at the highest energies, and so individual sources of cosmic rays cannot be determined by direct measurement. However, once they are near to Earth, its magnetic field is deviating the cosmic rays leading to a non-isotropic arrival of cosmic rays on the Earth: There are less cosmic rays arriving at the equator than at the poles due to the "latitude effect" [10] and there is a slight East-West asymmetry [11].

The energy spectrum (i.e., the distribution of energy) of cosmic rays has been measured over more than 12 orders of magnitude. Figure 1.2 shows the measured (all-particle) cosmic ray flux as a function of energy; it is power-law-like, with however a few distinctive features. First, there is a modulation at the lowest energies of the spectrum which is due to solar winds ("solar modulation") which is not intrinsic to cosmic ray production but to local observation conditions [13]. Then, there are at least two breaks or changes of photon index in the spectrum: One at about  $5 \times 10^{15}$  eV called the "knee" and one at about  $5 \times 10^{18}$  eV called the "ankle" [14]. Additionally, there is increasing evidence for a third spectral break at around  $4 \times 10^{17}$  eV called the "second knee" [15] and new CALET and DAMPE data seem to indicate a much finer structure with at least two more breaks as will be discussed later on when discussing the individual species contributing to the cosmic ray spectrum [16]. These breaks in the spectrum are usually interpreted as being due to a change of the major contributing acceleration mechanism and source population around these energies. So, it is believed that the main contribution comes from galactic sources below the knee and from extragalactic sources above the ankle and that there is a transition in-between.

That there is such a transition at some energy is suggested by low energy cosmic

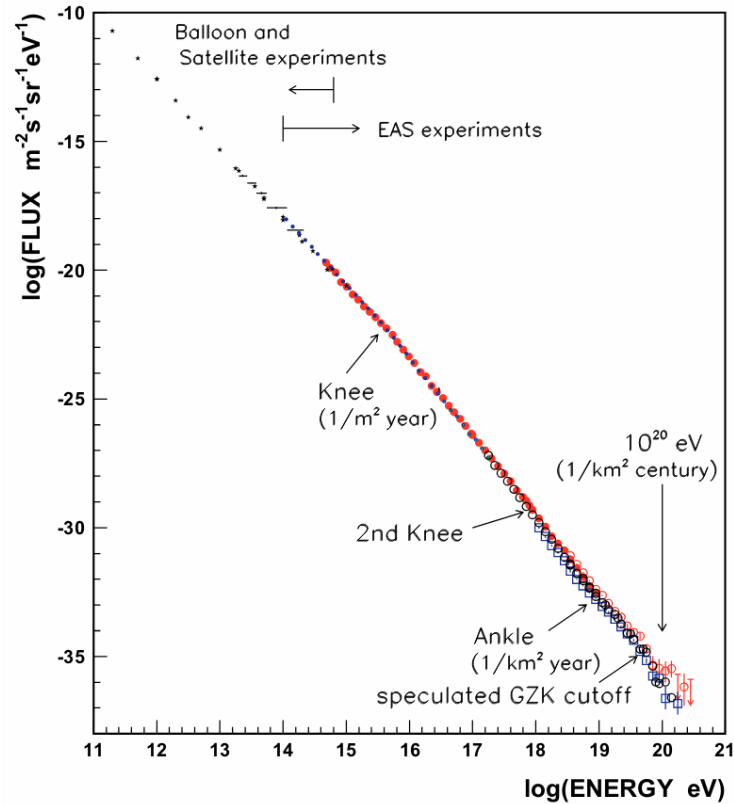


Figure 1.2: All-particle cosmic-ray spectrum measured by different experiments. The spectrum almost follows a power-law, but has some distinctive features: First of all, there is the solar modulation at low energies (which cannot be seen on the figure as it is at lower energies), then three spectral breaks (whereof the second one is not yet fully confirmed), called "knee", "second knee" and "ankle", and finally the theoretically predicted GZK cut-off at very high energies due to interaction of the cosmic rays with the cosmic microwave background. Reproduced from [12]

rays having a Galactic origin (as the cosmic ray density is different in the Milky Way than in the Magellanic Clouds [18]), and high energy cosmic rays almost certainly having an extra-galactic origin as their arrival directions on Earth have a large-scale anisotropy not correlated with any galactic feature above the scale of EeV [17].

This spectrum also shows that the flux of cosmic rays is decreasing extremely with energy: whereas one particle per second per square meter reaches Earth at energies of about  $1 \times 10^{11}$  eV, there is only one particle per year per square meter at the knee and one particle per hundred thousand years per square metre at  $1 \times 10^{20}$  eV, leading to the need for a strong increase of detector effective areas with energy to still have sensible rates. Here the effective area is defined as the equivalent area over which all particles would be detected, i. e., all the area over which particles could be detected multiplied by the local sensitivities. The effective area can depend on particle properties such as their energy. In addition, cosmic rays above  $1 \times 10^{20}$  eV are expected to interact with the cosmic microwave background (CMB) making them lose energy (Greisen-Zatsepin-Kuzmin effect) [19] and so to reach Earth with lower energy (except if they come from very close sources). This is expected to lead to a cut-off in the spectrum at these energies.

This all-particle cosmic ray spectrum is the sum of the spectra from different particle species. Even though cosmic rays are mostly protons, which constitute 89% of the cosmic rays reaching Earth, 10% of the cosmic rays are helium nuclei, with heavier nuclei up to uranium also contributing to these cosmic rays at a lower fraction [20]. Beside this hadronic component (i.e., the component constituted of nuclei), electrons and positrons are also part of the cosmic rays to a lesser fraction. One can also determine the spectrum of all these individual components. However, this is not possible over the whole energy range shown in figure 1.2, as the number of high energy particles of a given species is even further reduced by its composition fraction at the given energy. This individual particle cosmic ray spectra are shown on a smaller energy range for protons, helium, carbon, oxygen, neon, magnesium, silicon and iron in figure 1.3. The spectra seem to have a similar shape for all species. However, a closer investigation shows that the shapes of the individual species show small differences, and unexpected changes of slopes [15]. Indeed, recent CALET and DAMPE data show that both the proton and helium spectra have a break at around 500 GeV per nucleon and a break at around 10 TeV per nucleon which propagates to the all-particle spectrum as its main constituent are protons [16]. For the heavier nuclei, novel AMS results were presented at the International Cosmic Ray Conference 2021. They first of all confirmed a different behaviour of primary particle directly emitted by cosmic ray sources such as the already discussed helium, and carbon and oxygen and secondary particles produced in the interactions of these primary particles such as lithium, beryllium

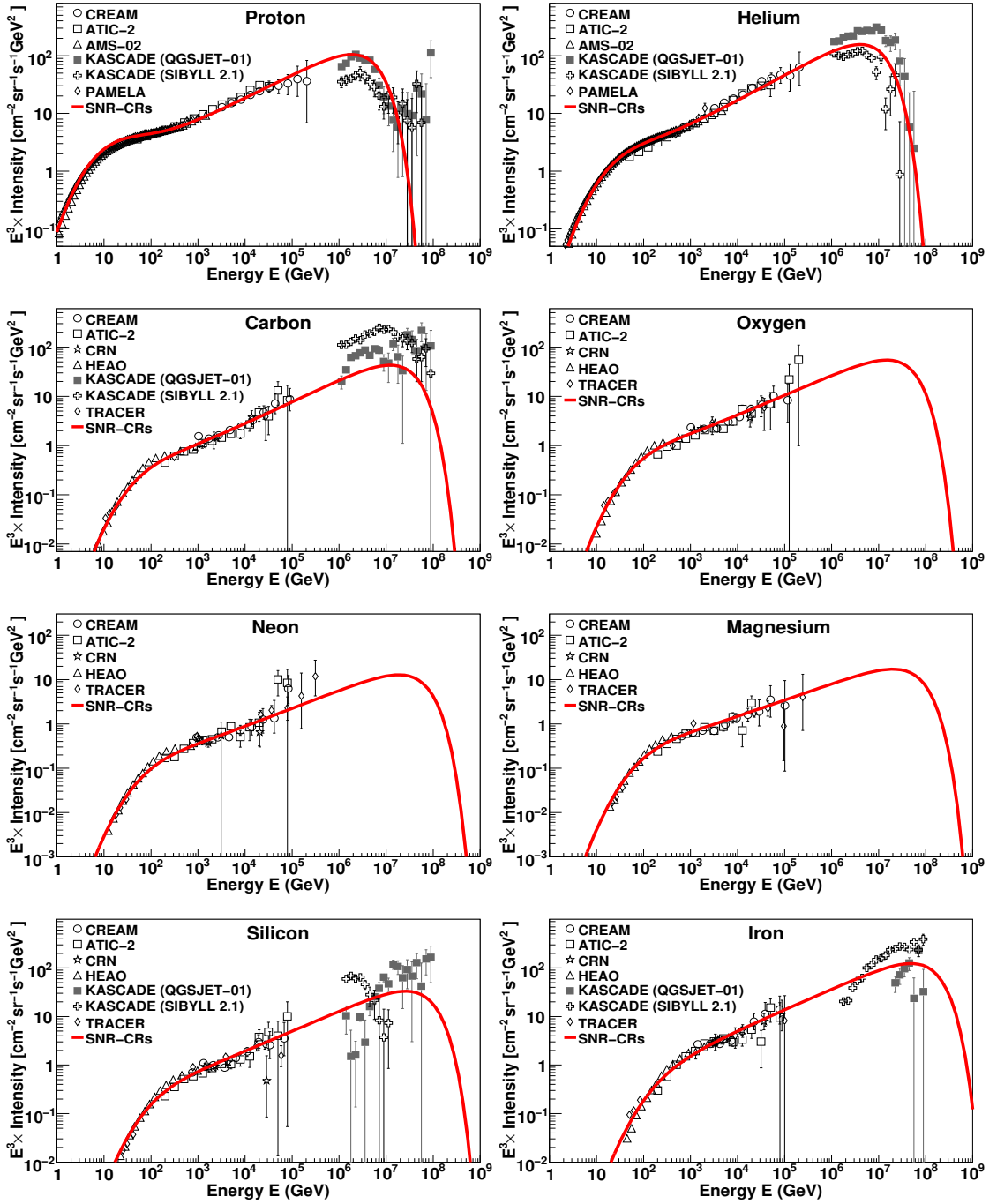


Figure 1.3: Spectrum of the individual elements constituting the cosmic rays as measured by different experiments. The shape is different from the all-particle spectrum due to the multiplication by  $E^3$  of the ordinate axis and the spectra of the individual elements have only been measured up to lower energies. The energy range reaches almost the ankle for the proton, helium, carbon, silicon and iron primaries whereas oxygen, neon and magnesium are only shown for lower energies. The red line is the prediction of a model which assumes the cosmic rays in this energy range being originating from galactic supernova remnants. Reproduced from [15]

and boron. Indeed, the aforementioned break is much stronger for the secondary particles than for primary particles which is most likely due to a propagation effect such as a change of the diffusion coefficient at the break energy. However, they also showed that whereas the spectra of the primary particles of helium, carbon and oxygen are well in agreement with each other and the spectra of the primary particles neon, magnesium and silicon are well in agreement with each other, there is a discrepancy between the spectra of these two categories which could be an indication for different injection sources. Fluor showed the typical spectrum in agreement with a secondary particle, whereas nitrogen, sodium and aluminium seem to be a mixture of a secondary and primary spectrum which seems to indicate that they are produced directly in sources as well as during propagation. For the leptonic component of the spectrum, first of all the electron spectrum shows a break at around 1 TeV. However, more interestingly, new PAMELA measurements of the positron fraction in the all-electron and -positron flux, confirmed an excess in positrons over a pure secondary productions in the interstellar medium, indicating the presence of sources injecting primary positrons.

These results are in tension with the simple view that the whole spectrum is explained by a single galactic component, which is thought to be due to emission from supernova remnants, and a single extra-galactic component. Indeed, models with at least a second galactic cosmic ray component, for which one explanation could be supernova explosions of Wolf-Rayet stars, seem to be preferred. In this model supernova remnants would dominate the cosmic ray spectrum up to the first knee, then Wolf-Rayet would dominate up to the second knee and for higher energies the extra-galactic component would dominate [12]. These indications for a complex model show that, even more than hundred years after the discovery of cosmic rays, the cosmic ray spectrum has not yet revealed all its secrets and that there is still ample room for discoveries.

## 1.2 Acceleration mechanisms of cosmic rays

After having discussed in detail the observation results on cosmic rays, this section explains how these charged particles can even reach such high energies and considers two acceleration mechanisms, initially developed by Enrico Fermi, and subsequently improved with time.

### 1.2.1 Second order Fermi acceleration

Second-order Fermi acceleration [21] considers completely ionized interstellar clouds which are magnetized. If a charged particle enters such a cloud which is moving with a velocity  $V$  (in the galactic reference system), it interacts elastically inside

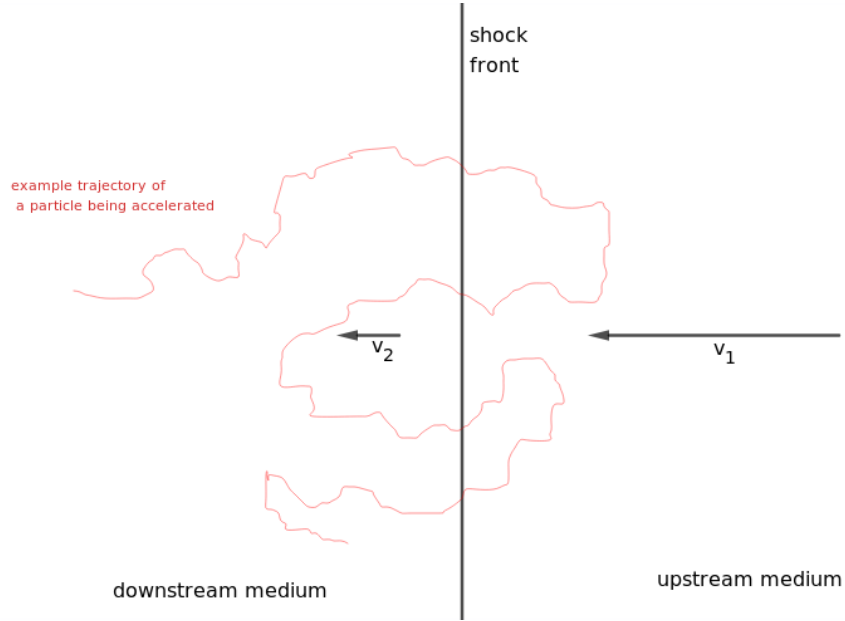


Figure 1.4: Illustration of first order Fermi acceleration principle in the shock rest frame. The unshocked upstream medium has a speed  $v_1$  in this frame and the already shocked downstream medium a speed  $v_2$ . In red the path of a particle passing the shock front multiple times and so being accelerated to high energies is illustrated.

the cloud. These interactions lead (in the galactic system) to an acceleration of particles entering head-on into the cloud and to a deceleration of particles entering from the back. As head-on collisions are more frequent, the particles gain energy on average and the average relative energy gain is:  $\langle \frac{\Delta E}{E} \rangle = \frac{4}{3} \left( \frac{V}{c} \right)^2$ , where  $c$  denotes the speed of light in vacuum (as it will throughout the whole thesis). This energy gain is of second order with respect to the diffusion speed of the clouds which means that the average energy gain is proportional to the squared speed. This leads to this mechanism often being inefficient as this diffusion speed is often much smaller than the speed of light ( $V/c \ll 1$ ).

### 1.2.2 First order Fermi acceleration

For first order Fermi acceleration [22], one considers a diffuse plasma medium through which a strong shock wave propagates. In the shock rest frame, the velocity of the upstream gas (i.e., in front of the shock) is  $v_1$  and that of the downstream gas (i.e., the gas that has passed through the shock)  $v_2$ . As the shock decelerates the upstream gas (in the shock rest frame),  $v_2$  is smaller than  $v_1$  and it can be shown that for a mono-atomic gas and a strong shock  $v_1 = 4v_2$ . This

follows from the Rankine-Hugoniot conditions, i.e., mass conservation, momentum conservation and energy conservation [23]. This situation is illustrated in figure 1.4.

Now we consider energetic particles upstream of the shock, isotropic in the rest frame of the upstream medium. If they cross the shock, they have in average a higher speed with respect to the downstream rest frame, as they pass from a medium in which they were isotropic to a medium in which they have a net velocity. Behind the shock the particles scatter in the downstream medium and become isotropic in the rest frame of the downstream medium. There is a non-zero probability that the particles cross the shock a second time from the downstream to the upstream medium, gaining speed again and becoming isotropic in the rest frame of the upstream medium due to scattering. At each cycle some particles escape the shock region, and so fewer particles of the initial population participate in each cycle. The average relative energy gain per cycle (i.e., for a crossing in both directions) is  $\langle \frac{\Delta E}{E} \rangle = \frac{4}{3} \frac{v_1 - v_2}{c}$ , meaning that this process is a first order process, in which the average energy gain is proportional to the speed. This process is much more efficient than second order processes for perturbation speeds which are often much smaller than the speed of light, such as for example in the shocks of supernova remnants and galaxy clusters [24]. Under the most extreme conditions, such as for gamma-ray bursts or active galactic nuclei, however, relativistic shocks are common [24].

To get the energy spectrum of the particle accelerated with this process, one needs to consider the escape probability for each cycle due to advection in the downstream plasma. It can be obtained from conservation laws and depends on the properties of the medium. It can be written as  $P_{\text{esc}} = \frac{v_1}{c}$  for a mono-atomic gas. This leads to a power-law spectrum for the energy distribution of the accelerated particles:

$$\frac{dN}{dE} \propto E^{-1 + \frac{\ln P_{\text{esc}}}{\ln(1 + \frac{v_1 - v_2}{c})}} \approx E^{-2}, \quad (1.1)$$

where  $N$  is the number of particles accelerated to a final given energy  $E$  before escaping. The last approximation uses again the Rankine-Hugoniot conditions for a monoatomic gas in a strong shock and so it only holds under these circumstances. The accelerated charged particles often then interact with surrounding electromagnetic fields and particles through diffusion. This leads in general to a softer (higher photon index) spectrum.

### 1.2.3 Maximum Energy

The previously described first order Fermi acceleration was considering an idealized system where particles cannot move laterally out of the shock region and which is

stable over all time. However, in reality the shock has a limited size and conditions are not stable over time. A first limitation on the maximum energy which can be reached in a limited size acceleration region is that the orbits on which the particles are cannot be bigger than the size of the region. Otherwise they are not confined. In magnetic fields, this orbit is defined by the Larmor radius  $R_L$ . It describes the radius of the circular movement of a charged particle in such a field. It must be smaller than the size of the acceleration region  $R$  leading to a maximum achievable energy of  $E_{\max} = \Gamma R c e Z B$ . Here  $e$  is the elementary charge (i.e., the magnitude of the charge carried by an electron),  $Z$  is the charge number of the accelerated particles,  $B$  the magnetic field strength and  $\Gamma$  the Doppler factor accounting for the speed of the acceleration region. This maximum energy criterion is known as the Hillas criterion [25].

Beside the size of the acceleration region, there are additional criteria which need to be taken into account:

- The acceleration time scale: acceleration of particles to very high energy can take a long time compared to the life-time of cosmic accelerators. No energies can be reached for which the acceleration would take longer than the age of the system.
- The cooling time scale: during acceleration processes, there are conflicting processes which lead to an energy loss of particles such as synchrotron radiation, inverse Compton scattering or Bremsstrahlung radiation<sup>1</sup>, which often become more important with increasing energy. Once particles start to lose energy at a rate equivalent to that at which they gain energy through the acceleration process, no further acceleration is possible.
- The escape time scale: as already discussed (and taken into account) for the first order Fermi acceleration, particles constantly escape the acceleration regions. This also sets limits on the maximum energy as escaped particles are not further accelerated. So, the number of particles still in the acceleration region decreases with energy.

#### 1.2.4 Beyond the test-particle regime: Modern Diffuse Shock Acceleration (DSA)

All the discussion in this section has so far been in a "test particle" regime. This means that the implicit assumption was that the acceleration of particles has no effect on the system. This is not true, in reality, there is a retro-action between the accelerated particles and the system as energy in the system is passed to the

---

<sup>1</sup>These processes are described in more detail in section 1.3

accelerated particles. This leads to changes in the system which need to be taken into account. They might render acceleration more or less efficient or even reduce the life-time of the acceleration system. Among other the potential formation of a shock precursor might contribute to this [26]. In more recent works on diffuse shock acceleration (DSA), based on Fermi acceleration, all these factors have been accounted for, leading to models which seem to better describe particle acceleration in astrophysical systems such as supernovae [26, 27].

## 1.3 Production of gamma rays

This section discusses how gamma rays are produced from high energy cosmic rays after having described their acceleration in the previous subsection. One distinguishes two different classes of gamma-ray production processes depending on the type of charged particles from which the gamma rays originate: in leptonic processes the gamma rays are produced from electrons and positrons, whereas in hadronic processes they are produced from protons (and, to a much smaller extent, from heavier nuclei). The main leptonic processes described below are synchrotron radiation, Bremsstrahlung, inverse Compton scattering and curvature radiation, whereas the main hadronic process is based on hadron collisions producing pions which subsequently decay.

### 1.3.1 Synchrotron radiation

Synchrotron radiation is produced when charged particles are accelerated<sup>2</sup> perpendicularly to their direction of propagation. In the processes relevant to astronomy, it is produced by high energy electrons and positrons accelerated by a magnetic field. The rate of energy loss of an isotropic population of charged particles (and so, the rate of emission of energy in photons) due to synchrotron radiation is:

$$-\frac{dE}{dt} = \frac{4}{3}\sigma_T c \frac{B^2}{2\mu_0} \left(\frac{v}{c}\right)^2 \gamma^2, \quad (1.2)$$

where  $\sigma_T$  is the Thomson scattering cross-section,  $B$  the magnetic field which accelerates the particles,  $\mu_0$  the vacuum permeability, and  $v$  and  $\gamma$  the speed and Lorentz factor of the particles. If the spectral distribution of the charged particle population follows a power-law with photon index<sup>3</sup>  $\alpha$ , the produced gamma rays follow a power-law with photon index  $1/2(1 + \alpha)$ . This means that the produced

---

<sup>2</sup>Here acceleration means a change of velocity. The speed is left unchanged for a radial acceleration, it is only the velocity direction which changes.

<sup>3</sup>For a power-law spectrum of the form  $dN/dE \propto E^{-\alpha}$  or a spectrum containing such a power-law factor,  $\alpha$  is called the photon index.

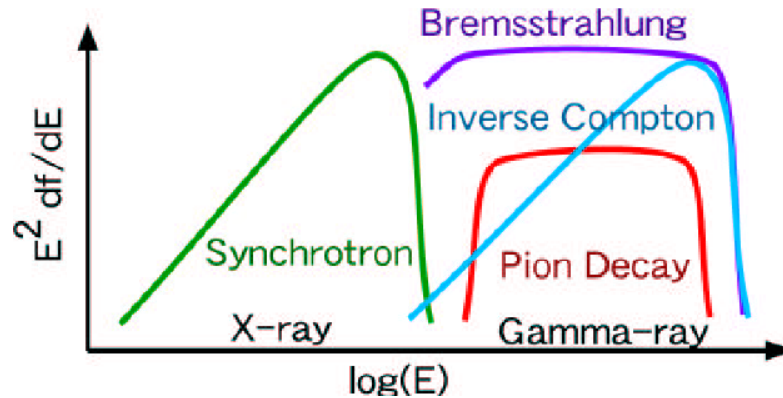


Figure 1.5: Illustration of the shape of the produced spectrum for the different acceleration mechanisms described in this section. Reproduced from [28]

gamma-ray spectrum is harder than the charged electron/positron parent spectrum, i.e., less steep. The shape of such a synchrotron spectrum is shown in figure 1.5.

However as can be seen from equation 1.2, the emission of synchrotron radiation leads to an energy loss of the particles in the parent distribution. This leads to a cooling time inversely proportional to the energy and the square of the magnetic field. This dependence with energy means that high energy particles cool down faster than low energy particles and get depleted earlier if they are not constantly resupplied. This can lead to a spectral cut-off in synchrotron spectrum from which the depletion of the parent electron/positron population can be assessed and so further information of its injection and surroundings can be gained.

Synchrotron emission has been observed in astrophysical sources from radio to low-energy gamma rays. Synchrotron radiation is characteristically polarized.

### 1.3.2 Bremsstrahlung

Bremsstrahlung radiation is produced by the interaction of an electron or a positron with the Coulomb field of an atomic nucleus. The rate of energy loss for a particle population is proportional to the energy of the particles. It follows that the photon index of the produced photon population is the same as that of the parent particle distribution. On average the photons produced in the Bremsstrahlung process have a third of the energy of the initial electrons or positrons. The shape of a Bremsstrahlung spectrum is also illustrated in figure 1.5.

### 1.3.3 Inverse Compton Scattering

In inverse Compton scattering, a high-energy electron or positron scatters on a low energy photon leading to an increase of energy for the photon and a decrease of energy for the charged particle. The cross-section for this process can be written in form of the unpolarized Klein-Nishina formula [29]:

$$\frac{d\sigma}{d\cos\theta} = \frac{3}{4}\sigma_T \frac{\epsilon_f^2}{\epsilon_i^2} \left( \frac{\epsilon_i}{\epsilon_f} + \frac{\epsilon_f}{\epsilon_i} - \sin^2\theta \right), \quad (1.3)$$

where  $\sigma_T$  is the Thomson cross section,  $\epsilon_i$  and  $\epsilon_f$  the initial and final energy of the photon and the scattering angle  $\theta$  the angular change of direction of the photon. From simple kinematics considerations, the final energy  $\epsilon_f$  only depends on the initial energy  $\epsilon_i$  and  $\theta$ :

$$\epsilon_f = \frac{\epsilon_i}{1 + \frac{\epsilon_i}{m_e c^2} (1 - \cos\theta)}, \quad (1.4)$$

where  $m_e$  is the electron mass (which has the same mass as a positron).

One usually distinguishes two regimes: the low energy ( $\epsilon_i \ll m_e c^2$ ) or "Thomson" regime in which the scattering is almost elastic ( $\epsilon_i \approx \epsilon_f$ ) and the cross-section reduces to the Thomson cross section:

$$\sigma \approx \sigma_T (1 - 2x) \approx \sigma_T, \quad (1.5)$$

where  $x = \frac{\epsilon_i}{m_e c^2}$ , and the ultra-relativistic "Klein-Nishina" regime ( $\epsilon_i \gg m_e c^2$ ) in which the cross-section can be approximated by:

$$\sigma \approx \frac{3}{8}\sigma_T \frac{1}{x} \left( \ln(2x) + \frac{1}{2} \right). \quad (1.6)$$

Whereas the cross-section is almost constant with energy in the Thomson regime, it falls off rapidly in the Klein-Nishina regime leading to a steepening of the spectrum. Indeed, an electron population with a power-law spectrum with photon index  $\alpha$  produces a gamma-ray power-law spectrum with photon index  $(1 + \alpha)/2$  in the Thomson regime and to the following more complex spectrum in the Klein-Nishina regime:  $dN_\gamma/dE_\gamma \propto E_\gamma^{-(\alpha+1)} \ln(x + \text{const})$ . In the Thomson regime, the rate of energy loss due to inverse Compton scattering of a single accelerated electron can be written as:

$$-\frac{dE}{dt} = \frac{4}{3}\sigma_T c U_\gamma \left( \frac{v}{c} \right)^2 \gamma^2. \quad (1.7)$$

There is therefore an easy relation between the power radiated in inverse Compton radiation  $P_{IC}$  and the power radiated in synchrotron radiation  $P_{\text{sync}}$  based on the

energy density in the radiation field (low energy photons on which the electrons scatter)  $U_\gamma$  and the energy density in the magnetic field  $U_B = B^2/(2\mu_0)$ :

$$\frac{P_{IC}}{P_{\text{sync}}} = \frac{U_\gamma}{U_B}. \quad (1.8)$$

In astrophysical sources, a process dubbed as synchrotron self-Compton considers a population of low energy photons that are produced through synchrotron radiation by high energy electrons moving through a magnetic field. Then, the same population of electrons interact with these low energy photons producing high energy photons through inverse Compton scattering. This leads to a typical two peak spectral energy distribution (SED, i.e., the spectrum over a big wavelength range reconstructed with multiple instruments), where one peak is due to the synchrotron radiation and the other one to the inverse Compton scattering as illustrated in figure 1.5 considering both synchrotron component (green curve) and the inverse Compton component (blue curve).

### 1.3.4 Curvature radiation

Curvature radiation [30] is produced when particles travel through a curved magnetic field and follow its field lines. In moderate magnetic fields the pitch angle between the magnetic field and the particle velocity changes slowly, which is why for synchrotron calculations often the initial pitch angle is used [31]. However, in strong magnetic fields the situation is very different as there the pitch angle can be reduced by orders of magnitude in very short timescales due to the damping of perpendicular motion during radiation making it necessary to consider the evolution of the pitch angle. This leads to the transition to the curvature radiation regime. Both the synchrotron and the curvature regime are approximations of the general description of a charged particle moving through a magnetic field which produces so-called synchro-curvature radiation. This curvature radiation is very relevant for some gamma-ray sources, such as pulsars (described in section 1.4). It is however not relevant for any study presented in this thesis and for this reason not presented in an as detailed manner.

### 1.3.5 Pion Decay

Gamma rays are not only produced from electrons and positrons, but can also be produced from protons and atomic nuclei. When a high energy proton interacts with a proton or nucleus in the interstellar gas, pions can be produced. There are three different types of pions: neutral pions ( $\pi^0$ ), positively charged pions ( $\pi^+$ ) and negatively charged pions ( $\pi^-$ ). Neutral pions decay predominantly in a pair of photons ( $\pi^0 \rightarrow \gamma + \gamma$ ) whereas charged pions decay predominantly into a

(anti-)muon and a (anti-)neutrino ( $\pi^+ \rightarrow \mu^+ + \nu_\mu$ ,  $\pi^- \rightarrow \mu^- + \bar{\nu}_\mu$ ). So, gamma rays can be produced by proton-proton (or proton-nucleus) interactions producing a neutral pion which subsequently decays to gamma rays. As mentioned earlier, this is the main hadronic process leading to gamma rays. However, proton-proton collisions can also produce other mesons of which some decay into gamma-rays, even though these processes have a much smaller contribution to the gamma rays produced in hadronic processes.

The average energy of these gamma rays is about one tenth of the initial proton energy. The produced spectrum is very similar to the spectrum of the initial proton population at high energy. It however has a characteristic bump at the half of the neutral pion rest mass (at 67.5 MeV), which constitutes the threshold for pion production and corresponds to the energy the emitted photons take in the pion rest frame, due to the neutral pions produced at low energies (energetically dominated by their rest mass). A typical pion spectrum is also illustrated in figure 1.5.

### 1.3.6 Resolving the different radiative processes

In practice, differentiating between these various radiative processes for observed gamma-ray emission is often very difficult. Indeed, each experiment can mostly only observe the spectrum over a small energy range to which it is sensitive and often there are no strong a priori theoretical constraints excluding a radiative process. For this reason, the spectra measured by multiple experiments are usually combined into an SED and different models are tested in order to find the model which fits best to the data and so constrain the models which describe the data. For inverse Compton scattering for example, the electrons producing this inverse Compton radiation are also expected to emit synchrotron radiation at lower energies in presence of a magnetic field. The absence of such emission at lower energy can so exclude models which require inverse Compton scattering and a high magnetic field. Leptonic models are in general mostly expected to emit in multiple wavelength bands through multiple different emission components, whereas hadronic emission is mostly only produced through pion decay and so only visible in a limited wavelength band. This gives one handle on the distinction of emission processes. Additional information could in future be gained by measuring neutrinos from a given source, as they are a clear sign of hadronic acceleration.

## 1.4 Gamma-ray sources

This section gives a short introduction to sources in which photons are accelerated up to gamma-ray energies. A big variety of such sources has been discovered since the advent of gamma-ray astronomy and numerous source categories emitting in

gamma rays are possibly still undiscovered, as the number of source categories discovered in gamma rays is still increasing. In the following, some of the most common gamma-ray sources are discussed.

### 1.4.1 Supernova Remnants

Supernovae can occur at the end of life of stars depending on their properties. Indeed, there are two different categories of supernovae. Supernovae of type II, Ib and Ic occur at the end of the life of a massive star with at least eight solar masses [32]. When it runs out of fuel radiation pressure can no longer counter-balance its gravity and the star collapses on itself. This leads to an explosion in which the external shell is ejected whereas the interior of the star collapses further to a neutron star or a black hole depending on the mass of the progenitor star. Supernovae of type Ia can occur in binary systems (systems with two bound astronomical objects) in which one of the objects is a white dwarf (remnant of a star which was not heavy enough to undergo a supernova explosion at the end of its life). This white dwarf can accrete matter from its companion making the white dwarf so heavy that it reaches the Chandrasekhar limit of 1.4 solar masses [33] and collapses. This leads again to a supernova explosion. The release of energy in both of these supernovae explosions is about  $1 \times 10^{58}$  J [34].

Supernovae are very important for the formation of solar systems as we know them, as they are the main producer of very common heavy elements [35]. Indeed, during the collapse of the supernova predecessor the pressure and temperature in its core is so high that the elements in it fuse into heavier elements. The origin of the different elements found in our solar system according to our current understanding is shown in figure 1.6.

Material ejected with speeds of about  $5000 \text{ km s}^{-1}$  to  $20\,000 \text{ km s}^{-1}$  [37] during the supernova explosion, gives rise to what is called a supernova remnant (SNR). This material creates a shock front in the interstellar medium. This so-called forward shock is slowed down by the surrounding medium leading to the formation of a second shock in reverse direction inward to the stellar ejection, the reverse shock. [38]. This process develops over three phases: First the "free expansion phase" in which the shock is barely braked by the surrounding medium and the shock velocity is so approximately constant. This phase lasts until the swept-up mass of the surrounding material has reached the initial mass of the ejecta. In the second so-called "Sedov phase", most of the energy has been transferred from the ejecta to the shock-heated shell of surrounding medium and the shock is adiabatically braked in this phase. After this phase, there is a third phase ("radiative phase") in which radiative cooling dominates the energy losses and the expansion speed of the ejecta. These three phases can last up to hundred or thousand of years. In these shocks, cosmic rays can be accelerated and subsequently create

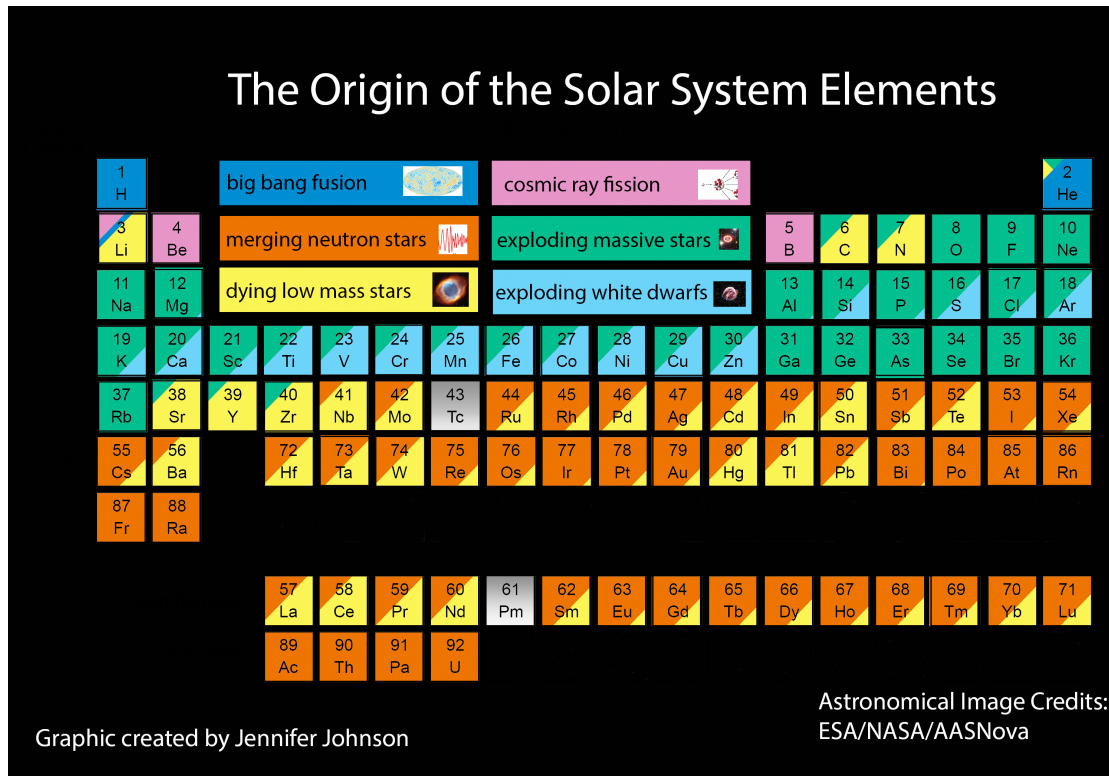


Figure 1.6: This figure illustrates the origin of the elements in our solar system according to our current knowledge. Hydrogen and helium were mostly produced during the big bang and are so as old as the Universe. Lithium, carbon and nitrogen and some heavier elements are mostly formed during nucleosynthesis in stars (i.e., during the fusion reaction fuelling the star). beryllium and bore are formed during the fission of heavier elements in cosmic rays. Then elements from oxygen to rubidium are mostly formed in supernovae. And finally, the most heavy elements are formed during the merger of neutron stars. Reproduced from [36].

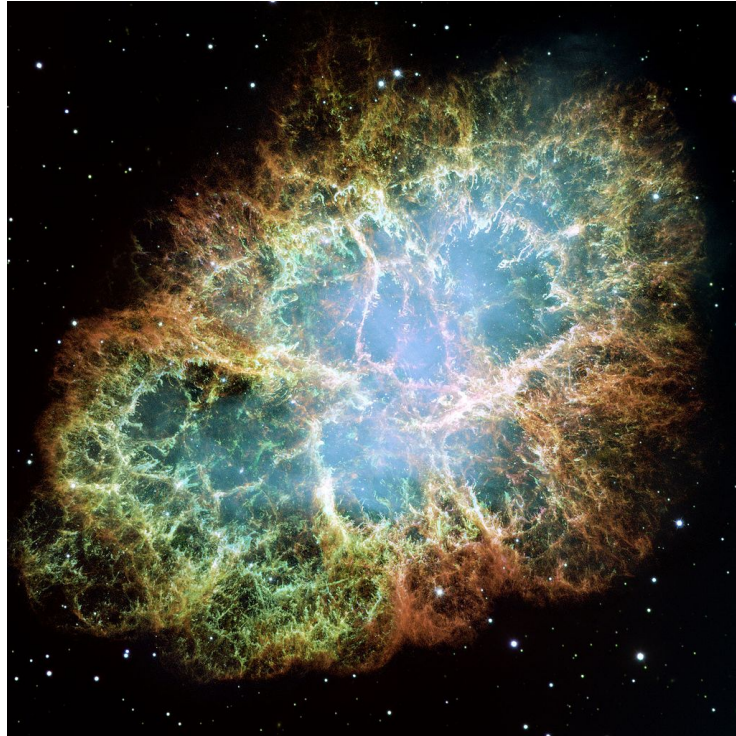


Figure 1.7: False colour mosaic image of the Crab Nebula taken with the Hubble space telescope. The Crab Nebula is a remnant of a supernova which exploded in 1054 and was observed by Asian astronomers at that time. The collapsed star which exploded is now a rotating and magnetized neutron star and called Crab Pulsar. The Crab Nebula is one of the brightest sources in gamma-ray astronomy as seen from Earth. Reproduced from [39].

gamma rays, mostly during the free expansion phase and Sedov phase. As particles are accelerated to higher and higher energies during the free expansion phase in which the shock velocity is approximately constant, the maximum particle energy is expected to increase linearly with time in this phase. After this phase the shock velocity decreases and so the maximum energy decreases too with time. Figure 1.7 shows an image of such a supernova remnant, the Crab Nebula.

### 1.4.2 Pulsar Wind Nebula

Pulsars are very fast rotating neutron stars with periods of seconds to milliseconds [41]. They are the final remnant of supernova explosions of massive stars. The reason why they rotate so fast is that the angular momentum of the much larger progenitor star is conserved and mostly retained in the neutron star, which only has a tiny fraction of its progenitor star's radius (about 10 to 15 km). They also have strong magnetic fields originating from the progenitor star (about  $1 \times 10^8$  T). In these, charged particles are accelerated and ejected at the polar caps or in outer regions extending to or beyond the light cylinder (i.e., the cylindrical surface with radius  $R_{LC} = c/\Omega$  on which particles rotating with the pulsar angular velocity  $\Omega$  would have the speed of light) [42]. These emitted jets can be observed from Earth when the jet direction intersects the observation direction, giving rise to a pulsed signal from the radio to the gamma-ray band.

The accelerated charged particles follow the field lines out of the pulsar magnetosphere until they reach the light cylinder, after the crossing of which they would have to rotate faster than the speed of light to rotate with the pulsar, and then escape. This leads to a highly magnetized wind of particles leaving the pulsar. This wind is decelerated as it expands in the cold supernova ejecta creating a wind termination shock in which electrons and positrons are accelerated and so creates a so-called pulsar wind nebula [42]. These electrons/positrons then produce (non-pulsed) synchrotron emission from the radio to beyond the X-ray band in the magnetic field of the pulsar wind nebula. Often the size of a pulsar wind nebula decreases with energy as high energy particles lose their energy faster and so do not travel as far as low energy particles. This emitted synchrotron photons then again interact with the relativistic particles in the shocked wind leading to the emission of gamma rays through inverse Compton scattering (in a Synchrotron Self-Compton scenario).

The star which formed the Crab Nebula, depicted in figure 1.7, became a pulsar after its supernova explosion, and its pulsar wind supports such a nebula.

### 1.4.3 Binary Systems

Stars in binary (or higher-order) systems are very common. The multiplicity frequency (i.e., the ratio of the number of systems with more than one star to the total number of systems) increases strongly with stellar mass; more than 50% of the systems with stars with masses above 5 solar masses are binary or higher order systems [43].

These systems can emit gamma rays if one of the two (or more) members is a compact object, i.e., a neutron star or a black hole, as these binaries are characterized by high magnetic fields and radiation densities [44]. This gamma-ray emission arises either, because the neutron star forms a pulsar creating a pulsar wind nebula or because the compact object accretes the stellar wind of the companion star. Due to the motion of these binaries around their common centre of gravity and to the fact that the neutron stars can have an intrinsically pulsed emission, the gamma-ray emission from these binary systems observed on Earth is often very variable and irregular in time.

### 1.4.4 Active Galactic Nuclei

Active galactic nuclei are super-massive black holes accreting matter at the centre of galaxies. They have masses of millions to billions times the mass of the sun. The accretion of matter onto the black hole leads to the formation of an accretion disk surrounding the black hole which can be heated up through the accretion and so lead to thermal emission. This accretion can power relativistic plasma jets as illustrated in figure 1.8, which shows an example of such an active galactic nucleus. In this case the nucleus is dubbed as radio-loud as these jets lead to a strong radio emission, opposed to radio-quiet active galactic nuclei in which such a jet does not form. Only about 10% of the active galactic nuclei are radio-loud. The directions of these jets follows the angular momentum of the accretion disc and the spin axis of the black hole. In these jets, gamma rays can be produced, probably by inverse-Compton scattering either on photons from the accretion disk or the broad line region or from photons emitted as synchrotron radiation inside the jet (Synchrotron Self-Compton scenario) [45].

The gamma-ray emission, its intensity and spectrum observed on Earth is highly dependent on the viewing angle on the active galactic nucleus and so they are classified in different categories according to the viewing angle [45]. Most active galactic nuclei observed in gamma rays are so-called blazars in which the jet is pointing towards Earth as they are the brightest as seen from Earth.

The emission from active galactic nuclei is variable on timescales from minutes to thousand of years [45]. The lower bound sets limits on the extension of the emission region, as the emission from a region of a given size cannot vary faster

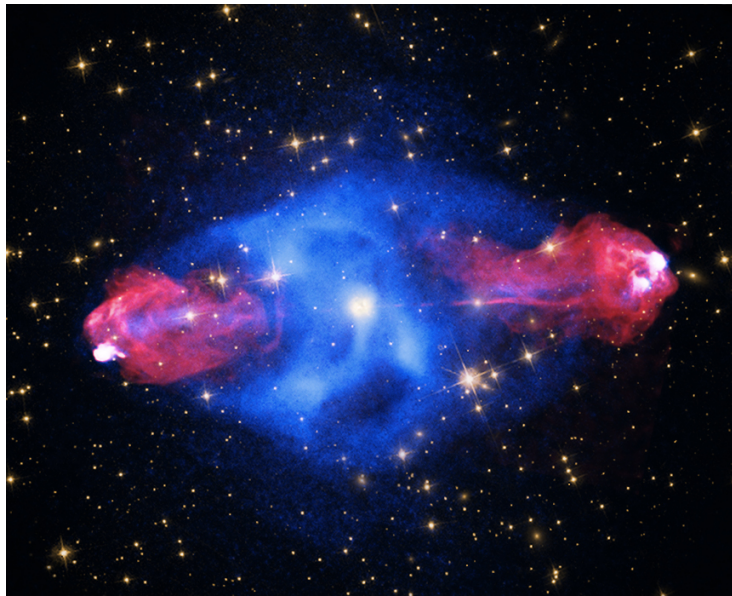


Figure 1.8: False colour image of Cygnus A, a galaxy with an active galactic nucleus at its centre, showing data from different experiments. X-ray data from the Chandra Observatory are shown in blue, radio emission in red and optical data from Hubble in yellow. The two jets formed due to the accretion of matter on the central black hole can be seen very well in the non-thermal radio emission. Reproduced from [40].

than the time needed to cross this region at the speed of light (according to the "causality argument" [46]).

### 1.4.5 Gamma-Ray Bursts

Gamma-ray bursts are very short, very intense emission of gamma rays and are the brightest electromagnetic explosions in the universe [47]. They are divided in two phases: A prompt phase in which an initial flash of gamma rays is produced and a longer lasting afterglow in which the emission is decaying slowly [48]. The prompt phase lasts from tens of milliseconds to minutes whereas the afterglow can last several months or even years [48].

Short gamma-ray bursts, whose prompt phase lasts less than a few seconds, are thought to be due to mergers of compact objects, and long gamma-ray bursts thought to be due to supernovae of very massive stars [48]. Gamma-ray bursts were first detected by satellite experiments in 1967 [49] and it took until 2018 for their first detection by a ground-based Imaging Atmospheric Cherenkov Telescope (IACT) array [50].

### 1.4.6 Other gamma-ray sources

In addition to these five source types discussed here, there are numerous other gamma-ray sources which cannot all be discussed here. Gamma-ray emission has been detected with IACTs from stellar clusters such as Westerlund I [51] in which individual sources might inject high energy particles, from starburst galaxies such as NGC 253 [52] and superbubbles such as 30 Dor C [53]. Moreover, a first nova has been detected with an IACT in August 2021 [54]. These recent discoveries of new source categories with IACTs in 2018 (Gamma-Ray Burst) and 2021 (Novae) show that gamma-ray astronomy is a very active field and that there might be many source categories still to be detected in very-high-energy gamma rays.

## 1.5 Detection of gamma rays

As cosmic gamma rays are absorbed by the atmosphere and so do not reach the ground, they were first observed by balloon and satellite experiments. One of the first successful satellite detectors was the OSO-3 satellite, launched in 1967, which detected 621 cosmic gamma-ray events [2]. The first satellite to detect several point sources was SAS-2 which was launched in 1972 [55, 56]. Then, a series of more advanced gamma-ray satellites such as COS-B, CGRO, INTEGRAL and *Fermi* were launched with increasing sensitivity and energy range [57, 58, 59, 60].

First ideas to indirectly detect gamma rays using ground-based telescopes to detect atmospheric showers of secondary particles produced by gamma rays<sup>4</sup> arose in the 60s [61]. Even though there have been many attempts to apply this technique, it took until 1989 for the discovery of the first point source with a ground-based Cherenkov telescope. In this year Whipple observed the Crab Nebula at TeV energies [62]. HEGRA was the first Cherenkov telescope array as it was constituted of five telescopes [63]. It thus allowed for the first time stereoscopic observations. Later on, more advanced Cherenkov telescope arrays reaching a higher sensitivity and a larger energy range were built.

This section first gives a short overview on the working principle of a modern space-based gamma-ray detector. Then, it discusses ground-based gamma-ray astronomy, and specifically Cherenkov telescope arrays. They are described in detail as it is the detector on which this work is based. Finally, this section gives a short overview of other ground-based techniques to detect gamma rays.

### 1.5.1 Satellite-based gamma-ray experiments

Currently, multiple gamma ray satellites are in operation. Some of them are general-purpose instruments such as AGILE, INTEGRAL and *Fermi* [64]. Others have a more specific purpose, such as *Swift*, which was specifically designed to detect gamma-ray bursts and is constituted of three different instruments sensitive to different energy ranges, namely gamma rays, X-rays and UV/optical, to fulfil its purpose [65].

Modern general-purpose gamma-ray satellites are mostly based on the pair creation principle. Such a satellite-borne pair creation detector is illustrated in figure 1.9. Pair creation is the conversion of a high energy photon into an electron and a positron in interaction with the Coulomb field of a nucleus. For this interaction to be possible, the photon needs to have at least an energy of twice the electron (and positron) rest mass of 511 keV. At high energies (MeV energies and above), pair creation is the dominant interaction of photons with matter (compared to Compton radiation and the photo-electric effect which are dominant at lower energies). Pair creation telescopes are constituted of multiple thin conversion foils made out of a dense material in which the conversion of the photon into an electron and positron can occur [60]. Behind each of these conversion foils, there is usually a detector plane which records the position of each charged particle passing it and so allows to determine in which foil the photon has been converted and record the tracks of the electron and positron after conversion. After their passing through the conversion foils and trackers, the electrons and positrons enter a calorimeter which allows their energy to be measured and so determine the energy of the initial

---

<sup>4</sup>This process is described in the following of this section.

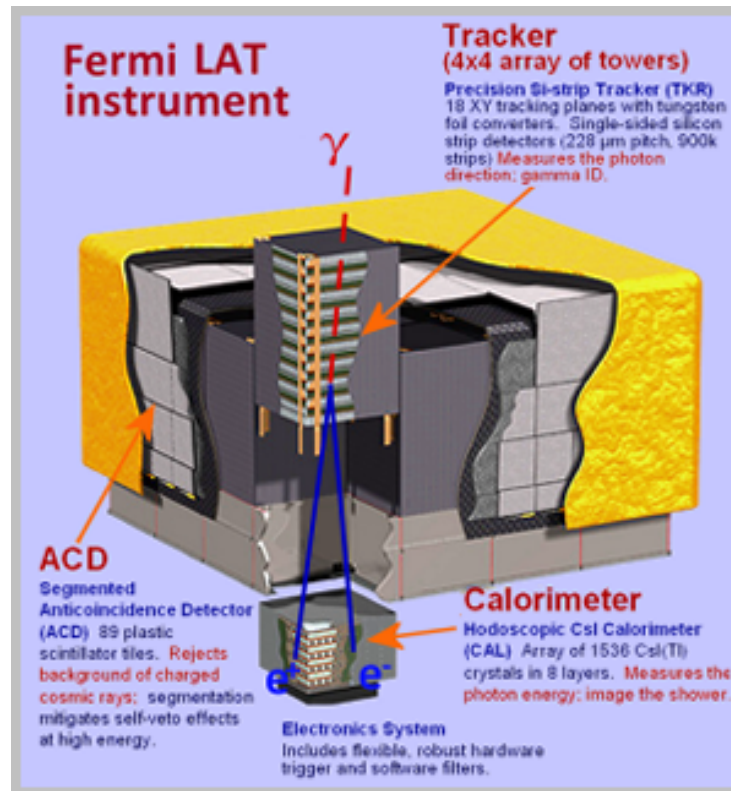


Figure 1.9: Scheme of *Fermi*-LAT, a space pair creation gamma-ray detector currently in operation. A gamma-ray entering the tracker, converts in a tungsten conversion foil into an electron and positron, which are then tracked by the silicon strip detectors. The electron and positron then enter the CsI calorimeter where their energy is measured. In addition, one can see the anticoincidence detector which rejects charged cosmic rays. Reproduced from [66].

photons. In the calorimeter, an entering particle initiates a particle shower of secondary particles in its dense material. The energy deposited in the calorimeter by these secondary particles is sampled by converting a well-known fraction (through initial calibration) of the energy in a measurable quantity (most often visible light). This then allows an energy determination of the electron and positron having entered the calorimeter and taking into account the energy losses in the tracker to reconstruct the initial photon energies. The whole detector is usually covered by an anti-coincidence unit which detects incoming charged particles and so prevents the misinterpretation of entering electrons or positrons as photons which converted inside the detector.

An example of a satellite that uses the pair creation principle is *Fermi*. *Fermi* consists of two different detectors, the Gamma-Ray Burst Monitor (GBM) and the Large Area Telescope (LAT). GBM is a specific purpose experiment to detect gamma-ray bursts based on scintillation detectors. LAT, whose working principle is illustrated in figure 1.9, is a gamma-ray detector based on the pair creation principle with tungsten conversion foils, fine granularity silicon detector planes and a caesium iodide calorimeter [60]. LAT has an instantaneous field of view of 20% of the sky and could cover the entire sky within three hours before a hardware failure on the motors of one of the solar panels in March 2018 restricting the rotation capabilities of *Fermi*. It is sensitive to energies from 20 MeV up to TeV energies.

The lower energy limit of such pair creation telescopes is due to pair creation being a less dominant interaction channel of photons at low energies (and not at all possible below 1.022 MeV) as Compton scattering takes over and to multiple scattering of the pair components in the tracker components deteriorating the direction reconstruction of the incoming photons. The upper energy limit is due to the small sensitive area. This means that the higher the upper energy limit one wants to achieve (at a given sensitivity), the bigger the required detector size. However, detector size for space-based experiments is limited due to the maximum load on rockets and prohibitive costs. For this reason, ground-based methods are used for the detection of very-high-energy gamma rays.

## 1.5.2 Imaging atmospheric Cherenkov telescope arrays

### Gamma-ray-induced atmospheric showers

A high energy photon entering the atmosphere interacts with the Coulomb field of an atomic nucleus of an atmospheric component leading to the production of an electron and a positron. This electron and positron then emit photons by Bremsstrahlung in interaction with a nucleus, which can again undergo pair production. These two processes so lead to a continuous multiplication of the number

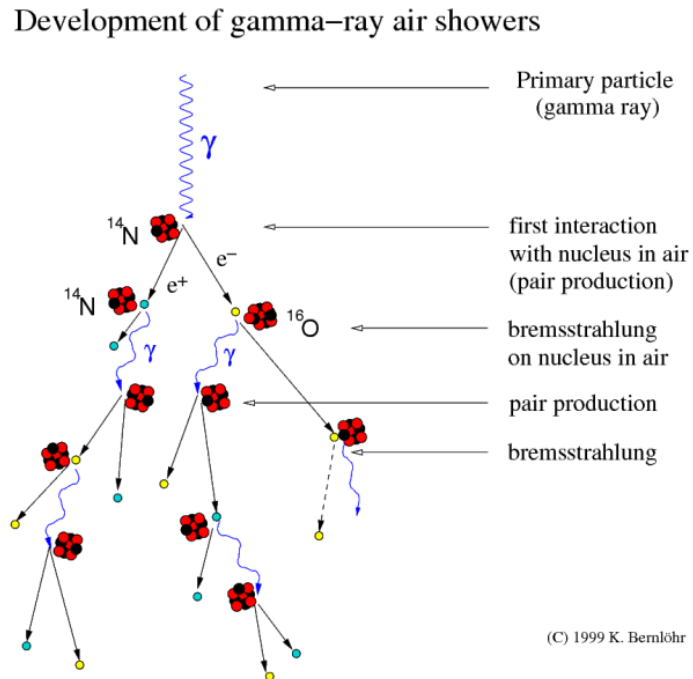


Figure 1.10: Scheme showing the development of an atmospheric shower for a gamma ray entering the atmosphere. The gamma ray interacts with the Coulomb field of an atmospheric nucleus leading to the formation of an electron and positron by pair production. These two particles then emit gamma rays by Bremsstrahlung which undergo pair creation again leading to extended atmospheric showers of particles. Reproduced from [67]

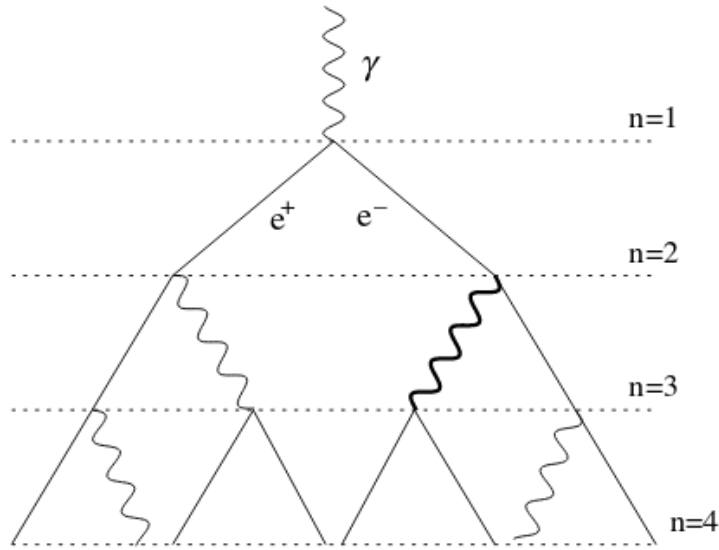


Figure 1.11: Development of an atmospheric gamma-ray shower as described by the simplified Heitler model. Reproduced from [68]

of particles creating a huge so-called atmospheric shower which can be constituted of billions of particles. The development of such an atmospheric shower is schematically shown in figure 1.10. During the creation of this atmospheric shower, the energy of the initial particle is distributed over the particles in the shower which leads to the eventual extinction of the shower: once the energy of the electrons and positrons is too low, they start ionizing and exciting atoms instead of creating photons by Bremsstrahlung. The critical energy  $E_C$  where Bremsstrahlung and ionization losses are equal is 85 MeV [68]. The shower extinguishes rapidly once the electrons and positrons constituting it have reached this energy.

These gamma-ray showers are often described by the very simplified Heitler model which can reproduce the basic features of shower development [68]. It is illustrated in figure 1.11. In this model, one assumes that each electron or positron loses half of its energy to a gamma ray after having traversed an atmospheric depth  $R$  and that each gamma ray undergoes pair creation leading to an electron and a positron with the same energy after the same atmospheric depth  $R$ . The atmospheric depth describes the amount of matter traversed by a particle and can be converted into a distance  $d$  knowing the density of the atmosphere  $\rho$  as a function of altitude  $z$ :

$$R = \int_{z_0}^{z_0+d} \rho(z) dz \quad (1.9)$$

One assumes that  $R = X_0 \ln 2$  [68], where  $X_0$  is the electromagnetic radiation

length in the atmosphere defined as the amount of matter an electron or positron needs to traverse for its energy to be reduced to  $1/e$  of its initial value [69]. The atmosphere has a radiation length of  $36.6 \text{ g cm}^{-2}$  [70] for a total thickness of about 28 radiation lengths [71]. The radiation length also corresponds to  $7/9$  of the mean free path of a photon before it undergoes pair production [69]. This factor of  $7/9$  is neglected in the Heitler model. The energy distribution of the produced particles is ignored as well for both Bremsstrahlung and pair creation and replaced by the simplified assumption that the daughter particles have 50% of the parent particle energy. All other energy losses are neglected too.

In the Heitler model, the evolution of the energy of the particles in the shower in function of the total traversed atmospheric depth  $X$  (defined as in equation 1.9 with  $d \rightarrow \infty$ ) can simply be written as:

$$E(X) = E_0 \exp\left(-\frac{X}{X_0}\right), \quad (1.10)$$

where  $E_0$  is the energy of the initial particle. The maximum of shower development occurs when its particles have reached the critical energy  $E_C$ , which gives the depth of maximal shower development  $X_{\max} = X_0 \ln \frac{E_0}{E_C}$  [68]. Using a hydrostatic atmospheric model in which the atmospheric pressure and density depend exponentially on the altitude, one can transform the atmospheric depth in an altitude and show that the altitude of shower maximum for a 1 TeV particle is at about 9 km above sea level [72].

One of the main difficulties in ground-based gamma-ray astronomy is that not only photons lead to atmospheric showers; charged particles can produce atmospheric showers too. High energy electrons and positrons lead to showers which can hardly be distinguished from photon induced showers on an individual basis as they develop in exactly the same way (beside electrons and positrons starting to emit Cherenkov radiation a bit higher in the atmosphere as they do not need to convert). However, one can disentangle them on a statistical basis as electrons and positrons reach Earth almost uniformly from all directions due to turbulent galactic magnetic fields, whereas photons travel straight once they have left the emission region and so can be attributed to individual sources. An excess of events from a given direction signs the presence of a gamma-ray source. In addition to electrons, positrons and gamma rays, high energy hadrons entering the atmosphere also lead to atmospheric showers. These differ from electromagnetic showers because of different elementary processes occurring in their development. Nuclear interactions in these showers lead to the creation of pions and K mesons, which decay in gamma rays, muons and neutrinos. This multitude of different particles and processes in these showers and larger transverse momentum exchanges lead to wider and much more irregular shower shapes and can be distinguished from electromagnetic showers due to this.

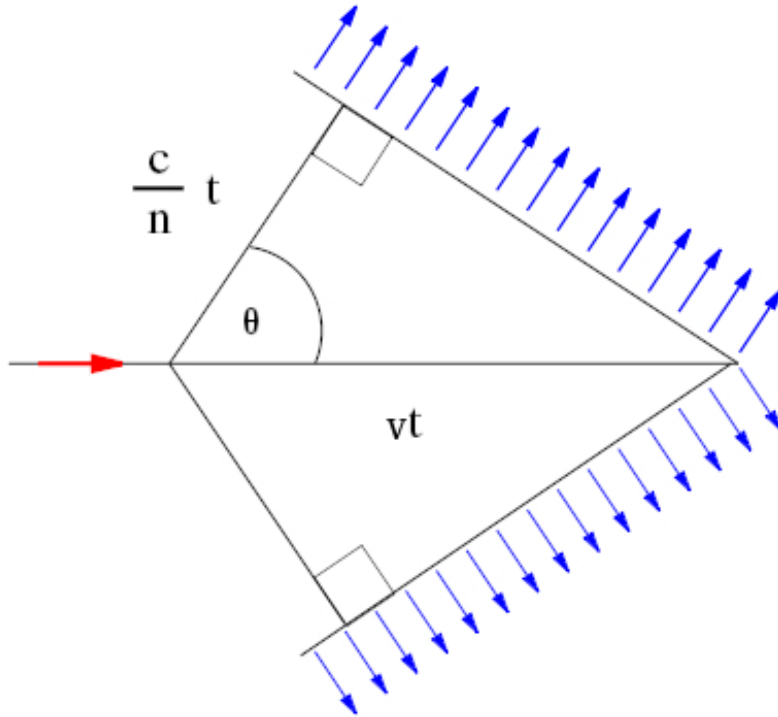


Figure 1.12: Scheme of the emission of Cherenkov radiation by a charged particle (whose path is indicated by the red arrow) traveling faster than the speed of light in a medium. The Cherenkov radiation is emitted under an opening angle  $\theta$  geometrically inferred from the speed of the light in the medium and the speed of the particle. Adapted from [74].

### Cherenkov radiation produced in atmospheric showers

Charged particles traveling with a speed  $v$  faster than the speed of light  $c/n$  through a medium with refractive index  $n$  emit Cherenkov radiation with an emission angle  $\theta = \arccos\left(\frac{c}{nv}\right)$  [73] as illustrated in figure 1.12. The number of photons  $N$  emitted per unit wavelength  $\lambda$  and per unit path length  $x$  of this radiation produced in a medium with a permeability equal to 1 is given by:

$$\frac{d^2N}{dx d\lambda} = 2\pi\alpha \frac{\sin^2\theta}{\lambda^2}, \quad (1.11)$$

where  $\alpha$  is the fine structure constant [75].

The speed of the electrons and positrons in atmospheric showers induced by gamma rays is faster than the speed of light in the atmosphere and so produce Cherenkov radiation. Even though the emitted Cherenkov spectrum has a  $1/\lambda^2$  dependence, most of the ultraviolet part of the spectrum is absorbed in the atmosphere, leading to the spectrum at ground peaking at wavelengths of about

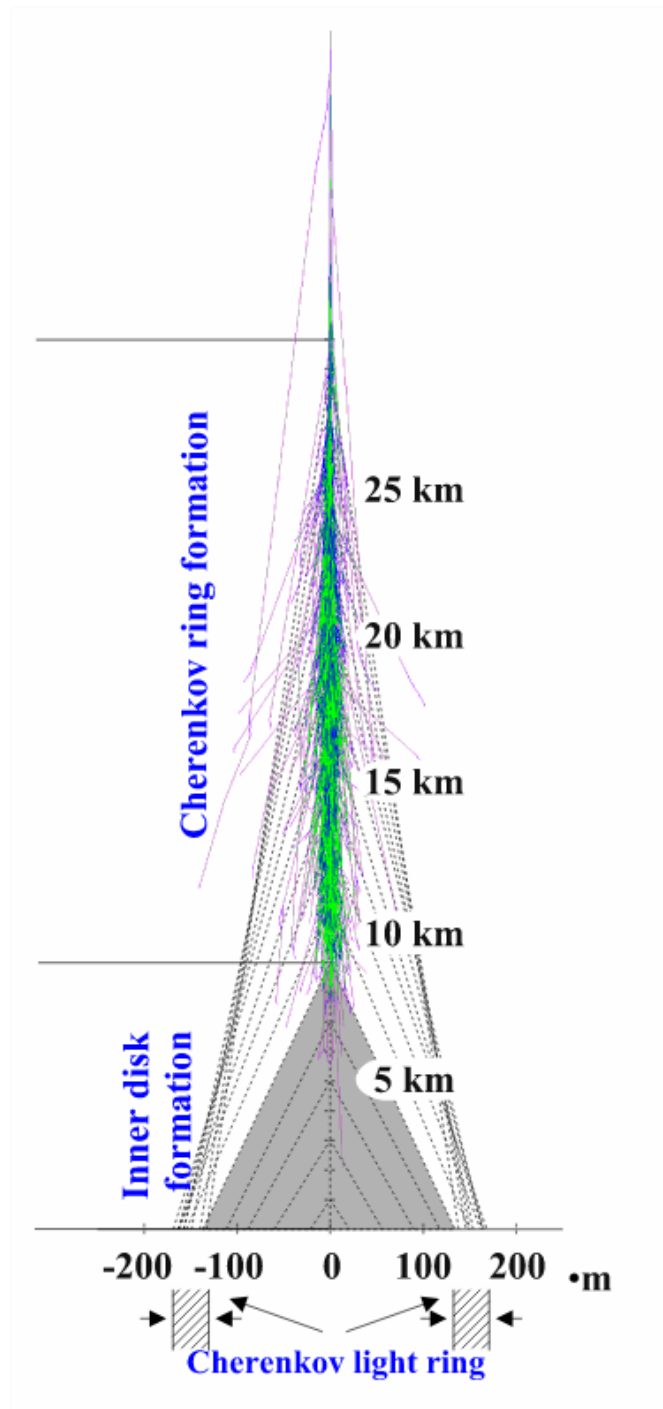


Figure 1.13: Illustration of the almost compensation of the decrease of the opening angle and the increase of the distance of propagation with the altitude leading to the formation of annulus of Cherenkov light on the ground. Reproduced from [72]

400 nm, which is the wavelength of visible violet light. The exact part of absorbed ultraviolet light depends on the altitude of emission of the Cherenkov radiation: The higher this altitude the more the ultraviolet part of the spectrum is absorbed. As the Cherenkov radiation is emitted with a precise opening angle and the particles in the shower are largely collimated, the emission at a given altitude leads to a ring on the ground whose radius depends on the distance of propagation and the refractive index at the altitude of emission (through the opening angle). Whereas the opening angle decreases as altitude increases, the distance of propagation increases with altitude and these both effects almost compensate each other (down to altitudes of 10 km [72]) leading to the formation of a light annulus on the ground with a radius of about 125 m [76]. Cherenkov radiation emitted at lower altitudes fills this annulus leading to a light pool which is brighter at the edge. The radius of the formed annulus slightly depends on altitude and energy, however does not differ much from 125 m for altitude between 0 m and 3500 m above sea level and photon energies below 1 TeV. For higher altitudes, the annulus starts to disappear, starting with the highest energies. The duration of such a Cherenkov event on the ground is few ns.

### **Detection of this Cherenkov radiation with optical telescopes**

This Cherenkov radiation emitted by atmospheric showers can be detected by Imaging Atmospheric Cherenkov Telescope (IACT) arrays as are described at the end of this subsection. Currently, there are three major Cherenkov telescope arrays in operation, namely MAGIC, VERITAS and H.E.S.S. These three arrays are shown in figure 1.14. MAGIC (Major Atmospheric Gamma Imaging Cherenkov) is constituted of two telescopes of 17 m diameter each located in La Palma, one of the Canary Islands. The MAGIC telescopes have a field of view of  $3.5^\circ$  and are able to cover an energy range from 50 GeV to 50 TeV [80]. VERITAS (Very Energetic Radiation Imaging Array System) is constituted of four telescopes of 12 m diameter each located in Arizona. The VERITAS telescopes also have a field of view of  $3.5^\circ$  and are sensitive to energies between 85 GeV and 30 TeV [81]. H.E.S.S. (High Energy Stereoscopic System) is constituted of five telescopes, four with a diameter 12 m and one with a diameter of 28 m, located in Namibia [82]. They have a field of view of  $5^\circ$  respectively  $3.17^\circ$  [83] and are able to cover an energy range from 20 GeV [84] to 100 TeV [82]. Being located on the Southern hemisphere, it is the only of the three arrays able to observe the Southern sky and in particular the central region of our Galaxy.

Following up on the success of these three existing arrays, a next generation IACT array, CTA (Cherenkov Telescope Array), is planned. This observatory will be constituted of two arrays, one in the Southern hemisphere, in Chile, and one in the Northern hemisphere, on La Palma, which will allow to observe both the

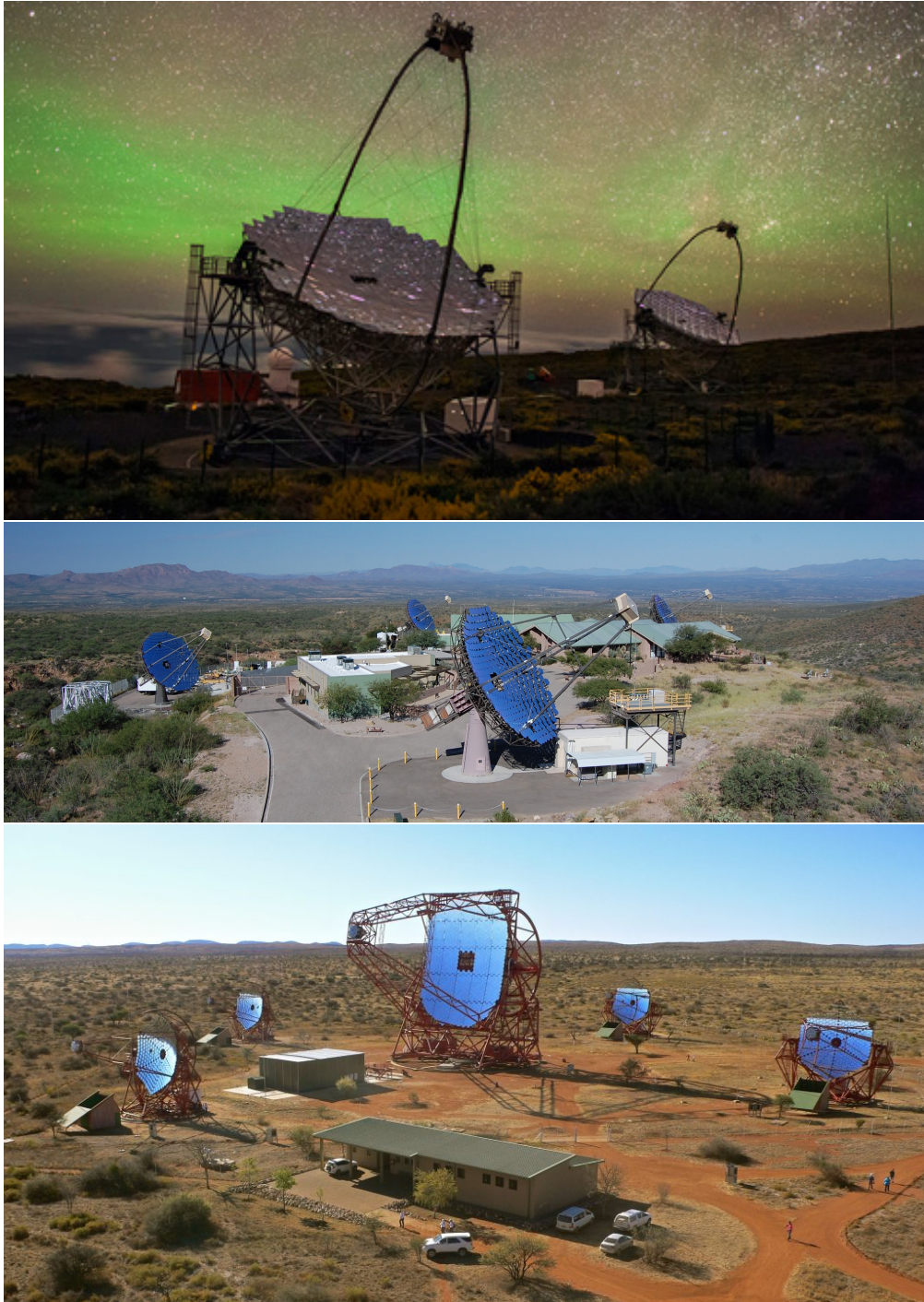


Figure 1.14: The three major Imaging Atmospheric Cherenkov Telescope Arrays currently in operation. Top: MAGIC, centre: VERITAS, bottom: H.E.S.S. Reproduced from [77], [78] and [79].

Northern and Southern sky. It will be constituted of telescopes of three different sizes: the Large-Sized Telescopes (LST) with a diameter of 23 m, the Medium-Size Telescopes (MST) with a diameter of 11.5 m and the Small-Size Telescopes (SST) which will be constituted of two mirrors - one with 4.3 m diameter and one with 1.8 m diameter [85]. The SSTs use a Schwarzschild-Couder design with two mirrors in order to achieve a large field of view with a small camera [86]. The use of three different telescope types will enable CTA to be sensitive to a larger energy range compared to existing arrays, from 20 GeV to 300 TeV [87]. In total, CTA is planned to have 19 telescopes on the Northern site and 99 telescopes on the Southern site [85] (as most of the Milky Way with its large number of sources can only be observed from the Southern site). This much higher number of telescopes and the use of novel technologies is expected to increase the sensitivity by one order of magnitude compared to current operational Cherenkov telescope arrays and to reach an unprecedented energy and angular resolution [87].

All the major Cherenkov telescopes currently in operation have the same operation principle. They are constituted of a big segmented mirror which reflects part of the faint Cherenkov light emitted by the atmospheric shower and focuses it on an imaging camera. This imaging camera has to be very fast as the duration of Cherenkov events is only few ns. For this reason, the pixels of the imaging camera are constituted of photo-multiplier tubes (PMT) on which light collectors, named Winston cones, are mounted to reduce the death space and shield the PMTs from light from the ground (albedo light). These PMTs are then connected to fast electronics to allow signal readout. The telescopes can be rotated in azimuth and altitude in order to be able to observe different positions on the sky.

The amount of emitted Cherenkov light being almost proportional to the primary particle energy, low energy gamma rays entering the atmosphere produce less Cherenkov light than high-energy gamma rays. For this reason, one needs larger mirrors to be able to collect enough light to detect gamma rays of lower energies. High-energy gamma rays are, on the other hand, less frequent. For this reason, in order to detect high energy gamma rays, one uses many telescopes with smaller mirrors spread over a large area to increase the chance of seeing such a gamma ray. Other important parameters of IACTs are the field of view, usually of the order of a few degrees, which determines which amount of the sky can be observed simultaneously, and the number of pixels (hundreds to a few thousand) which is important for the sensitivity and the angular resolution.

Combining IACTs in arrays of multiple telescopes allows stereoscopic observations. In these observations, gamma-ray events are recorded with multiple telescopes which reduces the background and improves the direction reconstruction of the shower and so the angular resolution. A more detailed description of the working principle of H.E.S.S., a Cherenkov telescope array, can be found in the



Figure 1.15: The HAWC observatory, a water Cherenkov observatory located at an altitude of 4100 m on the flanks of the Sierra Negra volcano in Mexico. Reproduced from [88]

next chapter as it is the instrument used in the preparation of this thesis.

### 1.5.3 Other ground-based gamma-ray detectors

In addition to IACTs, other detectors of atmospheric showers induced by gamma rays have been developed. One of the most successful is based on water Cherenkov detectors. They are constituted of large water tanks which are equipped with PMTs. If electrons and positrons produced in atmospheric showers enter these water tanks and travel faster than the speed of light in the water, they emit Cherenkov radiation which is then recorded by the PMTs. These detectors need to be at high altitude as otherwise most of the showers would be extinguished in the atmosphere before reaching the detector. These water Cherenkov detectors are sensitive to higher energy ranges and have much larger field of views than IACTs, but a worse angular resolution and are for this reason often referred to as "survey instruments". They are so complementary to IACTs.

HAWC (High Altitude Water Cherenkov observatory), displayed in figure 1.15, is one of the water Cherenkov detector currently in operation. It is located on the flanks of the Sierra Negra volcano in the Mexican state of Puebla at an altitude of 4100 m and is constituted of 300 water tanks, each one equipped with 4 PMTs [89]. HAWC is sensitive to energies between 100 GeV and 100 TeV and is able to observe

two-thirds of the sky in each 24-hour period [89].

SWGGO (The Southern Wide-field Gamma-ray Observatory) is a planned next generation water Cherenkov detector in the Southern hemisphere in order to complement the current instruments in the Northern hemisphere and cover a larger part of the sky at the highest energies [90]. It is planned to be built in South America at an altitude of more than 4500 m. It is foreseen to be constituted of a dense inner detector with about 4000 detection units and a less dense outer array with about 1000 detector units and so to have a bigger size than HAWC. This bigger size will increase sensitivity significantly compared to HAWC. The denser inner "core" detector is designed to decrease the energy threshold below 200 GeV, whereas the purpose of the outer array is to increase the effective area.

Beside these two examples introduced here, there are other detectors using this water Cherenkov technology, such as LHAASO (The Large High Altitude Air Shower Observatory) [91] currently under construction<sup>5</sup> in the Sichuan province of China and planned to be a multi-component experiment partially based on water Cherenkov detectors to detect cosmic rays and gamma rays, which are not introduced in detail here.

---

<sup>5</sup>As of October 2021, however construction is planned to be completed soon.



## Chapter 2

# The H.E.S.S. Experiment

The High Energy Stereoscopic System (H.E.S.S.), which is shown on the bottom of figure 1.14, is one of the three major arrays of Imaging Atmospheric Cherenkov Telescopes currently in operation. It is located in the Khomas Highland in Namibia at an altitude of 1800m above sea-level [92]. This location was chosen for its dry climate and remoteness and subsequent low light pollution leading to good sky quality for astronomical observations. Additionally, the altitude leads to less Cherenkov light being absorbed compared to observatories at lower altitudes. The array was built in two phases: In a first phase, which was completed in December 2003 [93], four identical Cherenkov telescopes were built on a square of 120m side length [92]. This distance between the telescopes results from a compromise between the need to record a typical shower with a Cherenkov light pool of 250m diameter in multiple telescopes and the need for a base as large as possible to have better stereoscopy [76]. The telescopes can be rotated in azimuth and altitude to freely point them at any position in sky in less than 2 minutes [94]. Their segmented hexagonal mirror of 12m diameter [82] is constituted of 380 individual round facets mounted in a Davies-Cotton design [95] focusing the light of the shower on a camera at a distance of 15m which is described in the next section [96]. This Davies-Cotton mount was chosen as it reduces the off-axis (Coma) optical aberrations. This comes however at the expense of a small anisochronism of about 4ns [97]. The four telescopes are called CT1 (in the East), CT2 (North), CT3 (West) and CT4 (South) as illustrated in figure 2.1 and are sensitive to gamma rays in an energy range in-between 100GeV and 100TeV [96]. To access lower energies, a fifth telescope, called CT5, was added at the centre of the array as illustrated in figure 2.1 in a second phase of construction which was completed in July 2012 [99]. The much bigger segmented mirror of this telescope, which has an almost rectangular shape and a diameter of 28m, allows to access energies down to below 20GeV [84]. It is composed of 875 individual hexagonal facets mounted this time in parabolic design, because the anisochronism would have been about

10 ns using a Davies-Cotton design which is too large to record light pulses lasting a few ns. The mirror focuses the light on a camera at a distance of 36 m [100].

## 2.1 Cameras

### 2.1.1 CT1-4

The cameras of the four smaller telescopes are constituted of 960 photomultiplier tubes (PMTs) arranged in 60 drawers (one of them is shown for illustration in figure 2.2) of 16 PMTs [101]. The PMTs have a field of view of  $0.16^\circ$  leading to a total field of view of  $5^\circ$  diameter. Winston cones are mounted in front of the PMTs to increase the effective collection surface by reducing the death space and to limit their field of view to the mirror to reduce noise from light reflected by the ground (Albedo). Each drawer contains, beside the 16 PMTs, the acquisition and control electronics for these PMTs as well as part of the trigger electronics. The remaining trigger and readout electronics of the camera is located in the camera body. In addition, to this local camera trigger, there is a central trigger in the control building making the coincidence between the different telescope triggers as H.E.S.S. uses a two level trigger as is discussed in detail in section 2.2. The array trigger rate in the original configuration with only the four small telescopes was about 200 Hz to 300 Hz, but CT5 has a mono trigger rate of about 1.5 kHz [102]. This increase in trigger rate when using the usual hybrid trigger mode in which CT5 is in mono mode (i.e., events are recorded when only CT5 triggers) and the other telescopes are in stereoscopic mode in coincidence (i.e., at least two telescopes need to trigger when CT5 is not triggering) led to a substantial number of lost events in the small telescopes due to their dead time of  $450 \mu\text{s}$ . For this reason and to reduce the failures of the aging electronics, the original cameras have been upgraded in 2015-2016. During this upgrade, the electronics have been changed while the PMTs have not been changed. A new readout chip technology allowed to reduce the minimum time between consecutive events to  $7 \mu\text{s}$ , leading to 21 % less lost events in the smaller telescopes when using them together with CT5.

### 2.1.2 CT5

The camera of the large telescope is constituted of 2048 PMTs in 128 drawers of 16 PMTs [103]. Each PMT has a field of view of  $0.07^\circ$  leading to a total field of view of  $3.2^\circ$ . This field of view is smaller than for the smaller telescopes in order not to end up with a too big camera and a too large pixel number. Each PMT has again its Winston cone in front and the electronics are similar to the original camera in the smaller telescopes. The main difference is a reduced dead time

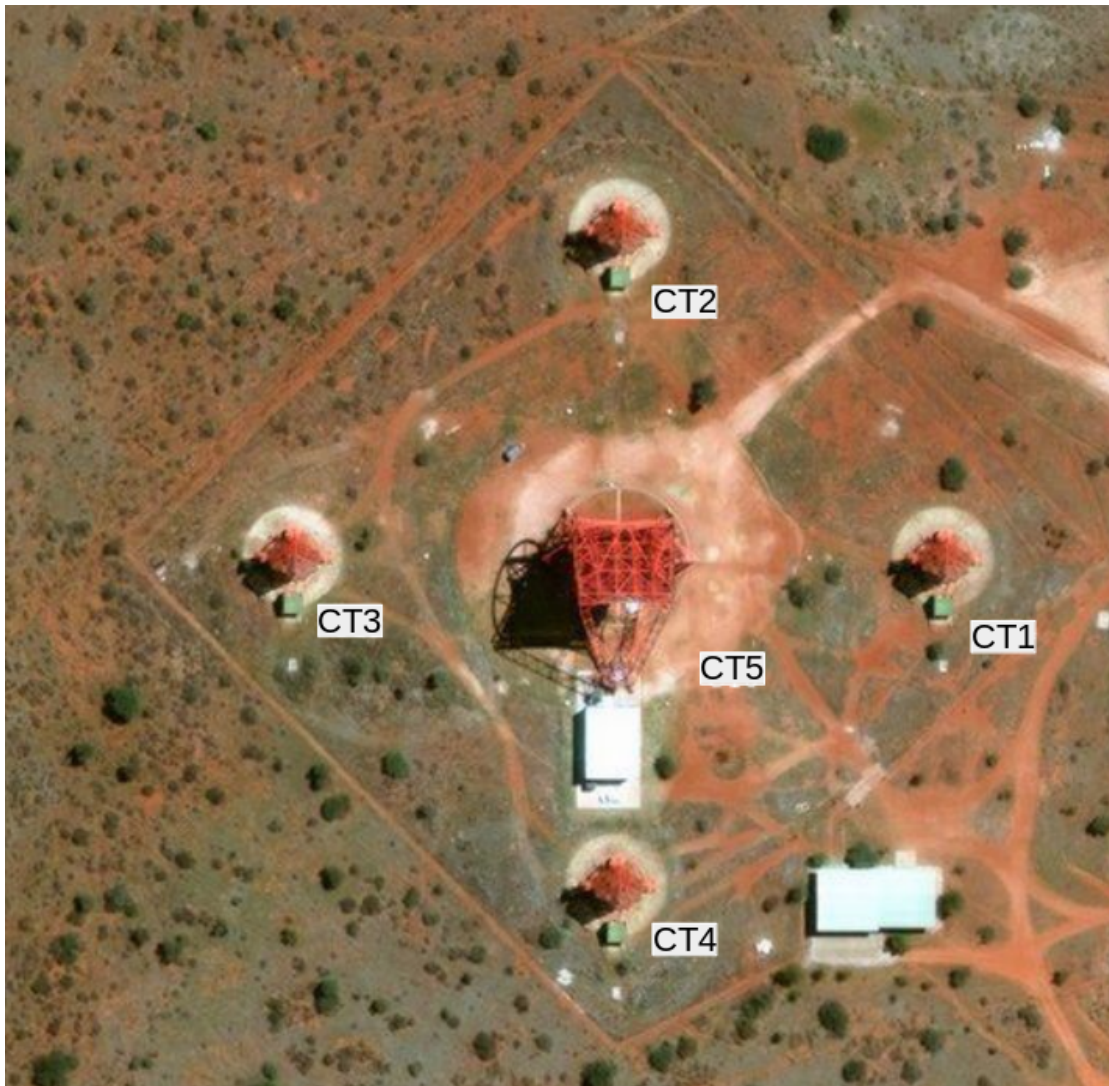


Figure 2.1: Picture illustrating the positions of the five H.E.S.S. telescopes (oriented as a standard map, i.e., North on the top and East on the right). Picture from [98] (Bing Maps).



Figure 2.2: One of the camera drawers with its 16 photo-multiplier tubes, the control and readout electronics from a HESS-I camera. Reproduced from [101]

(15  $\mu$ s [103]) to be able to handle the higher mono trigger rate of about 1.5 kHz. The original CT5 camera has been replaced by a new camera in 2019 in order to reduce the failures of the aging electronics and increase the up-time of CT5. The new camera, called FlashCam, is foreseen to be also used on the medium-sized telescopes of the southern array of CTA. It is constituted of 1761 PMTs in 147 drawers of 12 (respectively 11 for 3 of them) PMTs and has a hexagonal shape.

## 2.2 Readout & Trigger

For all the cameras beside the camera newly mounted on CT5, the signal recorded for each PMT is split into three channels, two sampling channels and one trigger channel [101, 103]. The two sampling channels have different gains to increase the dynamical range. For the original HESS-I cameras as an example, the high gain channel has a dynamical range from 1 to 200 photo-electrons and the low gain channel a dynamical range 15 to 1600 photo-electrons. The signal of these two channels is stored in analogue memory awaiting the trigger decision based on the trigger channel. The trigger decision occurs on two levels. The local level takes place directly in each camera. For this the camera is divided in different partially overlapping sectors and the event passes this first level if at least  $S_2$  pixels in a sector exceed a charge threshold corresponding approximately to  $S_1$  photo-electrons [106, 103]. In normal operations,  $S_1$  equals to 5.3 photo-electrons and  $S_2$  equals to 3 pixels in the original cameras of the smaller telescopes [106] and  $S_1$  equals to 4 photo-electrons and  $S_2$  equals 3.5 pixels in the original CT5 camera [103]. This non-integer value was used for CT5 to have a safety margin and make sure to accept events where 3 pixels pass the threshold. If this requirement is fulfilled in one camera, this camera sends a signal to the central trigger where the

second level decision takes place. The central trigger checks if the pattern of telescopes triggering in coincidence, i.e., simultaneously (within 80 ns) after correcting for the difference of the time of arrival of the photons according to the telescope pointing conditions [106], corresponds to a pattern to be accepted and usually checks whether a minimum number of telescopes triggered, where this minimum number can be different for different telescope types. If this second level trigger condition is passed, the signal of the two channels of all the pixels of the triggered telescopes is read out from the analogue memory and sent to the control building. The dead time mainly depends on the speed of this readout and is very different for the different camera types. For the four small telescopes, usually at least 2 triggering telescopes are required to ensure a stereoscopic view of the showers which improves reconstruction and rejection and reduces the triggering rate which was particularly important for the original cameras of the small telescopes due to their comparatively long dead time, but also reduces the amount of data which needs to be stored. As CT5 is also optimized to take data in mono mode, in many observations no additional triggered telescope is required to accept an event.

In FlashCam, there is only one channel per pixel which is continuously digitized. The local level trigger is based on this digitized signal by considering patches of 9 pixels, whereas the central trigger is checking the number of telescopes triggered in coincidence as before.

## 2.3 Calibration

The charge accumulated in each pixel of the camera is stored in the form of ADC counts. However, one would like to convert this quantity to a physical one directly related to the light actually emitted such as the density of Cherenkov photons. This so-called calibration involves multiple steps described below, based on its documentation in [101].

### 2.3.1 Pedestal calibration

First of all, the electronic baseline, the so-called pedestal, needs to be subtracted from the measured signal to be only left with the signal from the Cherenkov photons. The electronic pedestals are determined in special pedestal runs with closed camera lid while the telescopes are still in their shelter. The observation pedestals including instrumental effects such as the influence of the atmospheric temperature on the electronic baseline need to be determined for each observation run. They have a higher pedestal width due to the night sky background photons, the average pedestal value is however not shifted due to an AC coupling between the photo-multiplier tubes and the analogue ring sampler which samples the signal

and behaves like an RC circuit. They are computed by only considering the non-illuminated pixels of the telescope cameras in each triggered Cherenkov event. The pedestal is monitored continuously and subtracted from the measured ADC counts in each pixel for each gain channel. As the observation pedestals depend on camera temperature which might change during runs, they are recomputed as often as possible, approximately once a minute for a standard event rate.

### 2.3.2 Gain calibration

The gain describes the relation between the number of ADC counts and the number of photo-electrons. It is determined in special runs during which the telescopes remain in the camera shelter to prevent contamination from the night sky background. To do this, the PMTs are illuminated with an LED flashing at 70 Hz installed in the camera shelter at a distance of 2 m from the camera specially for the gain calibration (respectively with a laser with a default frequency of 1 kHz mounted at the centre of the dish for CT5 [103]). The intensity of this light source is adjusted to be able to measure the single photo-electron peak on the PMTs. The measured charge distribution is then fit to the expected one  $G(x)$  which is composed of a term representing the pedestal distribution (first line) and a sum of terms representing the resolution of the PMTs in function of the number of photo-electrons (second line) to determine the gain of the PMT in the high gain channel  $\gamma$ :

$$G(x) = N \frac{e^{-\mu}}{\sqrt{2\pi}\sigma_P} \exp\left(-\frac{(x - P_{HG})^2}{2\sigma_P^2}\right) + N \times N_S \sum_{n=1}^{\infty} \frac{e^{-\mu}}{\sqrt{2\pi n}\sigma_{\gamma_e}} \frac{\mu^n}{n!} \exp\left(-\frac{(x - (P_{HG} + n\gamma_{HG}))^2}{2n\sigma_{\gamma_e}^2}\right). \quad (2.1)$$

Here  $N$  is the total number of events,  $\mu$  the average number of photo-electrons per event,  $P$  the pedestal position in the high-gain channel,  $\sigma_P$  the pedestal width,  $\sigma_{HG}$  the single photo-electron peak width and  $N_S$  a normalization constant. This is only done in the high gain channel as the single photon electron peak can only be resolved in this channel. The low gain channel is calibrated with respect to the high gain channel as described in subsection 2.3.3.

The gain calibration in the new CT5 camera is very different from the gain calibration in the HESS-I cameras or the old CT5 camera, as the new camera is only constituted of one gain channel and the signal readout is different. If a camera trigger occurs in this camera, the waveform is readout with 32 samples locally in the camera. Depending on the height of this pulse, two different regimes are distinguished. Up to two thirds of the ADC range, the pulse height increases

linearly with the number of photo-electrons ("linear regime"). So, one can estimate the number of produced photo-electrons from the pulse height or the pulse width depending on the regime. For a higher charge, the pulse height saturates and adding a higher charge increases the pulse width ("non-linear regime"). To calibrate this conversion, a laser which can produce different pulse intensities with a diffuser illuminates the whole camera. The linear regime can then be calibrated with the single photo-electron peak. For the calibration of the non-linear regime, three pixels are permanently partially masked so that they receive less light and stay in the linear regime over the whole dynamical range of the other 1758 pixels. The non-linear regime of these pixels can then be calibrated by inter-calibrating them with the three masked pixels.

### 2.3.3 Cross-calibration of gain channels

The low gain channel, used to extend the dynamical range of the HESS cameras, needs to be calibrated with respect to the high gain channel. This is done during normal observation runs using events in the overlapping dynamical range of the two channels for the considered pixel. As the high gain is known through the gain calibration, one gets the number of produced photo-electrons for the given pixel in this event and so can infer the gain of the low gain channel.

### 2.3.4 Flat-field calibration

Flat-fielding is used to correct for differences in the collection and quantum efficiency of individual PMTs within a camera, i.e., the difference in the number of photo-electrons produced per photon for the different PMTs. Special flat-fielding runs are taken during which the telescopes are illuminated with a flashing LED (or laser depending on telescope type) at the centre of the telescope dish with a diffuser in front of it to illuminate the camera as homogeneously as possible. Then, differences in the responses of the different PMTs to this light source are corrected for. The so determined flat fielding coefficients are the same for both gain channels as they describe the difference in the conversion efficiencies of photons to photo-electrons of the different PMTs which occurs before the signal is split in gain channels.

### 2.3.5 Optical efficiency

The optical efficiency describing an absolute calibration of the conversion efficiency of Cherenkov photons into photo-electrons of the instrument depends on numerous parameters such as the reflectivity and transmittivity of the different optical elements and the collection and quantum efficiency of the PMTs whose individual

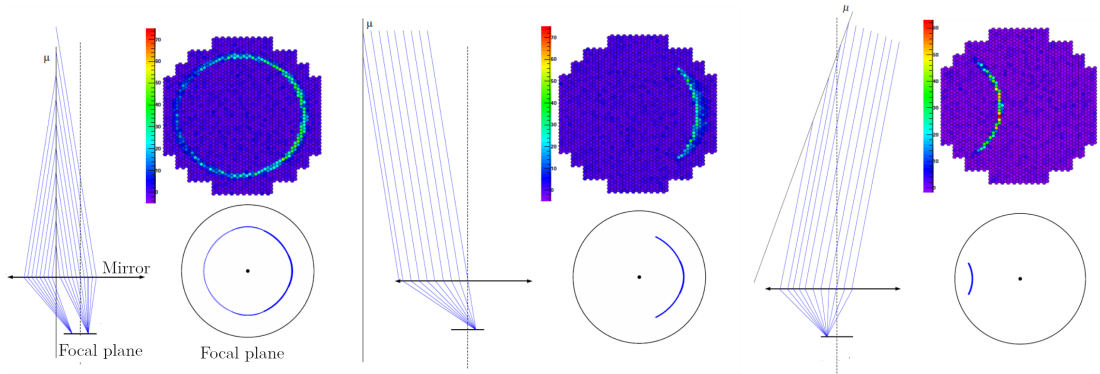


Figure 2.3: Illustration of the shape of the produced muon ring in function of impact parameter and inclination relative to the optical axis. Left: Muon passing mirror with a propagation direction perpendicular to the mirror plane. Centre: Muon passing close to mirror with a propagation direction perpendicular to the mirror plane. Right: Muon passing close to mirror with a propagation direction non-perpendicular to the mirror plane. Adapted from [107]

calibration at all wavelengths of the Cherenkov spectrum is hardly possible [107]. For this reason, atmospheric muons have been used by all major Cherenkov telescopes to determine the optical efficiency so far [108]. The spectrum recorded from the Cherenkov emission from particles identified as muons is very similar to the one recorded from showers induced by gamma rays except that it is less impacted by the atmospheric absorption of its ultraviolet part. This is due to the Cherenkov light recorded from muons passing through or close to the mirror (which are the muons which can be the most easily identified) is emitted at lower altitude. This small difference is corrected for by a conversion factor. In addition, muons barely emit Bremsstrahlung radiation due to their larger mass and can so travel a much longer distance than most other particles from the shower. They originate from hadronic interactions and can be emitted with large angle allowing gamma-ray telescopes to record light from a single muon.

The Cherenkov light from these single muons can be easily distinguished from other events as they produce a ring-shaped event if they pass through the mirror or an arc if they pass close to the telescope [107] as illustrated in figure 2.3. The total number of Cherenkov photo-electrons  $N$  produced in a circular mirror with radius  $R$  by a single muon hitting the telescope is given by the formula:

$$\frac{d^3N}{dl d\phi d\lambda} = \frac{\alpha}{2} \sin(2\theta_C) \frac{\psi(\lambda)}{\lambda^2} D(\phi) a(l, \lambda), \quad (2.2)$$

where  $l$  is the muon path length,  $\phi$  the azimuth angle in the focal plane of the Cherenkov photon,  $\lambda$  its wavelength,  $\alpha$  the fine structure constant,  $\theta_C$  the

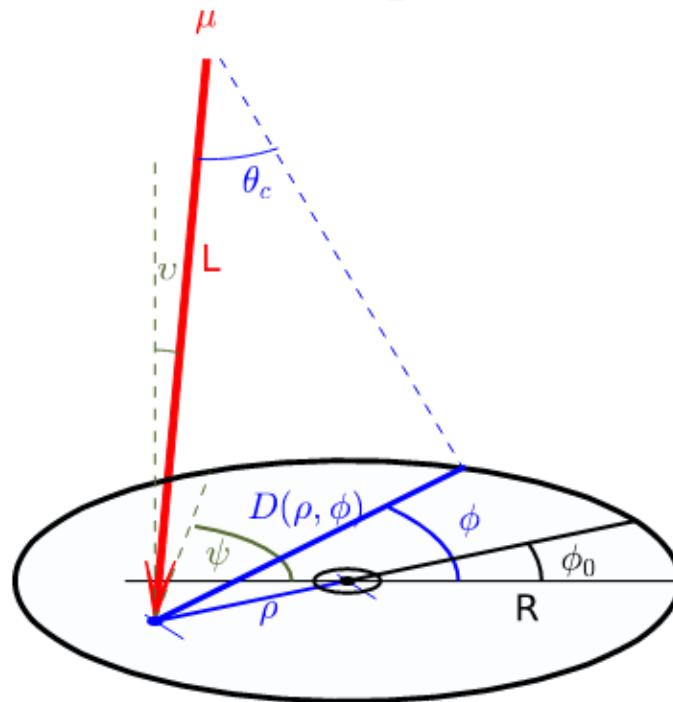


Figure 2.4: Sketch illustrating the different parameters introduced in this section. The red line illustrates the muon track which passes through the mirror of radius  $R$ , described by the black circle, at an impact distance  $\rho$  from the mirror centre. The muon generates Cherenkov light with the opening angle  $\theta_C$  over its tracks and so illuminates the mirror along the chord  $D(\phi)$ , where the azimuth angle  $\phi$  varies between  $0$  and  $2\pi$  as the Cherenkov light is emitted isotropically (with the given opening angle) around the direction of propagation of the muon. Reproduced from [108].

Cherenkov angle,  $\psi(\lambda)$  the optical efficiency and  $a(l, \lambda)$  the atmospheric attenuation [107].  $D(\phi)$  is the chord defined by the intersection of the plane of the mirror and the plane defined with the muon and Cherenkov photon propagation direction as illustrated in figure 2.4 and can be written as:

$$D(\phi) = \begin{cases} 2R\sqrt{1 - \left(\frac{\rho}{R}\right)^2 \sin^2 \phi} & \text{for } \rho > R \\ R\left(\sqrt{1 - \left(\frac{\rho}{R}\right)^2 \sin^2 \phi} + \frac{\rho}{R} \cos \phi\right) & \text{for } \rho \leq R, \end{cases} \quad (2.3)$$

where  $\rho$  is the muon impact parameter as defined in figure 2.4. Here two cases have to be considered: In the first case, the muon does not pass through the mirror and creates an arc in the camera. In the second case, the muon passes the camera mirror and creates a full circle in the camera. This formula is formally only valid for circular telescope mirrors, but the HESS-I mirrors are circular enough for this formula to be used. In contrast, CT5 is significantly non-circular and so the formula had to be adapted for this telescope. In addition, due to the point spread function of H.E.S.S. and the finite facet and pixel size, the ring has a finite width which is modelled with a Gaussian added to equation (2.2).

To determine the muon efficiency, muon events recorded in normal observation runs are used. To do this all the events are cleaned<sup>1</sup> and then a ring finding algorithm is used on the cleaned image to do a first selection of potential muon rings [107]. Then, the adapted version of equation (2.2) is adjusted to the cleaned image with a maximum likelihood fit. From this fit, the different parameters of the muon can be extracted. Among these parameters is the muon efficiency. The other parameters are used to perform a selection of well reconstructed muon rings (among other not contaminated by a hadronic shower). This muon efficiency can then be converted with the conversion factor for the difference in Cherenkov spectrum to the muon optical efficiency of gamma rays on an event-by-event basis. However, changes in the atmospheric conditions leading to changes in the fraction of absorbed Cherenkov photons cannot be fully disentangled from the muon optical efficiency using this method. This is, among other, why the muon efficiency is varying between runs and nights. A further reason for these variations is the limited number of muons per run (a few hundred to a few thousand depending among other on the camera type). To compensate for these fluctuations usually the average muon optical efficiency over a whole observation period is used.

The optical efficiency is in average less than 10% for H.E.S.S. This value is dominated by the quantum efficiency of the PMTs of about 20%, but the reflectivity of the mirrors (about 80%), the collection efficiency determined by the loss of photons between the mirrors and the PMTs (about 70%) and the shadow of the

---

<sup>1</sup>The image cleaning is discussed in section 2.4.1 about the reconstruction of the events of which image cleaning is an important part.

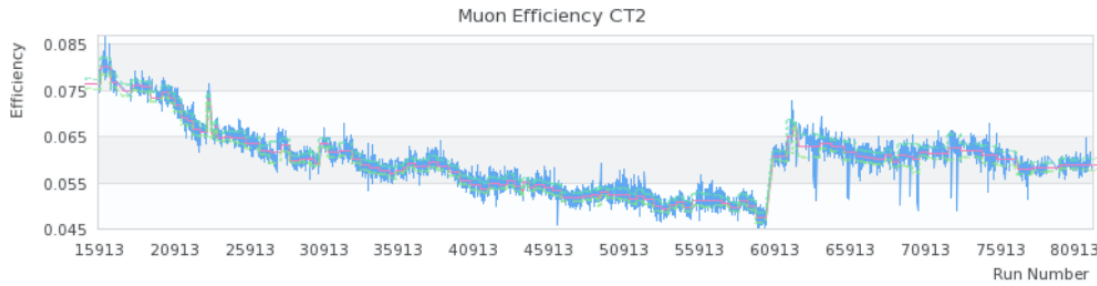


Figure 2.5: Evolution of the muon optical efficiency of a H.E.S.S. telescope as a function of run number. The slow decrease with time due to the degradation of the optical efficiency is well visible. One also sees one big jump caused by the replacements of the mirrors with new ones having a better reflectivity. Reproduced from [107].

cameras and masts (about 90 % unaffected) also play a role. It is decreasing with time due to the aging of the components of H.E.S.S. as illustrated in figure 2.5. Part of the lost efficiency could be successfully recovered in the past by cleaning or exchanging components of the optical system such as the mirror panes or the Winston cones.

### 2.3.6 Pointing corrections

To be able to determine the exact position of an observed source and to meaningfully combine the data taken with the different telescopes, one needs to know the exact pointing of the different telescopes. It is not enough to determine this once, as the pointing of the telescopes changes with time, mostly due to the slow sinking of the telescope structures into the ground due to the weight of the telescopes. The pointing of the H.E.S.S. telescopes is determined in regular pointing runs during which the telescopes are pointed towards bright stars selected in a way to get an isotropic distribution across the visible sky. This is done with closed camera lid [109]. The light of the stars is reflected by the mirror of the telescope, onto the camera lid and then recorded by the CCD camera in the centre of the dish which also records the light from eight (respectively 16 for CT5) LEDs attached to the camera frame. The position of the light spot from the stars is compared to the position of the light spot of the LEDs. The results from different pointing runs to different positions on the sky is used to adjust an 18-parameter mechanical model of the telescope deformation as function of azimuth and elevation. This model is used in observation runs to determine the exact pointing of the telescope at each position on the sky.

## 2.4 Separation & Reconstruction

The next important step after having applied the calibration is the separation and reconstruction of the individual events. The first aim is to do a first separation of gamma-ray events, which are the signal events, and background events (mostly charged cosmic ray induced atmospheric showers) whose rate is by orders of magnitude higher, making the separation challenging. However, even the best separation method does not lead to a perfect separation of gamma-ray and hadronic events, but instead the selected signal events are in most cases still dominated by background events. For this reason, one calls them gamma-ray candidate events and three main event classes are distinguished:

- Gamma-ray events are gamma-ray candidate events which are genuine gamma-ray events. They are the events which originate from the observed sources.
- Gamma-like background events are gamma-ray candidate events which are no gamma-ray events, so background events which were not identified as background events during the event classification.
- Hadron-like events are the events classified as background in the separation of gamma rays and background. They also contain both background and gamma rays since very strict selection cuts on gamma-like events are used in order to reduce the background as much as possible. However, if genuine background events are needed (such as for instance in the template background subtraction described in subsection 2.5.1), a very pure sample can easily be obtained by using a cut quite far from the gamma-like selection cut, as the hadronic background dominates by orders of magnitude.

Gamma-ray and gamma-like background events cannot be distinguished by a separation method. This is the reason why additional background subtraction methods are needed as described in subsection 2.5.1.

In addition to the separation, one wants to reconstruct the parameters of the primary particle whose signal is observed such as its direction, impact location and energy. The oldest successful separation and reconstruction method is the Hillas parametrization method which has been used since the beginning of ground-based gamma-ray astronomy. A newer and more sophisticated method used in H.E.S.S. is the so-called model reconstruction which is based on a semi-analytic shower model. These methods are described in more detail in the following. Beside these two methods discussed here, there are numerous other separation and reconstruction methods, among other template reconstruction using a full Monte-Carlo model, reconstructions based on analytic 3D models of the shower and reconstructions based on multivariate methods, some of them also used within H.E.S.S., which are not discussed in detail here.

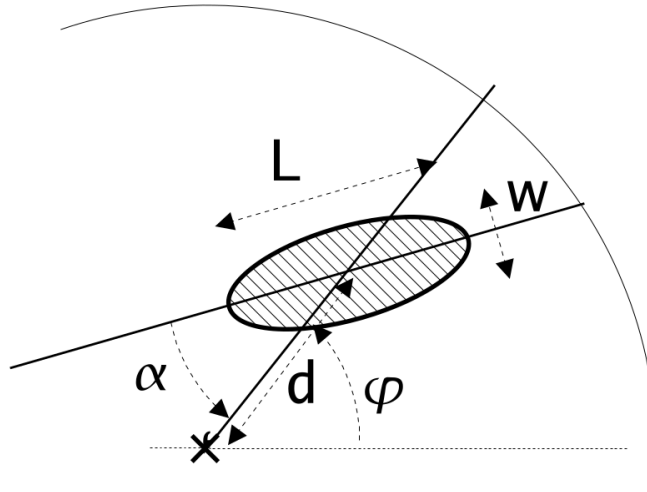


Figure 2.6: Definition of the Hillas parameters. Reproduced from [72]

### 2.4.1 Image cleaning

However, before doing any separation or reconstruction the calibrated image of an event needs to be cleaned to extract the pixels that have been illuminated by the shower from the others that only contain night sky background light. The main idea behind this cleaning is that showers illuminate coherently many pixels whereas night sky background is uncorrelated. This is usually done using a dual-threshold condition with thresholds  $thres_1$  and  $thres_2$ : The pixel is only kept if it has recorded at least  $thres_1$  photo-electrons and a neighbouring pixel has recorded at least  $thres_2$  photo-electrons or if it has recorded  $thres_2$  photo-electrons and a neighbouring pixel at least  $thres_1$  photo-electrons and set to zero otherwise [110]. This cleaning allows among other to eliminate isolated luminous pixels illuminated by stars. The thresholds have to be optimized in a way to eliminate as many as possible of these noise pixels while not eliminating too many low energy gamma-ray events. The values of the used thresholds within H.E.S.S. depend on the analysis, but are often chosen to be 7 and 10.

### 2.4.2 Hillas reconstruction

Due to their almost elliptical shape, images of gamma-ray showers in Cherenkov telescopes are traditionally parametrized by the so-called Hillas parameters. They are named after A. M. Hillas who introduced them in 1985 [111]. In this parametrization, the image of a shower is modeled by a two-dimensional ellipse, as illustrated in figure 2.6. This ellipse is described by its major axis (the length  $L$ ) and its minor axis (the width  $w$ ). Additional parameters are the total image amplitude

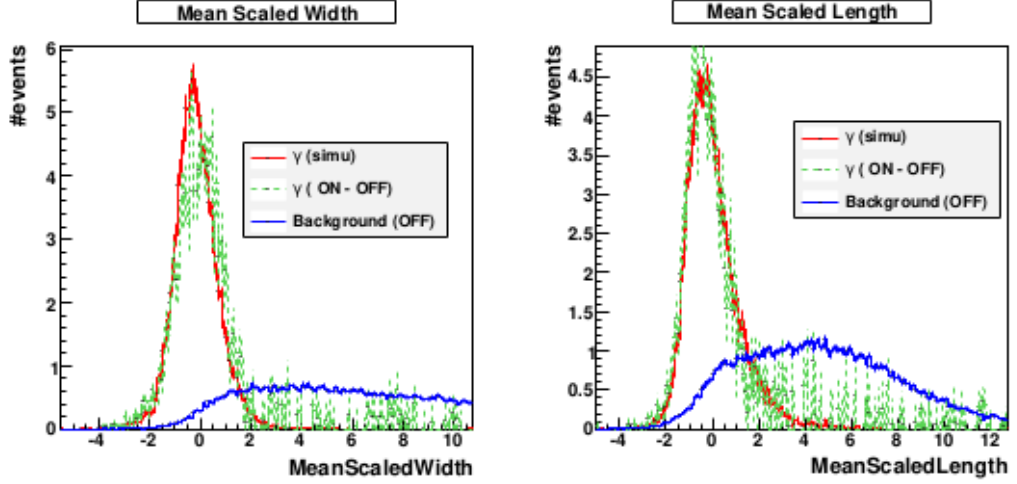


Figure 2.7: Distribution of the Mean Scaled Width and the Mean Scaled Length for gamma rays (red) and background events (blue). The gamma-ray distribution comes from simulations whereas the background one from a region without gamma-ray source. In green real (background subtracted) gamma-ray events from the Crab nebula are shown. The real gamma-ray distribution agrees well with the simulated one and one can easily set a cut to remove most of the hadronic events. Reproduced from [72].

(the size  $S$ ), the angular distance between the centre of the camera and the image centre of gravity (the nominal distance  $d$ ), the azimuthal angle of the image with respect to the main camera axis  $\varphi$  and the orientation angle of the image in the camera  $\alpha$  [112]. These parameters can be determined analytically from the recorded charge in each pixel and the position of the pixel.

There are different methods to discriminate gamma-ray candidates<sup>2</sup> from hadrons based on the Hillas parameters. The mean scaled cuts method is based on the comparison of the length  $L$  and width  $w$  of the actual image with its expectation value and variance (under the assumption it is a gamma ray) obtained from Monte Carlo simulations of gamma rays [112] in function of the size  $S$ , the reconstructed impact distance and the zenith angle of the observation [110]. In this method, the scaled

<sup>2</sup>Gamma-ray events cannot be completely separated on an event-by-event basis from charged particle events as some charged particle events are very similar to gamma-ray events. For this reason, a selected event is qualified as gamma-ray candidate: The event is potentially a gamma ray, but could also be a cosmic-ray event looking like a gamma ray.

width and length are defined as

$$SW = \frac{w - \langle w \rangle}{\sigma_w}, SL = \frac{L - \langle L \rangle}{\sigma_L}, \quad (2.4)$$

and can then (in stereoscopic mode, otherwise  $N_{tels}$  is just 1) be combined into the mean scaled sum

$$MSS = \frac{\sum_{tels} SW + \sum_{tels} SL}{\sqrt{2N_{tels}}}. \quad (2.5)$$

For gamma rays, the mean scaled sum should, by construction, follow a Gaussian distribution with mean 0 and standard deviation 1, whereas hadrons follow a much higher peaked distribution allowing a separation of both event types, as illustrated in figure 2.7 (which shows the mean scaled width and length separately). As the mean scaled sum is scaled as function of size, the selection efficiency is almost independent on energy and so does not bias the spectrum [72].

The Hillas parameters also allow the reconstruction of the shower directions. In single telescope observation, this is usually done using the Hillas length  $L$  and size  $S$  to compute, using lookup tables, the angular distance to the source. Due to the symmetry however, this leads to two degenerate solutions making the consideration of skewness and kurtosis of the image necessary - which are not part of the traditional image parametrization [72]. Stereoscopic observations make the direction reconstruction much easier as one can simply combine all the images taken of the shower: The source direction is given by the intersection of the major axes of the images in the participating cameras and the impact point using the intersection of the planes containing the telescopes and shower track [110]. The energy of the shower is usually determined based on the image size  $S$  and the nominal distance  $d$ , again using lookup tables [112].

### 2.4.3 Semi-analytic model reconstruction

In the model method, the raw images of the showers are compared to predictions from a semi-analytic shower model [113]. This model is derived from the longitudinal, lateral and angular distribution of charged particles in a shower. This distribution is obtained from Monte Carlo simulations which are then parametrized to give an analytic description of the shower.

The light density from a shower at a given position in the camera  $I(x, y)$  is then calculated by integrating over all parameters in the model, namely the altitude, the energy, position and direction of the charged particles and the wavelength and azimuthal angle around the charged particle of the produced Cherenkov photons. In addition, instrumental effects are taken into account and the night sky background noise contribution is added based on a detailed statistical analysis.

The actual images on the camera can then be compared to those obtained from the shower model by doing a log-likelihood fit to find the most likely model parameters for the incoming particle (energy, direction, depth of first interaction, impact) such that the actual image corresponds to the model image under the assumption that the incoming particle is a gamma ray. This fit is based on a pixel-by-pixel comparison of all pixels (so no cleaning is needed here) of the recorded intensity with the prediction from the model. As the model is only obtained from simulations on a given grid of parameters, an interpolation is performed where necessary.

The probability density to measure a signal  $s$  in a pixel when a signal  $\mu$  is expected is given by a combination of the Poisson distribution for the number of photo-electrons  $n$  and the photo-multiplier resolution described by a Gaussian of width  $\sqrt{\sigma_p^2 + n\sigma_\gamma^2}$  where  $\sigma_p$  is the pedestal width and  $\sigma_\gamma$  the width of the single photo-electron peak:

$$P(s|\mu, \sigma_p, \sigma_\gamma) = \sum_n \frac{\mu^n e^{-\mu}}{n! \sqrt{2\pi(\sigma_p^2 + n\sigma_\gamma^2)}} \exp\left(-\frac{(s-n)^2}{2(\sigma_p^2 + n\sigma_\gamma^2)}\right). \quad (2.6)$$

From this then the pixel log-likelihood  $\ln L = -2 \ln P$  is obtained and, by summing over the pixel log-likelihoods, the telescope log-likelihood can be defined [113]:

$$\ln L_{tel} = \sum_{\text{pixel } i} \ln L_i = \sum_{\text{pixel } i} -2 \ln P(s_i|\mu_i, \sigma_{p,i}, \sigma_{\gamma,i}). \quad (2.7)$$

This log-likelihood is then minimized using a Levenberg-Marquardt algorithm [114, 115] to find the best-fit model parameters (direction, impact, depth of first interaction and energy) for the recorded image. In this minimization the correlation matrix and so the uncertainty of the parameters is obtained too.

To qualify the goodness of the resulting fit, the goodness-of-fit is defined as normalized sum over all pixels of the difference of the actual pixel log-likelihood and its expectation value  $\langle \ln L \rangle |_{\mu_i}$ :

$$G = \frac{1}{\sqrt{2N_{\text{DoF}}}} \sum_{\text{pixel } i} [\ln L(s_i|\mu_i) - \langle \ln L \rangle |_{\mu_i}], \quad (2.8)$$

where  $N_{\text{DoF}}$  is the number of degrees of freedom, i.e., the number of pixels minus 6. To be more sensitive to changes inside the shower itself, the computation of the goodness-of fit is restricted to the pixels in the shower core (i.e., the pixels attributed to the shower) leading to the so-called shower goodness  $SG$ . This quantity is then averaged over all telescopes  $t$  to obtain the mean scaled shower goodness  $MSSG$ :

$$MSSG = \sum_t \frac{SG_t - \langle SG \rangle}{\sigma_{SG} \sqrt{N_t}}, \quad (2.9)$$

where  $N_t$  is the number of telescopes participating in the event and  $\sigma_{SG}$  the width of the  $SG$  distribution obtained from Monte Carlo simulations. The  $MSSG$  behaves as a Gaussian variable if the model from simulation describes real showers well.

As the model is built from Monte Carlo simulation of gamma-ray showers, it does not describe the hadronic background well. For this reason, hadronic showers tend to have higher values in  $MSSG$  than gamma-ray-induced showers and so one can separate hadrons from gamma-ray candidates by defining a selection cut on the  $MSSG$ .

## 2.5 Analysis

Being arrays of optical telescopes, Cherenkov telescope arrays can only observe during dark time without too much moonlight and are heavily impacted by meteorological conditions. In addition, a given source can only be observed for sufficiently high elevation (above  $30^\circ$  for H.E.S.S.). This makes it necessary to split the observations of a given source in observation runs which last 28 min for H.E.S.S. To simplify background subtraction and acceptance calculation (as discussed in detail in subsection 2.5.2), these observation runs are usually taken in so-called wobble mode: In this mode, multiple pointing positions (usually on a square pattern in angular space around the source) slightly offset ( $0.5^\circ$  to  $1^\circ$ ) from the source position are defined for the different runs taken on the same source. This splitting, in combination with the need to accumulate many hours of data on sources that are visible only during a fraction of the year, leads to data taken under very different meteorological and pointing conditions and potentially accumulated over multiple years for a given source.

To combine this data taken under very different conditions and produce reproducible results, a dedicated analysis software is needed. First of all, it needs to account for the remaining background in the gamma-ray candidate events (which are the majority of the events in all the reconstruction techniques) and the signal needs to be extracted by taking into account the very different gamma-ray acceptance (probability that an event is recorded and classified as gamma-ray candidate) of the telescopes under these different conditions. Then, it can compute the energy spectrum (i.e., the energy distribution of the produced gamma rays of the source), the light curves (i.e., the variation of the source luminosity with time) and the morphology (i.e., the spatial shape of the source) of the source.

### 2.5.1 Background subtraction

As the sample of gamma-ray candidates is in most cases still dominated by background events after event selection, one needs a robust subtraction method. Mainly

two different strategies are used. One either defines a control region where no emission is expected (i.e., without any known or putative source), usually inside the field of view of the same observation, and then subtracts the events recorded in the control region from the region of interest correcting for a potential acceptance difference [116]. Alternatively, one uses the events classified into a different class (i.e., background events) recorded inside of the region of interest and subtracts them from the gamma-ray candidate events correcting again for potential difference in the acceptance. In the following a prominent example of both strategies is described.

### Ring Background

In the ring background method [116], the control region (OFF region) is defined as a ring around the region of interest (ON region) large enough to have no expected signal from a potential source as illustrated in figure 2.8. If there is a region with known gamma-ray emission on this so defined ring, it has to be excluded from the control region. After having stacked the events from all the runs, the number of excess events remaining after background subtraction is defined as:  $N_{\text{excess}} = N_{\text{ON}} - \alpha N_{\text{OFF}}$ , where  $N_{\text{OFF}}$  is the number of events in the control region,  $N_{\text{ON}}$  the number of events in the region of interest and  $\alpha$  the correction factor for a different acceptance in the control region and the region of interest whose determination is discussed in the next section.

### Template background

In the template background method [117, 116], the background is determined based on hadronic events recorded inside the region of interest, but using a subset of the events failing the gamma-ray selection cuts as illustrated in figure 2.9. The cut used to define this second event class of hadronic events is usually chosen quite far from the gamma-candidate cut in order not to contaminate the hadronic events with gamma rays. The main advantage of this method is that there is no need to define a control region without emission. The number of excess gamma-ray events in the region of interest is defined as:  $N_{\text{excess}} = N_{\gamma\text{-candidate}} - \alpha N_{\text{Hadron}}$ , where  $N_{\gamma\text{-candidate}}$  is the number of gamma-ray candidate events recorded in the region of interest,  $N_{\text{Hadron}}$  the number of selected hadronic events recorded in the region of interest and  $\alpha$  the correction factor for the difference in hadronic and gamma-ray candidate acceptance. This background subtraction method relies on the assumption that no gamma-ray events are classified as hadronic events and so that  $N_{\text{Hadron}}$  is independent of the presence of a source. For this reason, it is so important to avoid contamination and to choose selection criteria quite far from each other.

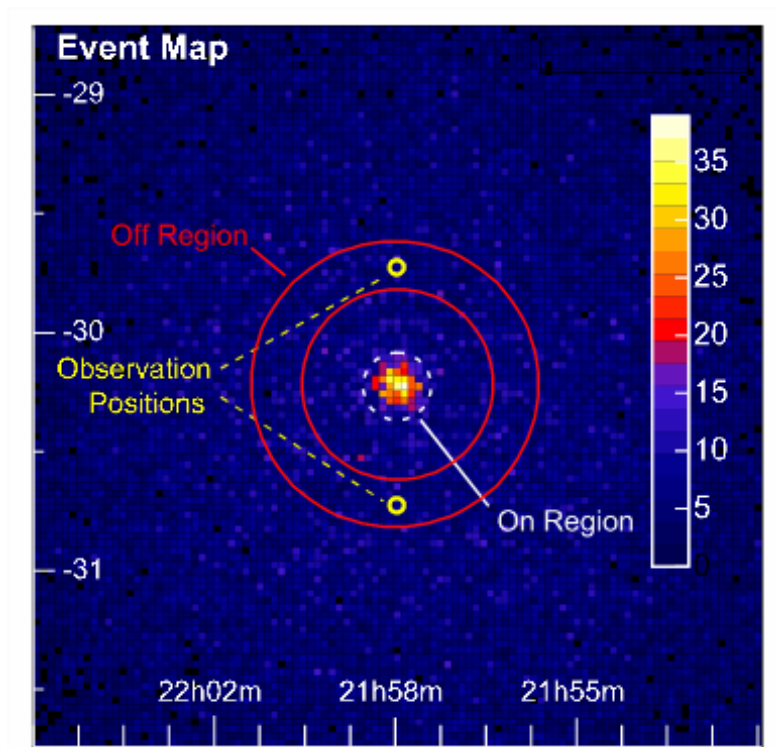


Figure 2.8: Counts map of gamma-ray candidate events from five hours of H.E.S.S. observations on PKS 2155-304 used as example to illustrate the ring background method. As usual, the data has been taken in wobble mode, here with alternating offsets around the target position of  $\pm 0.5^\circ$  in declination as indicated by the yellow marked observation positions. The ON region around the target position is marked by the white dashed circle. As can be seen there seems indeed to be a source indicated by the strong excess of counts in this ON region. The ring used as OFF region for the background determination is enclosed between the two red circles. Reproduced from [116].

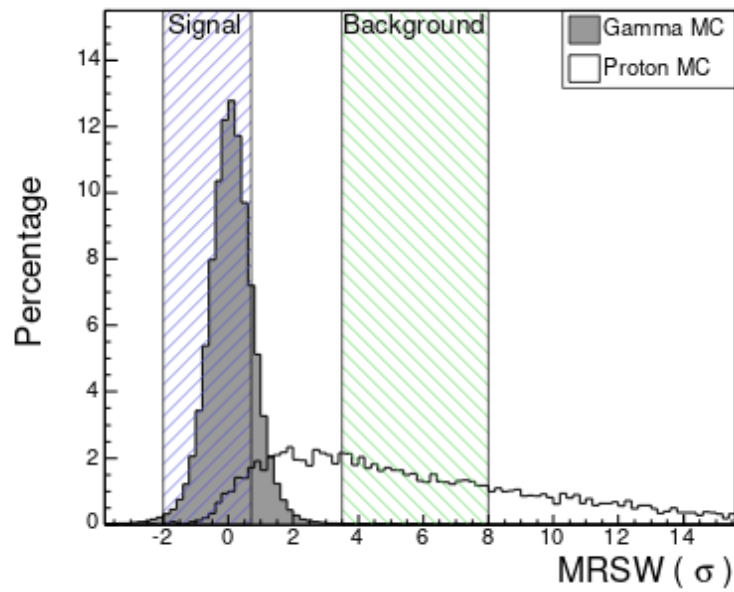


Figure 2.9: Distribution of the mean reduced scaled width (mean scaled width, as shown in figure 2.7, divided by the square-root of the number of telescopes) for simulated gamma rays (dark distribution) and simulated protons (bright distribution). As the distributions are significantly different, one can define a signal region of gamma-ray candidate events and a background region of background events for the template background subtraction. Reproduced from [116]

## 2.5.2 Acceptance calculation

The acceptance describes the probability that an event of a given energy and type triggers the system, is reconstructed and classified according to a given event class [116]. It is as such related to the effective area, which is defined as the equivalent area over which all particles would be detected, i.e., all the area over which particles could be detected multiplied by the local sensitivities. However, unlike the effective area, which can also depend on particle properties such as their type or energy, the acceptance describes probabilities on particle basis and also considers misclassification. The acceptance is needed to determine the  $\alpha$  factors in the different background subtraction methods and to compute the fluxes of detected sources as well as the energy spectra. One distinguishes three different types of acceptances corresponding to the different event classes defined in section 2.4: the acceptance to gamma-ray events, the acceptance to gamma-like background events (the gamma-ray candidate events which are not gamma rays) and the acceptance to hadron-like events [72]. The gamma-ray acceptance is obtained from simulation whereas the other two are usually obtained from the data with one of the two algorithms described in the following.

### Radial acceptance

The radial acceptance calculation method assumes that the response of the system is radially symmetric around the observation position [116]. This needs to the necessity of correcting the variation of zenith angle across the field of view which leads to changes in the trigger rate of the order of 2% to 3% on a run-by-run basis and neglects the inhomogeneities of the response in the camera breaking this symmetry [72]. It can be calculated on a run-by-run basis by determining the number of recorded events as a function of angular distance to the observation position. Regions with expected gamma-ray emission need to be excluded and are corrected for by weighting the events at the corresponding angular distance by a factor taking into account the covered area. This, however, does not work if this region is at the centre of the telescope, making averaging over runs or use of a different method necessary. To avoid this problem and to increase statistics, the radial acceptance is often calculated over multiple runs by default. This, however, as for the 2D acceptance discussed next, assumes that the acceptance does not vary in shape from one run to the next.

### 2D acceptance

The 2D acceptance calculation method relies on observation runs which were taken at slightly different pointing positions around the observed region of interest. If the runs have been taken in the usually used wobble mode, this condition is fulfilled. It

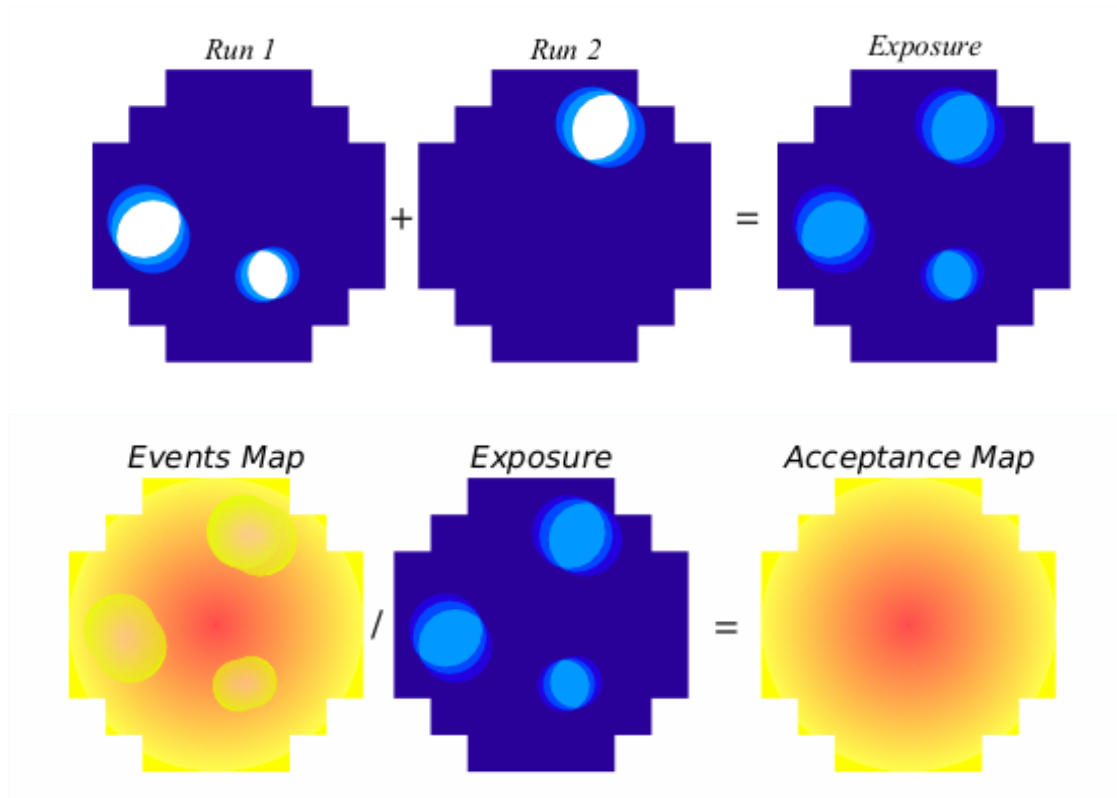


Figure 2.10: Illustration of 2D acceptance calculation. Top: Construction of exposure map by summing fraction of time in which each position in the camera was not part of an exclusion region over runs. The events map is constructed in a similar fashion: Instead of summing the fraction of time in which each position was not part of an exclusion region, the number of events recorded at each position while it was not part of an exclusion region is summed. Bottom: Generation of acceptance map by dividing events map through exposure map. Both reproduced from [72].

assumes that the acceptance in the camera field of view does not vary in shape from one run to another even though taken at slightly different pointing positions and so smears out all field of view-specific influences [72]. To obtain the 2D acceptance, first an exposure map for each run is constructed in which for each position in the camera the fraction of time it was an excluded region is determined as illustrated on the top of figure 2.10. Then, the exposure maps of all runs weighted by the number of events outside an exclusion region are summed in the camera frame. Finally, the acceptance map is obtained by dividing the events map (of the events being outside of an exclusion region) summed up over all runs in the camera frame by the summed exposure maps as illustrated on the bottom of figure 2.10.

### 2.5.3 Statistical significance

In the previous section, the determination of the number of excess events in a region of interest using different background subtraction and acceptance calculation methods was shown. It is, however, not this number of excess events which one is really interested in, as this number alone does not indicate whether one is just looking at a background fluctuation or a real gamma-ray source, but one would like to have a method to quantify the statistical significance of a source. For this one uses again the number of events  $N_{\text{ON}}$  measured in the region of interest (respectively  $N_{\gamma\text{-candidate}}$  for the template background method) and compares it with the expected number of ON-events  $\alpha N_{\text{OFF}}$  (respectively  $\alpha N_{\text{Hadron}}$ ) in the background only case obtained from a control region.

In gamma-ray astronomy, the statistical significance is usually determined using the Li & Ma method in which the significance is defined as:

$$S = \sqrt{-2 \ln \lambda}, \quad (2.10)$$

where  $\lambda$  is the likelihood-ratio between the two hypotheses that  $N_{\text{ON}}$  results from background events and signal events and that  $N_{\text{ON}}$  results only from background events [118]. The probability for the first case, i.e., to measure  $N_{\text{ON}}$  in the region of interest and  $N_{\text{OFF}}$  events in the control region expecting  $B$  background events (in the control region) and  $S$  signal events (in the region of interest) can be written as:

$$P(N_{\text{ON}}, N_{\text{OFF}} | S, B) = \frac{e^{-(S+\alpha B)} (S + \alpha B)^{N_{\text{ON}}}}{N_{\text{ON}}!} \times \frac{e^{-B} e^{N_{\text{OFF}}}}{N_{\text{OFF}}!}, \quad (2.11)$$

whereas the probability for the second case (the so-called null hypothesis) can be written as:

$$P_0(N_{\text{ON}}, N_{\text{OFF}} | B) = \frac{e^{-\alpha B} (\alpha B)^{N_{\text{ON}}}}{N_{\text{ON}}!} \times \frac{e^{-B} e^{N_{\text{OFF}}}}{N_{\text{OFF}}!}. \quad (2.12)$$

The optimal number of signal  $\bar{S}$  and background events  $\bar{B}$  (i.e., the one maximizing the probabilities) is then determined by setting the derivative of the probabilities

against these numbers to zero leading to  $\bar{S} = N_{\text{ON}} - \alpha N_{\text{OFF}}$  and  $\bar{B} = N_{\text{OFF}}$  in the signal and background case respectively  $\bar{B}_0 = \frac{N_{\text{ON}} + N_{\text{OFF}}}{\alpha + 1}$  in the background only case.

This then leads to the likelihood ratio:

$$\lambda = \frac{P_0(N_{\text{ON}}, N_{\text{OFF}} | \bar{B}_0)}{P(N_{\text{ON}}, N_{\text{OFF}} | \bar{S}, \bar{B})} = \left( \frac{\alpha}{1 + \alpha} \frac{N_{\text{ON}} + N_{\text{OFF}}}{N_{\text{ON}}} \right)^{N_{\text{ON}}} \left( \frac{1}{1 + \alpha} \frac{N_{\text{ON}} + N_{\text{OFF}}}{N_{\text{OFF}}} \right)^{N_{\text{OFF}}}, \quad (2.13)$$

and to  $S = \sqrt{-2 \ln \lambda}$  being expected to follow a Gaussian distribution with average 0 and width 1 in the case  $N_{\text{ON}}$  is due to Poisson background fluctuations only and so being a measure of the statistical significance of a potential source.

This method relies on a good knowledge of  $\alpha$  (the ratio of the expected number of background events in the ON- and OFF-region). This  $\alpha$  is also affected by uncertainties not taken into account in this significance calculation method and often also obtained from the analysed data. In this case, this method does not work well for very low statistics.

## 2.5.4 Energy spectrum determination

The energy spectrum of a source is its differential flux as function of energy. Its determination is again based on a log-likelihood comparison of the expected number of events and the observed number of events as for the determination of the significance of a source. However, for the spectrum determination this comparison is done in four-dimensional bins of energy  $E$ , zenith angle  $\delta$ , off-axis angle  $\psi$  and telescope optical efficiency  $\epsilon$  as the acceptance  $A(E|\delta, \psi, \epsilon)$  for different energies is very dependent on the last three parameters [72]. In addition to this variation of acceptance, one needs to take into account the fact that the reconstructed energy  $E_{\text{rec}}$  in an event does not completely corresponds to its true energy  $E_{\text{true}}$  [119]. For this reason, the resolution function  $R(E_{\text{rec}}, E_{\text{true}}|\delta, \psi, \epsilon)$  which is defined as the probability density function to measure a reconstructed energy  $E_{\text{rec}}$  for a given true energy  $E_{\text{true}}$ , and is again dependent on the observation conditions, is introduced. This resolution function is a so-called instrument response function (IRF) of the H.E.S.S. telescope. These IRFs describe how the H.E.S.S. system reacts to a given gamma-ray signal. Beside the resolution function, the point spread function PSF and the effective area are IRFs. The PSF, which also depends on  $E$ ,  $\delta$ ,  $\psi$  and  $\epsilon$ , describes the response of H.E.S.S. to a point source and the extended shape it has in the camera. As described here, in standard analyses these IRFs are produced in four-dimensional bins of  $E$ ,  $\delta$ ,  $\psi$  and  $\epsilon$  and then interpolated. In chapter 5, a novel analysis method which uses unbinned IRFs developed in order to detect interstellar diffuse emission is described.

The expected number of gamma-ray events  $n_\gamma$  in a given reconstructed energy

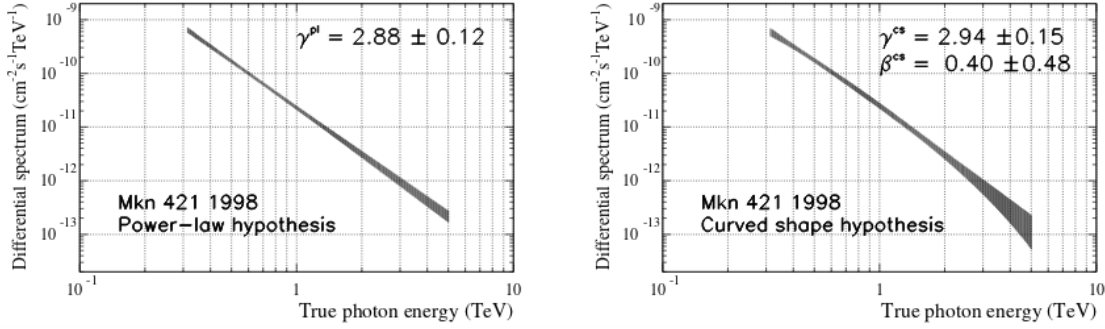


Figure 2.11: Illustration of the difference between different spectral shapes used in gamma-ray astronomy, here fit to the same 1998 dataset taken on Mkn 421 with CAT, a former Imaging Atmospheric Cherenkov Telescope. Left: Power-law spectrum. Right: Curved power-law spectrum. Reproduced from [119]

interval  $[E_{\text{rec},1}, E_{\text{rec},2}]$  for a given source spectrum  $\phi(E_{\text{true}}) = dN(E_{\text{true}})/dE_{\text{true}}$  can then be written as:

$$n_\gamma = \int_{E_{\text{rec},1}}^{E_{\text{rec},2}} dE_{\text{rec}} \int_0^\infty dE_{\text{true}} R(E_{\text{rec}}, E_{\text{true}} | \delta, \psi, \epsilon) A(E_{\text{true}} | \delta, \psi, \epsilon) \phi(E_{\text{true}}). \quad (2.14)$$

The determination of the spectrum  $\phi(E_{\text{true}})$  is usually based on a so-called forward folding technique in which one assumes spectral models  $\phi(E_{\text{true}}, \alpha)$ , where  $\alpha$  are potential free parameters of the model, and retains the model delivering the best fit to the data. Some of the numerous commonly used models in gamma-ray astronomy are:

- A power-law spectrum:  $\frac{dN}{dE} = N_0 \left(\frac{E}{E_0}\right)^{-\Gamma}$
- A curved power-law spectrum (log-parabola function):  $\frac{dN}{dE} = N_0 \left(\frac{E}{E_0}\right)^{\alpha - \beta \ln \frac{E}{E_0}}$
- A power-law spectrum with exponential cut-off:  $\frac{dN}{dE} = N_0 \left(\frac{E}{E_0}\right)^{-\Gamma} e^{-\frac{E}{E_C}}$ .

An example of a power-law and a curved power-law spectrum fit to the same dataset is shown in figure 2.11.

The likelihood  $P(N_{ON}, N_{OFF} | n_\gamma, n_h)$ , which is defined in the same way as for the determination of the significance, is then maximized for the different models [119]. This delivers the best-fit parameters  $\alpha$  and their uncertainties, the covariance matrix from which the uncertainty in flux at each energy can be determined, the expected number of events in each bin and the final log-likelihood from which a goodness-of-fit parameter can be determined.

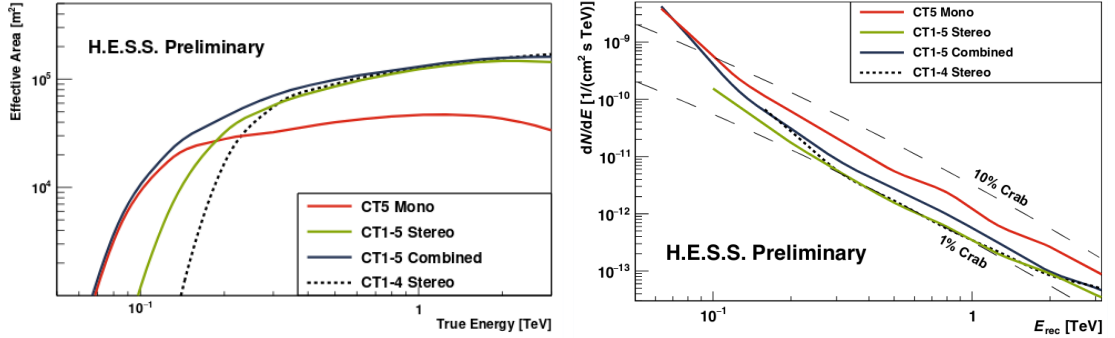


Figure 2.12: Left: Effective area (after selection cuts) of the semi-analytic model analysis for the different analysis modes. Right: Differential sensitivity of the semi-analytic model analysis for the three analysis modes of HESSII data, as well as for HESSI for comparison. Reproduced from [120].

## 2.6 Performance

As the H.E.S.S. array is constituted of five telescopes of two different types, different reconstruction methods are conceivable for the individual events of the data taken with all five telescopes [120]. Indeed all the events can be reconstructed stereoscopically in all telescopes as for observations with the four HESSI telescopes (*Stereo* mode) and so take advantages of the improved stereoscopic direction reconstruction discussed earlier. However, the reconstruction of monoscopic events from CT5 allows to significantly reduce the energy threshold as CT5 is much larger. For this reason, there is also a *Mono* mode in which events are reconstructed solely based on CT5. Finally, there is a *Combined* mode in which the event reconstruction leading to the smallest reconstructed direction uncertainty is retained for each event or the reconstruction which could be performed if an event is not recorded in telescopes of all types.

The performance of H.E.S.S. depends on the chosen reconstruction. *Mono* mode reaches the best performance at the lowest energies, whereas *Stereo* mode performs better at higher energies and *Combined* mode combines both. In addition, the performance decreases with zenith angles and depends on observational conditions and the instrument status. High night sky background or a high broken pixel fraction decrease for instance the performance. For this reason, the performance of H.E.S.S. under good conditions at 18° zenith angle is discussed here for the different modes based on Monte Carlo simulations using the semi-analytic model reconstruction [120].

The effective area for the different reconstruction modes is shown on the left of figure 2.12. One can see that above energies of about 300 GeV, the *Stereo* mode

using all five telescopes and the *Combined* mode perform similar to the *Stereo* mode using only the four HESSI telescopes, and so that the addition of CT5 does not improve the performance a lot at energies above this threshold [120]. Indeed, the performance of the CT5 *Mono* analysis is much lower above this threshold. However, the picture changes drastically at lower energies. Indeed, below energies about 100 GeV, the *Mono* mode starts to become much more performant than the *Stereo* modes. As expected, the *Combined* mode approaches the *Mono* mode at low energies and the *Stereo* mode at high energies, and so provides the best energy coverage.

The differential sensitivity for the different reconstruction modes is shown on the left of figure 2.12. It is here defined as the minimum source strength of a point-like source for it to be detected at  $5\sigma$  after 50 h of observation at a given energy range using five energy bins per decade [120]. The picture is similar than for the effective area, however the sensitivity is slightly worse in the *Combined* mode than in the *Stereo* mode at high energies, which indicates that there was still room for improvement in the selection cuts in the *Combined* mode compared to the *Stereo* mode at the moment this study was performed. However, the plot shows that H.E.S.S. is sensitive to a source with about 1 % of the Crab flux within 50 h over a large energy range.

The angular resolution, defined as the 68 % containment radius of the point spread function, is below  $0.1^\circ$  over the full energy range, and even below  $0.06^\circ$  in the TeV range and has only a small dependence on zenith angle [113]. The energy resolution is about 10 % over the whole sensitive energy and zenith angle range, and always between 5 % and 15 %.



# Chapter 3

## Improved calibration of optical efficiency at large zenith angle

### 3.1 Zenith angle dependence in the muon optical efficiency

As I discuss in chapter 4, an important part of the work presented in this thesis was the test of a novel optical efficiency calibration method for Imaging Atmospheric Cherenkov Telescopes using an unmanned aerial vehicle (UAV)-mounted artificial light source. To verify the performance of this method, I wanted to compare it with the so far used muon calibration method described in section 2.3.5. However, upon investigation of the UAV runs, I noticed that the muon optical efficiencies obtained from the runs performed for UAV calibration were significantly lower than the ones obtained from runs performed for normal H.E.S.S. observations. One of the main differences between UAV observation runs and normal observation runs is the fact that UAV runs are taken at much higher zenith angle than most observation runs (as also discussed in more detail in chapter 4).

For this reason, I investigated a potential zenith angle dependence of the muon optical efficiencies. The long-term variation of the optical efficiency as obtained from the muon calibration is dominated by the degradation of the telescopes' optical elements with time and so-called seasonal effects. These seasonal effects are not directly related to a change of the optical efficiency, but to the seasonal changes of the atmospheric conditions. These changes modify the atmospheric absorption of the Cherenkov light emitted by muons, leading to a seasonal variation of the Cherenkov light emitted from muons reaching the telescopes. This leads to a change of the optical efficiencies obtained with the muon calibration which is not due to a change of the physical optical efficiencies, but to a change of atmospheric conditions. On short time scales, changes in meteorologic conditions and the low

number of muons recorded in some runs lead to statistical fluctuations between individual runs and observation nights.

This means that in order to detect any potential small zenith angle dependence of the muon optical efficiency, one needs to integrate data over a long enough run range to mitigate the effect of run-to-run statistical fluctuations. To disentangle these run-to-run fluctuations from systematic effects, I proposed to first group them in zenith angle bands of  $5^\circ$  and then average in each band results from runs taken at similar times. This however resulted in too low statistics or the time range being too long leading to any potential signal being hidden by the seasonal variations. For this reason, I decided to build a running average optical efficiency which evolves with the seasonal variations and to compare the optical efficiency in each zenith angle band against this running average. However, as I wanted to check for a possible zenith angle dependence in the optical efficiencies, I only used low zenith angle runs between  $20^\circ$  and  $40^\circ$  for building the running average<sup>1</sup>. I computed this running average muon optical efficiency by averaging over the previous 30 runs taken with a zenith angle between  $20^\circ$  and  $30^\circ$  and the previous 30 runs taken with a zenith angle between  $30^\circ$  and  $40^\circ$  leading to an average over 60 runs in total. This led to a "current average muon optical efficiency" for each point in time, i.e., for each individual run, which should encompass seasonal variations. Then for each run, I normalized the optical efficiency by the "current average muon optical efficiency". This allows me then to look at the muon optical efficiency as a function of zenith angle over long time ranges without being impacted too much by seasonal variations.

The evolution of these normalized optical efficiencies as a function of zenith angle over a run range of 10 000 CT1-4 runs taken before camera upgrade is shown in figure 3.1 for CT1 for the about 3500 observation runs in this run range including CT1, but the dependence was similar in the other telescopes. The plot shows that the obtained muon optical efficiencies are stable for low zenith angles whereas there is a clear decrease with high zenith starting around  $50^\circ$  zenith angle. For run ranges including runs taken with CT5, the decrease with zenith angle was less pronounced, not only in CT5, but also in CT1-4. This completely unexpected behaviour is discussed in the next section.

## 3.2 Revisiting the event selection

As the muon rings used for the muon calibration are reconstructed in the individual telescopes and not in stereoscopic mode as they do not cross several telescopes, the different zenith angle dependence in CT1-4 when CT5 is included hints to a

---

<sup>1</sup>I did not use lower zenith angle runs, as they were too few in number to have a similar size angular range with as many runs per time interval.

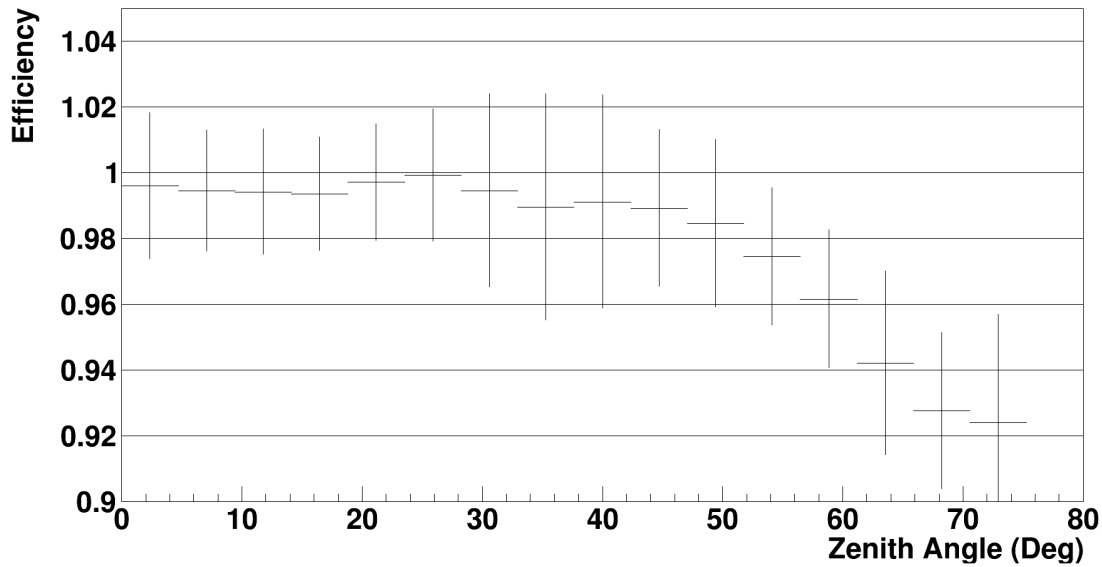


Figure 3.1: Optical efficiency normalized by running average over low zenith angle runs as a function of zenith angle for about 3500 runs for CT1. The uncertainty bars indicate the standard deviation of each bin value in order to illustrate the spread between the different runs.

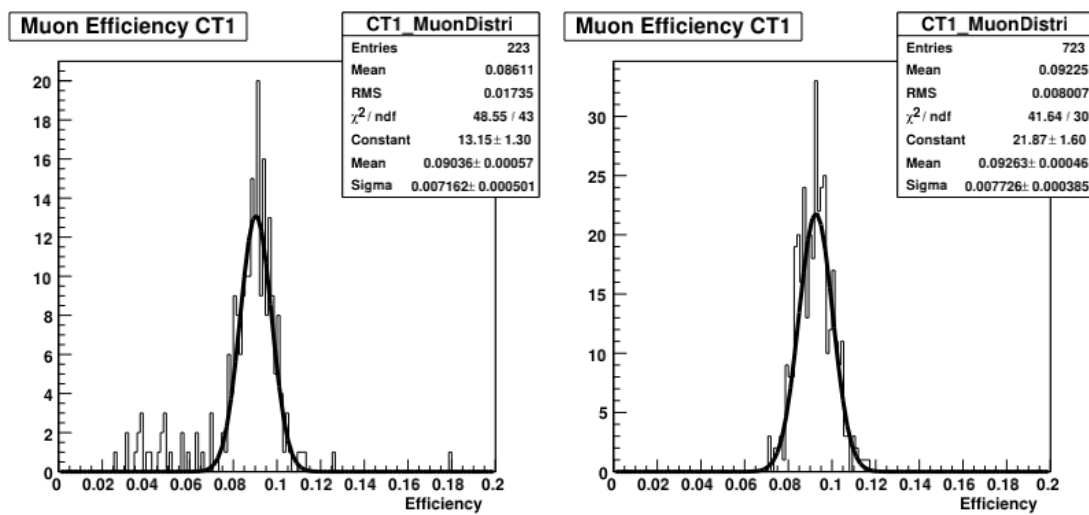


Figure 3.2: Distribution of muon optical efficiencies on an event-by-event basis. Left: For a high zenith angle run ( $63^\circ$ ). Right: For a low zenith angle run ( $14^\circ$ ).

problem in the event selection. I investigated the difference in the event selection by looking at two examples of normal observation runs, one taken at high zenith angle ( $63^\circ$ ) and one taken at low zenith angle ( $14^\circ$ ). The distribution of the muon optical efficiencies on an event-by-event basis, after applying quality cuts on the muon events, is shown in figure 3.2 for these two runs. The muon efficiencies are Gaussian distributed around a central value for the low zenith angle run, as one expects during the measurement of most physical quantities subject to statistical uncertainties. However, the distribution for the high zenith angle run shows a tail or second component on the left of the Gaussian distribution.

This indicates that the event selection behaves differently at high zenith angle and indeed looking at the events in this tail, it is visible that they are badly reconstructed. Hence, I had a closer look at the used and potential new cut variables. The distribution of the main potential cut variables as a function of the optical efficiencies before applying any cut (except for the selection of events well suited to fit a muon ring) is shown in figure 3.3 for the high zenith angle run. So far, mostly the distance of the camera centre to the reconstructed impact position of the muon and the intensity of the muon ring (i.e., the total number of photo-electrons in the muon ring) have been used as cut variables. However, the figure seems to indicate that the goodness of the fit, which has so far not been used in the event selection, might also be a good cut variable as most events with a particularly low or high efficiency have a higher goodness value. Here the goodness is again defined as difference of the actual log-likelihood of the fit and its expectation value normalized by the number of degrees of freedom as in section 2.4.3:<sup>2</sup>

$$G = \frac{1}{\sqrt{2N_{\text{DoF}}}} \sum_{\text{pixel } i} [\ln L(s_i|\mu_i) - \langle \ln L \rangle_{|\mu_i}], \quad (3.1)$$

meaning that a higher goodness value indicates a worse fit of the muon ring.

So, setting a minimum goodness cut removes most of the badly reconstructed muon events and leads to the disappearance of the high zenith angle tail in the muon efficiency distribution as illustrated in figure 3.4 at the cost of losing statistics. The distribution for the low zenith angle run is not impacted except that it is losing statistics too.

However, I noticed that this new cut on muon goodness is very efficient to select clean muon rings and thus allows to relax the cut on the minimum muon intensity without deteriorating the distribution of the efficiencies. This allows to recover and even increase statistics with respect to the initially implemented cuts

---

<sup>2</sup>The model used for the fit in section 2.4.3 was of course very different, since there I looked at a semi-analytic gamma-ring model whereas here I look at a muon ring model. However, one can still define the goodness of this fit in the same way in order to exclude the events with a bad fit.

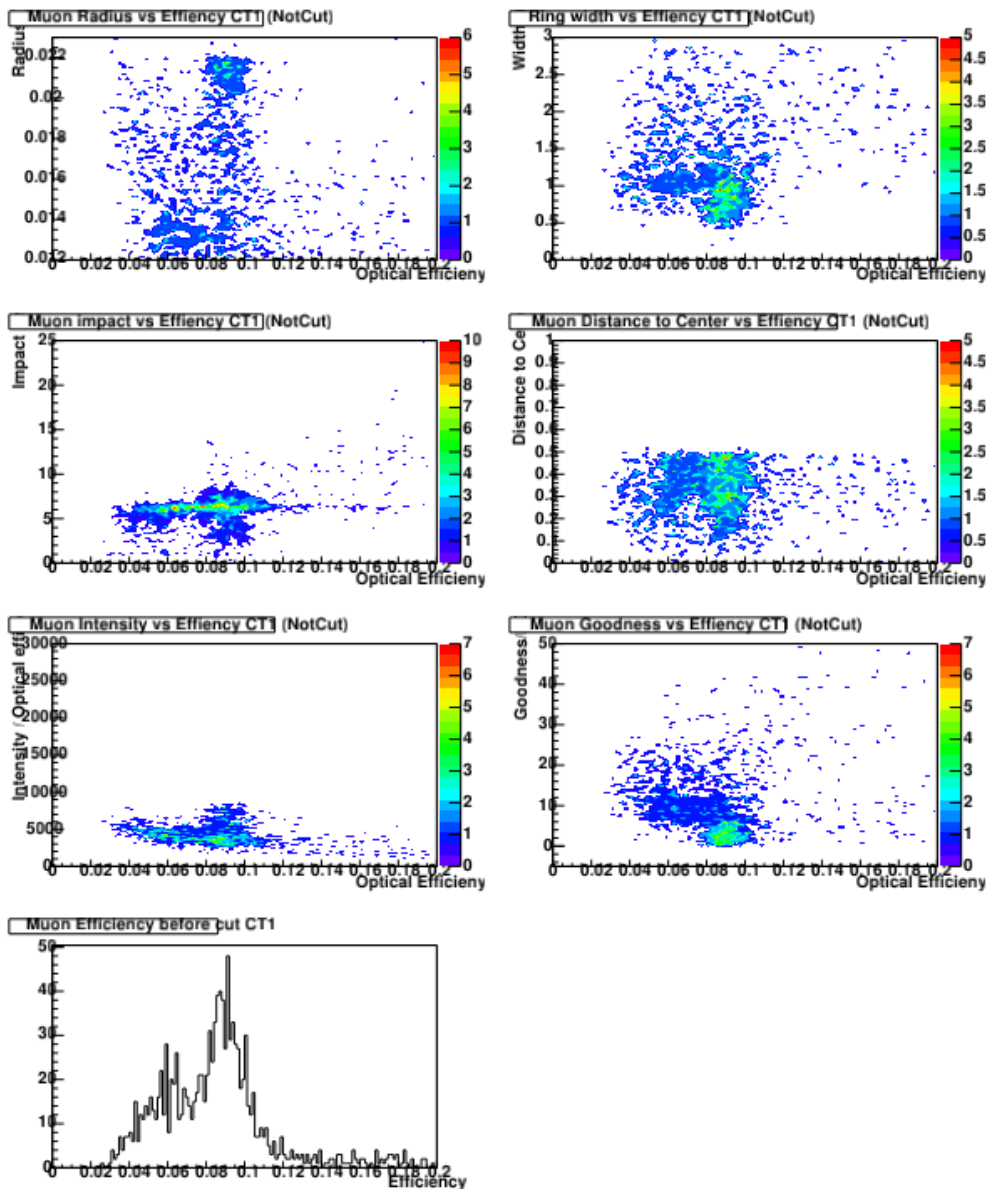


Figure 3.3: Muon optical efficiencies as a function of different cut variables used for the identification of well reconstructed muon events, before applying any cut beside an initial event selection, for the high zenith angle run. From left to right, top to bottom: Efficiency vs the radius of the fit muon ring; the width of the fit ring; the distance of the centre of the camera from the reconstructed impact position of the muon; the distance of the centre of the ring from the centre of the camera; the intensity of the muon ring; the goodness of the fit of a ring to the recorded light intensity (lower values indicate a better fit). In addition, the distribution of the optical muon efficiencies on an event-by-event basis before applying any cut is displayed on the bottom plot.

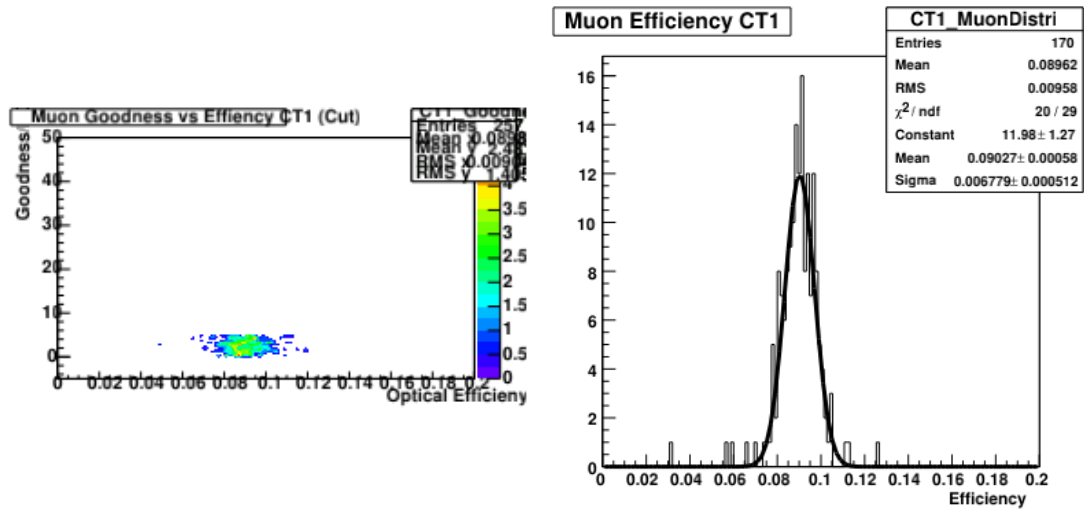


Figure 3.4: Left: Goodness of fit of the muon ring as a function of muon optical efficiency after applying the new goodness cut for the high zenith angle run; Right: Distribution of muon optical efficiency on an event-by-event basis after applying the new goodness cut for the high zenith angle run. The tail of badly reconstructed muons almost disappears.

(about 34% more selected muon rings for the high zenith angle run).

### 3.3 Cure of zenith angle dependence

This shows that these new cuts work well for the two considered runs, but it needs to be tested on a long run range to make sure that there are no unwanted side effects. To do this, the whole run range considered in figure 3.1 has been recalibrated using the new cuts. This led to no significant change for runs with zenith angle below  $50^\circ$ , showing that the new cuts perform similarly on this zenith angle range and that they can safely be used there. For runs taken at high zenith angle, the average muon optical efficiencies increased compared to before. Plotting again the optical efficiency normalized by the same running average as on figure 3.1 as a function of zenith angle, the muon optical efficiencies are almost constant with respect to zenith angle as illustrated in figure 3.5. This shows that these new cuts removing the badly reconstructed muons at high zenith angle remedy the zenith angle dependence of the optical muon efficiencies without having a bad impact on low zenith angle runs.

Similar tests have also been performed on run ranges including CT5 and after the camera update of CT1-4 and no negative side effects have neither been observed, while the zenith angle dependence was also resolved for these runs. In

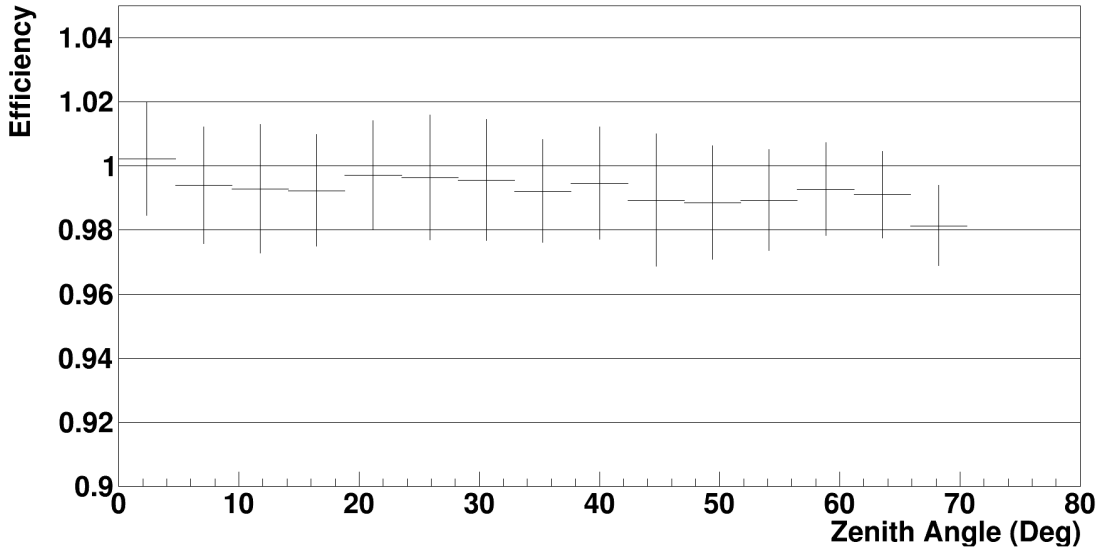


Figure 3.5: Optical efficiency normalized by running average over low zenith angle runs obtained using the new selection cuts as a function of zenith angle for about 3500 runs for CT1. The uncertainty bars indicate the standard deviation of each bin value in order to illustrate the spread between the different runs.

view of these results, these new cuts are now part of one of the standard calibration chains of H.E.S.S. and are so applied during the muon calibration of newly taken runs. In addition, all the runs taken at zenith angle above  $55^\circ$  have been recalibrated using the new cuts. This does not have a significant impact on the optical efficiencies used in H.E.S.S. analyses as they are averaged over the whole observation period, outliers are removed in this average and runs are taken at lowest possible zenith angle to reduce systematic uncertainties. Indeed, for normal observation runs the maximum used zenith angle is  $60^\circ$  and there are only very few runs between  $55^\circ$  and  $60^\circ$  zenith angle. However, having the correct muon efficiencies for high zenith angle runs too can be crucial when looking at the muon efficiencies of individual runs, for instance for debugging purposes or when trying to optimize an analysis.

### 3.4 Revisiting the muon optical efficiencies of the UAV calibration runs

After having removed this zenith angle dependence from the muon optical efficiencies, they were recomputed over the observation periods during which UAV calibration runs were taken. However, even though the muon optical efficiencies of

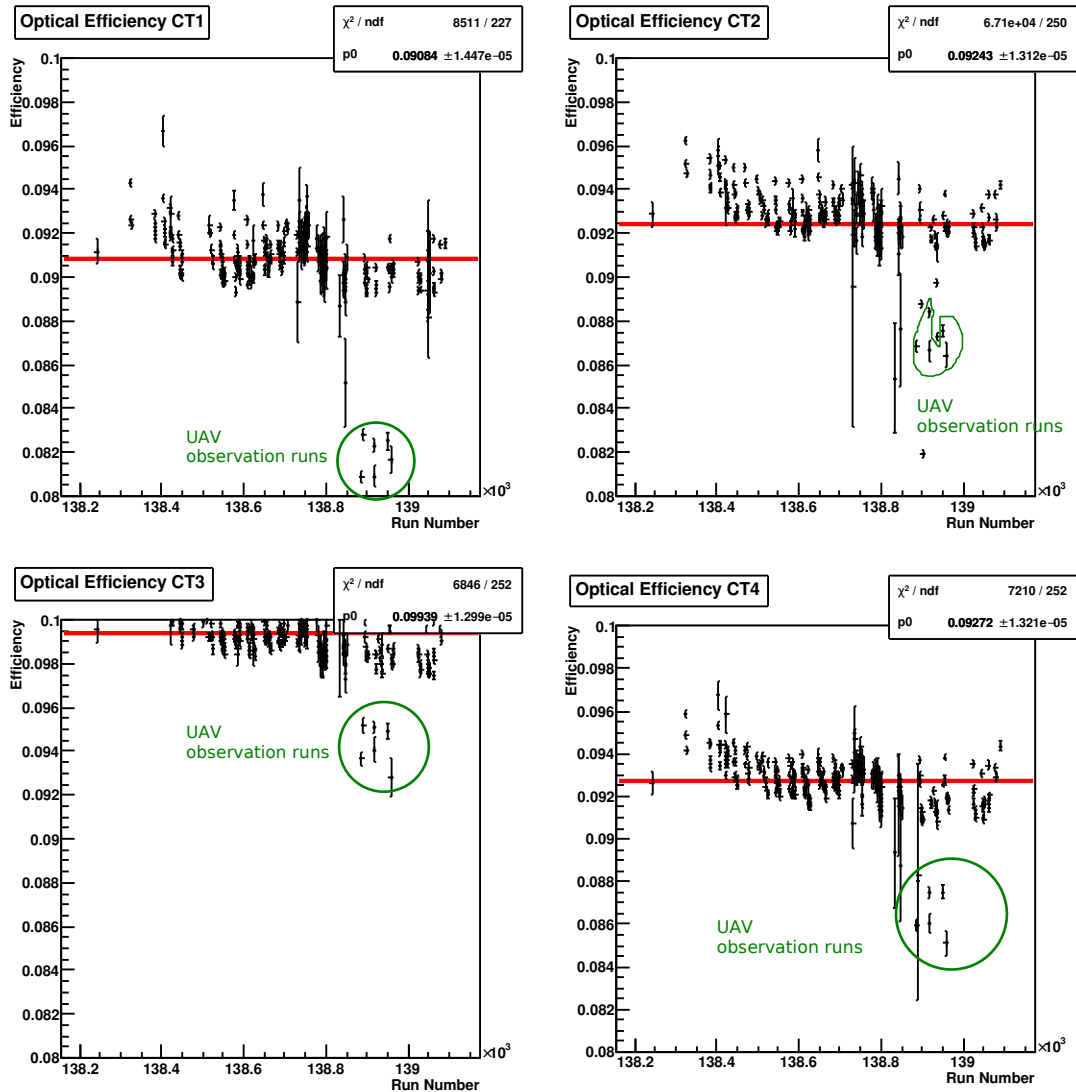


Figure 3.6: Optical efficiencies determined with the muon calibration method over one of the shift periods during which UAV calibration data has been taken using the four HESSI telescopes. The muon optical efficiencies of the runs taken in UAV calibration configuration are circled in green. They have clearly lower optical efficiencies than all the other runs taken in the same observation period.

the UAV calibration runs increased by 1% to 2%, they were still lower than the ones of normal observation runs taken in the same observation period as illustrated in figure 3.6. As there is no indication for any strong remaining zenith angle dependence, I started to investigate other differences between UAV calibration runs which could potentially cause such an effect.

Up to now, there have been two UAV calibration campaigns taken, one in May 2018 and one in November 2019, and during these two UAV campaigns slightly different settings were used. Whereas in the first campaign, only the four HESSI telescopes were used, some of the runs also included CT5 in the second campaign. Both of these configurations are also frequently used during normal observation runs, however other settings used during the UAV calibration runs are very uncommon for other runs, namely:

- The UAV calibration runs were taken at high zenith angle (about  $75^\circ$  in the first campaign and about  $63^\circ$  in the second campaign).
- During the first campaign, events were recorded even if they only triggered one telescope (so-called multiplicity 1 events) which is very uncommon for H.E.S.S. observations. For the second campaign, two triggering telescopes were required as is done during normal observations.
- The UAV calibration runs were taken in so-called convergent pointing, i.e., all the telescopes were pointing to the nominal UAV position instead of pointing parallel to a position on the sky.
- The telescopes were pointing to a fixed position instead of tracking a source.

Over the lifetime of H.E.S.S., a few hundreds of runs have been taken with multiplicity 1 and runs have also been taken while not tracking a source at fixed altitude and azimuth. As for the zenith angle, no obvious correlation could be found. However, only 5 runs have been taken in convergent pointing mode (except for the runs taken in UAV configuration) and they only contain very few muons due to having been taken with multiplicity 2, which makes a conclusive statistical comparison impossible. However, such a dependence on convergent pointing is very unlikely for the multiplicity 1 runs as the same muons should be recorded by the individual telescopes independently of the pointing of the other telescopes. So, none of these differences between UAV calibration runs and normal observation runs can explain the difference in the obtained muon optical efficiencies between these two run types at this stage.

The diminution of the muon optical efficiencies for UAV calibration runs is about 10% for CT1 and 5 to 6% for the other telescopes in the first campaign and 9% for CT3 and 1 to 4% for the other telescopes in the second campaign.

However, during the second campaign, the sky was covered and this together with the multiplicity 2 requirement led to very few muons being recorded. In addition, the impact of the covered sky on the recorded muon efficiencies is unclear as normal observations can only be taken in good weather conditions. However, the diminution is present in the first campaign too, and even stronger, even though it has been taken under good weather conditions.

It is important to note that these values show that the amount of the diminution is different in the different telescopes. The cause of this is as the reason for the diminution itself completely non-understood. However, this means that not only the absolute muon efficiencies, but also the relative muon efficiencies are impacted and so that one has to take this into account when trying to compare these relative efficiencies to the ones obtained with UAV calibration.

As the origin of this difference in the obtained muon efficiencies for UAV calibration runs and normal observation runs is completely unclear and no difference to normal observation runs could be seen with archival data having some of the characteristics of the UAV calibration runs, we proposed to take technical runs in the UAV calibration configuration at different zenith angle and in convergent and non-convergent pointing mode to disentangle potential reasons which could lead to this diminution. These observations have been accepted thanks to my findings and will be taken later this year (i.e., 2021) and can so unfortunately not be considered anymore for this work. For this reason, the period average muon efficiencies were used in this work as these are the efficiencies that have been well studied and have proven their reliability in numerous H.E.S.S. studies unlike the muon efficiencies obtained from UAV calibration runs.

# Chapter 4

## UAV calibration

### 4.1 Limitations of the muon-based optical efficiency calibration

As discussed in section 2.3.5, the calibration of the optical efficiency is an important step in the calibration of Cherenkov telescopes. For all the three major Imaging Atmospheric Cherenkov Telescope arrays, this is done with muon rings. This technique is used as muon rings have many properties which make them well suited for this task. First of all, the light yield recorded from a muon in a Cherenkov telescope does almost not depend on the energy of the muon as they are mostly ultra-relativistic to have a high chance to reach the telescopes, making it easy to predict the amount of light which could geometrically reach the camera. Then, muons which pass through the mirror of a telescope are easily distinguishable from other events due to their characteristic ring form. In addition, optical efficiency calibration with muons does not need any extra observation time (as many other calibration steps), as muons anyways constitute a background to the observed gamma rays in normal observations and the muons recorded during the regular observations can be used for the calibration. Last, muons have also a very similar Cherenkov spectrum to gamma rays. The only difference is that the recorded Cherenkov light from identified muons is emitted in average at lower altitudes than the recorded Cherenkov light from gamma rays making the ultraviolet part of their spectrum less impacted by atmospheric absorption. This also constitutes the biggest limitation of the muon calibration method: the optical efficiency in the ultraviolet range impacts the recorded muon events much more than the recorded gamma-ray events. Any wavelength dependent evolution of the optical throughput (i.e., among other in the quantum efficiency, mirrors, ...) can so not be properly monitored with muons alone. This increases the uncertainties of this method if its extent of this difference is not well assessed.

Current generation Cherenkov telescope arrays are, except for H.E.S.S., only constituted of telescopes of the same type, which reduces the impact of this limitation as the wave-length dependency of the evolution of the optical efficiency should be very similar from one telescope to the other<sup>1</sup>, leading to this effect only introducing an overall systematic uncertainty on the light yield of recorded events and not to an uncertainty which is different for each telescope. This then leads to an overall uncertainty on the light yield which is small enough to achieve the overall foreseen uncertainty budget. However, for the planned array CTA, the story is different. First of all, CTA will be constituted of three different types of telescopes which might not show the same wavelength dependent evolution of their optical efficiency. Then, CTA is planned to fulfil much higher requirements in systematic uncertainty than the arrays currently in operation: among other the systematic uncertainty on the overall energy scale should be below 10% and the uncertainty on the absolute intensity of the Cherenkov light in each telescope below 8% [121]. An improved version of the currently applied muon calibration technique will work well enough to reach these requirements for any wavelength independent degradation of the optical efficiency. To partially circumvent the limitation of the muon calibration being sensitive to the ultraviolet, the telescopes will be designed to only record a negligible part of the spectrum at wavelength below 290 nm (wavelength below which Cherenkov radiation from showers induced by primary gamma-rays is anyway almost completely absorbed). Nevertheless, the expected long-term wavelength dependent degradation of the optical systems might lead to an over-correction of the efficiency of up to 13% using only muons for the calibration of the optical efficiencies, making it impossible to reach the requirements. For this reason, the wavelength dependent degradation of the optical efficiency will be needed to be determined from time to time. To monitor this wavelength dependent degradation, different solutions have been envisaged, based mostly on ground-based or airborne artificial light sources illuminating the telescopes directly or indirectly. In my work, I have considered an airborne calibration source on an unmanned aerial vehicle (UAV), concept which will be discussed in more detail in the next subsection.

## 4.2 UAV calibration concept

The very recent evolution in flight performance of UAV due to improvement in battery performance and carbon fibre technology have rendered possible to use them for calibration tasks in astronomical facilities. One of the first facilities who

---

<sup>1</sup>Except for the PMT-to-PMT variations of the quantum efficiency. The effect of this should however be limited too due to the big number of PMTs per telescope (960 for each HESS-I telescope for instance).

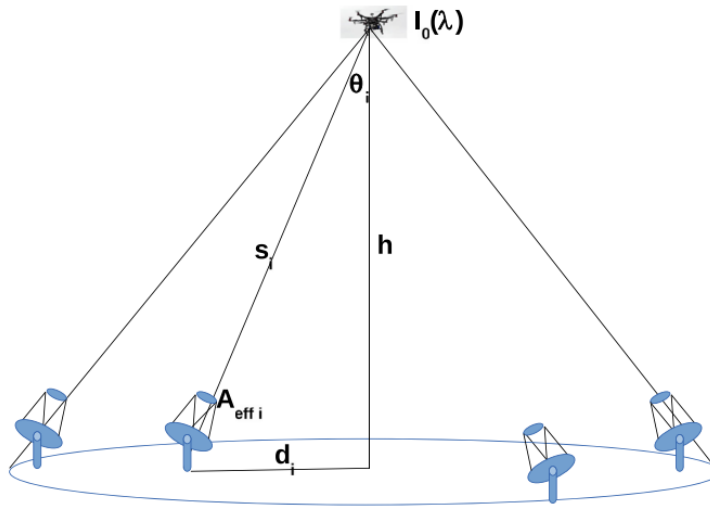


Figure 4.1: Principle of telescope optical efficiency calibration with a UAV. The UAV is put to a stable position above the array and an LED mounted on it is illuminating the telescopes of the array with light pulses. Reproduced from [123].

took advantage of this was the Pierre Auger Observatory which successfully used UAVs to determine the point spread function of their fluorescence telescopes [122]. In this thesis, first tests to use such a UAV to inter-calibrate Imaging Atmospheric Cherenkov Telescopes are discussed.

The basic idea is, as described in the feasibility study for using this technique with the future CTA array conducted by Anthony Brown [123], to have a UAV such as a hexacopter or octocopter communicating via radio with the ground station, and on which a pulsed wide-beamed light source, such as a light emitting diode (LED) with a diffuser, is mounted in order to be able to illuminate as many telescopes as possible. The UAV is then put to a stable position above the array to illuminate the telescopes as illustrated in figure 4.1. The LEDs are programmed to emit pulses of a few ns for the light recorded by the telescopes to be as similar as possible to light emitted by showers. To do a multi-wavelength optical calibration, one can simply mount multiple LEDs emitting light at different wavelengths on the UAV.

For large arrays, such as the Southern site of CTA, there has to be a compromise between illuminating as many telescopes as possible with an as equal amount of light as possible (and so similar distances of the UAV to the different telescopes), which requires a high altitude for the UAV, and altitude restrictions due to the battery performance of the UAV, the brightness of the LEDs and atmospheric absorption which needs to be kept at a minimum, especially for an absolute calibration. In addition, CTA South will be constituted of three different

types of telescopes with very different mirror sizes and so very different recorded intensities for the UAV being at the same distance. Both combined might lead to the necessity of having different UAV positions for cross-calibrating this array in order for the light to be in the dynamical range of each telescope. For the UAV being at a reasonable altitude of 1300 m, one would need about four positions to cross-calibrate CTA South [123].

### 4.3 Setup

Such considerations are not necessary for the H.E.S.S. telescope array on which we tested this calibration method due to its much smaller size. It is no problem to illuminate all telescopes, even for the UAV being at much lower altitude. For these tests, an off-the-shelf octocopter with 16 Ah lithium polymer batteries was used. On this UAV a UV LED flasher system was mounted, which was able to emit 4 ns pulses at a wavelength of 400 nm. In front of the UAV flasher system a 50° circular top-hat diffuser was installed.

Two test campaigns have been conducted so far, one in May 2018 and one in November 2019. In both of these test campaigns, the UAV was taking off at the H.E.S.S. residence which is 800 m South East from the centre of the H.E.S.S. array as illustrated in figure 4.2. This take-off location was chosen for multiple reasons. First of all, the UAV could not fly above the array as a safety requirement and being at larger distance reduces the requirement of light control at the take-off location making the handling of the UAV for this test campaign easier. Second, being at a larger distance reduces the altitude which the UAV needs to reach to be in the field of view of all telescopes which allows a longer stay at the calibration point with limited battery performance. The exact position of the take-off position was determined by the readily availability of electricity at the residence allowing to recharge the UAV battery between different runs during the same night. However, this large distance to the centre of the array also led to the UAV being at quite low elevation for these two campaigns, which is very different from regular observations. The configuration of the different runs taken during these two campaigns is summarized in table 4.1 and discussed in more detail in the following.

In the first campaign, three runs have been taken over two nights for which the UAV was going vertically up to about 200 m above ground level, leading to a zenith angle of about 75°. In this campaign, as a first test, only CT1-4, which were pointing convergently (i.e., all the telescopes were pointing to the same point at low altitude instead of pointing almost parallel as in usual observations) to the nominal UAV position, were used. The main reason for CT5 not being used, was that convergent pointing was not implemented at that time for CT5. For the first two runs, the UAV was flashing at a frequency of 1 Hz whereas for the last run the

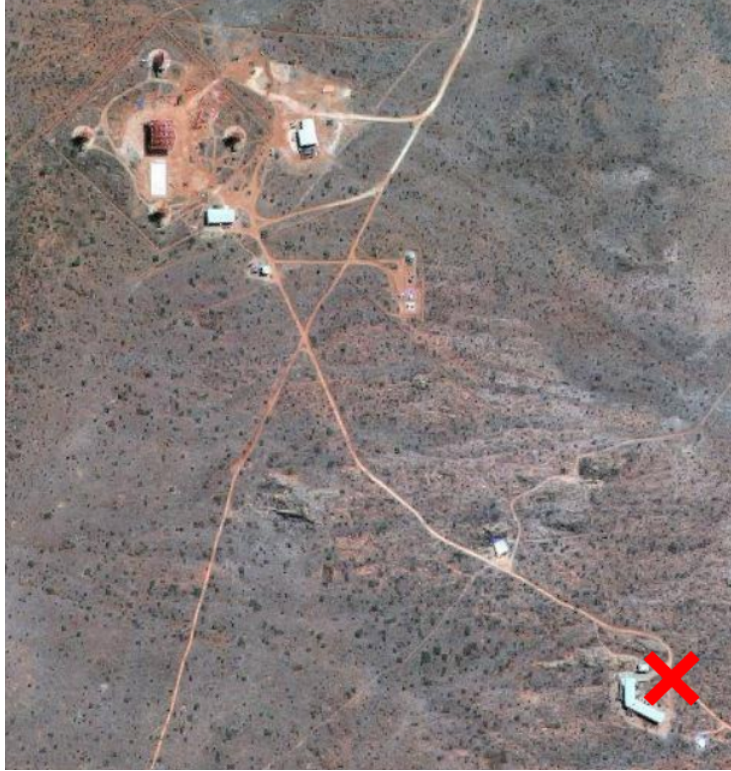


Figure 4.2: Illustration of the take-off position of the UAV. On the top left, one can see the H.E.S.S. array with its five telescopes. On the bottom right, one can see the residence with the approximate take-off location marked by a red cross. Picture reproduced from [124] (Google Maps).

Date	1st Campaign		2nd Campaign	
	May 2018		November 2019	
Number of runs	2	1	6	4
Zenith angle	75°	75°	63°	63°
Telescope configuration	CT1, CT2 CT3, CT4	CT1, CT2 CT3, CT4	CT1, CT2 CT3, CT4	CT1, CT2, CT3 CT4, CT5
Light source frequency	1 Hz	60 Hz	1000 Hz	1000 Hz
Brightness level of recorded images	Low	High	Different	Different
Minimum trigger multiplicity	1	1	2	2

Table 4.1: The different run parameters used in the different runs of the first and second campaign.

frequency was increased to 60 Hz. In addition, a different illumination setting was used in the last run, leading to 8 times brighter recorded images as is discussed in more detail in section 4.8.

In the second campaign, ten runs have been taken over three nights for which the UAV was going vertically up to about 400 m above ground level and CT5 was used this time. The chosen altitude was higher for two reasons: first of all, this reduced the zenith angle to about  $63^\circ$ , bringing the conditions closer to normal observations, even though it is still higher than the usual maximum zenith angle of  $60^\circ$ . Second, the H.E.S.S. telescopes are designed to focus at the height of the shower maximum at about 8 km above the H.E.S.S. array [125]. This leads to the images of the light emitted by the light source on the UAV to be very defocused in the cameras due to the UAV being much closer to the telescopes than the showers. For this reason, the images are extended in the camera and especially big for CT5 which has a smaller field of view, making it difficult to include the image in its camera for the UAV being only at a height of 200 m. For the UAV being at an altitude of 400 m, the images were, even though still extended, a bit smaller making it easier to include CT5. Four runs including all the five telescopes were taken in the last night whereas the remaining six runs only included CT1-4. Again, all the telescopes were pointing convergently to the UAV, however this time the frequency of the light source was set to 1000 Hz in order to have more events. In this campaign, different brightness levels of the light source were tested.

## 4.4 Calibration of the UAV data

Just like regular data, UAV data first need to be properly calibrated. This UAV data contains the UAV events needed for the inter-calibration and the cosmic background events as discussed in more detail in subsection 4.6.1. For the first campaign, I used the usual H.E.S.S. pedestal calibration described in section 2.3. For this, I only used the cosmic events as the number of illuminated pixels in the UAV events were very high. However, in the second campaign, the sky was covered. This was not a problem for recording the UAV events, as the UAV was well below the clouds, but reduced the number of recorded cosmic events in a telescope to about 100 for some of the runs, making a pedestal calibration only based on these events imprecise. Using the UAV events for the pedestal determination was not an option either, since the UAV was only moving little in the field of view and so many pixels were never free from UAV illumination in these events. For this reason, I used the pedestals obtained from a different run of the same observation period as pedestals for these runs. Testing this method on the data of the first campaign to check the impact of using the pedestals of a different run only led to changes in the computed average relative efficiencies of less than 2% in each

telescope and to an increase of its event-by-event standard deviation of less than 25 %. This shows that using the pedestals from a different run does not deteriorate the final results dramatically.

For the gain calibration, the cross-calibration of the gain channels and the flat-field calibration, standard calibration (using dedicated runs) was used. So, I performed these calibration steps with the methods described in section 2.3.

Afterwards, I interpolated the intensity in the non-operational pixels using the mean intensity of the neighbouring operational pixels. This is necessary as for the UAV events there is no reconstruction as for cosmic events. Indeed, as I discuss later on in more detail, the intensity is just summed up to determine the recorded intensity in a telescope. As the average number of illuminated non-operational pixels per event can go up to 10 % of the illuminated pixels for some telescopes in some runs, not recovering the intensity in these pixels might lead to an underestimation of the intensity and thus to an increase of the uncertainty on the obtained optical efficiencies. As the pixels of the H.E.S.S. cameras are hexagonal, this interpolation procedure consists in taking the average over six pixels for non-operational pixels which are not at the edge of the camera and all neighbouring pixels operational.

As a last step, I cleaned the images to remove the noise pixels not part of the UAV image using a dual-threshold procedure as described in subsection 2.4.1. The used thresholds were 5 and 7.

## 4.5 Monte-Carlo Simulation

Before the first campaign, I developed a Monte-Carlo simulation of the whole system to check that (at least in the simulation) everything looks as expected and our assumptions are fulfilled. One of these assumptions which I checked, and on which the whole inter-calibration relies, is that the quantity  $I \times d^2$ , even though expressed as a function of  $d$ , does not change when varying  $d$  for the photons of the UAV-mounted light source being uniformly emitted in solid angle, which can be easily derived from geometrical considerations. Here  $I$  is the sum of all photo-electrons in an event in a given telescope and  $d$  the distance of the UAV to the mirror plane of this telescope (i.e., the plane perpendicular to the telescope pointing direction containing the centre of the mirror). After the first and second campaign, I refined the simulation to be better able to reproduce the actual conditions and setup of the data taking and so to be able to do further cross-checks. But before coming to this, let me first describe the working principle of the UAV simulation.

### 4.5.1 Working principle of the Monte-Carlo simulation

For the simulation, I use pre-existing H.E.S.S. software as much as possible. The H.E.S.S. software consists of multiple independent simulation and analysis chains. In the chain used for this work, the shower simulation for the H.E.S.S. array is usually done with two main components: First, the shower simulation called *Kaskade* which simulates the propagation and interaction of the particles in the atmosphere is used. Afterwards, the interaction of the Cherenkov photons with the mirrors and the cameras and the propagation in between these elements as well as the electronic chain of the array (such as the trigger) is simulated with the detector simulation called SMASH [104] to produce raw data in a format identical to real data. As the detector simulation only propagates single photons, I completely re-use it for simulating the photons of the UAV once they have reached the telescopes with a few minor corrections for the correct implementation of convergent pointing. The shower simulation is designed to simulate the interactions of different particle types in the atmosphere and not to simulate photons emitted at low altitudes. For this reason, I only re-use small parts of its code (mainly the atmospheric absorption of photons) for simulating the propagation of the photons in the atmosphere.

I assume the light source mounted on the UAV to be a point source with isotropic emission even though only the photons which can possibly reach one of the telescopes are simulated. The position of the UAV, the position to which the telescopes are pointing, the wavelength of the light emitted by the light source, the duration of the pulses emitted by the light source, the number of photons to be generated per event and the number of events to be generated are the main input parameters of the simulation. Some of these parameters can be changed between the different generated events.

The first step of the simulation is to correct the number of photons to be generated for the limited solid angle over which photons are generated and to apply the quantum efficiency of the photo-multiplier tube of the H.E.S.S. telescopes to the number of photons to be generated. The correction for the solid angle can be switched off and the quantum efficiency is already applied at this stage not to waste computation time by simulating photons which would be anyway lost at a later stage. This can be done as the quantum efficiency is assumed to be a quantity which only depends on the wavelength of the photons and not on their propagation properties. Then, I generate the photons uniformly over the solid angle within which they can potentially reach the telescope. I attribute an emission time stamp to each photon assuming the photons to be emitted uniformly over the time interval defined by the pulse duration.

For the propagation of the photons from the UAV to the telescopes, the standard H.E.S.S. atmospheric model is used. This model is based on the considerations described in [105] and assumes the atmosphere to be constituted of  $N$  layers

with the altitude  $z_i$  and density  $\rho_i$  at all the  $N + 1$  layer  $i$  boundaries known. The density  $\rho(z)$  as a function of altitude  $z$  is then interpolated between the layer boundaries according to the formula:

$$\rho(z) = \left( \frac{\rho_i}{\rho_{i+1}} \right)^{-\frac{z - z_i^0}{z_{i+1} - z_i}}, \quad (4.1)$$

with  $z_i^0 = \frac{\log \rho_i \times z_{i+1} - \log \rho_{i+1} \times z_i}{\log \rho_i - \log \rho_{i+1}}$ . The mostly used model also used in this simulation consists of 49 layers with yearly average densities for Windhoek as they were determined in balloon flights undertaken in 1999 [104]. I propagate each photon in a straight line to the altitude of the telescope it can possibly hit and compute its position and arrival time at this point taking into account the integrated refractive index obtained from the atmospheric model. I afterwards remove the photon from the simulation with a probability equal to the computed absorption probability, which is again obtained from tabulated absorption probabilities at discrete altitudes and wavelengths and interpolation. Finally, I pass the photon to the standard detector simulation of H.E.S.S., which simulates the propagation of the photon from the altitude of the telescope, via the mirror and camera to the pixels and then its conversion to photo-electrons to get the charge accumulated in each pixel. At the end, it simulates the trigger, amplification and the digitization of the signal, using realistic pulse shapes. For simulating the trigger, the whole charge accumulated in the camera during an event is considered. Then, the camera is divided, as in the real trigger process, in different partially overlapping sectors and the event is only kept if the following condition is fulfilled in at least two telescopes: At least three pixels in a sector exceed a charge threshold corresponding approximately to four photo-electrons [106].

This detector simulation delivers the data in the same format as the actual observation data, i.e., the charge recorded in each pixel. As for the real data one would like to get back to a physical quantity and for this reason the simulated data needs to be calibrated too. For this, I use the same procedure as for the actual data. This calibration procedure relies on special calibration runs (especially for the pedestal and gain determination) which need to be simulated as well. For pedestal determination, I simulate 50 000 events with only night sky background and for gain calibration, I simulate 50 000 events with the LED usually used for gain calibration. Finally, I clean the resulting images with the same dual-threshold algorithm as the actual UAV events as described in section 4.4.

The simulation can be used in two different modes. First of all, it can be used to generate a given number of events for the UAV being at a given point in space, which allows to study the general behaviour of the whole setup. Second, it can be used to simulate all the events of an actual run, including the actual pointing directions of the telescope, and using for each event the actual reconstructed po-

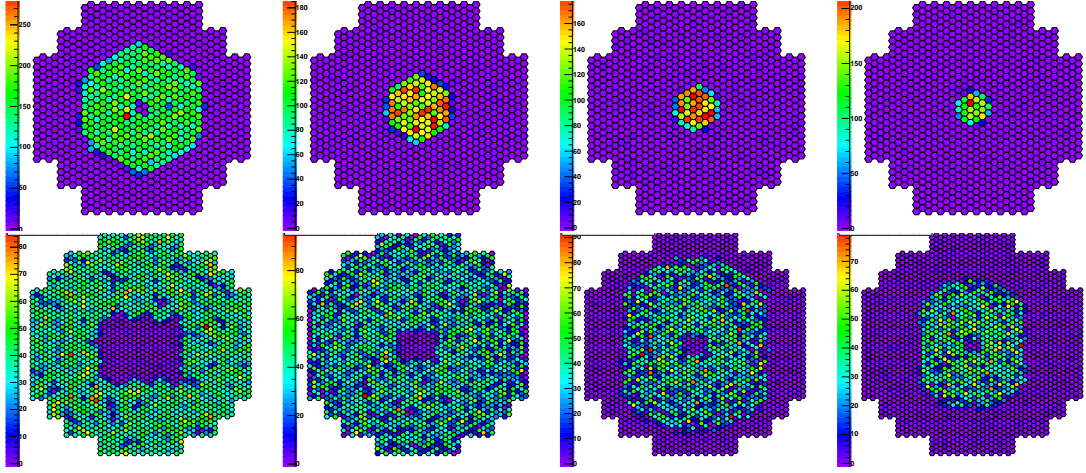


Figure 4.3: Simulated events, as seen by HESS-I telescopes (top) and the HESS-II telescope (bottom), of a calibration pulse emitted by a calibration system on a UAV holding a stationary position above the centre of the H.E.S.S. array at altitudes of 250 m, 500 m, 750 m and 1000 m (from left to right). The colour scale indicates the number of photo-electrons recorded in each pixel.

sition of the UAV and the actual non-operational pixels, which allows to study the behaviour of individual runs after data taking. This second mode follows a similar concept as the run-wise simulations recently developed within the H.E.S.S. collaboration and used in the diffuse analysis described in chapter 5. I describe the main results of the use of the simulation in the first mode in the next subsection. I describe the results obtained from the second simulation mode after the description of the analysis procedure used for the inter-calibration as the same analysis procedure is applied to these simulations.

#### 4.5.2 Simulating the general behaviour of the setup

As mentioned before (in section 4.5), I used the simulation to verify that  $I \times d^2$  is indeed independent of  $d$ . To do this, I simulated 500 events at 7 regularly spaced altitudes between 250 m and 1000 m and 20 regularly spaced horizontal displacements of the UAV to the centre of the array between 0 m and 950 m, leading to a total of 140 positions. I ran these simulations without any non-operational pixels, as their influence on the intensity is expected to depend on their distribution and can so not be accounted for by introducing a general correction factor, but have to be handled on a case-by-case basis respectively included in the systematic uncertainty, and without mispointings as they should be equivalent to a change of pointing direction of the telescopes. In figure 4.3, sample event displays are

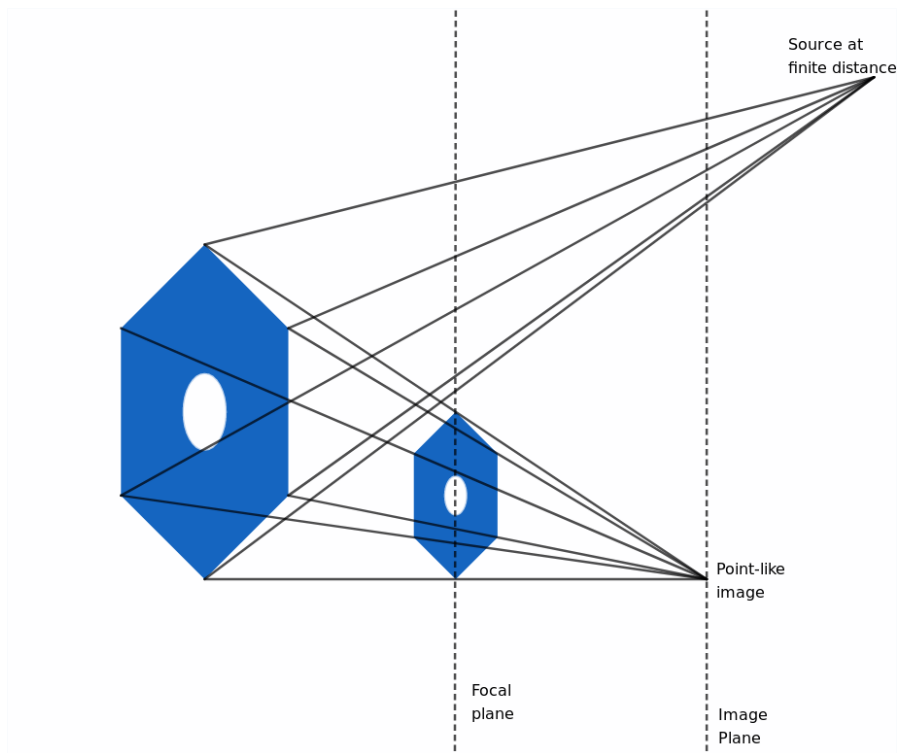


Figure 4.4: Illustration showing the image of a source at a finite distance on the H.E.S.S. camera. The light from a point-like source at a finite distance is reflected by a hexagonal HESS-I telescope mirror which has a hole in the centre in which the CCD camera used for the pointing corrections and the flat-fielding LED are located (and which is exaggerated on the figure). This mirror focalizes the light again leading to a point-like image on the image plane. For a source at infinity, the image plane would correspond within uncertainties to the focal plane of the camera. For a source at finite distance, the image plane is displaced with respect to the focal plane leading to an extended image following the shape of the mirror

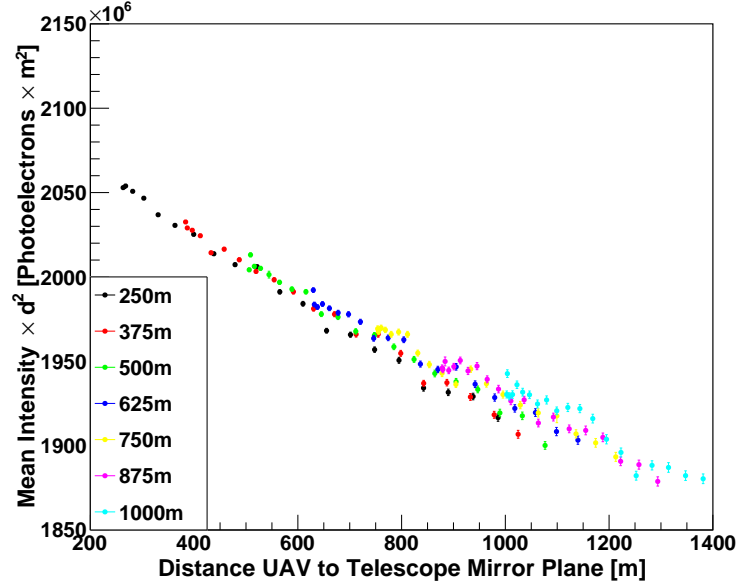


Figure 4.5:  $I \times d^2$  as a function of  $d$  for CT1 for events generated at 7 different altitudes and 20 different horizontal displacements of the UAV to the array centre including atmospheric absorption in the simulation.

shown for the UAV holding a stationary position above the centre of the array for different altitudes for the HESS-I and HESS-II telescope. As expected, the images get larger the closer the UAV to the telescope. Indeed, as mentioned before the telescopes are designed to focus at the emission altitude of the Cerenkov radiation, which is much higher than the altitude which a commercial octocopter could reach, and so the images are the more de-focused the closer the UAV to the telescopes. This leads to the image not being completely included in the camera for CT5 for low distances of the UAV to the telescope and so the amount of light reflected by the mirrors depending much more on the exact position of the UAV and so being much more difficult to predict. During actual observation, this is also a concern for larger distances as it is not possible to position the UAV as exactly as in simulation. This is one of the reasons why the second campaign was taken with the UAV at a higher altitude. In addition, it is clearly visible that the shape of the images follows the shape of the mirror, as expected from geometrical optics as illustrated in figure 4.4.

Figure 4.5 shows the evolution of  $I \times d^2$  as a function of  $d$  for the different positions at which the simulation was run for CT1. Unlike expected from considerations based only on the geometrical considerations,  $I \times d^2$  is slightly decreasing with  $d$ . This is due to atmospheric absorption as more photons are absorbed the

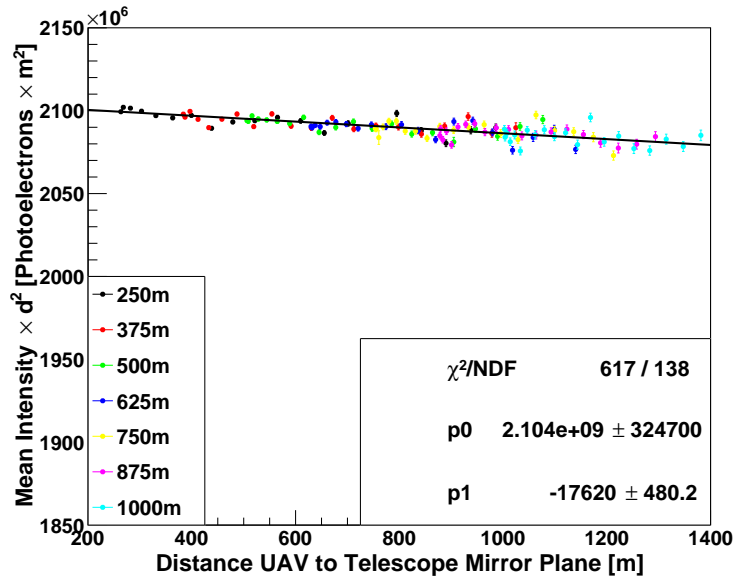


Figure 4.6:  $I \times d^2$  as a function of  $d$  for CT1 for events generated at 7 different altitudes and 20 different horizontal displacements of the UAV to the array centre with atmospheric absorption switched off in the simulation.

higher the integrated atmospheric thickness the photons pass (i.e., the higher the altitude of the UAV or the larger its horizontal offset to the centre of the array). To check whether the atmospheric absorption is responsible for the whole decrease, I repeated the simulations without atmospheric absorption and the resulting plot is shown in figure 4.6.

The decrease is significantly reduced, however a small decrease of about 1% over the whole distance range is left and so almost the whole decrease was due to atmospheric absorption. The extent of this remaining decrease depends strongly on the cleaning thresholds and completely disappears when reducing the camera signal thresholds applied during image cleaning, which indicates that a small fraction of the image (tails) is most likely cleaned away and that this fraction increases with the distance of the UAV to the telescopes because the images become smaller. Reducing the cleaning thresholds comes however at the expense of an increased amount of accepted night sky background variations and increased statistical uncertainties. As this decrease is an order of magnitude smaller than the decrease due to the atmospheric absorption and is also much smaller than the point-to-point variations discussed next, I did not change the cleaning thresholds. As an additional check, I also performed the whole data analysis presented in the following without cleaning, which only marginally impacted the inter-calibration

results beside increasing statistical uncertainties.

However, even though there is almost no global variation with  $d$  anymore, there are small point-to-point variations of about 1% which are bigger than the statistical uncertainties (which I simply computed by taking  $1/\sqrt{500}$  times the standard deviation of  $I \times d^2$  for the 500 events generated at each position). They are likely due to boundary effects when illuminating a different number of pixels and boundaries between pixels. This shows that  $I \times d^2$  is independent of  $d$  modulo this 1% point-to-point variations neglecting atmospheric absorption.

Including the atmospheric absorption again, the change of  $I \times d^2$  over the relevant range of  $d$  defined by the maximum distance between two telescopes of 169.2 m (diagonal of the square formed by the four HESS-I telescopes), which is much bigger than the registered movement of the UAV as discussed later (about 30 m altitude variation, mostly while the UAV was moving in and out of the field of view), is also about 1% for the given UAV telescope separation. To get a better handle on this uncertainty, I performed additional Monte-Carlo simulations, this time in the second simulation configuration, i.e., simulating the actual data taking runs with the UAV at its reconstructed position. From these simulations, the absorption probabilities of photons emitted in direction of the mirror centre of each individual telescope were computed for each recorded position and averaged. The average (over all the simulated events of both runs) absorption probabilities for a photon in direction of the different telescopes were 6.7%, 7.6%, 7.5% and 6.6% for CT1-4 respectively. I have applied these absorption probabilities as correction factors while computing the relative efficiencies as discussed previously. This led to a change of the relative efficiencies of about 0.5%.

## 4.6 Analysis procedure

In this subsection, I describe the analysis procedure I developed for the analysis of the UAV calibration runs. As I discuss later on in more detail, some of the runs taken during the two campaigns are unusable due to the too long pulse duration of the LED-based light source mounted on the UAV. This unfortunately impacts all runs including CT5. For this reason, in the following I discuss each step of the analysis procedure first for the CT1-4 telescopes and the necessary adaptations for runs including CT5 are discussed at the end of the description of each step. It is worth to note that as the analysis of the runs including CT5 could not be successfully completed and further adaptations might be necessary which cannot be foreseen at this stage of the analysis and so are not discussed in this section.

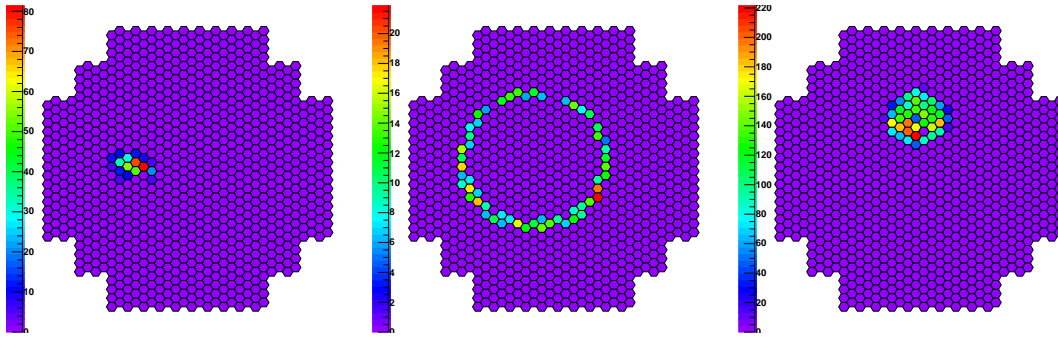


Figure 4.7: Event display examples for the different types of measured events. Left: Cosmic event; Middle: Muon Ring; Right: UAV Event. The colour scale indicates the number of produced photo-electrons.

### 4.6.1 Event selection

As illustrated in figure 4.7, there are three types of events in the datastream:

- Cosmic events, i.e., events from high energy photons, electrons or hadrons entering the atmosphere, which are characterized by an elongated elliptical or irregular shape. During UAV observation runs, the telescopes point convergently to the nominal UAV position at about 200 m to 400 m altitude in order to record the UAV light simultaneously in all telescopes whereas during normal observation runs the telescopes point parallel in direction of the observed source (as the distance to the source is much larger than any array related scale). As the bulk of the Cherenkov emission in the H.E.S.S. sensitive energy range is emitted at about 8 km above the H.E.S.S. array [125], the convergent pointing at much lower altitude makes it very unlikely that an atmospheric shower is in the field of view of three or four HESS-I telescopes and for this reason cosmic events are recorded by one or two HESS-I telescopes.
- Muon rings, i.e., Cherenkov rings produced by atmospheric muons (also originating from cosmic events) crossing the telescope characterized by their ring shape. They are recorded by one telescope.
- UAV events are characterized by their shape following the shape of the mirror (as described in section 4.5) and by them being recorded by all telescopes except if telescopes are not available due to dead-time.

From this list, one can see that UAV events tend to be recorded in a larger number of telescopes. In addition, for the first campaign the UAV was set up such that they have a higher image amplitude. However, before doing any event selection, I

needed to take into account that UAV events can be cut by the edge of the camera leading to only part of the intensity being recorded. For this reason, I applied a cut of  $0.034 \text{ rad}$  ( $\approx 2^\circ$ ) on the nominal distance (i.e., the angular distance between the centre of the camera and the image centre of gravity). I chose this cut based on a visual inspection of the evolution of the event displays as a function of nominal distance. For the two reasons mentioned earlier, I preliminary selected the events having been recorded in at least three telescopes and having a minimum image amplitude compliant with UAV events.

In the first campaign, the last run was taken with a very high amplitude and two runs with slightly lower amplitude. For the run with higher image amplitude, I set the minimum image amplitude to 20 000 photo-electrons. With this selection, UAV events are very well separated from background events as only 0.5 % of the events being UAV-like according to one of both cut variables are not UAV-like according to the other cut variable even though both cut variables are not expected to be strongly correlated within categories. This is illustrated again on the left of figure 4.8 with the distributions of the image amplitudes for events which are recorded in one or two telescopes and for events which are recorded in three or four telescopes. It shows that both distributions are very separated in the high image amplitude case as the distributions have very little overlap.

For the two runs of the first campaign with lower image amplitude, I could only set the minimum image amplitude to 2870 photo-electrons in order not to cut the distribution of the events recorded in three or four telescopes as can be seen on the right of figure 4.8. In these runs, 7.5 % and 13.5 % of the events being UAV-like according to one cut variable are not UAV-like according to the other one, considering only events which were recorded in at least two telescopes, as illustrated on the right of figure 4.8. This is due to the lower image amplitude threshold and the much higher background event rate. This indicates that the events selected as UAV events could be contaminated with cosmic events for the runs with lower image amplitude.

However, already from the data collected in the first campaign, it is possible to put much better constraints on the contamination fraction of events selected as UAV events. In total, six runs have been taken under very similar conditions (similar pointing directions, weather conditions, ...) in the first UAV campaign. I considered three of these runs as successful as there were UAV events completely included in the camera of all four telescopes. For one of the other runs the UAV was not entering the field of view of the telescopes at all and for a second one the image was so far on the edge of the field of view that it was never completely included in the cameras. For the third of these other runs, the image was also never completely included in the cameras and additionally one telescope was not working, which is why this run is not be considered in the following. In the five remaining

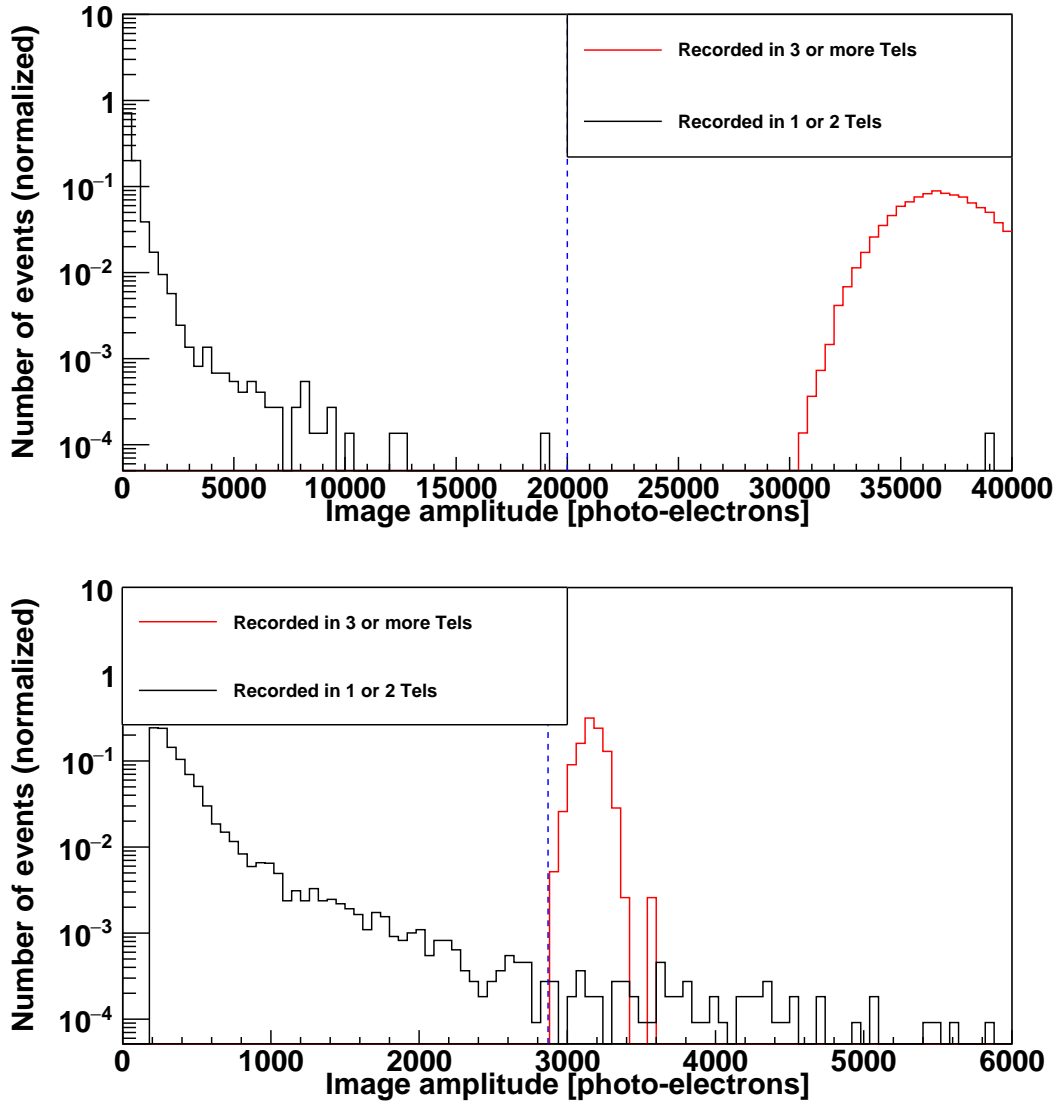


Figure 4.8: Normalized distribution of the image amplitudes in a given telescope for events recorded in one or two telescopes (black) and for events recorded in three or four telescopes (red) on logarithmic scale. Top: Run with higher image amplitude (Cut set at 20 000 photo-electrons – blue dashed line); Bottom: One of the runs with lower image amplitude (Cut set at 2870 photo-electrons– blue dashed line).

runs, there were in total about 480 000 events classified as cosmic events (fulfilling none of the two criteria which are used to select UAV events) in all telescopes in which they were recorded. There were, however, no events recorded in three or four telescopes (and not being rejected based on the nominal distance cut which rejects the cut UAV events) not satisfying the image amplitude cut valid for the considered run (20 000 photo-electrons for the run with the high image amplitude, 2870 photo-electrons for the two runs with lower image amplitude, no cut for the other two runs) which were not obviously caused by the UAV<sup>2</sup>. This shows that events having an image amplitude consistent with the image amplitude expected for UAV events in the considered run are the only events recorded in three or four telescopes which allows to put an upper limit on the contamination of the selected UAV events as discussed in the following. Using this, that there are 403 187 events clearly identified as cosmic events in the four runs beside the run with high image amplitude and that there are 85 207 events recorded in one or two telescopes in the run with the high image amplitude and assuming that the probability  $p$  for a cosmic event to be recorded in three or four telescopes follows a binomial distribution, there are no cosmic events recorded in three or four telescopes with a confidence of 99.1 % in the high image amplitude run. The values used in this calculation as well as the one that will be used in the calculation for the two other runs are summarized in table 4.2. Similarly, making use of the previous statement, that there are 242 324 events clearly identified as cosmic events in the three runs beside the two low image amplitude runs and that there are 148 367 and 97 976 events recorded in one or two telescopes in one and the other run with low image amplitude respectively and assuming that the probability  $p$  for a cosmic event to be recorded in three or four telescopes follows a binomial distribution, there are no cosmic events recorded in three or four telescopes with a confidence of 80.4 % and 91.5 % in both of these runs.

Given these very high confidence levels that there were no events recorded in three or four telescopes not due to the UAV, using the number of telescopes in which an event has been recorded as unique selection variable is still expected to achieve an almost perfect selection of UAV events. So, it is not necessary to use additional selections such as a high image amplitude to render UAV events distinguishable from cosmic events, but one could just use any light source intensity as long as the intensity hitting the pixels stays in the sensitive range of the H.E.S.S.

---

<sup>2</sup>There were in total four events recorded in three or four telescopes not fulfilling the image amplitude cut and not being rejected due to too high nominal distance: Two of them were recorded in three telescopes and have an image amplitude of less than 200 photo-electrons, but the typical hexagonal UAV shape (which is very different from the shape of cosmic events) in all three telescopes. For the other two, which were recorded in four telescopes, the UAV was at the edge of the field of view, but the event was not correctly rejected in one telescope based on the nominal distance cut due to noise in the camera creating additional illuminated pixels.

	High Image Amplitude run	Low Image Amplitude Run A	Low Image Amplitude Run B
Events clearly identified as cosmic events in runs with different image amplitude cut	403 187	242 324	242 324
Events recorded in 1 or 2 telescopes	85 207	148 367	97 976
Confidence level that there are no cosmic events in the run	99.1 %	80.4 %	91.5 %

Table 4.2: Table indicating the confidence level that there are no cosmic events polluting the UAV events for the different runs and the values used in their computation. The second column indicates the high image amplitude run and the two last columns the low image amplitude runs named with A and B as they will be later on when discussing the results. These upper limits were obtained assuming the probability for a cosmic event to be recorded in three or four telescopes follows a binomial distribution with the two possible outcomes: Either the event is recorded in one or two telescopes or the event is recorded in three or four telescopes.

telescopes. For this reason, lower intensities were used in the second campaign to produce events which are more similar to cosmic events and I based the final event selection only on the number of telescopes in which an event was recorded (for consistency between the two campaigns, but this leads anyway to the same selection of UAV events in the first campaign): I classified an event recorded in three or four telescopes passing the nominal distance cut as UAV event and an event recorded in one or two telescopes as cosmic event.

The fact that there are no cosmic events recorded in three or four telescopes is very different from usual observation runs. This is of course due to the four H.E.S.S. telescopes pointing convergently to the approximate location of the UAV at very low elevation (instead of pointing almost parallel as in usual observation runs): this leads the four telescopes to point to very different positions at the production altitude of the atmospheric showers and their Cherenkov radiation making it very unlikely for a cosmic event to be recorded by more than two telescopes. Indeed, the angle of the pointing direction between CT1 and 2, and CT3 and 4 was about  $2^\circ$  or  $3^\circ$  in the first campaign (where the UAV reached an altitude of about 200 m) and second campaign (where the UAV reached an altitude of about 400 m) respectively, whereas the angles of the pointing directions between the other telescopes were between  $8^\circ$  and  $9^\circ$  in the first campaign and  $7^\circ$  and  $9^\circ$  in the second campaign. For this reason, cosmic events are generally recorded in CT1 and CT2 or CT3 and CT4.

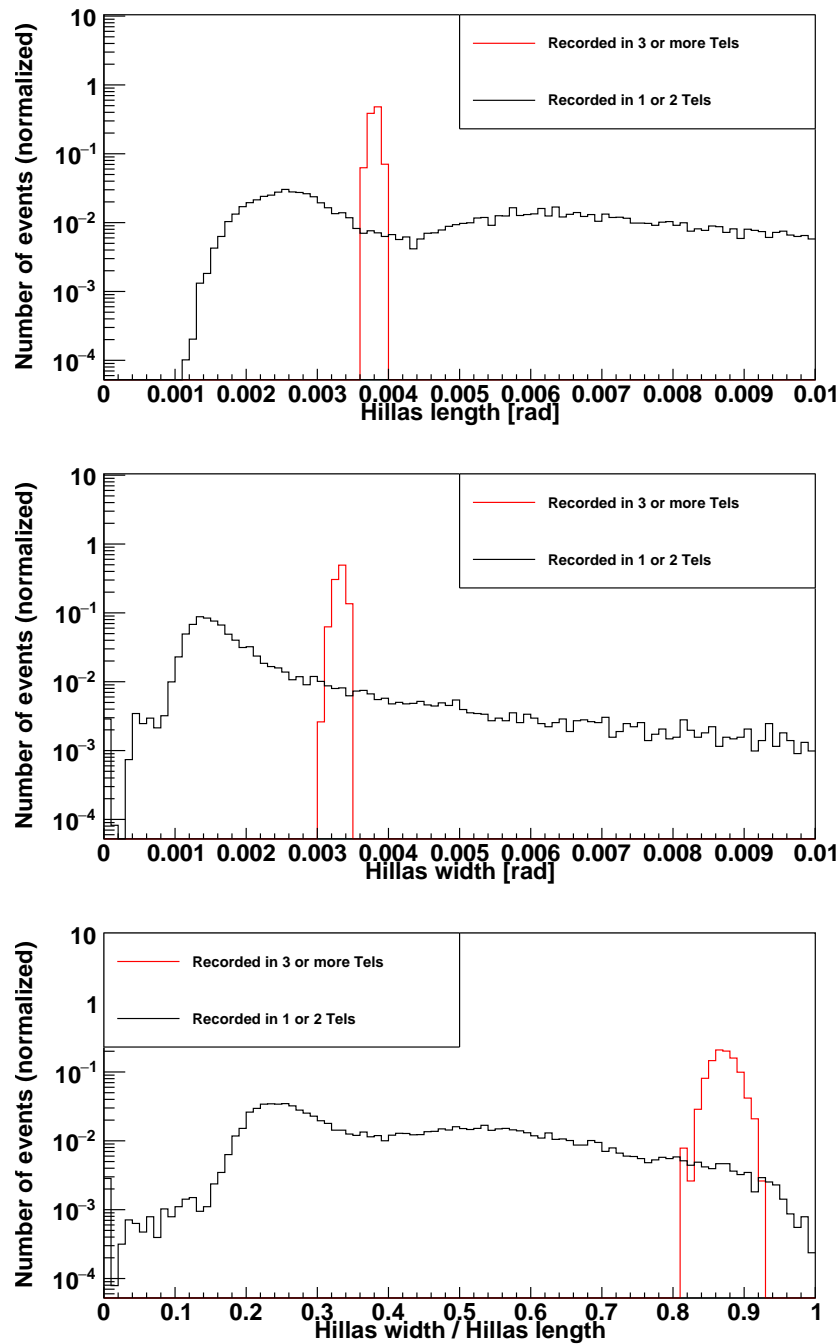


Figure 4.9: Normalized distribution of other possible selection variables in a given telescope for events recorded in one or two telescopes (black) and for events recorded in three or four telescopes (red) on logarithmic scale. Top: Hillas length; Centre: Hillas width; Bottom: Hillas width divided by the Hillas length.

I also looked at other possible discrimination variables in order to find the best suited one. They were based on the Hillas parameters which were described in subsection 2.4.2. Figure 4.9 shows the distribution of the Hillas length, the Hillas width and the Hillas width divided by the Hillas length for events which are recorded in one or two telescopes and for events which are recorded in three or four telescopes, using one of the low image amplitude runs of the first campaign. The distributions look very similar for all the runs except that the ratio between cosmic and UAV events is different. Even though all three variables tend to take lower values for events recorded in one or two telescopes, the distributions are still overlapping and so not so well suited for the discrimination as the number of telescopes in which an event is recorded.

Considering now the runs which were taken with five telescopes, we have to adapt the procedure to the different characteristics of CT5 and number of telescopes. As CT5 has a smaller field of view, the first thing which needs to be done is to reduce the cut on nominal distance for this telescope for UAV events to be completely included in the camera. I set it to 0.0075 rad ( $\approx 0.43^\circ$ ). Then, the main question is how to handle events which are recorded in two HESS-I telescopes and CT5<sup>3</sup>. Looking at some the event displays of these events, all of them seem to be cosmic events and so I decided for the runs including all five telescopes to select events recorded in four and five telescopes and fulfilling the respective nominal distance cut in all telescopes as UAV events.

### 4.6.2 Determination of the UAV position

The UAV was moving in the field of view during the runs due to drift in satellite navigation and atmospheric turbulence. This makes it necessary to have a precise tracking system for the UAV to get its position and so its distance to the different telescopes which is a crucial value for the inter-calibration to work as discussed in section 4.5. I performed this position determination with a simple triangulation using the images of the light source on the camera (the event displays): The centre of gravity corresponds to a direction (line of sight) in the field of view (with respect to the known pointing direction) of the considered telescope. This leads to a direction for the UAV for each telescope recording the event (situation illustrated in figure 4.10). If these directions were perfectly determined, there would be one intersection point at the position of the UAV combining the directions of all telescopes participating in the event. As they are not, among other due to statistical variations in the image, I used the analytically determined point corresponding to the minimum sum of squared distances to the lines of sight.

---

<sup>3</sup>As events recorded in four or five telescopes are also recorded in at least three HESS-I telescopes and so considered UAV events and events recorded in one or two telescopes could be

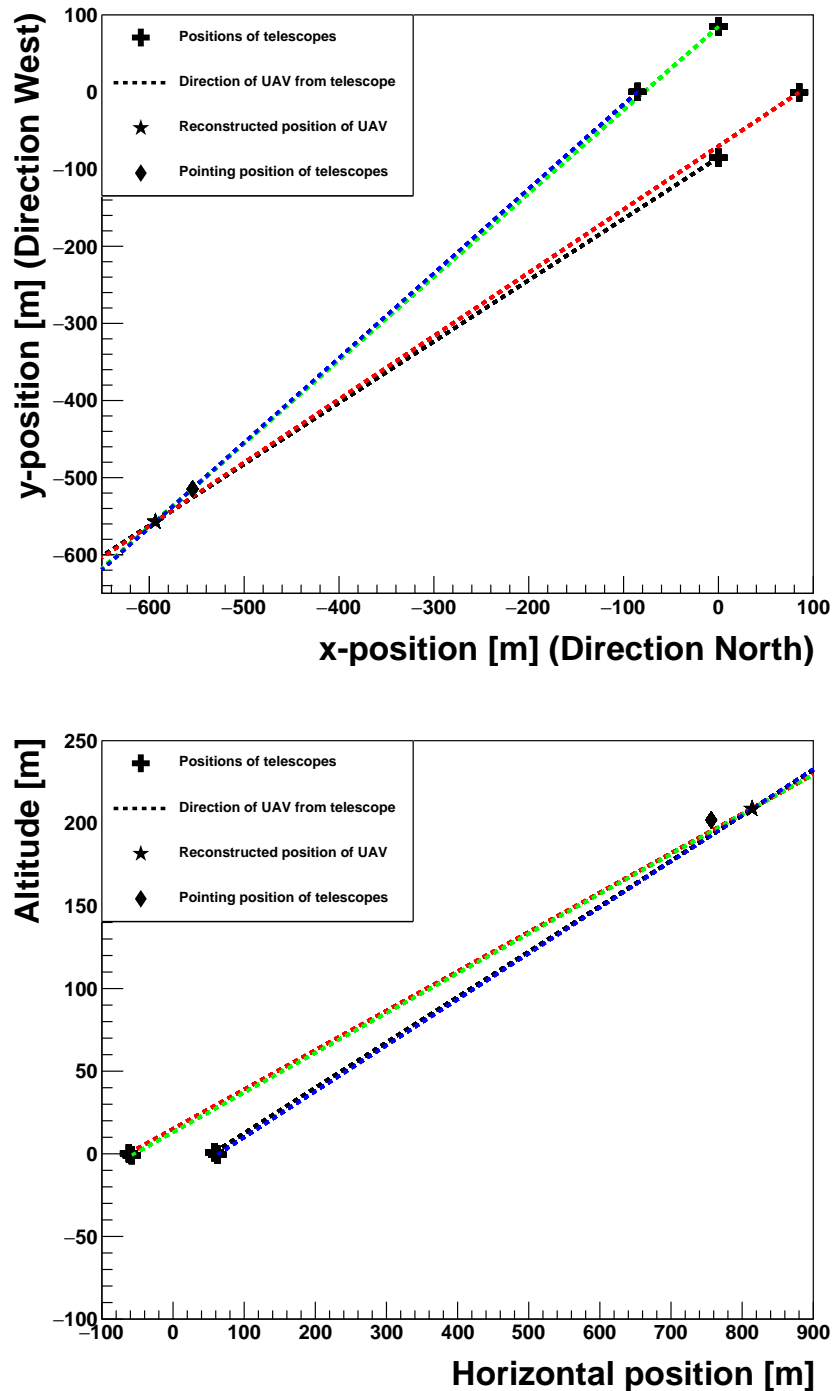


Figure 4.10: Projection on the ground plane (bird-eye perspective) (top) and the vertical plane defined by the UAV and the centre of the array (ground-observer perspective) (bottom) of the situation to illustrate the position determination of the UAV. The crosses indicate the position of the telescopes, the lines the direction in which the UAV has to be with respect to each telescope and the star the point closest to an intersection of the lines i.e., the reconstructed UAV position. The diamond indicates the pointing position of the telescopes.

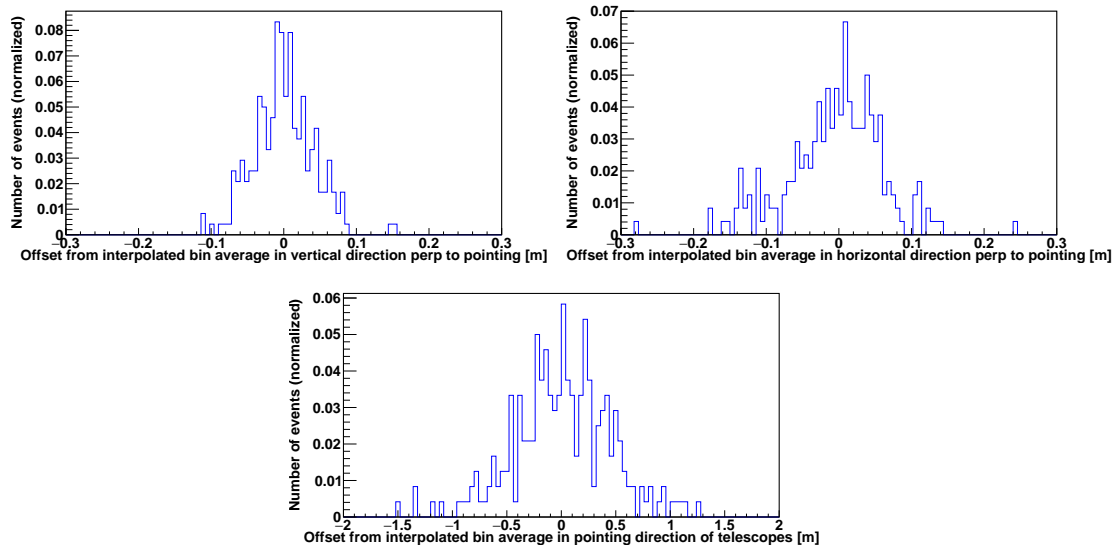


Figure 4.11: Distribution of offset in reconstructed UAV position from linearly interpolated 5-second bin average reconstructed position for one of the runs of the first campaign with a frequency of 1 Hz. As only bins with 5 UAV events and whose neighbouring bins have 5 UAV events were used, these distributions contain only 240 events of the about 400 UAV events recorded in at least three telescopes in this run. Top left: In vertical direction perpendicular to the pointing direction of the telescopes. Top right: In horizontal direction perpendicular to the pointing direction of the telescopes. Bottom: In pointing direction of telescopes. Note the different scale on the position axis for the bottom plot compared to the two top plots.

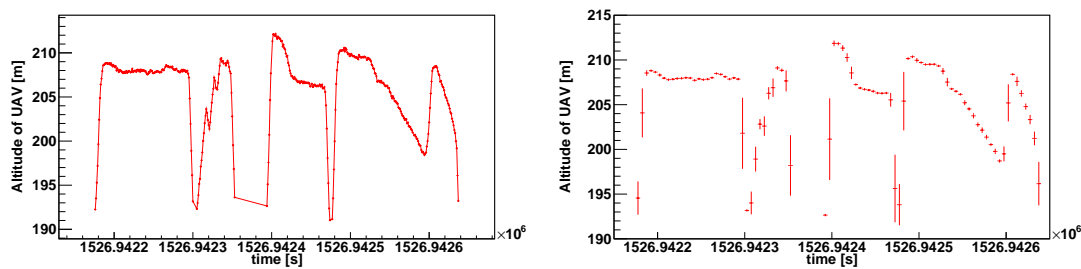


Figure 4.12: Movement in altitude of the UAV as determined with triangulation in the 1 Hz frequency run of the first campaign in which the UAV was moving a lot. One can see that the movement of the UAV, which was moving out of the field of view due to loss of altitude and moving in again three times, is tracked very well. The left plot shows the movement on an event-by-event basis whereas the right plot shows a binned version of this plot with hundred time-bins of 5 s. The uncertainty bars on this plot indicate the standard deviation of the altitude in each bin.

I determined the statistical uncertainty on these reconstructed positions by dividing the total duration during which the UAV was in the field of view (400 s to 500 s) in bins of 5 s. I then assumed that the position stayed relatively stable within these time bins and can be approximated by a linear movement. I computed the average of each position coordinate for each bin. I did this first for the two runs of the first campaign with a frequency of 1 Hz and I only considered the bins containing the expected five UAV events for its determination. I then linearly interpolated the position coordinates between the time bin centres to get an expected UAV position at each time (considering only the time bins which have two neighbours with five events). Afterwards, I computed the offset of the measured UAV position from the expected "5-second average" position and obtained a handle on the statistical position uncertainty. I assumed here that there is no significant acceleration during these 5 s, which is not completely true, and so the statistical uncertainties I derived here are rather to be viewed as upper limit on the statistical uncertainty. The distribution of the offset of the reconstructed position from the interpolated bin average reconstructed position is shown on an event-by-event basis in Figure 4.11 for one of the two runs. The distributions on this figure can be approximated with a Gaussian distribution, and the standard deviation of this Gaussian corresponds to the 1-sigma statistical uncertainty of the given position coordinate. This leads to a statistical uncertainty on the determined position in pointing direction of the telescopes of about 45 cm and in directions perpendicular to the pointing direction of about 5 cm (per axis) being equivalent to an angular uncertainty of  $12.3''$ . This angular uncertainty is similar in size to the spread in the residuals on the centre of gravity on the position determination which is discussed in detail in section 4.11. The much lower uncertainty perpendicular to pointing is expected as the telescopes are pointing almost in the same direction and so the lines of sight are nearly parallel along the pointing direction (see figure 4.10 for illustration). For the second run with a frequency of 1 Hz, the UAV left and re-entered the field of view three times during data taking (due to battery performance) leading to quick movements and accelerations, even on scales as small as 5 s. This is illustrated in figure 4.12, where the determined evolution of the altitude for this run is shown. On the left plot, one sees the unbinned representation, whereas on the right plot, the binned representation used to determine the statistical uncertainty of the method is displayed. As can be seen, a more or less stable UAV position was only reached before the first exit of the UAV out of the field of view. Repeating the same procedure as before on this small time interval, uncertainties of 5 cm and 40 cm respectively were found based on 35 events, and so with a much lower statistics than the previous 240 events. Given these lower statistics, this uncertainty is in good agreement with the previously found 5 cm and 45 cm. For the other runs,

---

recorded in HESS-I telescopes and so considered to be cosmic events.

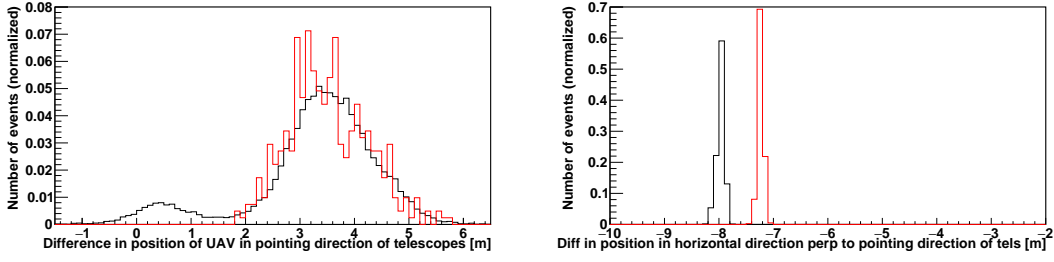


Figure 4.13: Distribution of the differences of the determined position coordinates with the field of view method and the GPS on an event-by-event basis for two runs of the first campaign (in black and red). Left: In average pointing direction of the telescopes (As the altitude of the H.E.S.S. telescope array is not known with precision, any possible offset of the altitude is not included in this plot. The altitude of the H.E.S.S. array was set such that it is consistent with the average altitude found with the FOV method.); Right: In direction perpendicular to average pointing direction in horizontal plane.

which turned out to be unusable anyway as shortly discussed in the introduction to this subsection, this procedure has not been carried out in such detail especially since an adaption of the time intervals and the number of events would have been necessary given that they have a much higher frequency. However, simply looking at the binned position evolution using again 5 s bins leads to standard deviations of the reconstructed position coordinates inside the bins which agree well with the previously quoted uncertainties (except for time intervals with strong movements).

I compared the results of this field of view method to a completely independent method, with no common systematic uncertainties. To do this, I compared the positions obtained with the field of view method to the ones obtained with the on-board GPS of the UAV, whose primary use was to allow the UAV to follow a predefined track. Figure 4.13 shows the difference between the positions obtained with the field of view method and the positions obtained with the GPS method on an event-by-event-basis for two runs of the first campaign. The maximum difference is 8 m or less in each coordinate. This difference is composed of a constant shift and a component varying with the reconstructed  $d$ . Perpendicular to pointing direction, the shift is 7 m to 8 m and the spread is very low (about 7 cm). In pointing direction, the mean is also shifted by about 3.5 m, but moreover the spread is now much higher reaching up to 1.1 m. This higher spread in pointing direction is due to systematics in the field of view method, because the pointing direction is not a preferred direction for the GPS. Concerning the absolute shift the picture is not so clear. It could come from systematics in the GPS method (which are expected to be up to 10 m), inaccurate knowledge of the position of the centre of the H.E.S.S. array or systematics in the field of view method. So, it is

not possible to constrain the systematic uncertainty of the field of view method below that of the GPS method in this comparison. Nevertheless, it shows that it is at maximum of the order of magnitude of 8 m, but could be as low as 1.1 m along the pointing direction and 5 cm perpendicular to pointing. These uncertainties (as well as the statistical ones) hold for this particular geometry (modulo the absence of any absolute altitude comparison) and might be different for other geometries, even though the used geometry has no particularity from which particular low or high uncertainties would be expected.

Including CT5 in the position determination, one needs to account for CT5 not being in convergent mode. Anyhow, convergent mode would lead to almost the same pointing direction as parallel mode because CT5 is at the centre of the array, and so the implementation of a convergent pointing mode for CT5 was not necessary. However, due to the height of the structure of CT5 convergent and parallel mode would lead to slightly different pointing directions and due to this, one needs to use the correct pointing directions of each telescope.

### 4.6.3 Inter-calibration of the telescopes

To inter-calibrate the telescopes, first I selected the events classified as UAV events in all telescopes, and for each event I computed  $I \times d^2 \times C$ , where  $C$  is a correction factor close to 1 accounting for atmospheric absorption and higher order geometric effects (whose numerical expression will be given in equation 4.2). As shown in section 4.5,  $I \times d^2$  is the same for all telescopes, modulo small percentage or lower level variations due to atmospheric absorption, point-to-point variations and higher order geometric effects for the relevant distance scales in this UAV calibration. I have incorporated the atmospheric absorption and the next order geometric effect accounting for UAV movements perpendicular to the mirror axis and the finite mirror size in the correction factor. This was not possible for point-to-point variations which occur on a much smaller scale below the precision of the position reconstruction. The correction factor  $C$  can be written as:

$$C = \frac{1}{1 - P} \times \frac{1}{1 + 2 \frac{d_{\perp}^2 + d_{\perp} \times r - 1/6 \times r^2}{d^2}}, \quad (4.2)$$

where the first factor is for the atmospheric absorption correction and the second factor the next order geometric correction. Here  $P$  indicates the average absorption probability of a photon in direction of the considered telescope, which was obtained from Monte-Carlo simulations as described in section 4.5,  $r$  the effective telescope radius and  $d_{\perp}$  the distance of the telescope mirror centre to the UAV in the direction perpendicular to  $d$  as illustrated on figure 4.14. As such, for each UAV-calibration event, the specific relative efficiencies  $\epsilon_i$  of the different telescopes

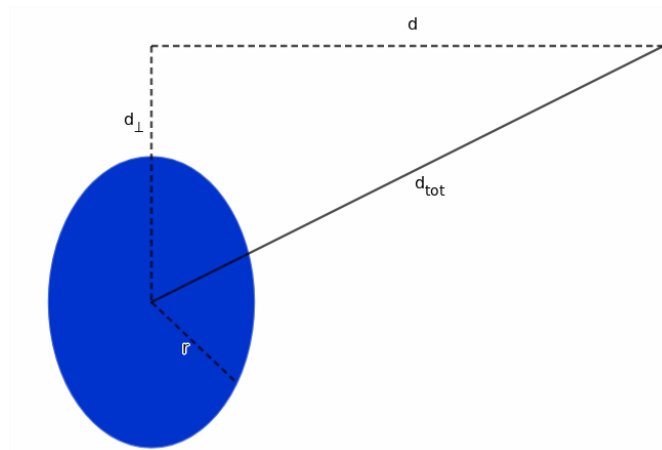


Figure 4.14: Neglecting atmospheric absorption, one can assume that a point light source creates a spherical wave which propagates isotropically in space with its intensity  $I \propto 1/d^2$ , where  $d$  is the distance to the source. When using a finite-size mirror to detect this wave, one needs to take into account that the distance from the light source depends on the position on the mirror. For the light source perfectly in focus, the distance to the light source increases with distance to the centre of the mirror. Otherwise, one needs in addition to take into account the perpendicular shift of the mirror compared to the light source. This figure illustrates the quantities involved in this correction. This leads to the intensity of the light hitting the mirror being of the form  $I \propto 1/d^2 + c(d, d_{\perp}, r)/d^4 + h.o.$ , with the quantities defined as in the text and *h.o.* indicating higher order terms. In the correction factor  $C$  terms up to order 4 were considered (i.e., up to  $1/d^4$ ) and the HESS-I mirrors were assumed to be circular. No higher order terms or more complex mirror shape were considered as the correction obtained with the order 4 term is already negligible compared to the point-to-point variations. The factor  $C$  contains in addition a correction for atmospheric absorption.

$i$  can be defined as:

$$\epsilon_i = \frac{(I \times d^2 \times C)_i}{\langle (I \times d^2 \times C)_j \rangle}, \quad (4.3)$$

with  $\langle (I \times d^2 \times C)_j \rangle$  the average of  $I \times d^2 \times C$  over all telescopes for the considered event. Then, I computed the run-wise relative efficiencies of each telescope by averaging over the events.

For the runs with CT5, I needed in addition to consider the difference in detector size of the different telescopes and the consecutive difference in solid angle covered and amount of reflected light. To do this, I divided  $I \times d^2$  by the total mirror area (i.e., the area covered by the individual mirror facets) of the considered telescope before putting it into the formula.

## 4.7 UAV data and pointing corrections

As described in section 2.3.6, the pointing of gamma-ray telescopes needs to be regularly determined as it evolves with time. This is usually done in regular pointing runs in which so-called pointing corrections to the nominal pointing are derived, leading to a pointing model which describes the pointing of the H.E.S.S. telescopes over a period of time.

However, information about deviations from the nominal pointing can also be gained from the UAV calibration data. Indeed, as discussed in section 4.6.2, I determine the most likely UAV position by a least square method from which residuals on the image centre of gravity can be derived. These residuals are, among other, due to deviations of the actual pointing from the pointing obtained from the used pointing model and therefore can be used to estimate these deviations and possibly improve the pointing corrections if the shift of the residuals due to mispointings can be disentangled from the shift due to other physical phenomena.

In the following study, I compare three different pointing models with the data taken in the first campaign: The so-called Null Model in which no pointing corrections are applied at all and two models obtained with the H.E.S.S. standard procedure to build pointing correction models, one constructed from data taken in November and December 2016 (the last one available at the moment of data taking) and one from data taken in May and June 2018, covering the period where the UAV runs were carried out, except for CT4 where no data from this period is available due to a hardware failure (therefore the last available pointing model from December 2017 and January 2018 was used for CT4). This last pointing model is the pointing model used throughout the rest of this study when not mentioned otherwise, as it is the pointing model fitting to the period of data taking.

To get an estimation for the order of magnitude of the shift of the residuals on the centre of gravity not due to mispointings and their variation between events, I

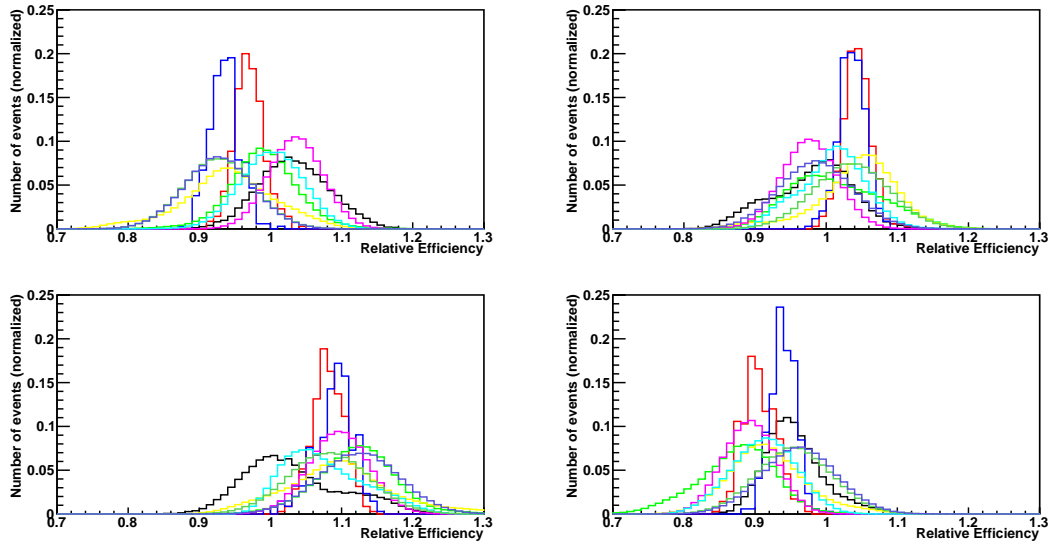


Figure 4.15: Normalized distribution of the relative efficiencies on an event-by-event basis for the different four-telescope runs and telescopes (without atmospheric absorption correction). The three runs of the first campaign are in black, blue and red respectively and the six four-telescope runs of the second campaign in the other colours. The distributions are normalized by the number of events due to the very different number of events in the different runs. Top left: CT1; Top right: CT2; Bottom left: CT3; Bottom right: CT4

use the simulation described in section 4.5, this time in the second mode in which actual runs are simulated. I run this simulation once with (using the actual broken pixels in the run on an event-by-event basis) and once without broken pixels, as broken pixels are expected to play a big role in shifting the centre of gravity too. This allows me to give an estimation of how much one could improve the pointing corrections by being better able to recover the intensities of the broken pixels. Large residuals in the data compared to Monte Carlo simulation is an indication of an imperfect pointing model. One improvement possibility consists in shifting the centre of gravity by its average offset and including this correction in the pointing model.

## 4.8 Pulse duration problem

As discussed in section 4.3 and summarized in table 4.1, three UAV runs with CT1-4 were taken in the first campaign and ten UAV runs in the second campaign, six with CT1-4 and four with CT1-5. The normalized distributions of the

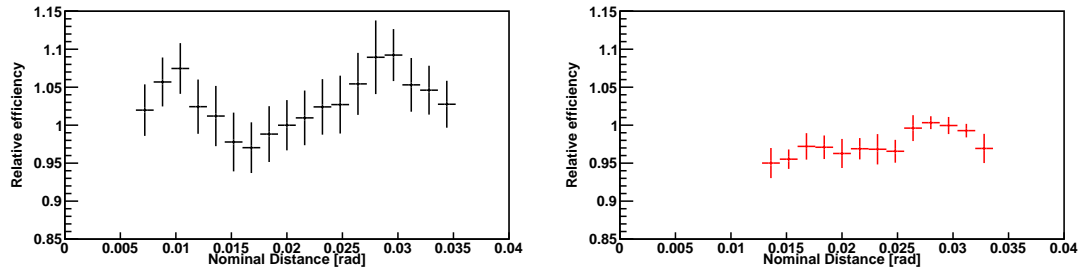


Figure 4.16: Evolution of the relative efficiency of one of the HESS-I telescopes as a function of the angular offset from the centre of the camera (nominal distance) in a binned representation with a bin width of 6.25 mrad. One of the runs with a broader normalized relative efficiency distribution is shown on the left (the one shown in black in figure 4.15) and one with a narrower distribution on the right (the one shown in red in figure 4.15). Uncertainty bars indicate the standard deviation of the efficiency in each off-axis bin.

relative efficiencies, as obtained with the UAV calibration method, on an event-by-event basis are shown in figure 4.15 for the four different telescopes and the nine runs including CT1-4 in both campaigns. These plots come from an early implementation of the inter-calibration method and do not include the atmospheric absorption correction. This however does not change anything in the problematic behaviour of some runs discussed next. As can immediately be seen in the plots, the red and blue distributions, which are both for runs taken in the first campaign, differ significantly from the other distributions. Indeed, the distributions of these two runs are much narrower. A closer look shows that the relative efficiency varies with the position of the images in the camera (as the UAV moves within the field of view) for the runs with a broader distribution of normalized relative efficiencies. This is illustrated on the left of figure 4.16 which shows the evolution of the relative efficiency with angular offset from the centre of the camera (nominal distance) for one of the runs having a broader distribution in one of the telescopes. The right plot of the same figure shows the same evolution for one of the runs with a narrower relative efficiency distribution, and the variation of relative efficiency with angular offset is much weaker in this case. These two plots showing the evolution of the relative efficiency with angular offset for one particular run and telescope in each category are representative for the behaviour in all the telescopes and all the runs of the same category. This seems to indicate that there are two different categories of runs whose relative efficiencies behave completely different.

I noticed this difference already after the first campaign, because one of the runs from the first campaign had a broader relative efficiency distribution than

the two others. The main differences between the two categories known at the time were, as indicated in table 4.1, that the run with broader distribution was taken with an 8 times higher image amplitude which was thought to be due to a higher intensity of the light source at that time and a pulsation frequency of the light source which was 60 Hz instead of 1 Hz as for the other two runs. As the frequency of the light source was still much lower than the rate with which cosmic events are recorded in usual observation runs at lower zenith angles (about 400 Hz at zenith considering runs without CT5 after the camera change in CT1-4) and the rate of produced photo-electrons by the light source in the different illuminated pixels (0.6 MHz) was much lower than the average rate of produced photo-electrons by night sky background (100 MHz [101]) and as no frequency dependence of the behaviour of H.E.S.S. can be seen in normal observation runs, it was concluded that the frequency difference is not the reason for the difference between the runs. The high image amplitudes, however, led to total intensities over all pixels in the camera which were much higher in UAV events than in usual cosmic events. This leads the recorded signal inside the pixels to be out of the design specifications of H.E.S.S. and in an untested regime, which means that it is not possible to predict how the camera system will react to the signal. There might be elements saturating, additional delay during triggering and recording the signal, instabilities due to accumulation of charge or other unspotted effects, which we thought after the first campaign to be the most likely reason for the dependence of the relative efficiencies on the position of the image in the camera.

For this reason, in the second campaign the runs were taken with different and lower light source intensities than in the first campaign to be able to quantify a potential intensity dependence in the obtained relative efficiency distributions. However, as can be seen in figure 4.15, all the runs of the second campaign behave as the high image amplitude run of the first campaign, meaning that the image amplitude was not the reason for the different behaviour of this run. A deeper investigation in the difference in behaviour led to the realization that the duration of the pulses emitted by the light source was about 4 ns for the runs with a narrower normalized relative efficiency distribution and about 64 ns for the other runs. Such a long pulse duration is a problem, since the digitization window of the HESS-I telescopes is only 16 ns [106] leading to a truncation of longer signals. The lost part of the signal cannot be recovered, as it depends on the exact trigger time which is subject to statistical variations (as the photon emission by the light source is a statistical effect and so the signal is slightly different between the different events) and potentially also to small systematic differences between the individual cameras. So, only recording part of the signal leads to this broader distribution due to higher statistical variations between the events and potentially to a systematic offset.

I checked that this longer pulse duration could indeed lead to such a broadening

	Run A		Run B		Muon (Observation period average)	
Telescope	Relative Efficiency	Statistical uncertainty	Relative Efficiency	Statistical uncertainty	Relative Efficiency	Statistical uncertainty
1	0.930	0.001	0.970	0.001	0.97	0.0002
2	1.044	0.001	1.054	0.001	0.99	0.0002
3	1.095	0.002	1.072	0.001	1.06	0.0002
4	0.931	0.001	0.903	0.001	0.99	0.0002

Table 4.3: Run-averaged relative efficiencies for each telescope in the two successful runs and their statistical uncertainties (standard uncertainty on the mean). The muon relative efficiency averaged over the observation period is given for comparison. In run A, 343 four-telescope UAV events were recorded and in run B 350.

of the relative efficiency distribution with the help of the Monte-Carlo simulation, by running it once with a pulse duration of 4 ns and once with a pulse duration of 64 ns with the same total integrated intensity. The simulation with 64 ns pulses led to relative efficiency distributions which were broader by a factor of 4, showing that too long pulse duration is the main reason for broader relative efficiency distribution.

This broader and potentially shifted relative efficiency distributions for the runs with 64 ns pulses would lead to higher statistical and systematic uncertainties as obtained from the 4 ns runs and for this reason their data was qualified as unusable for the remainder of this analysis. As one run of the first campaign and all the runs of the second campaign (the four-telescope as well as the five-telescope runs) were taken with pulse lengths of 64 ns, this only leaves us with two successful runs from the first campaign taken with CT1-4, which are called run A and run B from now on.

## 4.9 Results on remaining successful runs

The relative efficiencies obtained for each telescope in the two different remaining UAV calibration runs, considering only events which were UAV-like in all four telescopes and statistical uncertainties are shown in table 4.3 (here again with the correction for the atmospheric absorption). Additionally, the deviation between the relative efficiencies obtained from the two runs is shown in the table 4.4. I computed it by taking the sample standard deviation from 0 of the differences of the obtained relative efficiencies of the runs, with the sample standard deviation

	Run A	Run B	Muon
with respect to default calibration	8.3	7.8	4.0
with respect to run A	/	3.1	5.5
with respect to run B	3.1	/	6.3
with respect to Muon calibration	5.5	6.3	/

Table 4.4: Deviations between different relative calibrations in [%] obtained for the different runs, the default inter-calibration (i.e., no correction for different efficiencies of the telescopes at all) and the previously used (period-averaged) muon inter-calibration.

defined as:

$$s = \sqrt{\frac{1}{N-1} \sum_{i=1}^N (x_i - \bar{x})^2}. \quad (4.4)$$

Here,  $N$  is the number of used telescopes, i.e., 4,  $x_i$  is the difference between the relative efficiencies for telescope  $i$  and  $\bar{x}$  the mean of the  $x_i$ 's which is 0 by definition (as the relative efficiencies always sum up to 4).

Computing this, I find that the relative efficiencies for the two successful runs deviate by 3.1%. This shows that the UAV inter-calibration leads to very reproducible relative efficiencies for runs taken under the same observation conditions, even if taken in different nights, at least for these two runs.

I computed the expected statistical uncertainty on the relative efficiencies by dividing the standard deviation on the relative efficiency by the square root of the number of events minus 1. The obtained values are between 0.001 and 0.002 as can be seen in table 4.3. This means that the obtained efficiencies are not completely consistent between the two runs. This is illustrated again in figure 4.17 where the normalized distributions of the relative efficiencies on an event-by-event basis are shown for the different runs and telescopes.

Looking deeper into this, I found that the relative efficiency varies slightly with the position of the image of the UAV in the camera. This is illustrated in figure 4.18 which shows the evolution of the relative efficiencies of the four telescopes with nominal distance for run B (and so shows the right plot of figure 4.16). The plot shows a clear variation of the relative efficiencies with nominal distance above the statistical uncertainties, indicating a systematic dependence. Unfortunately, it is not possible to show the evolution of the relative efficiency with the nominal distance for run A as the position of the UAV was much more stable in this run and so the nominal distance was almost constant.

Nevertheless, there seems to be a small but clear dependence of efficiencies on the position of the image in the camera as can be seen in run B or by the difference between run A and B. There are many possible explanations for this:

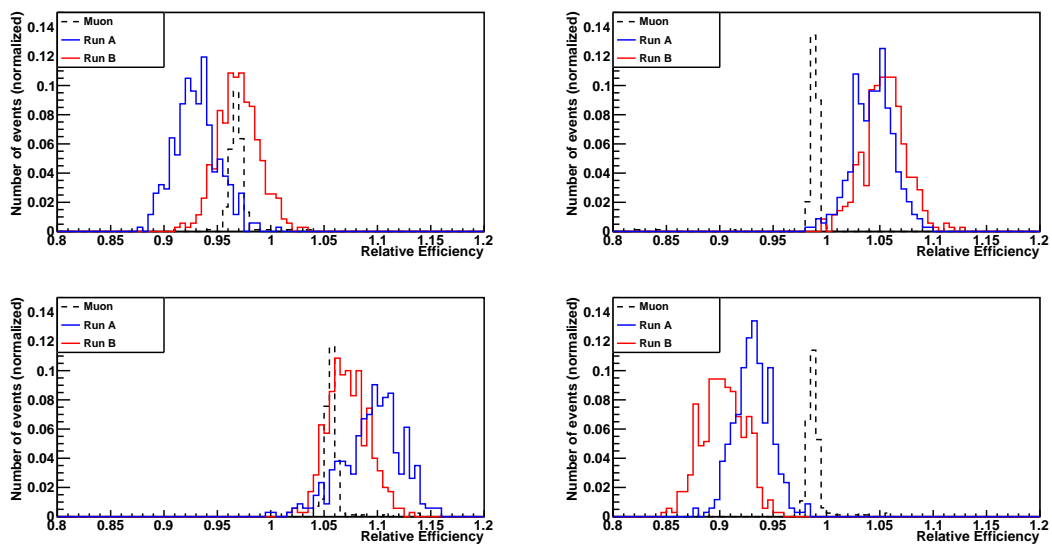


Figure 4.17: Normalized distribution of the relative efficiencies on an event-by-event basis as determined with the UAV for run A (blue) with 343 four-telescope UAV events and run B (red) with 350 four-telescope UAV events for the 4 telescopes. In addition, the distribution of the relative muon efficiencies over the whole observation period on a run-by-run basis is shown in dashed black. It has been rescaled to the height of the other distributions for easy comparison. Top left: CT1; Top right: CT2; Bottom left: CT3; Bottom right: CT4

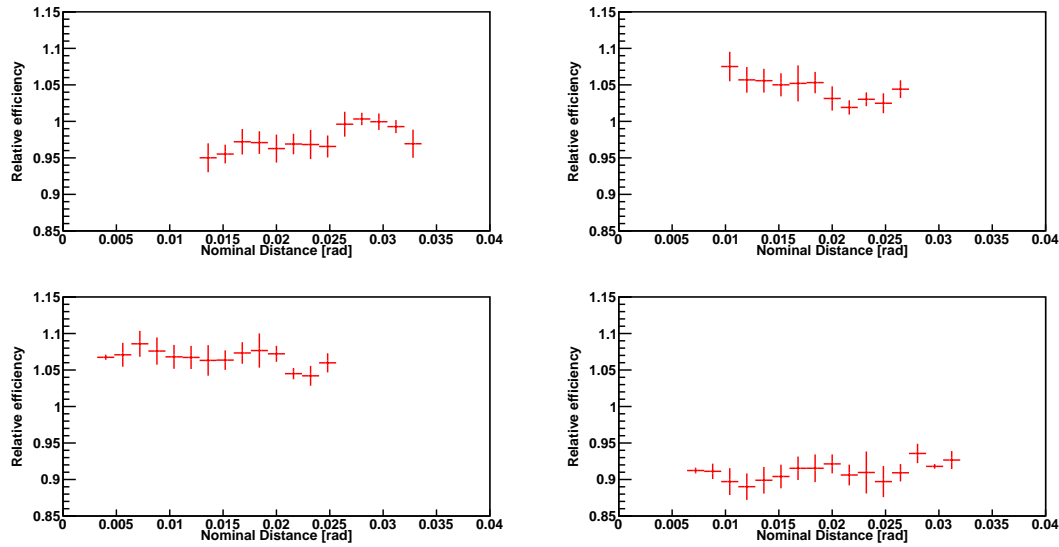


Figure 4.18: Evolution of the relative efficiency with the nominal distance for each telescope for run B with a bin width of 6.25 mrad. Uncertainty bars indicate the standard deviation of the relative efficiency in each bin. Top left: CT1; Top right: CT2; Bottom left: CT3; Bottom right: CT4

- First of all, there are the broken pixels which lead to missing intensity in the image. Even though they are interpolated, it is not possible to exactly recover the amount of light which hit them. This leads to a change of the total reconstructed intensity which is highly dependent on the exact position of the image in the camera.
- Second, systematic uncertainties in the position determination lead to systematic uncertainties on the distance  $d$  and so to an inaccurate correction of the expected intensity for the difference in distance of the UAV to the different telescopes. The effect of these systematic uncertainties could depend on the position of the UAV and so alter the computed relative efficiencies depending on the position of the UAV.
- Third, the point-to-point variations found in the simulation which have been neglected play a role at percent level.
- Fourth, the uncertainty in the atmospheric absorption model and possible differences in the atmospheric conditions between the two runs might play a role.
- And last but not least, the uncertainties in the flat-fielding, the difference

between the wavelengths of the flat fielding LEDs (370 nm) and of the UAV-mounted light source (400 nm) and a possibly inhomogeneous mirror response would also introduce a dependence on the camera position of the image on the found relative efficiencies.

So, there are many potential reasons which could explain or contribute to this small change of the computed relative efficiencies with the position of the image of the UAV in the camera, and other small effects not considered here could contribute too. To disentangle the contribution of each of these phenomena a more systematic study in a future UAV campaign will be necessary. Such a campaign is under preparation, as is discussed in section 4.13.

## 4.10 Comparison with muon optical efficiency calibration

The first UAV calibration campaign led to very reproducible results in the two runs taken successfully, however to exclude any potential hidden systematic uncertainties a comparison with an independent, reliable method would be helpful. The method of choice here is the muon optical efficiency calibration described in 2.3.5 as it is the standard method used for optical efficiency calibration by all three major Imaging Atmospheric Cherenkov Telescopes currently in operation and has been extensively studied.

However, as discussed in section 3.4, it turned out that the muon optical efficiencies computed from UAV calibration runs are too low compared to that from other runs. As the efficiency which has proven its reliability within H.E.S.S. is the observation period averaged muon efficiency and not the one from individual UAV calibration runs, it is this one which is used for this comparison. The averaging also allows to remove the run-by-run variation of the muon optical efficiency.

This calibration method based on atmospheric muons relies on completely different processes than the UAV calibration method, and is therefore not expected to have any common systematic uncertainties, beside atmospheric absorption and the uncertainties intrinsic to any calibration procedure using a light source outside of the telescopes. The main common uncertainties are the telescope operational uncertainties present in all telescope observations, namely mostly the uncertainties on pedestal and flat fielding. One could expect an additional uncertainty from the gains. However, any such uncertainty should lead to an over- or underestimation of the signal in this pixel and so taken into account by the flat-fielding and hidden in its uncertainty. The cleaning could in principle also introduce an uncertainty, however as discussed in the simulation section, removing the cleaning leads to an increase in the statistical uncertainties while only marginally changing the inter-

calibration results. Beside that, the broken pixels which are interpolated might introduce an uncertainty for the UAV calibration. However, the muon calibration is based on the comparison of a recorded muon ring with a modeled muon ring on operational pixels as described in section 2.3.5, and is not impacted by this uncertainty. This leaves us with the atmospheric absorption, the pedestals and the flat fielding as common uncertainties. As discussed in the simulation section, the change due to atmospheric absorption assuming average atmospheric conditions in the relative efficiencies was about 0.5%. It is difficult to qualify the uncertainty of this value, given the limited number of measurements available under Namibian atmospheric conditions and this so needs further investigations during which the UAV is moved to different positions. However, as the muon optical efficiency calibration is based on data from multiple very different pointings (216 runs over 25 nights), the effect of the atmospheric absorption on the computed average relative efficiencies is expected to average out over these different pointings and so this is not a common uncertainty for the relative efficiencies. The uncertainty on the pedestals is mostly qualified by the pedestal width compared to which potential systematic offsets are completely negligible. The average high gain and low gain pedestal widths converted from ADC counts to intensities were between 0.87 and 1.09 photo-electrons and between 0.76 and 0.98 photo-electrons respectively. As the pedestal widths of the individual pixels are independent, this number can be multiplied by the square-root of the average number of illuminated pixels, between 33 and 47, to get the overall uncertainty due to pedestals in an event. This value was between 4.6 and 6.8 photo-electrons for the different telescopes and gain channels. These values need to be compared to the standard deviation of the recorded intensity in the UAV events which was between 83 and 176 photo-electrons and so more than an order of magnitude larger than the uncertainty due to pedestals. This shows that the statistical uncertainty in the recorded UAV light between the events is much larger than the statistical uncertainty due to pedestal width. A similar comparison can be done for the flat fielding uncertainty. The average flat fielding uncertainty in each pixel is between 0.4% and 0.5% of the recorded intensity. Using that these relative uncertainties are statistically independent, this leads to an uncertainty between 0.06% to 0.08% over all the illuminated pixels. The relative uncertainty of the intensity of a single UAV event is between 2% and 4%. However, the effect of this uncertainty is statistically independent for all the UAV events whereas the effect of the uncertainty on the flat-fielding is the same for all the events as the flat-fielding is determined once for the whole observation period. For this reason, the relative uncertainty on the UAV intensity needs to be normalized to the number of events which leads to values between 0.14% and 0.22%. So also here the uncertainties due to the statistical variations in the intensity are higher, even though the difference between both uncertainties is not as

Run identification	A		B	
Pointing Model	Quad mean Residual	Quad mean Spread	Quad mean Residual	Quad mean Spread
Null Model	61.38	16.25	62.14	20.60
11-12/2016	37.26	15.52	25.87	16.68
05-06/2018	11.21	14.00	9.24	16.16
Simulation	7.01	12.23	11.38	13.71
Sim wo Broken Pix	4.11	12.00	5.23	11.35

Table 4.5: Quadratic mean (over telescopes and position coordinates) of the average residuals and of the spread of the residuals (in arc seconds) for the two runs and the different pointing models. Null Model: Model without any pointing corrections; 11-12/2016: H.E.S.S. standard pointing model based on data from November and December 2016; 05-06/2018: H.E.S.S. standard pointing model based on data from May and June 2018 (i.e., taken around the measurement period), except for CT4 where data from December 2017 and January 2018 was used; Simulation: Residuals obtained from simulation using broken pixels detected in data of runs and perfect pointing; Sim wo Broken Pix: Residuals obtained from simulation without broken pixels and perfect pointing

large.

As there are no other common uncertainties, the muon calibration method is well suited for a cross-check of the UAV inter-calibration method. For this reason, table 4.3 also shows the relative efficiencies obtained with the standard muon calibration method averaged over the whole observation period of 25 nights and figure 4.17 the distribution of the muon relative efficiencies over the whole observation period on a run-by-run basis (only considering normal observation runs). The relative efficiencies obtained from the UAV calibration deviate by within 5.5% and 6.3% from the relative efficiencies obtained from the muon calibration for run A and B respectively. As both methods are not expected to have any common systematic uncertainty beside telescope operational uncertainties, this deviation by about 6% for the two different runs, is a strong indication that the uncertainties of both methods are of the same order of magnitude or even less.

## 4.11 Pointing Correction

As discussed in section 4.7, I compared the residuals on the centre of gravity from the position derived from three pointing models and two simulation variants (with and without broken pixels). Examples of the obtained distribution for these

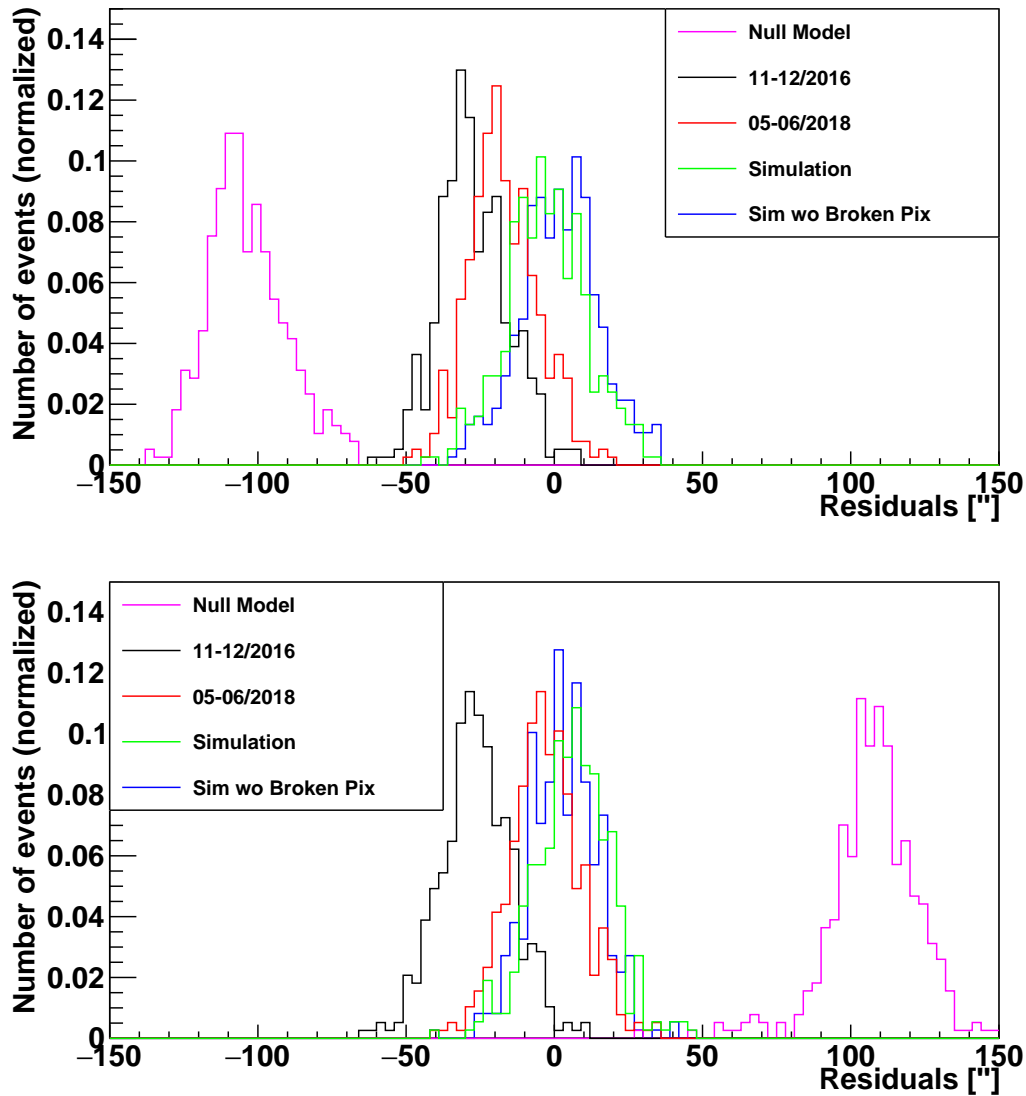


Figure 4.19: Distribution of residuals on centre of gravity for different pointing models described in section 4.7 for one telescope and one of the two camera coordinates per run. The shown telescope and camera coordinate were chosen in a way that the residual distribution corresponds the most to the average distribution for the model and run (as they were looking quite differently for the different telescopes and runs). Top: Residuals on x-coordinate of centre of gravity in CT2 for run A. Bottom: Residuals on x-coordinate of centre of gravity in CT3 for run B.

residuals for the five cases are shown in figure 4.19 for one telescope and coordinate per run. Additionally, the quadratic means (i.e., the root mean square RMS) over the four telescopes and two camera coordinates of the residuals and the spread of the residuals is tabulated in table 4.5 for each case and run. Comparing only the three pointing models used on the taken data to start, the residuals from the Null Model (i.e., the model which does not use any pointing corrections at all) are much higher than the residuals using pointing corrections (factor 5 to 7 using the most recent pointing model). This shows that the pointing corrections work as expected and need to be used to properly measure the UAV position.

Comparing the initially available pointing models (at data taking) from 2016 to the ones covering the actual period of data taking 18 months later, there also is an improvement of a factor 3 in the quadratic means (which could even slightly increase if an up-to-date pointing model for CT4 would be available). This shows again the importance of using up-to-date pointing models as the pointing of the telescopes evolves with time (among other due to the very slow sinking of the foundation of the telescopes into the ground). Using out-dated pointing models leads to a much less precise pointing direction of the telescopes rendering the pointing corrections partially ineffective on comparatively small time-scales of 18 months as the multiplicative factor is higher between the recent and the outdated pointing models than between the Null Model and the outdated pointing model.

I thus showed that it is possible to compare different pointing models with the UAV data and classify them, but have not discussed yet whether it is possible to compare the models to what is achievable with pointing corrections and whether it is possible to improve the pointing corrections with the UAV. For this reason, I performed simulations to disentangle the part of the residuals due to mispointings from the part due to other phenomena. These simulations were run using the simulation code described in section 4.5 which should encompass all the physical phenomena as much as possible assuming however perfect pointing. I executed them once with and once without broken pixels. For the simulation with broken pixels, I used the same broken pixels as in real data.

Figure 4.19 and table 4.5 show that the squared means of the residuals are about 2 times higher in the simulation with broken pixels (which have been interpolated during the data analysis as described in section 4.4) than in the one without broken pixels. The interpolated broken pixels thus also lead to a shift of the centre of gravity of the image even though the shift due to mispointings is much larger (as can be seen by comparing the Null Model to data driven models). This means however that it is not possible to get rid of the residuals by just correcting the mispointings as they are also due to broken pixels and further phenomena (as the residuals are also non-zero in the simulation without broken pixels).

Comparing now the residuals obtained from the simulation with broken pixels

to the residuals on the data obtained using the H.E.S.S. standard pointing corrections, there is no big difference for the two runs: The residuals from the simulation are a bit smaller for run A whereas they are a bit larger for run B. This similar size of the residuals shows that there is no room for improvement left as the most recent pointing correction model already achieves the same residual size as expected without mispointings.

Due to this, I tested a possible method for improving the residuals using the pointing model from 2016. It consists in shifting the coordinates of the centre of gravity in each telescope by their determined average offset. I obtained a quadratic mean of the residuals of  $1.32''$ . Applying the method iteratively, I achieved even lower residuals ( $0.04''$  for 3 iterations for example). This shows that shifting the coordinates of the centre of gravity by their average offset is a very efficient method to lower the residuals. They are, however, now lower than in the simulation (in which perfect pointing was assumed) which means that there is an “over-correction”. The shifting of the centre of gravity lowers the residuals no matter where they come from. The shift does not only account for mispointings, but also for broken pixels and other effects which are not necessarily consistent over runs. However, if they are not consistent over runs a correction during calibration runs makes no sense.

One would have to disentangle the shift in residuals due to mispointings and to other effects. This could partially be done by increasing the number of configurations in which UAV calibration data is taken (different positions of the UAV and pointing positions of the telescopes, trying to illuminate the telescopes regularly over the whole field of view) which would allow to eliminate or average out effects due to the position of the image of the UAV in the camera such as illuminating always the same broken pixels. Additionally, one could go further in trying to recover the light in broken pixels: Instead of interpolating taking the average of the six neighbouring pixels, one could recover its intensity for example by fitting a model image to the recorded data, obtained either from simulation or by averaging over recorded data. Last but not least, it might be possible to get the size of the shift from simulation and so not to take into account the part of the shift present in the simulation too for the correction even though this would require a very precise and accurate description of all the involved physical phenomena.

The spread of the residuals is the highest for the Null Model, lower for the outdated pointing model and the lowest for the pointing model covering the period of data taking. This is most likely due to telescope mispointings leading to an offset of the determined position of the UAV from the real position resulting in a shift in the residuals depending on UAV position which manifests itself by an increased spread. The spread in the simulation is lower due to not simulating mispointings and pointing variations and we have again that smaller residuals lead to smaller spread of residuals.

The uncertainty of source position determination with H.E.S.S. due to systematic pointing uncertainties was found to be between  $10''$  and  $20''$  per axis [126] leading to a pointing uncertainty of  $20''$  to  $40''$  per axis and per telescope, assuming the mispointings of the four telescopes to be independent. Part of this uncertainty comes from a hysteresis effect, meaning that the bending of the masts depends on deformations undergone at earlier position. This cannot be corrected for by a static pointing model, but could in principle be corrected on a run-by-run basis by looking at stars with known position passing through the field of view of H.E.S.S. This allowed me to further confirm the order of magnitude of these uncertainties as the found difference between the measured positions and the known positions of stars for the different runs is following a Gaussian distribution with a standard deviation between  $15''$  and  $20''$  (per axis) depending on the exact configuration. The residuals obtained with the most recent pointing model have similar size (table 4.5) showing that the amplitude of the mispointings obtained with the UAV data is consistent with the amplitude of the mispointings obtained with other methods and that the UAV already now achieves similar accuracy without elaborated method of recovering broken pixels. The variation of the pointing of the H.E.S.S. telescopes within runs is less precisely known, however one gets values of less than  $10''$  using the positions of stars which is substantially less than the values found with the most recent pointing models. This might be due to statistical variations in the distribution of the photons in the UAV images increasing the statistical uncertainty of the reconstructed position with the UAV. The consistency of the obtained position offsets could be assessed in a more precise way by directly comparing the residuals from the UAV position determination with the offset in the star pointing, however, there were too few stars visible in the two UAV runs to make this possible. This might be considered in the next campaign.

## 4.12 Timing

As discussed in section 4.3, the UAV was set up in such a way that it was emitting light pulses at regularly spaced time intervals. The frequency of these pulses was 1 Hz for the two successful runs of the first campaign, 60 Hz for the non-successful run of the first campaign and 1000 Hz for the runs of the second campaign. The regularity of these pulses makes it possible to do timing studies with the UAV data and verify the accuracy of the H.E.S.S. timing and the correct attribution of the time stamps to the individual events. As the precision of the recorded event central trigger time stamps in the UAV campaign was 100 ns, it is not necessary to take into account the difference in the propagation time of the photons from the UAV to the telescope array as the movement of the UAV between events was substantially less than 30 m.

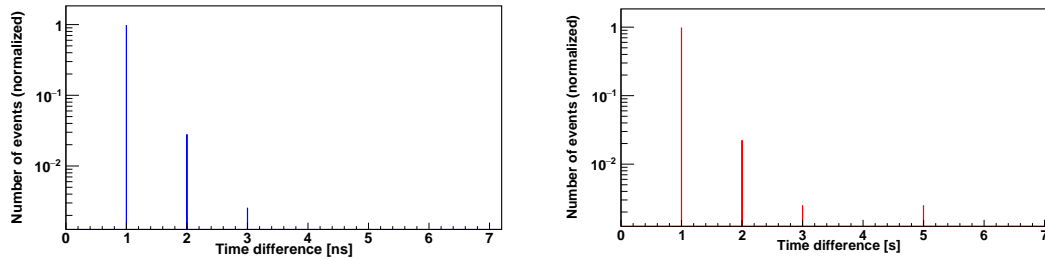


Figure 4.20: Normalized distribution of the time difference of two consecutive UAV events. Left: Run A. Right: Run B. In these two runs the UAV pulses were produced with a frequency of 1 Hz and the time differences between events are multiple of this period.

The distribution of the time difference (as indicated by the event time stamps attributed by the central trigger of H.E.S.S.) between two consecutive events in run A and run B is shown in figure 4.20. As expected by the LED pulse frequency of 1 Hz of these two runs, by far most of the consecutive events have a time difference of 1 s (note the logarithmic scale of the plot). However, some of them have a time difference of 2, 3 or even 5 s for one of the events. This higher time difference for some of the events is due to some of the LED pulses not being recorded as UAV events. Indeed for run B, some of the events were not recorded or not completely included in some telescopes and not selected as UAV event due to the movement of the UAV (and it moving in and out of the field of view). However, most of the "missing" events are due to two or more telescopes not recording the event due to dead time. Indeed, when one of the telescopes triggers on an event, this event needs some time to be processed leading to the unavailability of the given telescope to record further events until the end of the processing of this event. This time during which the telescope is unavailable is called dead time and the typical dead times of the different cameras are discussed in section 2.1. The dead time in run A and B was mostly due to cosmic events, as they were much more numerous than the UAV events. The number of "missing" events while the UAV was in the field of view of all telescopes agrees well with the expected dead time of the H.E.S.S. telescope system or part of it. As an example, for run A the UAV was inside the field of view of the four telescopes for 407 s and the expected four telescope live fraction (i.e., the fraction of time during which none of the four telescopes was affected by dead time) was 85.86 % which agrees well with 343 UAV events being recorded in all four telescopes.

That all the consecutive events have a time difference which is an entire multiple of the LED period constitutes again a verification of how well the event selection works and that there are no cosmic events accepted in these two UAV calibration runs. Indeed, cosmic events do not hit the telescope synchronous with UAV events

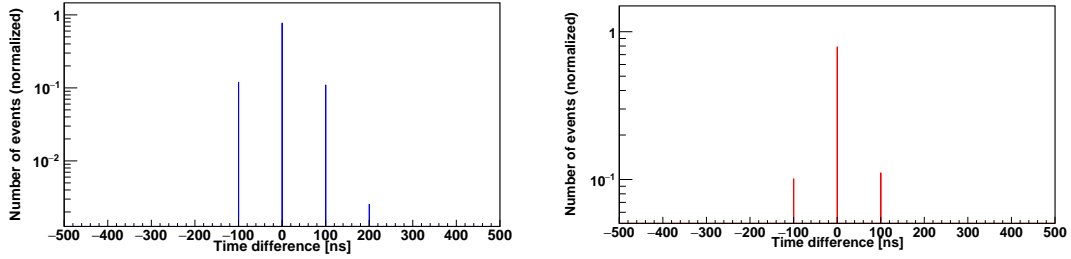


Figure 4.21: Zoom in on the individual bins of figure 4.20: Normalized distribution of the deviation from a one second multiple of the time difference in nanoseconds between two consecutive events. Left: Run A. Right: Run B.

and so if any cosmic event would be accepted one should see an entry at a non-integer value in the distribution. Additionally, it also verifies that the LEDs emit pulses in very regular time intervals with the expected frequency and that the H.E.S.S. telescopes are able to record these times with a very high precision and attribute them correctly to the events.

To determine the precision of these time stamps, a zoom-in in the individual bins of the distribution in figure 4.20 can be done. This is shown in figure 4.21, where the distribution of the time difference is shown on a nanosecond scale for the two successful runs of the first campaign. The same is shown in figure 4.22 for the third run of the first campaign, one of the four-telescope runs of the second campaign and one of the five-telescope runs of the second campaign. As mentioned before the time stamps attributed to the events by H.E.S.S. only has a precision of 100 ns which is why the distributions shown on these figures are discrete with a difference between individual entries of 100 ns. The unsuccessful runs with a too long pulse duration can be used in this timing study since the problem of the too long pulse duration is that the event is not completely recorded, however the trigger still occurs at the beginning of an event and so the triggering time is independent from this too long pulse duration.

The histograms of the time differences between two consecutive events shown here on a logarithmic scale are all very peaked around the central value which always corresponds to the expected time difference obtained from the frequency, except for the run with a pulse frequency of 60 Hz as there the peak is distributed over the two 100 ns bins the closest to the value corresponding to its period, which is not an entire multiple of 100 ns. All the other values are at most 200 ns away from the central bin. However, these bins contain much less events. This shows that the recorded time difference between individual events deviates at most by 200 ns from the expected one. In addition, the distributions are all very symmetric, which shows that there is no clock drift between the UAV and the H.E.S.S. array up to the level of hundreds of nanoseconds over the timescale of the whole duration

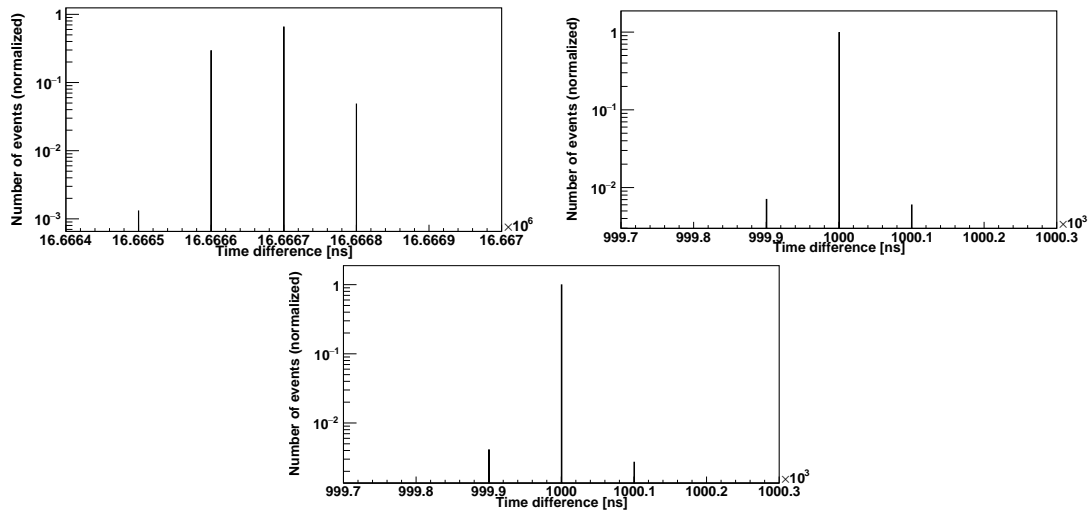


Figure 4.22: Normalized distribution of time difference in nanoseconds between two consecutive events. Top left: Unsuccessful run of first campaign. Top right: One of the four-telescope runs of the second campaign. Bottom: One of the five-telescope runs of the second campaign.

of the observation of the UAV.

Overall, the relative UAV timing and the relative H.E.S.S. array timing agree within hundred nanoseconds both on small scales as well as on larger scales up to 10 min. This indicates that the UAV also allows to verify the timing of a Cherenkov telescope array. There are some small differences of about 200 ns which are very close to the precision with which the time stamps have been read out. They could be related to this limited readout precision, but also to the precision with which the LEDs mounted on the UAV is pulsed which has not been characterized so precisely.

Increasing the precision with which a timing comparison between the UAV and a telescope array is done to verify and characterize the timing of the telescope array is not a difficult task. First of all, one would have to characterize the timing of the LEDs mounted on the UAV better and potentially optimize it. This would even allow an absolute timing calibration of the array by attributing time stamps to the pulses emitted by the LEDs. To avoid mixing the events between the UAV and the array, one could even imagine using a recognizable timing pattern on the UAV by changing the time difference between consecutive events according to a pattern. Second, at some point one would also have to include the travel time of the light between the UAV and the telescopes, which is slightly different for the different telescopes. This could be done by using the position reconstructed with the field of view method, would however come at the cost of also being impacted by

its uncertainties reducing the maximum achievable precision, without optimising this method, to few nanoseconds. Knowing the emission time of the light and the time the light has been recorded by the individual telescopes on the other hand, could allow to improve the position reconstruction, especially along the pointing direction. This would however require a precision of the time stamps at picosecond level.

### 4.13 Conclusions

In this part of my thesis, I have presented the results of the first ever inter-calibration of a Cherenkov telescope array with a UAV-based light source which also constitutes the first inter-calibration of a Cherenkov telescope array with a single light source. This inter-calibration was performed with a first-generation prototype constituted of a custom-tailored 400 nm LED-based light source mounted on a multi-rotor UAV. This UAV was positioned inside the field of view of the four HESS-I telescopes (for the first successful campaign) and illuminated all of them with its pulsed light sources, leading to the calibration pulses being recorded. The telescopes were then inter-calibrated based on the total amount of light each of them recorded. The obtained inter-calibration deviated by 5.5 % and 6.3 % respectively with the muon calibration for the two successful runs. As both of these inter-calibration methods are based on very different physical processes, they are not expected to have any common systematic uncertainties, beside those intrinsic to all calibration methods based on a light source at a distance of hundreds of meters from the telescopes. As they are on a smaller scale as discussed previously, this is an indication for both methods having uncertainties of this order of magnitude or less. This means that UAVs are well suited to inter-calibrate Imaging Atmospheric Cherenkov Telescope arrays and that inter-calibrations with a single light source on an event-by-event basis would indeed be possible.

This novel inter-calibration technique already delivers results with uncertainties at few percentage level at its first attempt with a non-optimized first-generation UAV prototype. This uncertainty will be improved first of all through a better understanding of the systematic uncertainties by including more physical phenomena in their determination and by comparing the results of this UAV-based inter-calibration to further independent methods beyond the standard muon-based optical efficiency calibration method, such as the air shower optical efficiency calibration method [127]. Then, it will also be reduced through further iterations of the UAV prototype with a custom-tailored UAV platform, improvements to the calibration platform and a better integration of the calibration payload to the flight platform [123].

Beyond inter-calibration, I have also shown that it is possible to verify the

pointing corrections of the H.E.S.S. telescopes using the observed UAV data by comparing the effect that different telescope pointing models have on this data, and this without taking any additional data. This constitutes an additional method to verify that the pointing corrections of H.E.S.S. improve the direction reconstruction of incident Cherenkov photons with respect to using no pointing corrections at all and that it is crucial to use a recent pointing model, taking into account a change of the pointing of the telescopes with time (among other due to the sinking of the foundation of the telescopes into the ground) leading to outdated pointing corrections which become ineffective. For a final implementation, this would of course have to be done with the UAV at numerous different positions to verify a complete pointing model and not only verify it locally in one given configuration as has been done so far.

In addition, I showed that the UAV data allows to easily verify the time stamping of the H.E.S.S. array system to at least the level of 100 ns, by looking at the time distribution of events. This illustrates that the UAV is well suited for some trouble shooting tasks, as it is able to procure a well-known and modifiable external signal to all the telescopes of the H.E.S.S. array simultaneously.

Beyond inter-calibrating the relative optical efficiencies of Imaging Atmospheric Cherenkov Telescope arrays and confirming their pointing accuracy, the UAV could also be used in other calibration tasks. Among other, using the UAV-based inter-calibration method, it is, unlike with the muon calibration method, easily possible to perform a multiwavelength calibration: one can just switch the used light source to one with a different wavelength (after assuring of course that it still fulfils the requirements for the inter-calibration). So, one can monitor wavelength dependent effects such as wavelength dependent degradation of the telescopes' optical system and the wavelength dependency of the quantum efficiency of the photo multiplier tubes. A further possible calibration task for a UAV could be to monitor the transparency of the lowest layer of the atmosphere, either by mounting meteorological instruments on the UAV (as proposed in [123]) or by trying to infer the atmospheric absorption from the amount of light recorded in the different telescopes.

So, future planned campaigns cannot only ameliorate the systematic uncertainties in the inter-calibration and potentially go beyond verification for the pointing corrections, but also will allow us to quantify the potential of a UAV system for these calibration requirements. These future campaigns will build on the success of the first campaign and the lessons learnt from the second campaign, in which we managed to include CT5 in the data taking procedure and so record the calibration flashes by different telescope types, increase the altitude and so reduce the zenith angle of the UAV and keeping it at a stable position at this altitude for more than 5 minutes and to increase the UAV frequency by a factor of 1000, and so even

though no usable data resulted from it, we managed to test many improvements in the data taking.

## Chapter 5

# Introduction to interstellar diffuse emission and a novel detection method

Beside the emission from the individual sources, which have been described in detail in section 1.4, one also expects interstellar diffuse emission at GeV and TeV energies. This interstellar diffuse emission is a very extended emission produced by the interaction of cosmic rays with the interstellar medium, magnetic fields or radiation fields. Interstellar diffuse emission has been detected in many energy bands. At gamma-ray energies, interstellar diffuse emission from the Milky Way, which is mostly due to hadronic cosmic rays interacting with the interstellar medium, is even the dominant signal above 100 MeV for the Fermi gamma-ray satellite [129].

Even though ground-based gamma-ray telescopes only operate at slightly higher energies than *Fermi*-LAT, it is much more challenging for them to observe interstellar diffuse emission due to their comparatively small field of view. Indeed, it is smaller than the extension of most regions from which interstellar diffuse emission is expected. This leads among other to the impossibility to use any background subtraction method based on the definition of a control region without signal inside the field of view (as described in section 2.5.1) and makes the development of new analysis techniques mandatory. Nevertheless, in 2014 H.E.S.S. could put a lower limit on a signal from interstellar diffuse emission and unresolved sources along the Galactic Plane [130]. To do this, it used a control region for background subtraction inside the field of view defined iteratively excluding regions passing a given significance threshold and everything between a galactic latitude of  $-1.2^\circ$  and  $1.2^\circ$ . This choice of the latitude range was a compromise between having a large exclusion region and having enough events for a proper background subtraction using a control region within the fields of view of the individual runs. However, this means that the control region is potentially polluted by large scale

diffuse emission (which is why H.E.S.S. could only obtain a lower limit with this method).

In this chapter, I start by discussing interstellar diffuse emission and its origin in more detail, before coming to the Large Magellanic Cloud (LMC) and its interstellar diffuse emission, which has been the main object of this work. Then, I discuss in more detail why the standard analysis methods described in section 2.5 cannot be used for detecting and properly characterizing interstellar diffuse emission and introduce the novel analysis method developed by a small group of people within the H.E.S.S. collaboration to analyse extended emission based on a run-by-run simulation of the taken data.

## 5.1 Interstellar diffuse emission

So far, I mostly considered the emission processes of gamma rays and cosmic rays and then their interaction in the atmosphere and human-built detectors. In this section, I will now discuss how these particles propagate from the source to Earth. Even though photons travel straight and can be attributed to the sources where they were produced, the space through which high energy particles propagate after source emission is not at all empty, especially inside galaxies. Indeed, there is gas, radiation and magnetic fields in the interstellar space which photons and charged particles can interact with [129]. These interactions can lead to the production of diffuse gamma-ray emission which is not associated to individual sources and mostly extended.

The first ingredient necessary to the production of gamma-ray interstellar diffuse emission is a source which injects cosmic rays into the interstellar space. One of the principal sources of these galactic cosmic rays is believed to be supernova remnants [129]. Interstellar diffuse emission can be either produced from injected hadrons or electrons and so one distinguishes a hadronic and leptonic component. The second ingredient is a component with which these cosmic rays interact to produce diffuse emission.

Through their propagation, hadronic cosmic rays mostly interact with interstellar gas [131]. The collision of these hadrons (mostly protons) with the matter produces pions as described in section 1.3.5. The neutral pions decay mostly into pairs of gamma rays which constitute the recorded diffuse emission. Due to the relatively flat interaction cross section, the energy spectrum of the produced gamma rays reflects the energy spectrum of the parent cosmic ray population, however with a characteristic bump at half the neutral pion rest mass (at 67.5 MeV).

Leptonic interstellar diffuse emission is produced in the interaction of electrons with gas or photons [131]. The interaction with the gas occurs through Bremsstrahlung as described in section 1.3.2 and the interaction with low energy

photons through inverse Compton scattering as described in section 1.3.3. Electrons can also produce gamma rays by synchrotron radiation in galactic magnetic fields, but this contribution is expected to be minor compared to the other three sources of interstellar diffuse emission and to occur mostly at lower energies.

The gas inside the Milky Way is constituted of hydrogen (89 %), helium (10 %) and few heavier nuclei (1 %) [131]. The hydrogen in this gas can be in form of atomic hydrogen, molecular hydrogen and ionized hydrogen [129]. The spatial distribution of the atomic hydrogen can be determined by emission in its 21 cm spectral emission line. Molecular hydrogen is mostly concentrated in large clouds and is hard to directly observe as radiative transitions in molecular hydrogen are weak as hydrogen has no permanent dipole moment and rarely excited in cold gases [132]. Its presence is inferred from the presence of carbon monoxide (which is detected through its emission spectral line at 2.6 mm) or other molecules. This requires however a good calibration of the abundance ratios between molecular hydrogen and the considered molecule which is not always easy to achieve. Ionized hydrogen can be traced using pulsar dispersion measures, i.e., the broadening of the duration of the pulsar pulse due to the presence of free electrons in ionized hydrogen plasma. Other methods to trace ionized hydrogen are to use the H-alpha spectral emission line at 656.28 nm or through the Bremsstrahlung emission in the radio band produced by free electrons traveling through the Coulomb fields of the ionized hydrogen atoms (free-free emission) [133]. All-sky maps of the distribution of the three gas species are shown in figure 5.1. The Galactic Plane can be prominently seen on the three plots, showing that there is an accumulation of the three species around it. Molecular hydrogen tends to be concentrated in massive molecular clouds and ionized hydrogen in star forming regions. Atomic hydrogen on the other hand is the most massive component in the interstellar medium and is observed in all directions.

The interstellar radiation field (constituted of photons) arises from the emission by stars, the reprocessing of this starlight by interstellar dust as well as the cosmic microwave background [129]. Its distribution can be obtained with the help of models of the total emission arising from stars, the dust distribution and scattering, absorption and re-emission properties of the dust [129].

The observation of diffuse emission allows to characterize all the processes involved in its production. Indeed, as diffuse emission is produced by the interaction of cosmic rays with a target component, any information on one of these components allows to derive constraints on the other one. These constraints are the stronger the more one knows which processes could contribute to the diffuse emission.

Measurements of the hadronic component allow to constrain the hadronic part of the cosmic ray spectrum. Comparing the cosmic ray spectrum determined in

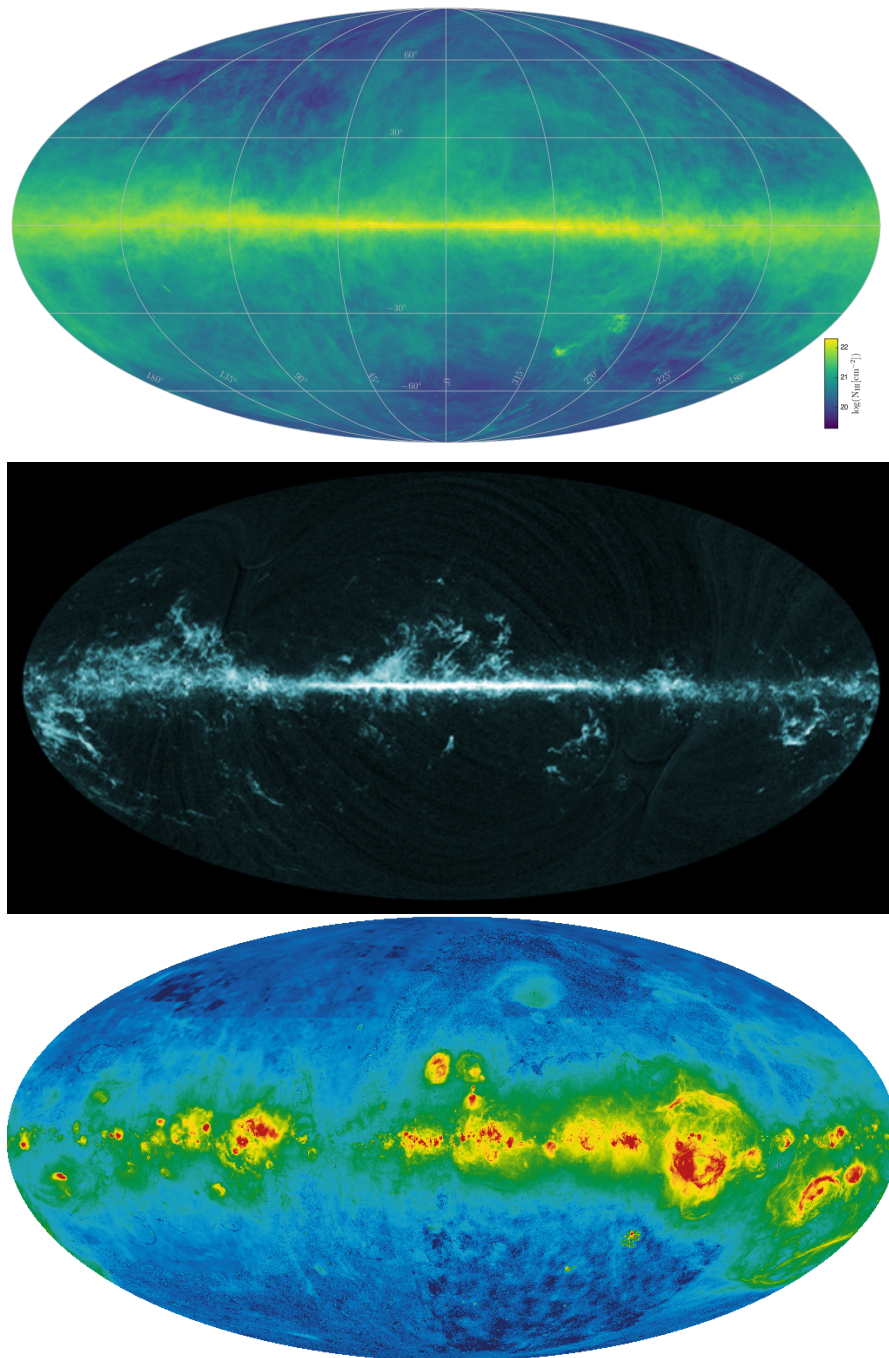


Figure 5.1: All-sky maps of the distribution of the different hydrogen species within and around the Milky Way. Top: All-sky column density map of atomic hydrogen gas using EBHIS and GASS data (integrated over all the velocity range) reproduced from [134]. Centre: All-sky image of the carbon monoxide distribution as seen by Planck reproduced from [135]. As mentioned in the text, carbon monoxide is used to trace molecular hydrogen. Bottom: All-sky  $H\alpha$  map tracing ionized hydrogen recombination using data from the Virginia Tech Spectral line Survey (VTSS), the Southern H-Alpha Sky Survey Atlas (SHASSA) and the Wisconsin H-Alpha Mapper (WHAM) reproduced from [136].

this way at different positions or with the one locally measured at Earth leads to insights in the propagation of cosmic rays. Then, the high diffusion length of high energy protons leads to a distribution of high energy protons which is expected to be almost homogeneous over large scales. The diffuse emission produced by the interaction of this homogeneous component with gas is therefore a good tracer for the distribution of gas and constitutes a further cross-check of existing spectroscopic observations (i.e., measurements through spectral emission lines) of gas densities. On the other side, local excesses could also be an indication for the presence of a cosmic accelerator and so their studies could help to discover new types of accelerators.

The leptons are, at least at the very high energies considered in this study, more impacted by radiative losses during propagation and are expected to be more localized. For this reason, a leptonic component of diffuse emission allows to trace the population of accelerated electrons near sources and so constrain the distribution of sources and particle propagation and permit the discovery of new sources of known or unknown type. The study of both processes also increases our knowledge about cosmic ray particle interactions and radiation processes.

Last but not least, gamma-ray interstellar diffuse emission can constitute a background for all potential new source discoveries. And so, characterizing it better leads to a better understanding of this background and so to a better disentanglement of the emission of this background from source emission.

## 5.2 The Large Magellanic Cloud and its interstellar diffuse emission

The Large Magellanic Cloud (LMC) is a satellite galaxy of the Milky Way. It is located at a distance of only 50 kpc [137] and can be seen with naked eyes from Earth's Southern hemisphere. From Earth, we have a nearly face-on view on it [87], as can be seen in figure 5.2 which shows the Magellanic Clouds. This optimal configuration reduces source confusions and so makes the observation of its individual sources easier. The LMC is a very active star forming galaxy: For a volume of only 2 % of the Milky Way, it has 10 % of its star formation rate [87]. It is believed that an interaction with its neighbouring galaxy, the Small Magellanic Cloud (SMC), which is also an active star forming region, might have recently increased this activity [139]. As a result, numerous interesting sources such as supernova remnants, ionized hydrogen regions, bubbles and shells have been observed at different wavelengths [87].

Due to its position in the Southern Hemisphere the LMC is a prime target for H.E.S.S. and is not visible for the other Imaging Atmospheric Cherenkov Tele-



Figure 5.2: Optical image of the two Magellanic Clouds - The Large and the Small one. Reproduced from [138].

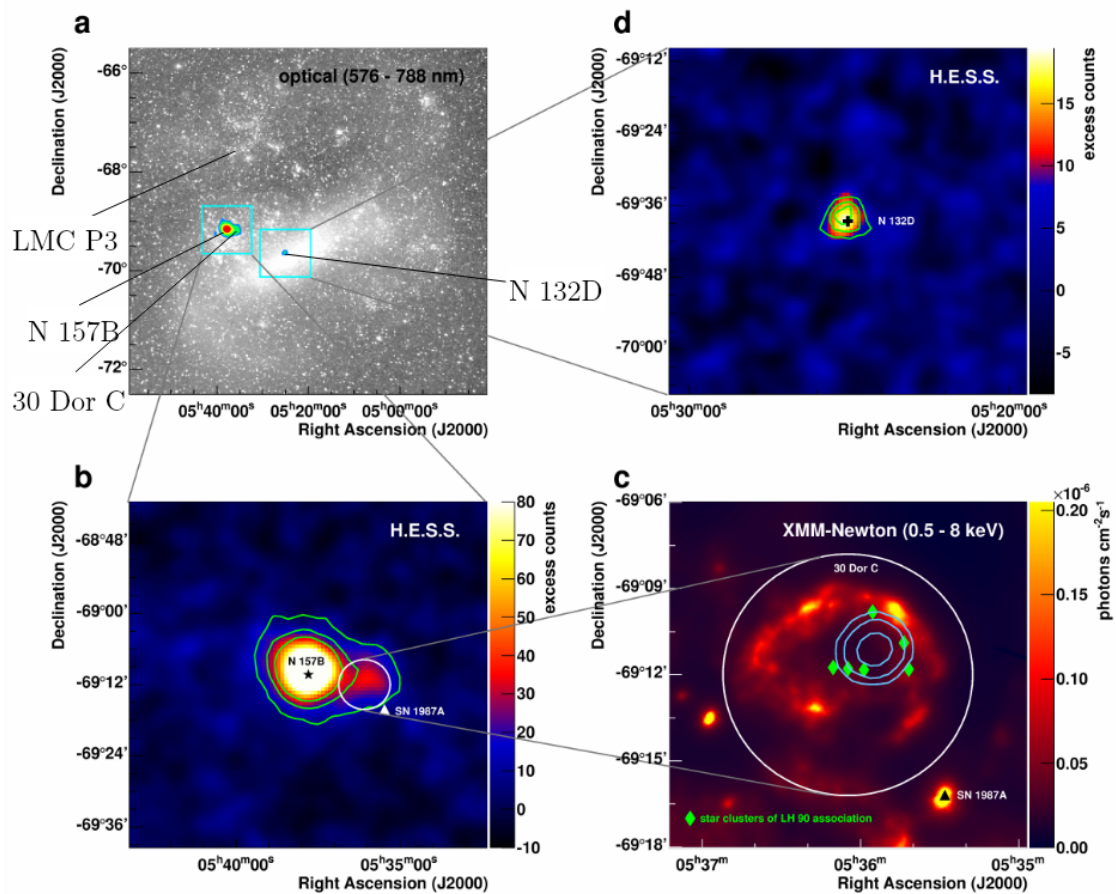


Figure 5.3: Sky maps of the Large Magellanic Cloud showing the four H.E.S.S. detected sources. Top left: Optical map of the entire LMC with the position of the H.E.S.S. sources marked. Top right: Excess counts map of the gamma-ray emission seen by H.E.S.S. around the region of N 132D obtained using the ring background method. Green lines indicate 3, 4 and 5 sigma statistical significance of the gamma-ray signal. Bottom left: Excess counts map of the gamma-ray emission seen by H.E.S.S. around the region of N 157B and 30 Dor C obtained using the ring background method. Green lines indicate 3, 5, 10 and 20 sigma statistical significance of the gamma-ray signal. Bottom right: XMM-Newton X-ray flux image of the region around 30 Dor C. The superimposed cyan lines indicate the 68 %, 95 % and 99 % confidence level contours of the position of the gamma-ray source. Adapted from [53].

scopes. Four sources in the LMC have so far been detected with H.E.S.S. [53, 44]. Their positions in the LMC are shown in figure 5.3. All of them are consistent with being point sources when observed with H.E.S.S. The brightest of these sources is the pulsar wind nebula N 157B surrounding the pulsar PSR J0537-6910. With the Crab Nebula, which has been the first point source discovered by a ground-based gamma-ray telescope as discussed before, it is one of the brightest pulsar wind nebulae. From its X-ray and gamma-ray emission, it has been concluded that this pulsar wind nebula is embedded in a strong radiation field and a relative weak magnetic field and is probably part of the stellar cluster LH 99. At an angular distance of only  $9'$  (i.e., 130 pc), there is a second source, the superbubble 30 Dor C. A superbubble is a cavity with an extension of the order of hundreds of pc filled with less dense gas atoms than the surrounding interstellar medium. It is usually carved by multiple supernovae and stellar winds. 30 Dor C has the largest known X-ray synchrotron-emitting shell with a size of 47 pc. It is thought to have been produced by multiple supernovae explosions in LH 90 and can also be observed in the optical and radio. Further South is the core-collapsed supernova remnant N 132D which is aged about 6000 years. It exhibits strong thermal X-ray emission. In addition, to the X-ray and gamma-ray, it can also be seen in the radio and infrared. Last, to the east is the gamma-ray binary LMC P3 which has been discovered more recently by H.E.S.S. [44]. Its position is consistent with the X-ray source CAL 60 and it is thought to be a binary system of an O-type star and most likely a neutron star, even though a black hole cannot be completely excluded. It exhibits periodicity with an orbital period of 10.3 days. Beside these four discovered very-high-energy sources, a very interesting source candidate is the remnant of the supernova SN 1987A which exploded in 1987 and which was the first supernova visible to the naked eye since 1604 and the only one so far from which neutrinos (that could be attributed to the supernova) have been detected on Earth. However, no emission from this supernova has been detected so far at gamma-ray energies. This is interesting as some models suggested gamma-ray emission early in the development of a supernova remnant and a non-detection with H.E.S.S. puts constraints on these models. For the first time, one could observe the onset of emission from a supernova remnant if this remnant will be detected by H.E.S.S.

Extended gamma-ray emission has been reported at GeV energies by *Fermi*-LAT, but so far, such emission has not been observed in very high energy, in particular by H.E.S.S. The latest paper on interstellar diffuse emission in the LMC by the *Fermi*-LAT collaboration is called "Deep view of the Large Magellanic Cloud with six years of *Fermi*-LAT observations" and has been published in 2015 [140]. It discusses not only extended emission, but also the four point-like sources discovered with *Fermi*-LAT in the LMC so far. As H.E.S.S., they detected emission consistent with the position of the pulsar wind nebula N 157B, but were not able

to disentangle whether it comes from N 157B and / or its associated pulsar PSR J0537-6910. Two other sources are spatially consistent with N 132D and LMC P3. For LMC P3, later on a periodicity of 10.3 days was discovered in the *Fermi*-LAT data which could be confirmed with X-Ray and radio observations [141]. In addition, they have detected the pulsar PSR J0540-6919 and could measure its period of 16 ms [142], which has not been detected with H.E.S.S. so far. However, *Fermi*-LAT could not detect the superbubble 30 Dor C and, as H.E.S.S., it could also not detect the supernova remnant of SN 1987A.

Coming back to the search for interstellar diffuse emission the *Fermi*-Lat collaboration presented in their paper, the first step of the analysis is the usual procedure of subtracting a background model containing all known emission not coming from the LMC. It consists of the Galactic interstellar emission, the isotropic *Fermi* background (accounting for isotropic diffuse gamma-ray emission and residual cosmic rays classified as gamma rays) and previously detected known isolated sources in the region not part of the LMC. The normalization of the first two components and the spectral parameters of each individual source are left free and in a maximum likelihood fit to the data. For the modelling of the diffuse emission and the remaining individual sources (the ones already discussed before) in the background subtracted data, three different approaches are used: An analytic model, an emissivity model and various template models. In the analytic model, the remaining emission is represented by point-like sources (supposed to describe the individual sources) and 2D-Gaussian shaped sources (supposed to describe the diffuse emission). First, two easily distinguishable point-like sources and a point-like source identified by its pulsations are in the model. Then, iteratively further point-like and 2D Gaussian components are added to the model by fitting them with a likelihood procedure to the data keeping the parameters of the other components fixed. New components are added until the change in test statistics TS was less than 25, where TS is defined as:

$$\text{TS} = 2(\ln(L) - \ln(L_0)), \quad (5.1)$$

where  $L$  is the likelihood of the fit with the additional component and  $L_0$  the likelihood without the added component. If the change in the TS value is less than 25 the component is not added to the model and no component of the same type is added to the fit any more. When no additional component yields a change in TS value above 25 the procedure is stopped and the positions and sizes of all the components are re-optimized with a likelihood fit starting from the brightest component. Finally, the spectra of all the components are optimized by trying different components.

The emissivity model is very similar to the analytic model, but instead of fitting 2D Gaussians after the fit of the point-like sources, it uses 2D Gaussians multiplied with the gas column density. This model is physically motivated as interstellar

diffuse emission in the 0.1 to 100 GeV is dominated by the interaction of cosmic rays with interstellar gas. As before, all the positions and sizes, and after that the spectra are re-optimized after having found all the components with a  $TS \geq 25$ . In the template fitting approach, the emission is fit once with an ionized gas map of the LMC and once with a total gas map (i.e., atomic, molecular and ionized gas). These fits are performed multiple times while testing the changes when adding different combinations of the sources found with the other approaches with free spectral parameters to the fit.

The fit with the ionized gas map leads to the disappearance of PSR J0540-6919 as all the significant emission at its position is reproduced by the gas map. This ionized gas map indeed shows a peak in the very active region of LMC around PSR J0540-6919, N 157B and 30 Dor C. However, the pulsations of PSR J0540-6919 are observed with *Fermi*-LAT and so the ionized gas template does not properly describe the data. The fit with the total gas template leads to a TS value which is by more than 700 lower than for the two other approaches (with about 20 fewer degrees of freedom) and is not considered further due to its bad performance. This very different performance compared to the ionized gas map is due to the dominance of atomic hydrogen in the LMC which means that the gas template of total hydrogen and atomic hydrogen are very similar [143]. The emissivity model shows the best performance, by having a TS value which is higher by 73 than the one of the analytic model for two additional degrees of freedom. This means that the emissivity model is preferred with a statistical significance of about  $8\sigma$ .

The results obtained with the emissivity model and the analytic model are very similar, as illustrated in figure 5.4. The point-like sources are the same by construction and there are four Gaussian components in the analytic model compared to five in the emissivity model. However, a closer inspection discussed in the *Fermi* paper shows that two of the Gaussian components in the emissivity model have an almost coincident position and that the fit is not deteriorated significantly when fitting both of them using the same spectral parameters, indicating that it might be just one component with a more complex morphology. So, in the end, both models show very similar components. One large-scale component is spanning the whole LMC and could be linked to cosmic rays accumulated over long time-scales and interacting with interstellar gas. The other three components have smaller scales and are surprisingly in rather gas-poor regions of the LMC. To explain this, one would need a local over-density of cosmic rays if the emission of these components is indeed due to hadronic interstellar diffuse emission. To find a source for such a local over-density, the local environment of these three emission components was looked into in the paper. It is illustrated with the corresponding potential sources of cosmic rays in figure 5.5. There is no obvious correlation which would hold consistently for all three components. However, the component G3 / E2 illustrated

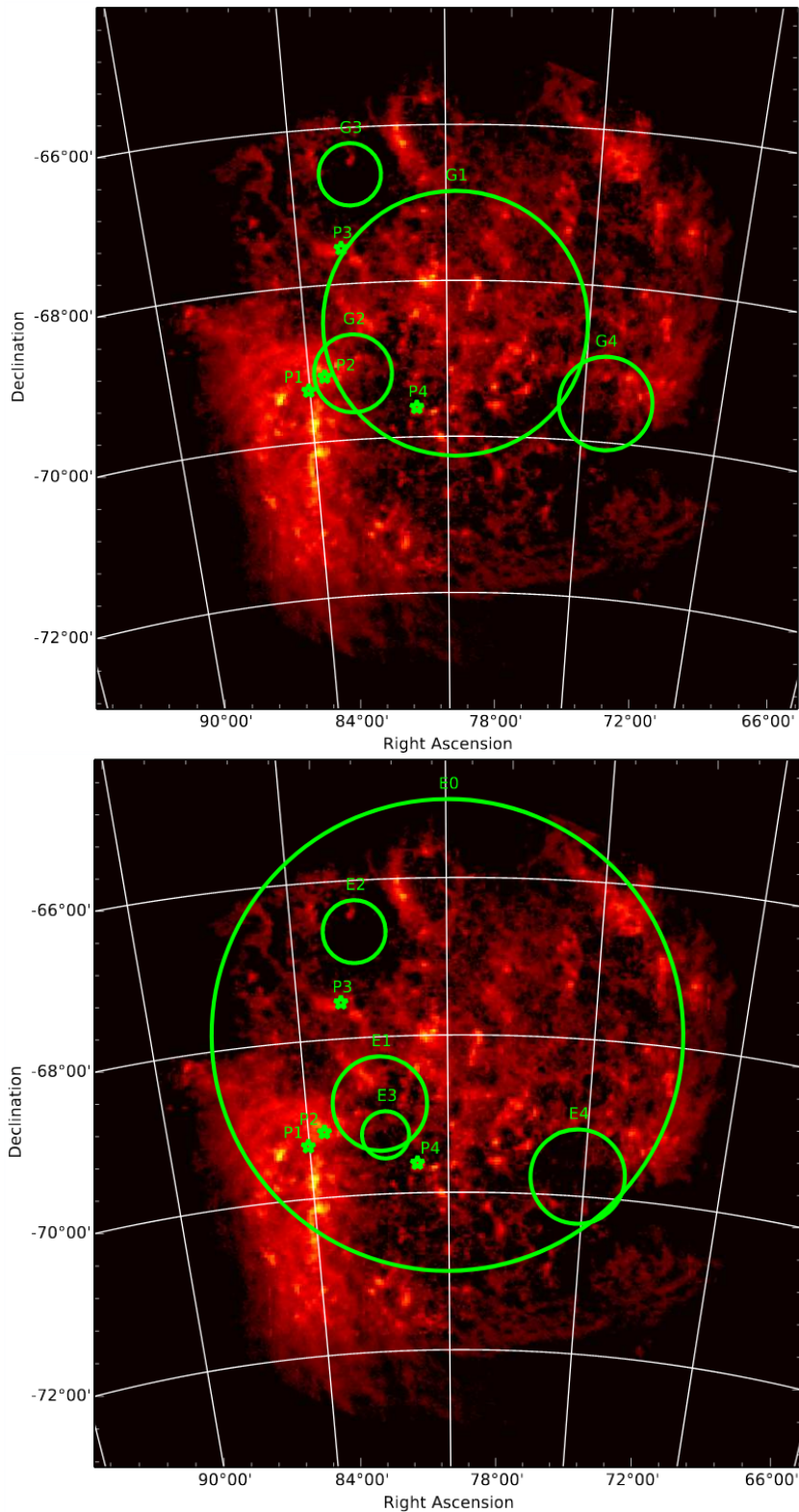


Figure 5.4: Illustration of the fit model components of the *Fermi*-LAT analysis. The point sources are indicated by the green stars, the Gaussian emission components by the green circles which ( $1\text{-}\sigma$  extent) on the top for the analytic model and on the bottom for the emissivity model. The coloured map in the background indicates the total gas column density distribution. Reproduced from [140].

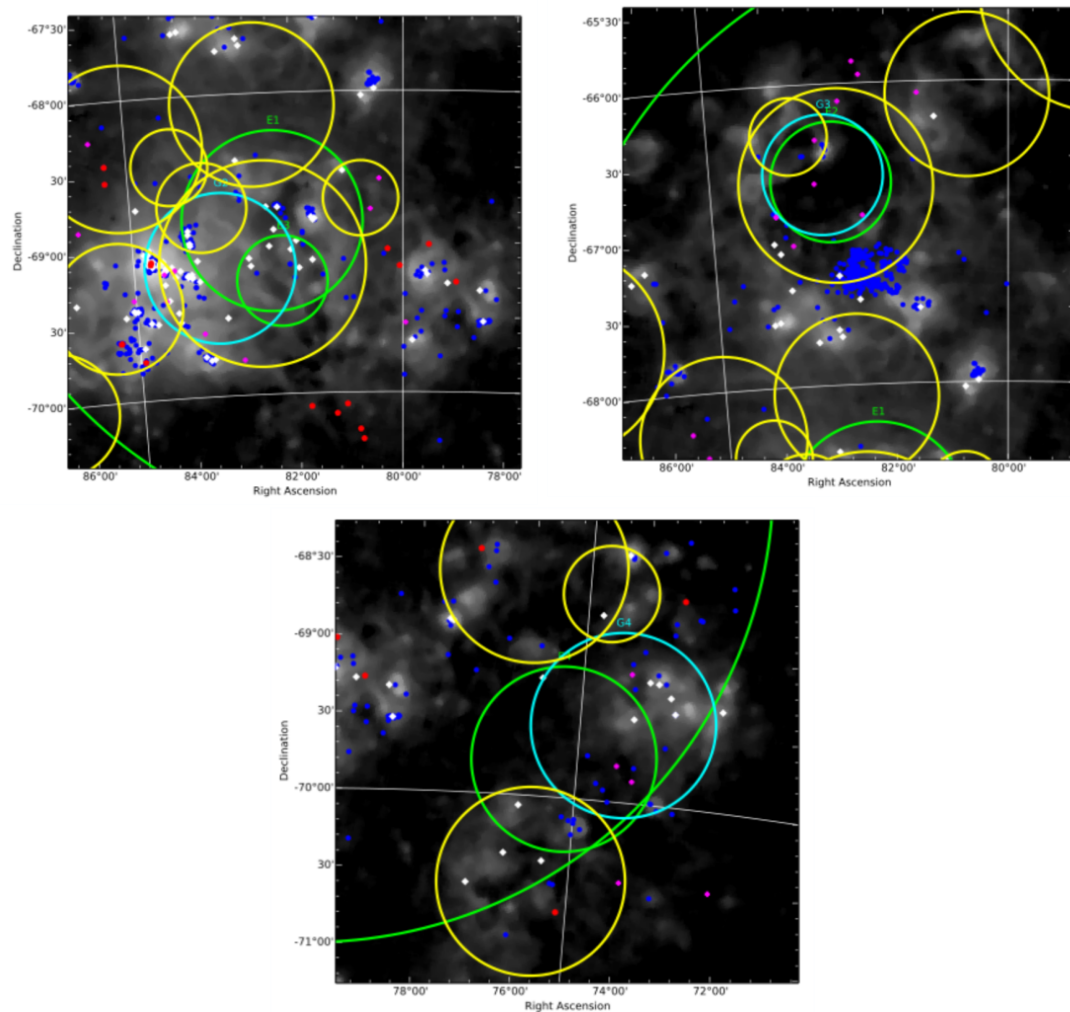


Figure 5.5: Illustration of the environment of the different small-scale extended emission regions found in the *Fermi*-LAT analysis. Top left: Environment of G2 / E1+E3. Top right: Environment of G3 / E2. Bottom: Environment of G4 / E4. The components resulting from the analytic model are in cyan and the ones in the emissivity model in green. Pulsars are indicated by magenta pluses, Wolf-Rayet stars by white diamonds, stars of spectral type B0-3 by blue dots, high-mass X-ray binaries by red dots and supergiant shells by yellow circles. The map in the background is a so-called hydrogen alpha map which shows the emission resulting from ionized hydrogen through its 656.3 nm emission line. Reproduced from [140].

on the top right plot is spatially coincident with a void<sup>1</sup> surrounded by a supergiant shell and the component E4 / G4 on the bottom plot also seems to be in a quite empty region. The component formed by E1 and E3 respectively G2 on the other hand, is in a more crowded region, even though there are not many young stars inside the region, but the absence of voids in some of the supergiant shells surrounding it might indicate that projection effects complicate the picture in this region. So, there might be an association of emission components with cavities and supergiant shells, even though there is not enough evidence to confirm such a scenario, especially due to the lack of a strong identification of the sources which would inject the cosmic rays in these cavities. This association would however explain why the three smaller components are found in rather gas-poor regions.

However, not all of the extended emission observed with *Fermi*-LAT is necessarily due to hadronic diffuse emission. As discussed in the previous subsection, diffuse emission can also be produced by inverse Compton scattering, which could explain the smaller scale components. However, at least the components E2 and E4 are in regions with low strength of the interstellar radiation field and there are no known sources injecting the electrons necessary for such a scenario. In addition, these electrons should also produce synchrotron emission observable in the radio band assuming the magnetic field not to be particularly low which has not been seen, which makes such a scenario unlikely for these two components.

Another potential source of such extended emission could be a big number of unresolved low-luminosity gamma-ray sources which mimic a continuous extended emission component. The *Fermi*-LAT collaboration showed that each of the small-scale components could be described by about five point-like sources, which could be of the same type as sources already discovered with *Fermi*-LAT, but of lower luminosity, such as pulsars, their surrounding wind nebulae and supernova remnants. Additional sources of this type not detected with *Fermi*-LAT have already been seen at other wavelengths as can be seen in figure 5.5 (see for instance: [144, 145]).

Interstellar diffuse emission from the LMC has not only been observed at gamma-ray energies, but also at other wavelengths. X-ray observations by ROSAT, and later on XMM-Newton, have revealed numerous discrete point-like sources, most of them being X-ray binaries and supernova remnants [146, 147]. On top of these sources, extended emission has been seen as illustrated in figure 5.6 obtained from ROSAT data. No XMM-Newton results for extended emission are shown here, as the increase in angular resolution from ROSAT to XMM-Newton came at the cost of a lower field of view and so no full survey of LMC has been performed with XMM-Newton due to observation time constraints. The origin of this extended emission is most likely hot interstellar gas undergoing thermal

---

<sup>1</sup>A void here indicates the cavities filled with less dense gas atoms and fewer sources than the surrounding medium delimited by supergiant shells or superbubbles.

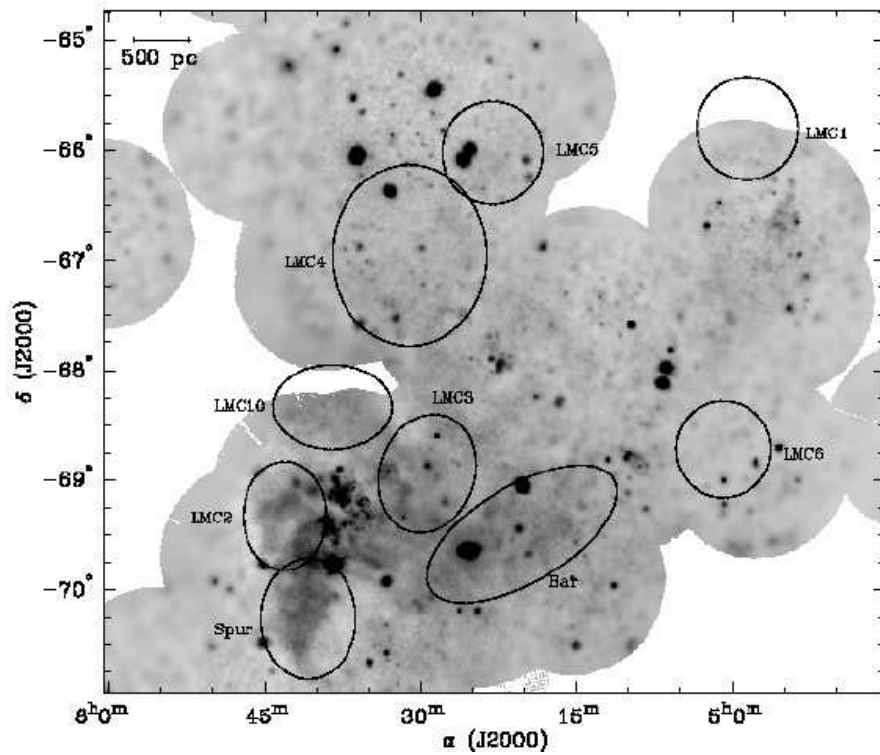


Figure 5.6: ROSAT mosaic map of the LMC for X-ray energies between 0.44 keV to 2.04 keV in a logarithmic scale in intensity. Various supergiant shells as determined from ionized hydrogen emission (LMC1-10), the Spur and the Bar are shown as ellipses. Reproduced from [146].

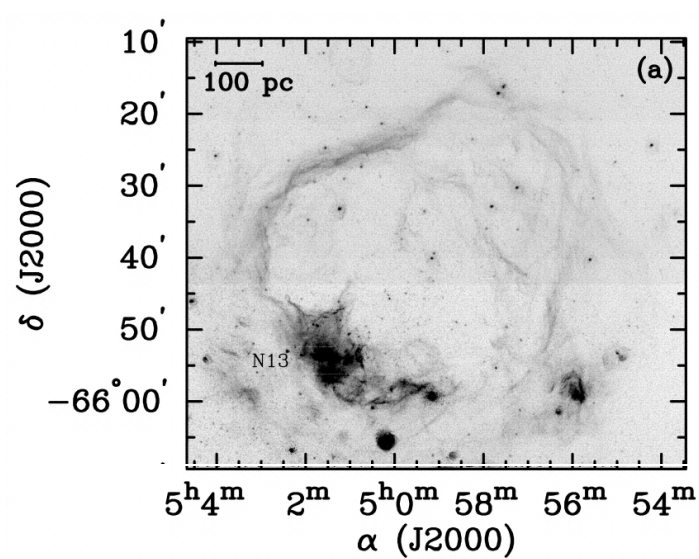


Figure 5.7: Ionized hydrogen map as seen by the hydrogen  $\alpha$  emission line around the X-ray emission region LMC1 of figure 5.6 obtained from the Magellanic Cloud Emission-line survey [148]. A shell like structure can clearly be seen. Reproduced from [146].

emission and its components have scales from about 10 pc to 3000 pc. Most of this extended emission comes from supergiant shells as seen from a comparison of the X-ray maps with the ionized hydrogen maps on which shell like structures can be clearly seen as illustrated as example for the component LMC1 (of figure 5.6) in figure 5.7. There are two notable exceptions which do not have an ionized hydrogen counterpart: the LMC Spur and the LMC bar. The LMC bar is the largest region of diffuse X-ray emission and constituted of a stellar population with many ionized hydrogen regions. Part of its X-ray emission could be due to unresolved sources, however an unrealistic high density of unresolved sources would be needed to account for all of the emission. The X-ray Spur is a region in the South of supergiant shell LMC2 and the region with the second highest average X-ray surface brightness of LMC. The origin of its X-ray emission is unclear, even though it was suggested that it represents the blowout of the hot gas interior to LMC2 into the halo of LMC [149]. This is however difficult to accommodate with no indications of an outflow being seen in the optical [150]. The X-ray map from the ROSAT observations and the location of the different supergiant shells, the LMC Spur and the LMC Bar are shown in figure 5.6.

### 5.3 Why the standard analysis underestimates emission from very extended sources

Current Imaging Atmospheric Cherenkov telescopes have fields of view of about  $3^\circ$  to  $5^\circ$  diameter. This makes the observation of interstellar diffuse emission much more challenging than the observation of point-like or moderately extended sources. Indeed, interstellar diffuse emission is characterized by large extension and so mostly exceeding the field of view of Cherenkov telescope arrays. In addition, interstellar diffuse emission is often not expected to have very strong gradients or small-scale structure and so the change of the level of signal is expected to be small over the field of view of these telescopes. These challenges come in at multiple levels in the analysis.

First of all, the background subtraction usually relies on the definition of a control region inside the field of view as described in the section 2.5.1. However, if the extension of diffuse emission exceeds the field of view, any control region inside the field of view is inevitably contaminated with diffuse emission. This leads to an over-estimation of the background and consequently to an under-estimation of potential diffuse emission. The H.E.S.S. collaboration has tried to get around this in the 2014 publication on interstellar diffuse emission in the Milky Way [130] by judiciously choosing control regions inside the field of view which are as little contaminated by interstellar diffuse emission as possible. These control regions were

defined by iteratively excluding regions passing a given significance threshold and everything between a galactic latitude of  $-1.2^\circ$  and  $1.2^\circ$ . This method led to the detection of extended emission along the Galactic Plane. However, as mentioned earlier, this choice of latitude range is a compromise between having large exclusion regions and having enough events for a proper background normalization. For this reason, the control region is most likely contaminated with an unknown amount of background. So, “the reported signal is considered to represent a lower limit compared to what might be detected with improved analysis strategies”, as stated in the paper. So, to go beyond this lower limit, a background subtraction not based on the subtraction of the background determined inside the field of view needs to be considered.

To circumvent this, one could consider getting the background from a control region which is not inside the field of view, such as by using the ON-OFF scheme formerly used in very-high-energy gamma-ray astronomy. This ON-OFF scheme consists in taking consecutively two runs with the observation position shifted in right ascension, one on the region of interest (ON observation) and one on a region without any known source (OFF observation). The observation conditions for the ON- and OFF-region are then similar, as both observation runs have been taken consecutively and towards the same zenith angle, and the OFF-observation can be used as control region for the background subtraction. This, however, leads to the necessity to have an OFF-run for each ON-run which doubles the amount of observation for having a proper background subtraction. This is not viable when combining 100 or even 1000 hours of observation when needing deep exposure over a region extending the field of view of the telescopes as in the search for interstellar diffuse emission. To avoid this necessity of taking the double amount of data, the field-of-view background has been developed [116]. In this background subtraction method, a generic background model is generated from OFF runs, or ON runs with masked sources. This background model is usually generated for multiple zenith angle bins (because this is the observation parameter which has the biggest impact on the background model), but it is also possible to introduce a binning in other observation parameters. The normalization of this background model is then usually defined by an adjustment to the data masking the regions with expected emission. The main difficulty with this approach is that interstellar diffuse emission is mostly expected in galaxies. Galaxies are regions with high night sky background which might lead to a different behaviour of the background which needs to be subtracted. For this reason, it is preferable to determine the background from OFF-region with a similar amount of night sky background. However, these regions are mostly galaxies and often crowded with gamma-ray-emitting objects and possibly even interstellar diffuse emission and also often not available in the right zenith angle band, making this approach

difficult. Nevertheless, there are ongoing efforts to use this method to detect extended emission [151, 152, 153, 154]. In this work, however, a different method less prone to systematics through night sky background is investigated.

As a background subtraction based on the definition of a control region in- or outside the field of view seems to be difficultly viable, a template background-based approach such as the one described in section 2.5.1 seems to be the right way to go. This background subtraction method needs a well-known acceptance (as all background subtraction methods do) which leads us to the second challenge of the search for interstellar diffuse emission. Indeed, interstellar diffuse emission is expected from regions with high, but also not completely homogeneous night sky background. These inhomogeneities lead to a variation of the acceptance with position on the sky on a small scale. In the most commonly used 2D acceptance calculation method (and in the radial acceptance method when summing over multiple runs) different observation runs are summed in the camera frame to obtain the acceptance. This smears out all field of view-specific influences such as varying night sky background as described in section 2.5.2. This smearing out of night sky background in the calculated acceptances increases the systematic uncertainties of any diffuse analysis, especially when combining a huge number of observation runs. Using the simpler radial acceptance without summing over runs does also not solve this issue. Indeed, it assumes a radial symmetry around the observation position (beside correcting for zenith angle) and so does not consider inhomogeneities in the response of the camera breaking this symmetry. This leads to increased systematic uncertainties especially when combining a huge number of observation or at high zenith angle.

This shows that none of the traditional analysis methods of gamma-ray astronomy is fully well suited for the study of extended emission inside galaxies and that novel analysis methods are necessary. A novel analysis method better suited for this kind of analyses developed within the H.E.S.S. collaboration is described in the following.

## 5.4 Run-wise simulations

As shown in the previous section, a novel analysis method with a different background subtraction and acceptance determination method is necessary in order to detect largely extended emission. This novel analysis method starts with a novel simulation procedure. Until now, all major Cherenkov telescope arrays have used basically the same Monte-Carlo simulation strategy: simulations were generated a priori with different values for the most relevant parameters (atmospheric profile, zenith angle, azimuth angle, participating telescopes and camera configuration, ...) and the rest of the configuration being kept unchanged for all simulations [155].

From these simulations the so-called instrument response functions (IRFs), i.e., among other the point spread function, effective area and energy dispersion of H.E.S.S., are generated for the different parameter values. For a given observation run, the IRFs are then interpolated in these tabulated parameter values. Even though this interpolation in the most important parameters helps to achieve a more precise result than using just one parameter value for each parameter, it is a simplification which introduces again systematic uncertainties, especially under high night sky background conditions.

For this reason, a new simulation scheme based on so-called run-wise simulations has been implemented within the H.E.S.S. collaboration [155]. These run-wise simulations are not produced a priori before the data taking, but after the observation runs have been taken. The idea is to simulate each run individually with its actual settings, which is why they are called run-wise simulations. This allows to use the actual observation conditions for the simulation and so removes any necessity for an interpolation. It also allows to increase the number of variable parameters in the simulation without an increase of the necessary computation time and so to get the simulations much closer to the observational reality [156]. The parameters from the observation used for the run-wise simulations are:

- The array configuration (i.e., which telescopes participate in the run)
- The start and end time of the observation
- The pointing position of the telescopes (which allows to properly include zenith angle dependencies)
- The position of the observed source (i.e., the direction from which the photons arrive)
- The optical efficiency of each individual telescope
- The transparency coefficient which represents the atmospheric transparency
- The camera focus
- The trigger settings
- The life-time fraction of the individual telescopes
- The non-operational pixels
- The gain of the individual photo-multiplier tubes
- The gain ratio between the high and low gain channel of each photo-multiplier tube

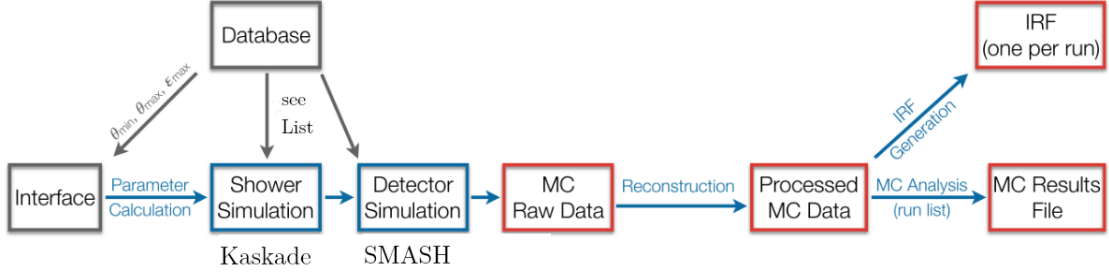


Figure 5.8: Overview flowchart of the production process of run-wise simulations. Adapted from [155].

- The flat-field coefficient of each pixel
- The night sky background recorded in each pixel

Most of these parameters come out of the calibration and so it is crucial to have a well-understood and reliable calibration framework which can be reproduced in simulation.

The production of run-wise simulations for a given run is schematically illustrated on figure 5.8. First, the run number, desired statistics level defined by the differential flux at 1 TeV and the photon index  $\Gamma$  of the simulation need to be specified [155]. In addition, a source position can be specified, otherwise it is read automatically from the database for runs where a given source was observed [156]. This source is usually assumed to be a point-like source, but for diffuse analyses a uniform diffuse cone angle around the source position can be set. These parameters, as well as the array configuration, the zenith angle and the relative optical efficiencies of the telescopes, are then used to compute the maximum impact distance of the primary photons from the centre of the array, the minimum energy of the simulated primary photons and finally the number of events to be simulated according to the input energy spectrum using a maximum energy for the simulated primary photons which is often set to 100 TeV. Then, the primary photons to be simulated are uniformly distributed between the start and end time of the run read out from the database and also over the circle defined by the diffuse cone angle if such an angle has been defined. Then, all the observation parameters used for run-wise simulations listed in the previous paragraph are read out from the database and the simulation of the atmospheric showers produced by the primary photons are simulated with the "*Kaskade*" software. Its output is directly passed to the "*SMASH*" software (without saving the intermediate results on disk to reduce the needed disk space) which performs the detector simulation. During this procedure, the pointing position of the telescopes is updated at the beginning of the simulation of each particle to simulate the tracking of the trajectory of a

source on the sky. In addition to these primary photons from the source, night sky background photons with a rate according to the one measured in the observation are simulated in each pixel.

The output of these run-wise simulations can then be analysed in the same way as actual data [155]. If one wishes to have a simulated source with a more complex spectrum than a power-law spectrum or a steeper spectrum than the simulated one<sup>2</sup>, the simulations can be re-weighted by weighing individual events or throwing away events. Similarly, any source morphology can be implemented in the simulation or mimicked by re-weighting or throwing away events.

The run-wise simulation production is fully implemented in the HESS software (and was so already when I started my work on interstellar diffuse emission). Run-wise simulations can easily be produced by specifying a list of runs, the differential flux, the photon index and if applicable the source position and the diffuse cone angle as well as the software version, simulation configuration and analysis profile (defining among other the event selection and reconstruction). In order to avoid the production of the same run-wise simulations multiple times by different collaboration members, the run-wise simulation production within H.E.S.S. is based on a request system.

## 5.5 Generating Instrument Response Functions and Background Models from run-wise simulations

The idea of this novel analysis method is then to use these run-wise gamma-ray simulations to generate instrument response functions and a background model for the gamma-like events (i.e., the hadronic events which are wrongly classified as gamma rays after reconstruction) for the background subtraction, assuming that it is possible to generate a background model of gamma-like events from simulated gamma rays. This allows not to rely on the definition of a control region (likely polluted by interstellar diffuse emission) for background subtraction or a stacking mechanism for the acceptance maps which smears out all field of view dependencies as discussed in section 5.3. This background model generation is done by simulating a diffuse source for each run with run-wise simulations and the distribution of the primary photons produced by this source is then assumed to correspond to the distribution of the gamma-like events and used as background model [157]. This strongly relies on the similarity of gamma-like and gamma-ray

---

<sup>2</sup>If a source has a very steep spectrum, simulating a softer spectrum with run-wise simulations allows to have a more equal number of simulated events in each spectral energy bin and avoids very large statistical uncertainties at high energies from the simulation side.

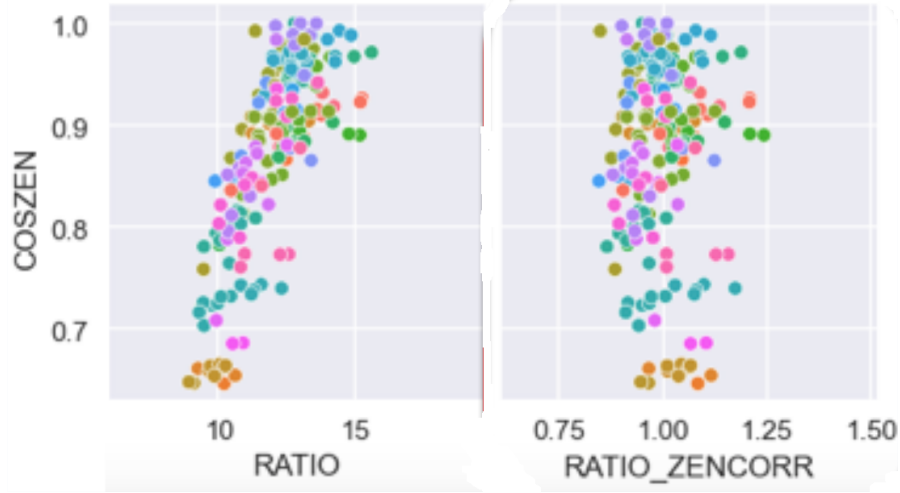


Figure 5.9: Cosine of the zenith angle against the ratio of the number of simulated events to the number of recorded events for different OFF runs. Left: Before zenith angle correction. Right: After zenith angle correction. The ratio not being centred around 1 on the left plot is due to an increased simulation statistics compared to the expected number of events in order to reduce statistical uncertainties. This difference in simulation statistics is "automatically" taken into account when performing the linear fit for the zenith angle correction. Reproduced from [157]

showers so that the gamma-like acceptance can be simulated with gamma rays. The detailed procedure of this background model and IRF generation as well as the foundation of the assumption of the similarity between gamma-like and gamma-ray events are discussed in the following of this subsection.

First of all, diffuse run-wise simulations need to be generated for all the runs part of the analysis. This is done with a diffuse cone angle of  $3^\circ$  with the cone centred on the centre of the field of view [157]. Before doing any analysis, it is necessary to check that the behaviour of the run-wise simulations corresponds to the behaviour of the observation background. For this, the number of events in OFF-runs has been compared to the number of events in the corresponding run-wise simulations in a first step. As the hadronic background is almost isotropic due to galactic magnetic fields and the initial simulated photon distribution has also been isotropic, the ratio between both quantities should be constant with respect to all variables. However, a small dependence on zenith angle has been discovered which led to a relative root mean square error of the ratio of the number of simulated events and the number of recorded events of 11.3%. It has been corrected by fitting the zenith dependence with a linear fit in the cosine of the zenith angle and using the fit parameters as correction factors. This led to a reduction of the relative root mean square error to about 7.3%.

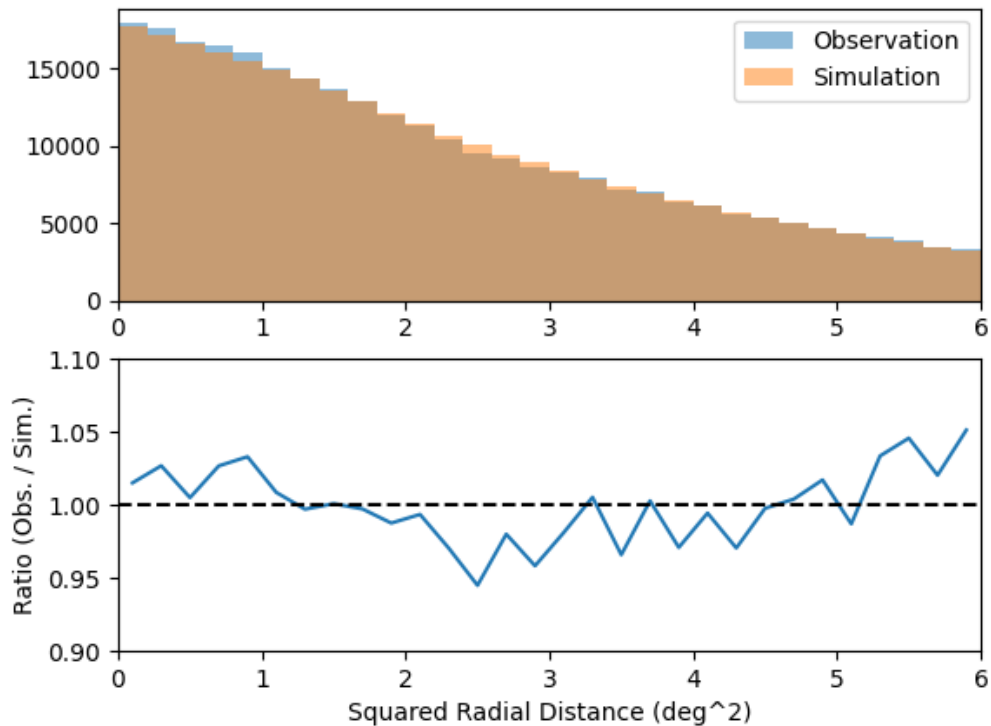


Figure 5.10: Top: Distribution of background events in an observation run and simulated events in the corresponding run-wise simulation as a function of the squared radial distance of the event from the pointing position of the run. Bottom: Ratio of these both quantities. A discrepancy of up to 5% can be seen between observation and simulation. The wiggles in the bottom plot are due to limited statistics within one run. Reproduced from [157].

In a second step, the comparison of the number of simulated events and the number of recorded events has been done within individual runs (i.e., against a parameter which is different for different events within a run) and not only between different runs anymore. A small difference with radial distance of the event to the pointing position of the run of the level of up to 5% was found as illustrated in figure 5.10 where the distribution of events as a function of the squared radial distance is shown for OFF-observation runs and simulated events in the corresponding run-wise simulations [157]. A procedure has been put in place to correct such a difference. It consists first of all in selecting an OFF runlist with different regions of interest without any gamma-ray source [158]. The runs in this OFF runlist should be selected in a way that their distribution is as isotropic as possible in all the relevant observation parameters and especially zenith angle. The idea is then to produce run-wise simulations for this runlist and attribute a weight to each simulated event such that the radial distance dependence disappears. To do this, the runlist is in a first step randomly split in a training and a test dataset such that the training dataset contains 7/8 of the runs and the test dataset 1/8 of the runs. Then, the correction weight  $w$  is assumed to depend on the squared radial distance  $x$ , the true energy (i.e., the energy input in the simulation)  $E$  and the zenith angle  $\text{zen}$ . From these quantities, a model for the correction weights is built containing 4 free parameters to be adjusted:

$$w = E^{\gamma_{\text{sim}} - \gamma_{\text{bkg}} + C_E \log_{10} E} + p_{\text{lin}} \times x \times \text{zen} + p_{\text{quad}} \times x^2 \times \text{zen}, \quad (5.2)$$

where  $\gamma_{\text{sim}}$  is the photon index input in the simulation. The 4 free parameters to be fit are  $\gamma_{\text{bkg}}$ ,  $C_E$ ,  $p_{\text{lin}}$  and  $p_{\text{quad}}$ . The real photon index of the background emission is described by  $\gamma_{\text{bkg}}$  and the spectral curvature by  $C_E$ .  $p_{\text{lin}}$  describes a term linear in the squared radial distance multiplied by the zenith angle and  $p_{\text{quad}}$  a term quadratic in the squared radial distance multiplied by zenith angle. Using this parametrization of the weights of each simulated event, the squared sum of the difference in counts between the simulated and actual dataset over energy, squared radial distance and zenith angle bins is minimized (least square fitting method) using the training dataset. This leads then to best-fit values for the 4 parameters and so to a best-fit weight for each simulated event. Finally, the weighted mean absolute error (MAE) is calculated on the test dataset using the best-fit weights.

This procedure is repeated for the 7 other possible splits in training and test datasets such that each event is once in the test dataset [158]. Then, the individual fit parameters are weighted according to their MAE and summed over the 8 splits and the new parameters, the average MAE and the standard deviation of the MAE over the splits are stored. The entire procedure is finally repeated 100 times using different random dataset splits and the results from each of this 100 repetitions is stored.

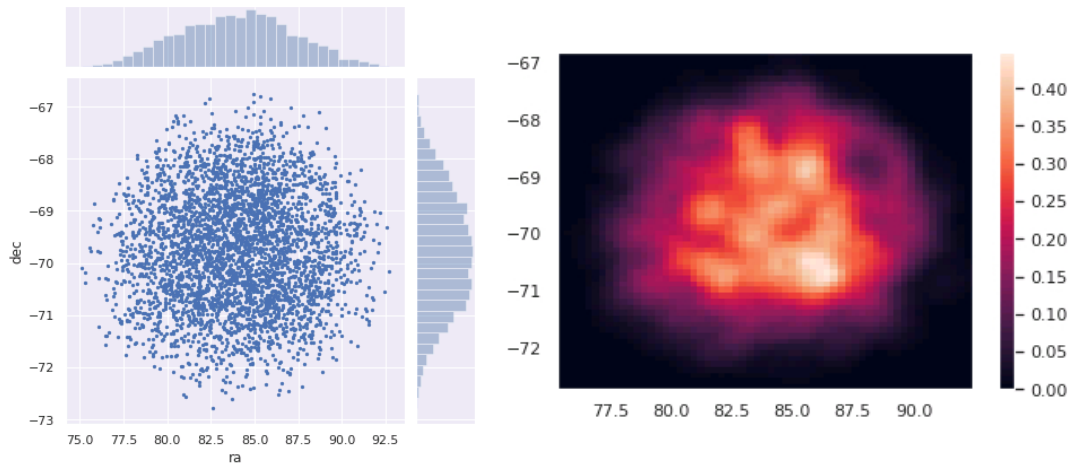


Figure 5.11: Left: Distribution of simulated events in angular space for one run. Right: Generated binned background model for the same run by smoothing the simulated events with a kernel density estimation.

To apply these radial corrections to a given run which may contain gamma-ray emission, for each simulated event its weight is computed from the parameters of each of the 100 repetitions and the median weight is applied to the simulated event [158]. These radial corrections can then be validated by comparing the MAE obtained on the dataset used to produce the radial correction to the MAE of an independent validation dataset to make sure there are no indications for over-fitting.

These radial corrections were initially produced for studies of the Milky Way, for zenith angles between  $5^\circ$  and  $40^\circ$ . These are the radial corrections used for the Cen A and NGC 253 datasets presented later in this study. However, LMC and SMC are at much higher zenith angle, and so need a radial correction model valid at higher zenith angles. For this reason, I generated a new radial correction model valid between  $40^\circ$  and  $60^\circ$  using 194 OFF-runs taken at zenith angles between  $38^\circ$  and  $62^\circ$  without any known very-high-energy gamma-ray source, which I then used for the LMC and SMC analysis.

After having generated the radial correction model, this model is used to calculate the correction weights of the run-wise simulation on a run-by-run basis for the runs used for the actual analysis [157]. Then, the point-spread-function, the effective area and energy dispersion of H.E.S.S. are generated from the simulated event list by checking which of the simulated events were recorded by H.E.S.S. and comparing the input energy and angular position of the simulated events with the reconstructed ones. After that, the background models are generated using the radial correction weights. To do this, the distribution of simulated events with

a reconstructed energy above a given threshold is generated for each individual run as illustrated on the left of figure 5.11. This distribution is then smoothed on a run-by-run basis with an Epanechnikov kernel with a bandwidth  $h$  of  $0.4^\circ$ , as illustrated on the right of figure 5.11, leading to a background model for each run. The Epanechnikov kernel, defined as (including the bandwidth  $h$ )

$$K(x) = \begin{cases} \frac{3}{4h} \left(1 - \frac{x^2}{h^2}\right), & \text{for } |x| \leq h \\ 0, & \text{otherwise,} \end{cases} \quad (5.3)$$

is the kernel which leads to the lowest asymptotic mean square error [159]. The background model is finally binned with a bin size of  $0.1^\circ \times 0.1^\circ$  and rescaled to match the expected background flux. The background models generated in this way obviously do not contain any energy information except for the minimum energy cut. This means that it is not possible to do any spectrum analysis with these background models. In principle, it would be possible to get energy-dependent background models by binning the events in energy when generating the background models, however this would require an adaptation of the radial corrections.

This background generation was tested again on OFF-runs taken on regions without any known H.E.S.S. source using a runlist completely independent from the one used for generating the radial corrections [157]. In this runlist, runs on seven fields of view with different observing conditions were included. After having verified that the generated background maps on the considered fields of view visually agree with the counts map from the taken data, the best-fit background normalization for the individual runs was computed (using the fitting procedure described in the following section) in order to look for a potential remaining correlation between the background normalization and the observation conditions. This best-fit background normalization is plotted as a function of the main observational parameters, namely the night sky background, the azimuth angle, the zenith angle, the right ascension and the declination in figure 5.12. One can see that overall, the remaining correlations are small, even though there are indications for a slight positive correlation for zenith angle and right ascension. However as runs on a given field of view are taken with almost the same right ascension and also mostly with a very similar zenith angle, such a small correlation is not worrisome. Another interesting point which is visible from these plots is that there is almost no correlation between the best-fit background normalization and night sky background. This is due to the night sky background being taken into account in the run-wise simulation and indicates that the background model generation from run-wise simulations is working as well in high night sky background regions than in low night sky background regions. However, the range of this plot does not exceed 100 MHz, which is due to there not being any higher night sky background region with no known source observed by H.E.S.S. and that it is the average night

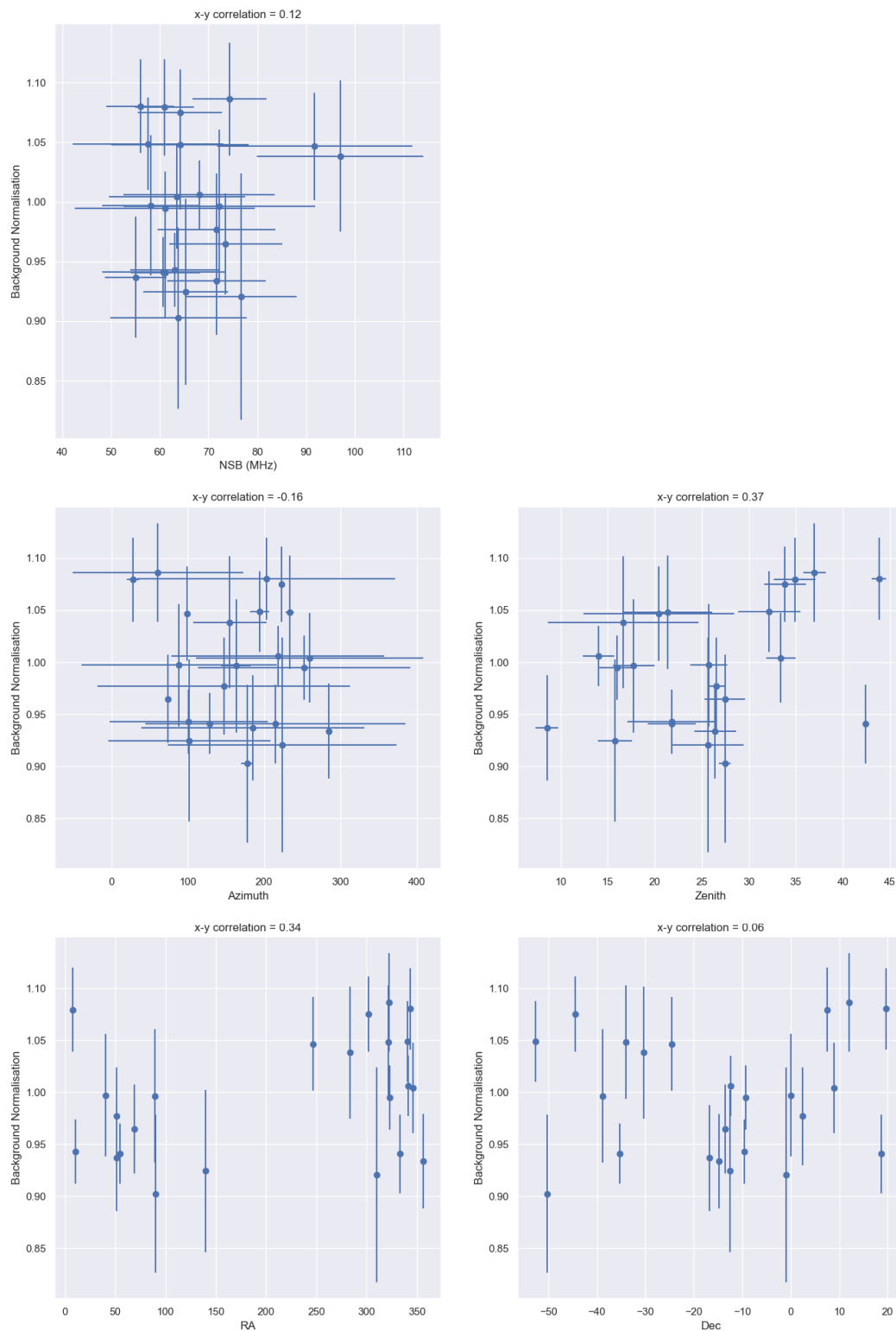


Figure 5.12: Best-fit background normalizations as a function of different observation parameters for different fields of view. The uncertainty bars indicate the population standard deviation of the values obtained from the different runs on the same field of view. Top: Background normalizations as a function of night sky background. Centre left: Background normalizations as a function of azimuth. Centre right: Background normalizations as a function of zenith. Bottom left: Background normalizations as a function of right ascension. Bottom right: Background normalizations as a function of declination. Reproduced from [157]

sky background over the whole region of interest, whereas in the LMC locally night sky backgrounds up to 200 MHz are reached. Such high night sky backgrounds are taken into account as well in the run-wise simulation and there is no indication for a steepening of the correlation on the plot in figure 5.12. These plots also illustrate the systematic uncertainty on the average background normalization predicted by the run-wise simulation for a given field of view. Indeed, the average offset from 1 of the best-fit normalization amounts up to 5%. As this offset also includes statistical uncertainties, the predicted average background normalization for a given field of view has a systematic uncertainty of less than 5% in average.

Afterwards, the systematic uncertainties on the background models generated with this procedure were assessed. For this, the systematic uncertainty determination method described section 6.2 was used, however here with a maximum offset of  $2^\circ$ . Four of the seven previously considered fields of view were used (the ones without any detection with *Fermi*-LAT and no hint for emission) and the systematic uncertainties were computed for them [157]. The average field-of-view systematics found with this method were of the level of 2%. However, on one of the fields of view values up to 3.1% were reached. No correlation between these systematic uncertainties and the night sky background could be found. This shows that systematic uncertainties, in average at the level of 2%, need to be taken into account and may exceed statistical uncertainties, especially in very deep exposure regions.

## 5.6 Analysis procedure

Once we have determined a good background model, one can start to search for large scale diffuse emission that would appear on top of this background. The idea is to determine simultaneously the parameters of all the different emission components in the region of interest using a likelihood fit to find the contribution of each model. The different components are the background, the known sources, the interstellar diffuse emission and the unresolved sources. I derived the background model from the previously presented run-wise simulations and masked the known sources as determining their properties was not the aim of this study. In this first stage for the search of interstellar diffuse emission, I followed a similar approach as Fermi in their LMC analysis I presented previously and tried to fit extended emission with Gaussian shaped components. In the presence of extended emission, diffuse emission can then be disentangled from unresolved sources using more complex models in the same likelihood fit at a later stage.

First, I selected the dataset for the analysis. The different selection criteria and the used datasets, which I discuss in more detail in section 6.1, led to selections of hundreds of runs which is much more than used in most H.E.S.S. analyses. This

is due to the expected interstellar diffuse emission being located in well observed galaxies with numerous interesting sources and the combination of data taken on different pointing positions to a common dataset which is not so common in gamma-ray observations. After the selection of the dataset, diffuse run-wise simulations are produced for all of the runs in the dataset. The simulated statistics were equivalent to 200 times the recorded Crab flux at 1 TeV. Then, I computed the radial correction weights and the IRFs for each run, and finally determined the background models.

At this stage, all the ingredients for the actual fit were ready. As a first step, I masked all the known sources with a mask of  $0.3^\circ$  radius and applied a maximum radial offset cut of  $2^\circ$  around the pointing position for each run as the performance of the radial corrections rapidly degrade for larger offsets. Then, I defined the Gaussian components to be added to the fit. These Gaussian components are supposed to represent the emission morphology and I folded them as such with the IRFs and the exposure to obtain the predicted counts map in the fitting procedure. As mentioned before, there is no energy information in the background models and so no spectrum information can be derived. For this reason, I fixed the photon indices of the Gaussian components to 2. This left me with four remaining parameters to be fit for each component: the centre (two angular position coordinates), the angular extension and the amplitude. In addition to these Gaussian components, one run-wise background model per run was part of the fit. The shape of these background models was fixed, however the normalizations of the background models were left free, adding one additional parameter per run to the fit. This led to the number of free parameters in the fit being the number of runs plus four additional parameters per Gaussian component.

I performed tests trying to fit all these parameters simultaneously in a global likelihood fit, however as expected the fit became non-converging fast when adding more than a hundred of observation runs. This is on the one hand due to the sheer number of parameters in the fit, but on the other hand potentially also to a certain amount of degeneracy in the fit. Indeed, for runs taken at exactly the same observation position, the background models are expected, even though being not exactly the same due to different observation conditions (which is the reason for the use of run-wise simulations), to be similar. This possibly leads to a certain level of degeneracy between the background normalizations of runs taken at the same (or even at close) observation position(s). In order to include all the runs (passing selection criteria) taken on a source to have the highest possible sensitivity an adaptation of the fitting procedure was necessary. The best option seemed to go for an iterative fitting procedure, in which I did not determine all model parameters simultaneously anymore. Instead, I adjusted different parameters successively in different fit iterations. This implies that some correlation between the parameters

of the different models were not correctly taken into account when determining the best-fit parameters.

The implemented iterative fitting procedure consists of two steps. In the first step, I adjusted the background normalizations alone, without including any Gaussian components for extended emission on a run-by-run basis. Then, I fixed the background normalizations to the fit values for the individual runs and stacked the counts maps, exposure maps, instrument response functions and background models with fixed normalizations of the different runs to one common dataset including all runs. In a second step, I fit this common dataset with the previously obtained background model. In this iteration, the free parameters are the overall background normalization and the parameters of the Gaussian components.

Instead of one big fit with hundreds of parameters, this iterative method leads to many small fits with all of them one parameter (the background normalization of the considered run) except the last one which has one parameter for the overall background normalization and four additional parameters per Gaussian. This comes at the expense of not fitting all parameters simultaneously anymore. Indeed, in the first step the background normalizations are fit without any extended model, which leads to an over-estimation of the background if there is substantial extended emission. This is partially counterbalanced by leaving the overall background normalization in the final fit free, but if there is a local component, this can of course not be completely accounted for by reducing the background normalization over the whole region of interest. Fitting the background normalizations over the whole region of interest (except for the masked sources) tends to underestimate the contribution of extended emission if it spans a big part of the H.E.S.S. field of view and to overestimate the background normalization of the runs taken in its direction. This method is called *Method B* in order to distinguish it from the methods introduced in the following and summarized in table 5.1.

However, the background models generated from the run-wise simulations do not only deliver a prediction of the background shape, but also a prediction of the background normalization. The systematic uncertainties on these background predictions amount to less than 5%, as discussed in the previous section. So, one could try to use background normalizations produced by run-wise simulations. This would avoid the potential overestimation caused by a local diffuse component, but has the disadvantage that any systematic over- or underestimation of the background over a given field of view is accumulated over the runs taken on this field of view and might lead to significant differences, especially in the very deep exposure fields I consider in this study. This method is called *Method A* in the following.

An alternate approach would be to fit the background normalizations while excluding any regions with excesses or deficits. A definition of exclusion regions

based on physical arguments seems however difficult for LMC, as the emission seen by *Fermi*-LAT is very extended (compared to the H.E.S.S. field of view), and there are also no other a priori reasons why not the entire LMC should be filled with diffuse emission. For this reason, I chose a data driven approach: subtracting the background models directly from the observed data without refitting the normalizations can deliver a prediction for regions with excesses or deficits on the basis of which exclusion regions can be defined. I used two different methods to define these exclusion regions in this study. First of all, I based the exclusions on the Li & Ma significance map (computed as described in section 2.5.3) produced using a top-hat convolution kernel with a size of 3 pixels of  $0.1^\circ$  side length, such as the ones which will be shown for the systematic studies in figure 6.9. Then, I excluded everything above  $2\sigma$  or below  $-2\sigma$  in order to exclude excesses and deficits symmetrically. I voluntarily selected a low threshold in order to reduce the impact of physical excesses as much as possible. This low threshold also cuts off part of the statistical fluctuations, however as the significance distribution generated by statistical fluctuations is symmetric, this does not have an impact on the fit background normalizations - beside the impact of the systematic uncertainty in the initial background normalization used to define the exclusion regions whose impact is discussed at the end of this paragraph. This allows then to refit the background normalizations only based on regions without any significant excess or deficit. It is however based on the significance of an excess or a deficit and so the definition of these regions strongly depends on the exposure accumulated on a given region beyond statistical uncertainties. Indeed, the more exposure is accumulated on a physical excess, the more significant it becomes. For this reason, a second method to define the exclusion regions using an exposure independent definition (except for statistical variations) was used. In this method, the residuals over background are used as direct qualification for the systematics level (or a signal beyond systematics level) and everything above 6.5% or below -6.5% is excluded. This value was picked as it leads to similar exclusions as the significance criterion in galactic regions at deep exposure. This way of defining the exclusion regions might be problematic in local very high exposure regions, where a very significant signal does not pass the residuals over background threshold and is removed by the fit background normalizations, however one can avoid this by checking the remaining maximum significance. After having defined these additional exclusion regions (beyond the masked sources), I adjusted the background normalizations on the remaining of the region of interest. To make sure that there are still enough events in each run to determine the background normalizations, I verified that each run had at least 40 event counts outside of the exclusion region in the background model (of the about 800 to 1000 total counts in the background model depending on zenith angle) leading to a statistical uncertainty of about maximum

Method	Background normalizations	+ / -
<i>A</i>	Directly from run-wise simulations	+ No overestimation due to Diffuse - Systematics of bkg accumulated
<i>B</i>	Fit over whole region of interest (except known H.E.S.S. sources)	+ Bkg norms fully from data - Overestimation due to Diffuse
<i>C</i>	Fit using exclusion regions based on significance	o Impact of diffuse reduced o Bkg norm systematics reduced - Depends on observation time
<i>D</i>	Fit using exclusion regions based on residuals over bkg	o Impact of diffuse reduced o Bkg norm systematics reduced + Independent of observation time beside fluctuations

Table 5.1: Summary of the used methods to determine the relative background normalizations in the first step of the iterative fitting procedure. The first column indicates the method, the second column the way the background normalizations were determined and the third column gives some of the advantages and disadvantages of the method.

15 % for the individual runs assuming a Poisson distribution (leading to an overall statistical uncertainty of about 1 % when combining 200 runs under the unrealistic assumption that all of them have only 40 surviving counts). This was the case for the runs which I selected for the analysis. The method using exclusion regions based on significances will be called *Method C* in the following and the one using exclusion regions based on residuals over background *Method D*. However, even when using the normalizations predicted by the run-wise simulations to determine the exclusion region (as in *Method C* and *D*), the exact shape of this exclusion region depends on the normalization obtained from the simulation and so an over- or underestimation of this normalization leads to a stronger cut on negative (respectively positive) values and so to an over- (respectively under-)estimation of the fit background normalizations, even though the effect is much smaller than in *Method A* where the background normalizations from the run-wise simulation are directly without doing any adjustment. So, *Methods C* and *D* rely on a good prediction of the background normalization from the run-wise simulations too.

This then leads to four different methods to determine the background normalizations in the first step of the two-step iterative fitting procedure:

- In *Method A*, I use directly the background normalizations from the run-wise simulations.
- In *Method B*, I fit the background normalizations over the whole region of

interest (except for the known H.E.S.S. sources) on a run-by-run basis.

- In *Method C*, I fit the background normalizations using exclusion regions based on significance.
- In *Method D*, I fit the background normalizations using exclusion regions based on significance and fitting the background normalizations using exclusion regions based on residuals over background.

All these four methods are summarized again in table 5.1 to have a quick overview of the methods. As each of these four methods has its advantages and disadvantages as discussed before, all four methods have been investigated in this study. After this first step, I fit the overall background normalization together with a given number of diffuse components on a stacked dataset with the relative background normalizations fixed.

As discussed before, I perform these fits using a maximum likelihood fit. So similar to the Fermi analysis presented previously, it is possible to define a test statistic to compare different models fit to the same dataset. The difference in test statistic  $\Delta TS$  is defined as:

$$\Delta TS = 2(\ln(L_1) - \ln(L_2)), \quad (5.4)$$

where  $L_1$  and  $L_2$  are the maximum likelihoods of the two models to be compared.

## 5.7 The advantage of the run-wise method for the analysis of extended sources

Comparing this novel run-wise-simulation-based background and acceptance determination method to the more standard methods discussed in section 5.3, one can immediately see the advantages it has in the search for extended emission, in particular in regions in which there might be a high night sky background. First of all, the method does not rely on the definition of a control region for the background determination as the background is directly obtained from simulation. This opens the possibility to investigate emission covering the whole field of view of H.E.S.S. or extending even further, even though the possible need to adjust the background normalization of the individual runs in the run-wise method is still problematic as this might lead to an over-estimation of the background. Second, the template background methods developed so far, among other to avoid this kind of problems, all rely on some sort of acceptance calculation. This acceptance was mostly obtained using the radial or the 2D acceptance method. All of these

methods have the problem that they smear out, or do not take completely into account, field of view dependent changes in the acceptance. The run-wise simulation method avoids this by generating the acceptance from the simulation which should encompass field of view dependent changes of the acceptance.

However, all these optimizations come at some costs. Beside the normalization issue discussed before, the generation of the background model and the acceptance relies on the simulation of gamma rays. This relies on two assumptions: first that the simulated gamma rays represent real gamma rays well enough, i.e., that the simulation is realistic, and second that gamma-like events are gamma-like enough to be represented by true gamma rays, modulo the corrections discussed in section 5.5. That these assumptions are well justified has been shown in the same section by looking at OFF-runs and showing that using the run-wise simulation-based background models for the background subtraction on empty fields leads only to background systematics of 2% in average. This shows that this background subtraction method works and so that simulated gamma rays describe the gamma-like background well enough for the background subtraction to work within the given systematic uncertainties.

# Chapter 6

## Interstellar diffuse emission in the Large Magellanic Cloud

After having discussed a novel run-wise simulation and template fitting based analysis method well suited in the search for extended emission in the previous chapter, this chapter discusses its application to interstellar diffuse emission in the Large Magellanic Cloud. Beside the main target, the Large Magellanic Cloud, I introduce the Small Magellanic Cloud as second potential target for the search for interstellar diffuse emission. Additionally, I use deep-exposure targets without any expected significant extended emission, namely Centaurus A and NGC 253 for a further qualification of systematic uncertainties.

I start this chapter by describing the used regions of interest and data in detail and discuss the motivation for their selection. Then, I describe the systematics studies performed for the validation of the method at deep exposure performed on Centaurus A and NGC 253. Finally, I discuss the analysis results obtained on the LMC and SMC and possible physical interpretations for the excess seen in the LMC. A comparison of the results obtained on the LMC using this novel analysis method and a standard ring background subtraction method can be found in appendix B.

### 6.1 Characterization and particularities of the used datasets

The main region of interest in this analysis was the Large Magellanic Cloud from which extended emission is expected. An additional region of interest is the Small Magellanic Cloud in which interstellar diffuse emission is also expected, even though at a lower level, and less extended than in the LMC. This dataset is therefore included in the present analysis. Both of these galaxies are extensively

described in section 5.2. In addition, two other regions are used in this analysis: Centaurus A and NGC 253. Centaurus A (Cen A) is an active galactic nucleus in an elliptic galaxy called NGC 5128 and it has been first seen with H.E.S.S. in 2009 [160]. Jets from this source have been detected in radio and X-ray and the source itself in the 90s in MeV and GeV energies by CGRO. In 2020, H.E.S.S. could also show that the very-high-energy emission is extended on very small scales and so that it can resolve the inner jet [161]. NGC 253 is a so-called starburst galaxy, i.e., a galaxy in which there is star formation in a very localized region with a very high gas density, usually in the centre of the galaxy [52]. This very high-density gas also leads to a high supernova explosion rate and so to the acceleration of cosmic rays and subsequently gamma rays. It has been first detected by H.E.S.S. in 2009 [162]. The idea of these last two datasets was to use them as an additional cross check of the method and an additional handle to systematic uncertainties in deep exposure datasets from regions without expected extended emission. For this systematic study, regions in which there are no sources would have been preferable, however deep exposure datasets are necessary to assess systematics which might be hidden by statistical variations in lower exposure datasets. Yet, due to the limited available observation time, it is not viable to observe empty sky for hundreds of hours with H.E.S.S. and observations of detected sources where deep observations were undertaken had to be used for this systematic study. For this reason, Cen A and NGC 253 were selected for this systematic study as both of them have been deeply observed, they are not in a crowded field with numerous sources and are not expected to have strong very extended emission at H.E.S.S. sensitive energies, even though some emission from the jets cannot be excluded for Cen A.

As discussed in chapter 2, the H.E.S.S. telescope array has undergone multiple hardware changes over its almost 20 years of operation. It started as a four-telescope system to which a larger fifth telescope was added in 2012. In addition, the cameras of these two different telescope types have both been changed at different times (2014 and 2019), leading to four different phases of H.E.S.S. operation with different hardware configurations. Additionally, there are observations in which not all telescopes participate, mostly due to unavailabilities of one or more telescopes due to technical problems or because observation goals can be best achieved with one particular telescope type (the larger CT5 telescope is for example best suited for low energy observations). This leads to even more different configurations in which H.E.S.S. data has been taken. Differences between the behaviour of run-wise simulations and observation background would in principle needed to be checked for all of these configurations and different zenith angle and radial correction models would have to be generated for each of them. In addition, each of them might introduce its own systematic uncertainties. For this reason, I

performed the very first analysis using this novel method using only one telescope and camera configuration: I used only runs taken with exactly the four HESS-I telescopes with their initial cameras, which comprises most of the data taken on the regions of interest between 2003 and 2012 and most of the data between 2012 and 2015 taken without CT5.

In addition to this configuration-based selection, I applied quality cuts to the data in order to select runs taken under good sky conditions and without technical problems that cannot be reproduced by the run-wise simulation. These quality cuts are applied on a run-by-run basis within H.E.S.S., so no runs are partially accepted. These cuts which are here discussed in more detail are summarized in table 6.1. First of all, the H.E.S.S. quality cuts for standard HESS-I analyses were applied. These standard cuts consist first of all of a minimum run duration of 5 min to have a sensible number of events in the run and a maximum duration of 100 min. Then, there are limits on the array trigger rate and their stability as well as on the individual telescope trigger rate stability as unexpected trigger rates are a strong indication for problematic runs: A too low trigger rate often indicates bad meteorological conditions leading to fewer recorded events, a too high trigger rates means that there are more events than expected indicating that H.E.S.S. is not only triggering on the expected cosmic events but might be strongly impacted by parasitic light sources. Instabilities in the trigger rate might be an indication for clouds moving in and out. In addition to this trigger rate problems being an indication for bad meteorological conditions, they might also be due to technical problems in one or several of the telescopes or the array system. Then, the meteorological conditions at the H.E.S.S. site are constantly monitored with radiometers mounted on each of the HESS-I telescopes which give an indication for cloud coverage and a relative humidity detector. Cuts are also applied on these measurements to avoid a too high cloud coverage or a too high humidity. Then, runs are rejected if the measured star positions (through night sky background) do not match the expected ones as this is an indication for mis-pointings or if there are more than 15 % of broken pixels in at least two telescopes. In addition to these standard cuts, additional cuts adapted to this run-wise analysis method were defined. The minimum run duration was increased to 20 min to have a high enough event statistics in each run to properly fit the background normalizations. Then, the requirements on the radiometer were increased from one to three telescopes to make sure the meteorological conditions are good and there are no clouds moving in the field of view of only some telescopes as run-wise simulations cannot reproduce covered sky whose impact cannot be solely described by the radiometer values. Limits are not only imposed anymore on the array trigger rate but also on the telescope trigger rate and a limit on the transparency coefficient is set again to ensure good atmospheric quality. As discussed before, two different radial correction models

Cut variable	Selection cut
Telescope configuration	Exactly 4 HESS-I telescopes
Camera configuration	Initial HESS-I cameras
Run duration	20 min to 100 min
Central Trigger	
Zenith angle corrected trigger rate	100 Hz to 600 Hz
Trigger stability	$\leq 10\%$
2-fold live time fraction	$\geq 80\%$
Individual Telescope Triggers (fulfilled in $\geq 3$ telescopes)	
Zenith angle corrected telescope trigger rate	100 Hz to 300 Hz
Telescope trigger stability	$\leq 10\%$
Dead time fraction	$\leq 15\%$
Radiometer conditions (fulfilled in $\geq 3$ telescopes)	
Radiometer status	Working properly
Radiometer temperature	$-999\text{ }^{\circ}\text{C}$ to $-20\text{ }^{\circ}\text{C}$
Radiometer stability	$\leq 3\text{ }^{\circ}\text{C}$ RMS
Relative humidity	$\leq 90\%$
Transparency coefficient	$\geq 0.8$
Indication for mispointings from stars in the field of view (fulfilled in $\geq 3$ telescopes if stars are in the field of view)	
Displacement of stars from nominal position	
in x-direction	$-100''$ to $100''$
in y-direction	$-100''$ to $100''$
Rotation of stars with respect to nominal positions	$-10^{\circ}$ to $10^{\circ}$
Broken pixel fraction (in $\geq 3$ telescopes)	$\leq 15\%$
Zenith angle range	
Cen A & NGC 253	$5^{\circ}$ to $40^{\circ}$
LMC & SMC (all runs fulfilling cut)	$40^{\circ}$ to $60^{\circ}$

Table 6.1: This table shows a summary of all the selection cuts used for the selection of runs used in the diffuse analysis.

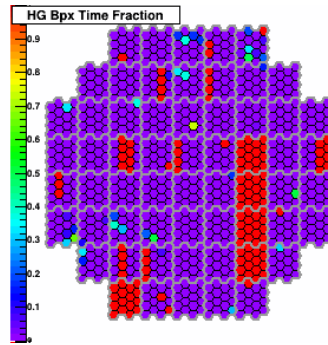


Figure 6.1: Example of multiple adjacent broken drawers making part of a camera participating in a given run non-operational and so to events hitting this part of the cameras not to be recorded. These runs have been excluded for this reason.

were used, one valid for zenith angle below  $40^\circ$  and one for zenith angles between  $40^\circ$  and  $60^\circ$ . As the Magellanic Clouds can only be observed at high zenith angles due to their position on the sky, I used the high zenith angle models for those sources. On the other hand, Cen A and NGC 253 can be observed at lower zenith angle and as lower zenith angle observations are preferred due to the lower impact of atmospheric absorption, they have been mostly observed at lower zenith angle. For this reason, I had to use the high zenith angle radial corrections for these two sources and set a maximum zenith angle cut of  $40^\circ$  to exclude the very few runs of Cen A taken at higher zenith angle (which were not numerous enough to allow for an own analysis at high zenith angle). That the datasets used for the systematic study use a different radial correction model than the dataset in which extended emission is searched for is not optimal as the radial correction model might also introduce its own systematic uncertainties which are not the same for the different models due to their difference in zenith angle<sup>1</sup>. This is however unavoidable since no other sources at high zenith angle have been observed as deeply as LMC and SMC. In addition to these zenith angle cuts an additional minimum zenith angle cut of  $5^\circ$  has been set, because the background models are so far generated for the run-averaged azimuth angle and the azimuth varies too fast for runs taken close to azimuth.

Even though defining this run selection criteria allows to exclude problematic runs, not all problems within a run can be completely automatically detected. Among other, accumulations of multiple broken pixels (or rather of multiple drawers of broken pixels) can be problematic as this leads to a whole part of the camera being unusable and so events hitting that part of the camera not being detected

<sup>1</sup>It is worth to note that this would persist even using only one radial correction model, as it would still not be possible to test it at deep exposure at high zenith angle with the Cen A and NGC 253 data.

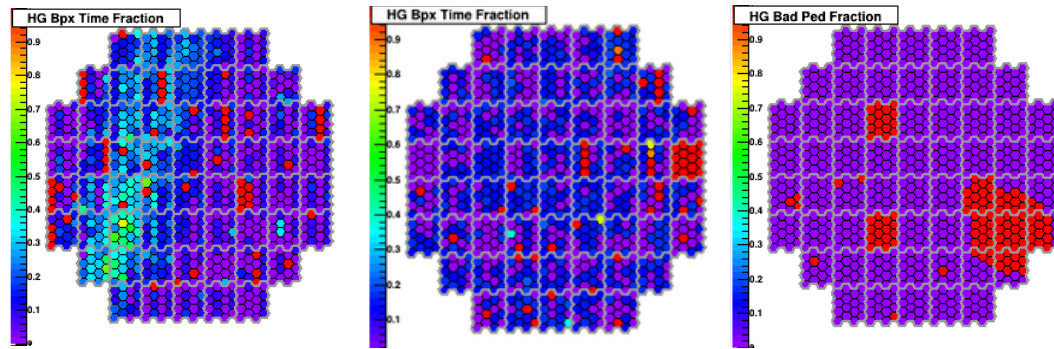


Figure 6.2: Different patterns on the broken pixel and bad pedestal displays observed in one camera in single runs which led to the exclusion of the respective runs.

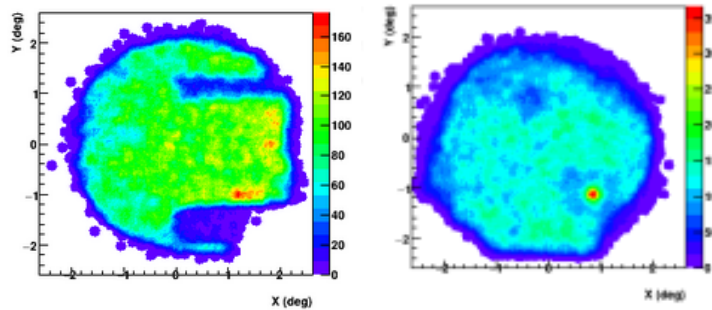


Figure 6.3: Examples of runs excluded due to pathological centre of gravity maps. Left: Deficit of events from two line-like regions in the sky. Right: Hotspot at the edge of the centre of gravity map.

whereas the same number of broken pixels distributed more regularly over the camera would be less problematic. For this reason, runs which had multiple adjacent broken drawers in one of the cameras, as was for example the case for the run shown in figure 6.1, have been excluded based on manual inspection. Other runs showed pattern on the broken pixel or the bad pedestal display in one of the cameras as illustrated in figure 6.2. These runs as well as one run for which the pedestal was bad in one whole camera were excluded too.

In addition to the broken pixel and bad pedestal displays, the so-called centre of gravity maps, which show the distribution of the centre of gravity of all the individual events in a given run in a 2D plot, can deliver hints to calibration issues. They can be both produced in the camera frame and as a projection on the sky, which is the one I am interested in here. The left of figure 6.3 shows such a centre of gravity map. One can see that it is mostly radially symmetric, except for two lines which much fewer events, meaning that there are two lines on the

	Number of selected runs	Exposure accumulated around	Masked known sources
LMC	230	Mostly around the central position of the map, i.e., around the region of SN1987A, N 157B and 30 Dor C Some exposure accumulated further away from this position	N 157B, 30 Dor C, N 132D & LMC P3
SMC	42	Three different pointings across SMC	No known H.E.S.S. sources in SMC
Cen A	349	All runs centred on Cen A except comparatively small wobble offset	Cen A & 1ES 1312-423, a blazar
NGC 253	237	Centred on NGC 253 except wobble offset	NGC 253

Table 6.2: Number of selected runs, description of region around which exposure is accumulated and known H.E.S.S. sources which have been masked for the four considered datasets.

sky from where much fewer events have been recorded. These lines are usually due to broken pixels, however no broken pixels have been detected at the relevant position in the camera and this might be an indication that not all broken pixels have been detected automatically. Nonetheless, this feature is highly problematic as it means that there are missing events from some directions of the sky and for this reason the runs showing it have been excluded. Other runs show a hotspot in the centre of gravity maps of one camera as illustrated on the right of figure 6.3. This might indicate a noisy pixel recording too high intensities and so dragging the centre of gravity to its position. For this reason, these runs have also been excluded.

These were all the problems which could be identified by manual investigation at the calibration plots of the individual runs and so all the other runs passing the selection criteria defined before were retained for the main analysis.

The number of retained runs applying the selection criteria discussed above, the region around which the exposure has been accumulated, and the known H.E.S.S. sources (which are not included in the analysis and have been masked with a mask of radius  $0.3^\circ$  as described in section 5.6) are discussed in table 6.2. The total accumulated exposure in these runs and the disposition of the masks to mask the known sources is shown in figure 6.4. No plot showing the masks for the SMC is shown as there are no masks in the SMC region of interest due to the absence of

	LMC	SMC	Cen A	NGC 253
Total number of runs on source	1629	918	766	587
Total number of 4-telescope HESS-I runs	474	239	477	481
Total number of 4-telescope HESS-I runs fulfilling standard cuts	382	166	428	426
Number of runs failing:				
Minimum run duration cut	22	12	26	29
Minimum radiometer stability cut	13	2	6	2
Minimum transparency coefficient cut	0	30	6	35
Corrected telescope trigger rate cut	113	80	7	52
Zenith angle cut	0	0	12	66
Manual inspection	4	0	22	5
Remaining runs	230	42	349	237

Table 6.3: Table summarising the total number of runs taken on a target, the number of four-telescope runs taken in the HESS-I era on a target and the number of these runs fulfilling the standard cuts for the four regions of interest. Then, the number of runs failing each additional cut and the number of runs failing manual inspection are indicated, and finally the remaining number of runs after selection for each dataset.

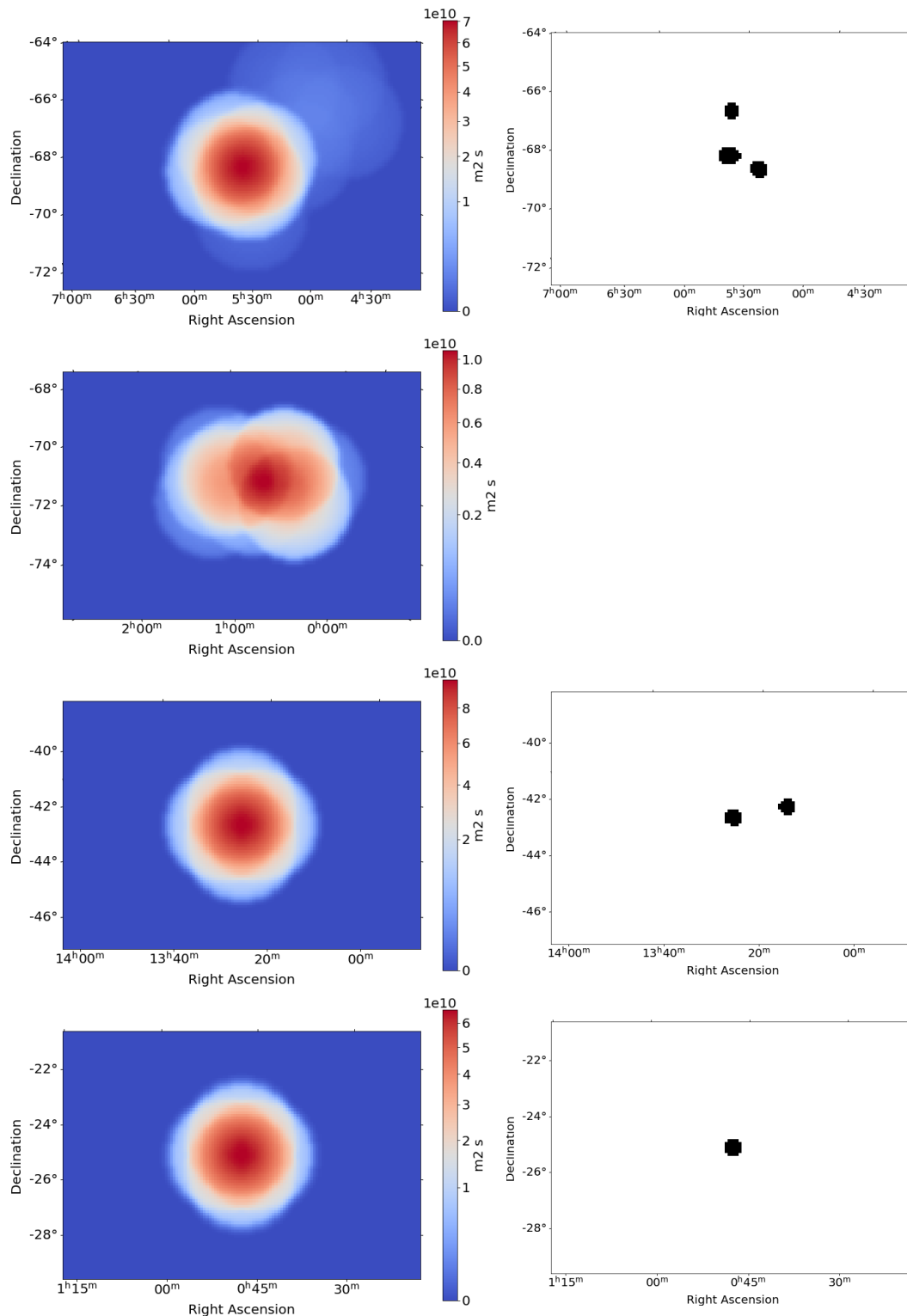


Figure 6.4: Total exposure and disposition of the masks to mask the known sources for the different datasets. **Top:** LMC. Left: Total exposure of the 230 used runs. Right: Disposition of the masks. The 4 known sources N 157B, 30 Dor C, N 132D and LMC P3 are masked even though there are only 3 masks which is due to N 157B and 30 Dor C being so close that they are behind one big mask. **2<sup>nd</sup> line:** SMC. Total exposure of the 42 used runs. As there are no known sources for SMC, no masks have been defined for the SMC dataset. **3<sup>rd</sup> line:** Cen A. Left: Total exposure of the 349 used runs. Right: Disposition of the masks. The 2 known sources Cen A and 1ES 1312-423 are masked. **4<sup>th</sup> line:** NGC 253. Left: Total exposure of the 237 used runs. Right: The mask masking NGC 253, only known source in the region of interest.

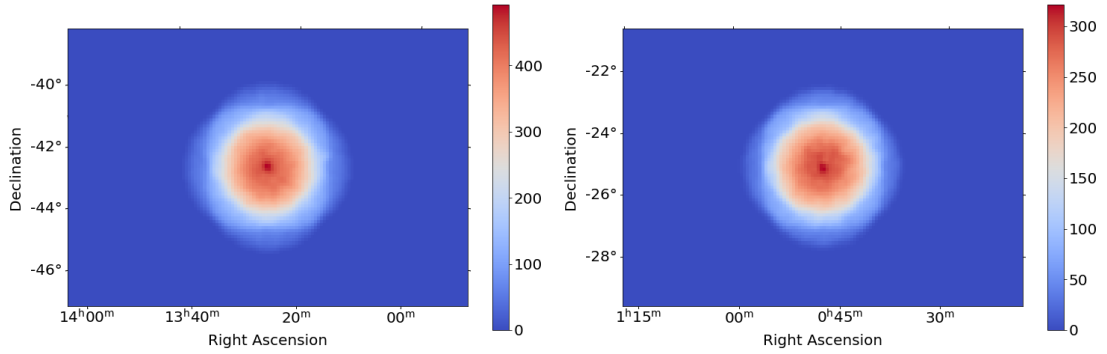


Figure 6.5: Counts maps of Cen A (left) and NGC 253 (right). The colour scale indicates the number of counts in each bin.

any known source.

The effect of the different cuts as well as the restriction to four-telescope runs taken with the initial HESS-I cameras is illustrated in table 6.3. The first thing to note is that only 29% of the runs taken on the LMC have the right camera configuration and that adapting the procedure to other camera configurations would lead to a big increase in statistics. This increase in statistics will even grow as H.E.S.S. is still taking data on the LMC with the current camera configuration. However, as mentioned earlier, for this first analysis of LMC data with this novel method, only one camera configuration was used in order to reduce systematic uncertainties. Secondly, the cuts used in this analysis are rather strict to have a good control over the systematics. For LMC for instance, only 49% of the runs survive the quality cuts, however, 19% are already removed by standard cuts. For NGC 253, the picture is similar whereas for Cen A 73% of the runs survive the run selection. The situation looks particularly bad for SMC, where only 18% of the runs survive cuts (however 31% of the runs are already removed by the standard selection). This might be due to the runs on SMC having been taken under worse weather conditions than usual. In order to increase statistics an adaptation of the cuts and a study on how this impacts systematic uncertainties would be necessary. As the main focus of this work is however on LMC, I did not do this to keep the systematics on this source as low as possible and not to have different event selections for different regions of interest.

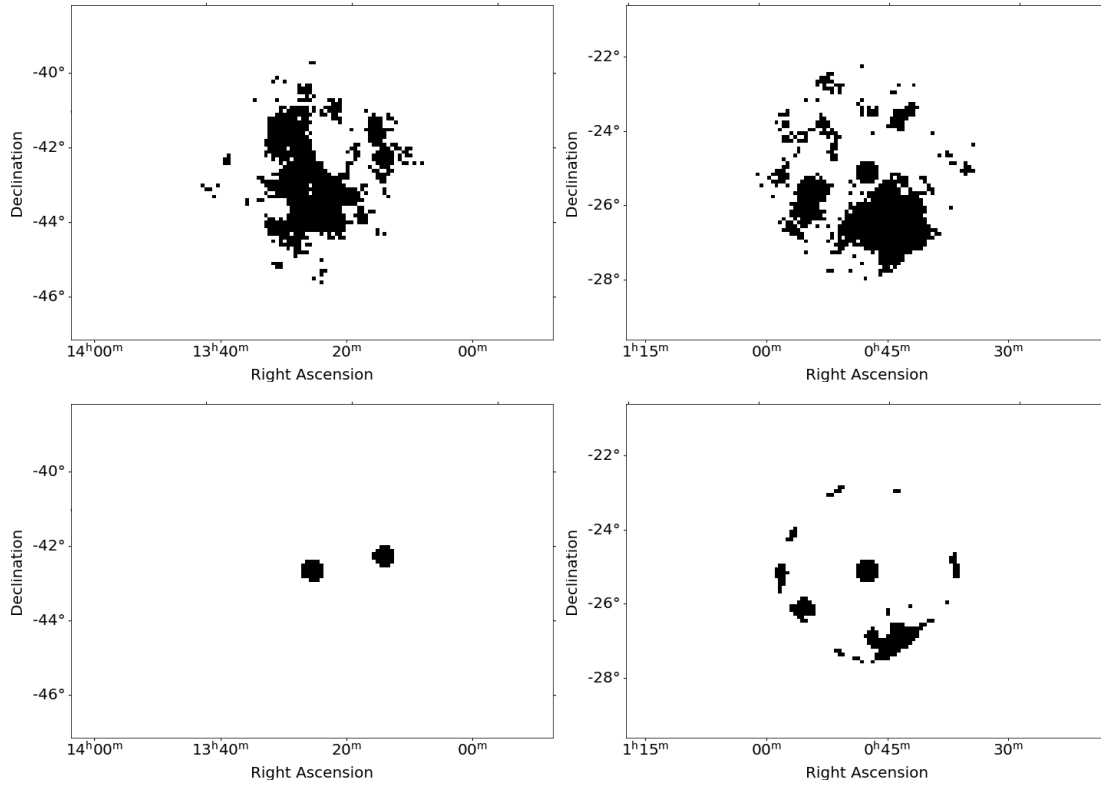


Figure 6.6: Exclusion regions defined in the different background subtraction procedures. Top left: Cen A, *Method C*. Top right: NGC 253, *Method C*. Bottom left: Cen A, *Method D*. Bottom right: NGC 253, *Method D*.

## 6.2 Systematics study on sources without any expected extended emission

As discussed in the previous section, the Cen A and NGC 253 datasets were used for a further assessment of the systematic uncertainties of the novel method used in this work in deep exposure datasets. The counts map obtained for both of these sources on the dataset described in the previous subsection are shown in figure 6.5. Both counts maps follow very much the exposure maps as would be expected for a background-only observation. The exceptions to this are the known central sources Cen A and NGC 253 which are clearly visible on the centre of the counts map as much more counts are recorded from their direction than would be expected from a background-only contribution. 1ES 1312-423, which is in a much lower exposure region for the selected dataset, on the other hand cannot be seen directly on the Cen A counts map.

Then, I applied the four different background subtraction procedures described in section 5.6, so once I directly subtracted the background models created from the run-wise simulations (with just refitting the overall background normalization and keeping the relative normalizations between runs constant) (*Method A*) and three times I refit and then subtracted the background normalizations of each individual run, once over the whole region of interest (*Method B*), once using significance-based exclusion regions (*Method C*) and once using residuals over background-based exclusion regions (*Method D*) as summarized in table 5.1. The exclusion masks used to fit the background normalizations for the two later background subtraction methods can be seen in figure 6.6. One can see that whereas the exclusion regions in *Method C* exclude a big part of the two regions of interest, the exclusion regions in *Method D* exclude nothing for Cen A (one can only see the two masked sources) and some parts of the edge of the region of interest for NGC 253. As there are no additional masks for this background subtraction method for Cen A, it leads to exactly the same results as *Method B* and for this reason, for Cen A only the results for the three other background subtraction methods are shown in the following. Concerning *Method C*, even though a big part of the region of interest is excluded, there is also still an ample part not excluded, and so none of the runs was problematic concerning the remaining number of events to determine the background normalizations.

The residual maps after background subtraction for *Method A* and *Method B* are shown for both sources in figure 6.7. One can see that most of the counts which can be seen on the Counts maps in figure 6.5 can be attributed to the background model as the range of the colour scale (indicating the difference in the number of counts from different parts of the region of interest) is reduced by an order of magnitude. The remaining residuals are extremely similar for the four different background subtraction methods for Cen A as well as for NGC 253, and any difference can hardly be seen by eye. This is illustrated here for two of the methods. I do not show the other methods due to the similarity of the residual maps and so I only show the two methods with the most different residual maps. This shows that the relative normalizations are very well predicted by the run-wise simulations after applying the zenith and radial corrections, so that a refitting of these relative normalizations does not lead to a sensible difference in the residuals.

This leads to the question how close to 1 the individual fit relative and the overall background normalizations are for the four methods. For *Method A*, the fit overall normalization was 1.02 for Cen A and 0.98 for NGC 253, showing that the predicted overall background normalization is off by only 2% for both of these sources. The background normalizations fit on a run-by-run basis for *Method B* are shown on the top of figure 6.8. If the spread in this background normalizations between individual runs only comes from statistical variations (which is a rough

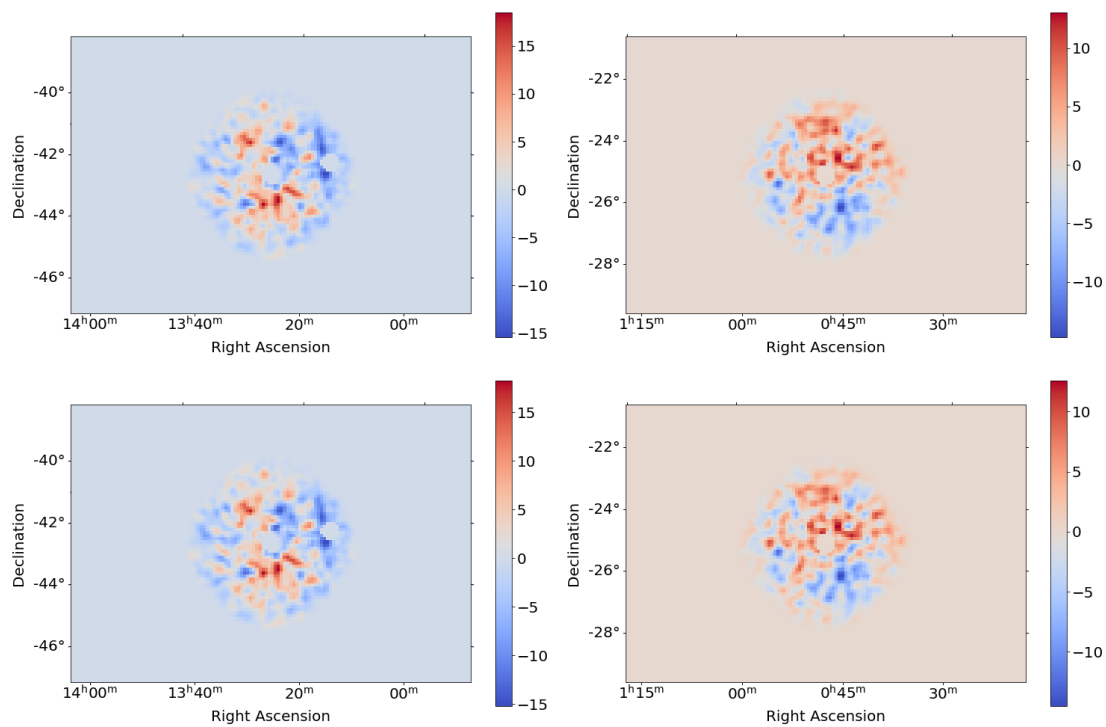


Figure 6.7: Residual maps after background subtraction with masked sources. The colour scale indicates the number of counts in each bin. Top left: Cen A using *Method A*. Top right: NGC 253 using *Method A*. Bottom left: Cen A using *Method B*. Bottom right: Cen A using *Method B*.

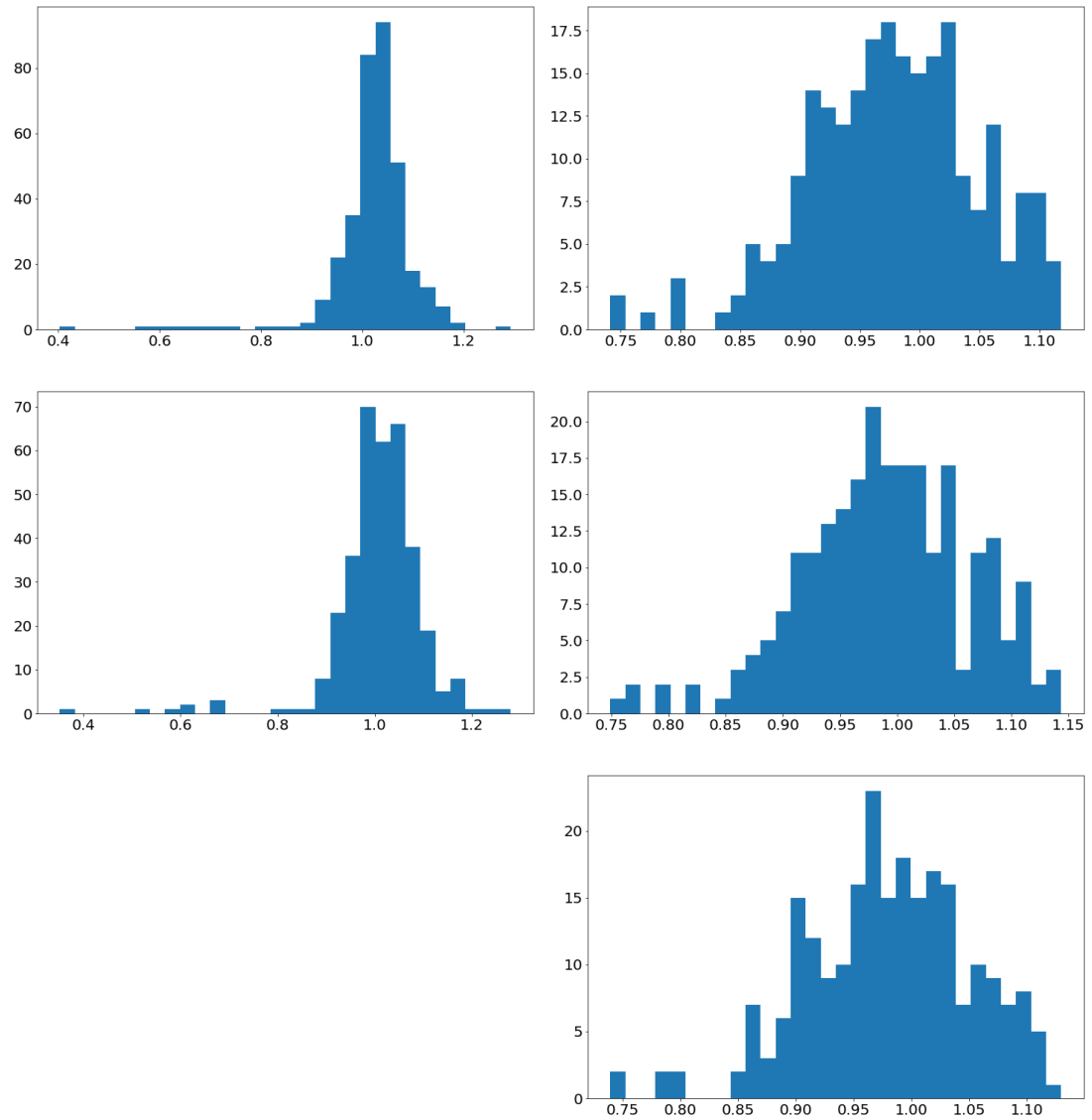


Figure 6.8: Fit background normalizations (on a run-by-run basis) of Cen A (left) and NGC 253 (right). Top: *Method B*. Centre: *Method C*. Bottom: *Method D*. Please note the different scale due to the low background normalization tail of Cen A.

simplification, there are indeed many systematics involved as discussed later on), one would expect them to follow a Gaussian distribution. Fitting a Gaussian to these background normalizations leads to a Gaussian with an average value of 1.02 and 0.98 for Cen A and NGC 253 respectively and standard deviation of 0.08 and 0.07 respectively. Whereas for NGC 253, all the normalizations are close to the central values, the distribution of Cen A has a large tail due to few individual runs with comparatively very low normalization. A closer investigation on these runs looking again at the calibration diagnostics, recorded meteorological conditions and array parameters did not show any particularities. As there is no a priori reason to exclude these runs and the influence of this low number of runs on the final result is very small, these runs were kept in the analysis even though the best-fit background normalizations seem to be off from the run-wise prediction. The best-fit background normalizations using *Method C* and *D* shown on the bottom of figure 6.8 are similar to the ones fit over the entire field of view and the tail in the distribution for Cen A is present here to. The only minor difference in the distribution is that using *Method C* the average fit background normalization is a bit closer to 1 being 1.01 for Cen A and 0.99 for NGC 253, whereas the standard deviation is still very similar to before with 0.09 and 0.07 respectively. Using *Method D*, there is no difference for Cen A as this adds nothing to the exclusion regions and also for NGC 253, the average and the standard deviation of the distribution are the same (within the 3 significant figures used here) than without exclusion regions as could have been expected from the very small additional exclusion regions at the edge. This shows that for all the methods for both sources, the average best-fit background normalizations only differ by 2% from 1 and have a small spread. In addition, it also shows that the results do not depend a lot on the used method in the absence of any excess.

Having discussed the background normalizations, let us come back to the analysis results using the four background subtraction methods. The significance maps after this background subtraction, computed using the Li & Ma significance calculation presented in subsection 2.5.3 with a top-hat convolution kernel with a size of 3 pixels (each pixel having a side length of  $0.1^\circ$ ), are shown for both sources in figure 6.9. Overall, the significance maps show a very good agreement and the differences discussed in the following are only minor. For *Method A*, the Cen A map seems to tend more towards positive significances whereas the NGC 253 map seems to tend more towards negative significances, as would have been expected from the fit background normalizations. On the Cen A map, there seems to be a non-significant excess which agrees well with the orientation of the jet whereas there is a deficit in the NGC 253 map in which goes below  $-5$  sigma. However, these Li & Ma significance maps computed significances assume only statistical variations. They do not account for systematic uncertainties, which are higher in

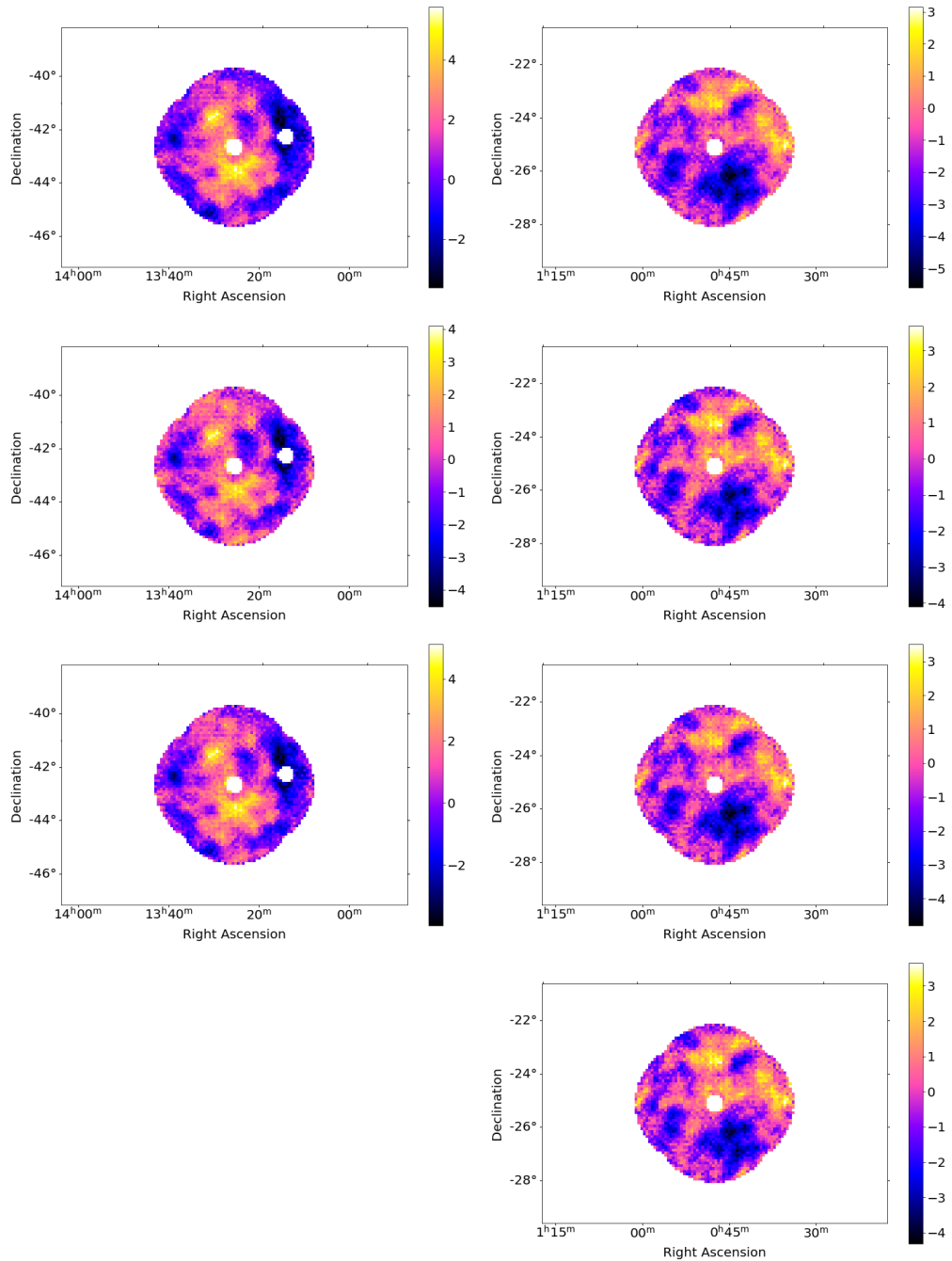


Figure 6.9: Li & Ma significance map using a top-hat convolution kernel with a size of 3 pixels (each pixel having a side length  $0.1^\circ$ ) after background subtraction with masked sources, left for Cen A and right for NGC 253. Top: *Method A*. 2<sup>nd</sup> line: *Method B*. 3<sup>rd</sup> line: *Method C*. 4<sup>th</sup> line: *Method D*. For *Method D*, only the results for NGC 253 are shown, as *Method D* leads to exactly the same results as *Method B* for Cen A (see main text).

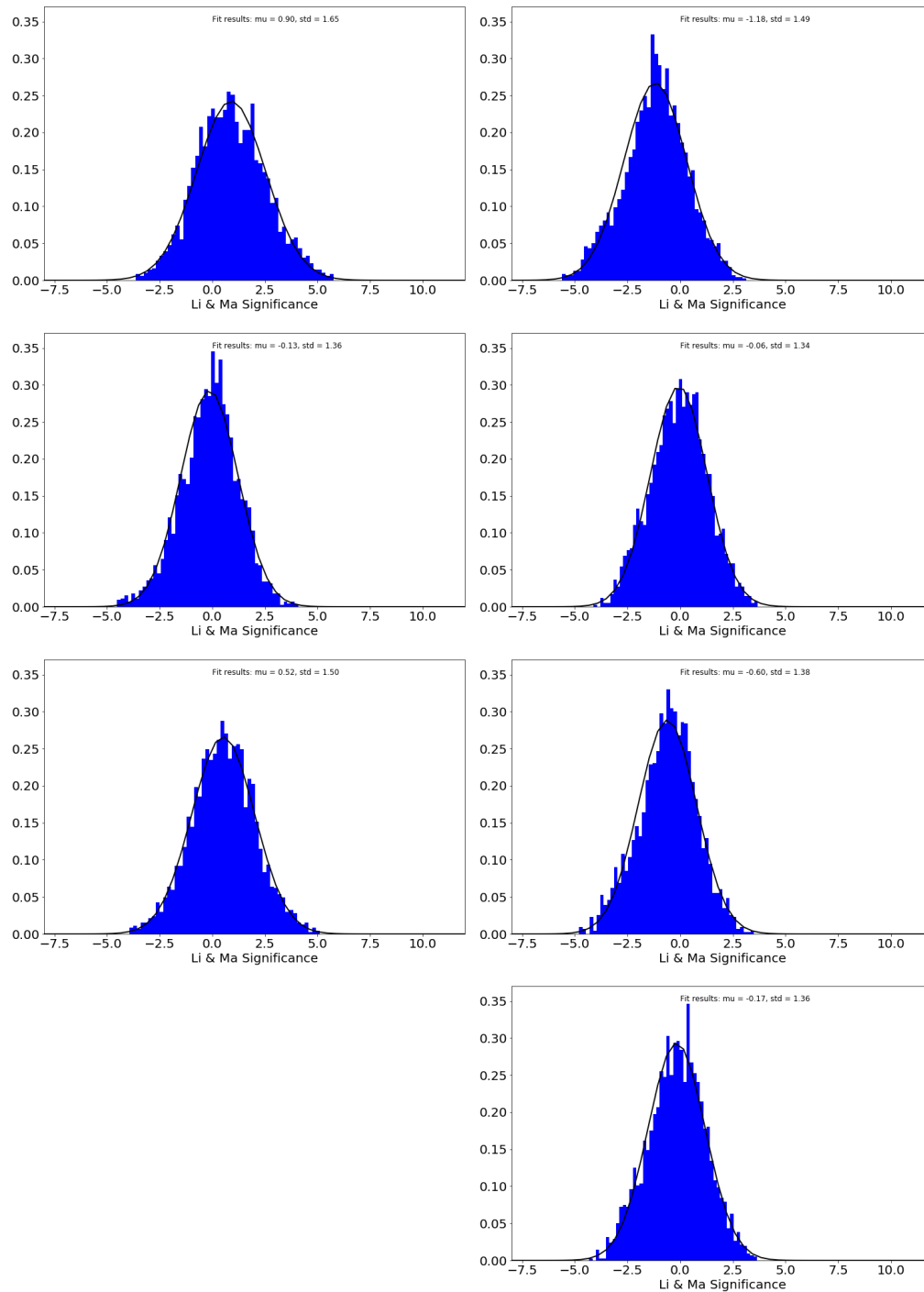


Figure 6.10: Li & Ma significance distribution over the entire region of interest (except for the masked sources), left for Cen A and right for NGC 253. Top: *Method A*. 2<sup>nd</sup> line: *Method B*. 3<sup>rd</sup> line: *Method C*. 4<sup>th</sup> line: *Method D*.

these deep exposure analyses than in most H.E.S.S. analyses performed with lower exposure. These systematic uncertainties are discussed more in detail later in this section. In *Method B*, the significance maps are centred on 0 and the variation over the region of interest is a bit lower, but the excesses and deficits stay at the same location as expected as all the observations considered in this analysis have a similar pointing position. In *Method C* and *D*, the significance maps are centred between these two cases which can be understood because the most extreme excesses and deficits are masked. However, overall, the location and morphology of the seen excesses and deficits stay the same. The distribution of the significances in the individual pixels is shown for the different models in figure 6.10. For an empty field of view with only statistical uncertainties the distributions should follow a Gaussian with mean 0 (no overall excess or deficit) and standard deviation 1. However, one can notice again that in *Method A* the average is shifted by about 1 sigma from 0, whereas it is very close to 0 in *Method B*. This illustrates again that *Method A* might lead to a systematic small under- or overestimation of the background normalizations depending on the field of view. However, this does not mean that *Method B* performs better, at least for non-empty regions of interest, as also parts of an extended physical excess might then be fit by the background. The average values of the Gaussian fit to the significance distribution using *Method C* and *D* are again between  $-0.60$  and  $0.52$  and are much closer to 0 than for *Method A* – especially when using *Method D*. This shows that *Method D* allows to counter-balance the under- and overestimation of the background normalizations while being less impacted by a potential inclusion of signal into the background model during the fit. Then, the standard deviation is much larger than 1 for all the distributions shown here (between 1.34 and 1.65 as can be seen on the figure), which is an indication for the presence of systematic uncertainties leading to local high or low significance regions. This standard deviation is the largest for *Method A*.

A further indication for systematic uncertainties is the deficit in the NGC 253 maps (as seen on figure 6.9) indicating that they are above the level of statistical uncertainties as the deficit is very significant. In addition, it is also present in all of the sub-datasets when dividing the whole dataset in four equally sized sub-datasets of about 50 runs. This makes it very unlikely that a few pathological runs are at the origin of this deficit. These systematic uncertainties need to be quantified in order to exclude that any potential excess is only due to systematics.

For doing this, I first discuss the involved quantities as in [163]. In each region  $M$  inside the region of interest a given number of counts  $C_M$  has been recorded and there is a background prediction  $B_M$  for this region. Due to the statistical and systematic uncertainties,  $C_M$  and  $B_M$  are not equal. One can define the residuals  $R_M = C_M - B_M$ . The systematic uncertainties considered here are due to the

background models not perfectly representing the actual data. One can introduce a relative systematic uncertainty factor  $f_M$  which accounts for the difference between the hypothetical perfect background model  $B_{true,M}$  and the actual background model  $B_M$ :  $B_{true,M} = (1 + f_M)B_M$ . As the systematic uncertainty is not constant over the region of interest, the value  $f_M$  depends on the selected region  $M$ . The distribution of  $f_M$  values over the whole field of view has then an average  $f$  and a root mean square  $\text{RMS}(f)$ . The average  $f$  is, except for statistical variations, 0 by construction when fitting the background normalizations. The root mean square  $\text{RMS}(f)$  on the other hand quantifies the fluctuation of  $f$  in the field of view and so contains information about the systematic uncertainty over the whole field of view.

The  $\text{RMS}(f)$  is estimated following a method developed by Markus Holler [163]. This method relies on the assumption that all pixels are free from any gamma-ray emission and correspond only to background. The counts  $C_M$  in a region  $M$  are then Poisson distributed with expectation value and variance:

$$\text{E}(C_M) = \text{Var}(C_M) = B_{true,M} = (1 + f_M)B_M. \quad (6.1)$$

Using that  $R_M = C_M - B_M$  and assuming that  $B_M$  is not subject to statistical variations one gets for the residuals:

$$\text{E}(R_M) = f_M B_M \quad (6.2)$$

$$\sqrt{\text{Var}(R_M)} = \sqrt{\text{Var}(C_M)} = \sqrt{1 + f_m} \sqrt{B_M}. \quad (6.3)$$

As  $f$  is 0 by construction, typically  $f_M \ll 1$  and so  $\sqrt{\text{Var}(R_M)} \approx \sqrt{B_M}$ . Using this and equation 6.2:

$$\frac{\text{E}(R_M)}{\text{Var}(R_M)} \approx \frac{\text{E}(R_M)}{B_M} = \frac{f_M B_M}{B_M} = f_M. \quad (6.4)$$

This means that for a given realization, the value of  $R_M/B_M$  is statistically scattered around  $f_M$  by:

$$\sigma_{stat} \left( \frac{R_M}{B_M} \right) = \frac{\sqrt{\text{Var}(R_M)}}{B_M} = \frac{1}{\sqrt{B_M}}. \quad (6.5)$$

The systematics level is then assessed by selecting a set of  $n_M$  regions randomly distributed in the region of interest for which the systematics level is to be determined and computing  $R_M/B_M$  for each of these realizations. As  $R_M/B_M$  is statistically scattered around the systematics level  $f_M$  for each region  $M$ , the probability density function of the realization of  $R_M/B_M$  is represented by a normalized Gaussian with average approximately  $\mu_M = f_M$  and standard deviation

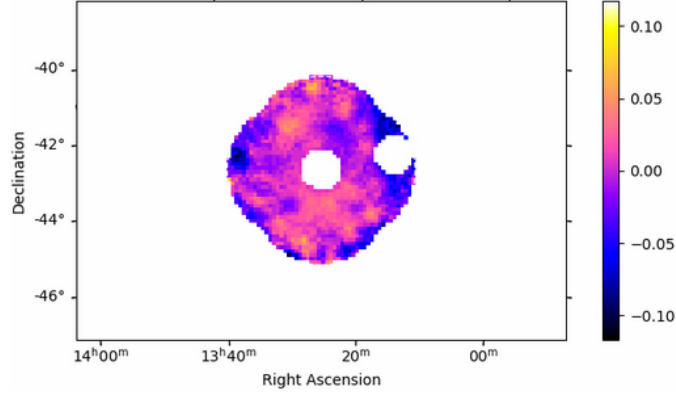


Figure 6.11: Residuals over background map for Cen A using *Method A*.

$\sigma_M = 1/\sqrt{B_M}$  (according to equation 6.5):

$$\text{PDF}(x, f_M) = \frac{1}{\sqrt{2\pi/B_M}} \exp\left(-\frac{(x - f_M)^2}{2/B_M}\right), \quad (6.6)$$

where  $x$  represents the possible values for  $R_M/B_M$  and  $B_M$  is computed from the considered region. For all samples, the probability density function is then the superposition of the probability density functions of the individual regions:

$$\text{PDF}(x, f_{sys}) = \sum_{M=0}^{n_M} \text{PDF}(x, f_M), \quad (6.7)$$

leading to a so-called kernel density estimation. This probability density function then provides a reference to which the measured  $R_M/B_M$  distribution is compared to, which is done by computing the sum of the squared differences of the distribution on an evaluation grid.

The distribution of  $f_M$  is not fully known: the average  $f$  is known, except for statistical variations. It is 0 when the normalizations are fit.  $\sigma_f$ , the value of choice to characterize the systematics level, is unknown. For this reason,  $\sigma_f$  is sampled to find its optimum value, i.e., the value which leads to the best agreement between the measured and reconstructed distribution of  $R_M/B_M$  (using the least square minimization on an evaluation grid as mentioned before).

I used this procedure to estimate the systematics level in the regions of interest after background subtraction assuming that there is no gamma-ray emission coming from these regions (except from the known sources which have also been masked for this systematics estimation). For this estimation, 5000 sample regions of a radius of  $0.25^\circ$  inside a radius of  $2.5^\circ$  around the centre of the region of interest are selected. The resulting residuals over background map is shown as example

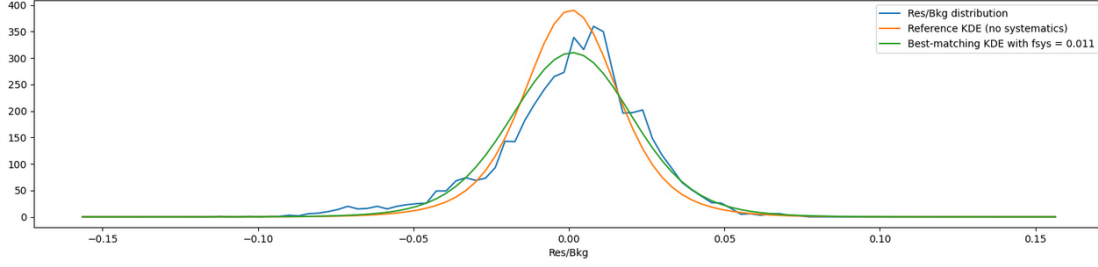


Figure 6.12: Estimation of systematic uncertainties by adjusting the actual residuals over background distribution with a kernel density estimation for different systematic levels, as example for Cen A using *Method A*. Blue: Actual distribution of residuals over background in the 5000 sample regions. Green: Kernel density estimation with best-fit  $\sigma_f$ . Orange: Kernel density estimation with  $\sigma_f = 0$  for reference (and using the average background instead of the background of the individual regions).

for Cen A for *Method A* in figure 6.11. Then, the residual counts divided by the background counts in each of these 5000 regions is filled in a histogram, leading to the blue histogram in figure 6.12. The resulting distribution is then adjusted with a kernel density estimation as discussed before, leading to the green distribution on the same figure. The orange distribution shows the optimal kernel density distribution with no systematic uncertainties for reference. The best-fit  $\sigma_f$  equals then 0.011 in this case which quantifies the fluctuation of the systematic uncertainty factor in the field of view and is the value used to characterize the systematic uncertainty here. So, there is a systematic uncertainty of 1.1% in the Cen A region of interest using *Method A*.

In the same way, I deduced the systematic uncertainties for the other configurations, leading to a systematic uncertainty of 1.1% for Cen A for all methods, 2.4% for NGC 253 for *Method A* and 2.1% or 2.2% for NGC 253 using the other methods. The slightly lower systematic uncertainties when using *Method B*, *C* or *D* can be explained by these uncertainties being reduced to some extent when fitting the normalizations. More interestingly, the systematic uncertainties are much higher for NGC 253 than for Cen A. However, the systematic are expected not to be necessarily the same for all fields of view (as observation conditions can differ between fields of view) and such a behaviour could already be seen when discussing the systematics in lower exposure regions in section 5.5. Overall, the level of systematics is also for NGC 253 not higher than for other sources with lower exposure on which the method was tested. It is just the deep exposure which makes them look more significant on the significance map which only accounts for statistical uncertainties. However, the much lower systematic level for Cen A whose computation assumes the absence of any gamma-ray emission indicates that

there is no significant excess in this region of interest. So, the excess on the Cen A significance map in figure 6.9 which agrees with the orientation of the jet is clearly non-significant and much lower than the potential level of systematic uncertainties.

As discussed previously in section 5.6, the next step of the analysis would be to fit any potential excess with a Gaussian component to characterize it better. As explained, this Gaussian component is supposed to represent the emission morphology and so folded with the IRFs and exposure. Even though there is no hint for extended emission in these two datasets, this procedure was followed to perform exactly the same procedure on this dataset used to quantify the systematic uncertainties than on the actual datasets on LMC and SMC. As discussed before, there is no energy information in the background model and for this reason the spectrum was fixed to a power-law with photon index 2, leading to four remaining free parameters: the two position coordinates, the extension and the amplitude of the Gaussian component. For the same reason, the analysis is performed in one big energy bin spanning from 300 GeV to 10 TeV. This one energy bin is not only used for the counts and background maps, but also to describe the exposure. This makes any amplitude prediction (using this integrated exposure directly) highly unreliable as the difference in exposure with energy is not at all considered any more, even more so after stacking numerous runs taken under different observation conditions and so with very different energy dependences. A more involved amplitude determination using a forward folding method under different photon index assumptions taking into account the energy dependence of the exposure, point spread function and energy dispersion on a run-by-run basis is presented in the physical interpretation of the results. For now, I do not quote the amplitude and indicate the ratio of counts in the Gaussian component to the total number of counts instead.

The resulting Gaussian parameters (except for the amplitude), the fit overall background normalizations (when adding the Gaussian component to the fit), the difference in the TS value and statistical significance when adding a Gaussian component to the fit compared to the fit without a Gaussian component and the ratio of the counts in the fit Gaussian component compared to the total counts in the whole region of interest are shown in table 6.4 for the seven configurations. The position and extension of the Gaussian component agree very well independent of the method of background subtraction for both sources, showing that the four background subtraction methods lead to similar morphological results. Considering the fit overall background normalization, the difference in TS compared to the fit in the same configuration without the Gaussian component and the ratio of the counts in the fit Gaussian component compared to the total counts in the whole region of interest, the differences between the four background subtraction methods are larger. Indeed, the ratio of total counts in the Gaussian component

Source <i>Method</i>	Cen A			NGC 253			
	<i>A</i>	<i>B/D</i>	<i>C</i>	<i>A</i>	<i>B</i>	<i>C</i>	<i>D</i>
Fit overall bkg norm	1.01	0.99	1.01	0.94	0.97	0.96	0.97
Fit parameters of Gaussian							
Right ascension [°]	201.4	201.3	201.3	11.60	11.62	11.65	11.62
Declination [°]	-44.05	-44.05	-44.06	-24.08	-24.10	-24.05	-24.03
Extension [°]	0.6920	0.6487	0.6487	1.633	1.540	1.608	1.638
$\Delta$ TS w.r.t. fit without Gaussian	31.74	27.58	28.79	66.83	40.70	44.20	45.01
Statistical significance of Gaussian	$5.2\sigma$	$4.8\sigma$	$4.9\sigma$	$7.9\sigma$	$6.0\sigma$	$6.3\sigma$	$6.4\sigma$
Ratio of counts in Gaussian [%]	0.73	0.63	0.66	3.85	2.80	3.05	3.11

Table 6.4: Fit overall background normalization, fit Gaussian parameters, improvement in TS and statistical significance with respect to the fit without a Gaussian component and ratio of total counts in the Gaussian component after adding a Gaussian component to the fit for the four configurations for Cen A and NGC 253.

and the difference in TS are larger in *Method A* than in *Method B*. This can be explained by the fact that there is already a readjustment before the Gaussian fit when refitting the background normalizations which partially removes potential excesses and so reduces the excess fit by the Gaussian component. However, as these excesses are non-physical, but part of the systematics, this is not a problem at this stage. And again, in *Method C* and *D*, the resulting values are between the ones obtained from the two other methods, however closer to the ones obtained in *Method B*, showing that these non-physical excesses are also reduced a lot when using exclusion regions while fitting the background normalizations, even though slightly less than when not doing so.

When comparing the resulting fit components for both sources, one sees that the Gaussian fit to NGC 253 seems to be much more significant (from the TS value) and has a much bigger ratio of counts. However, whereas for Cen A there is an excess in the significance map, there is a deficit for NGC 253. As the Gaussian amplitude was constrained to positive values (as there cannot be a physical meaningful deficit), this leads to the Gaussian component being very large and covering almost the whole region of interest for NGC 253 and following the exposure map, except for it being shifted a bit away from the deficit. This is illustrated in figure 6.13 where the counts in the Gaussian component are shown for both sources. Again, due to the similarity of the maps for the different background subtraction

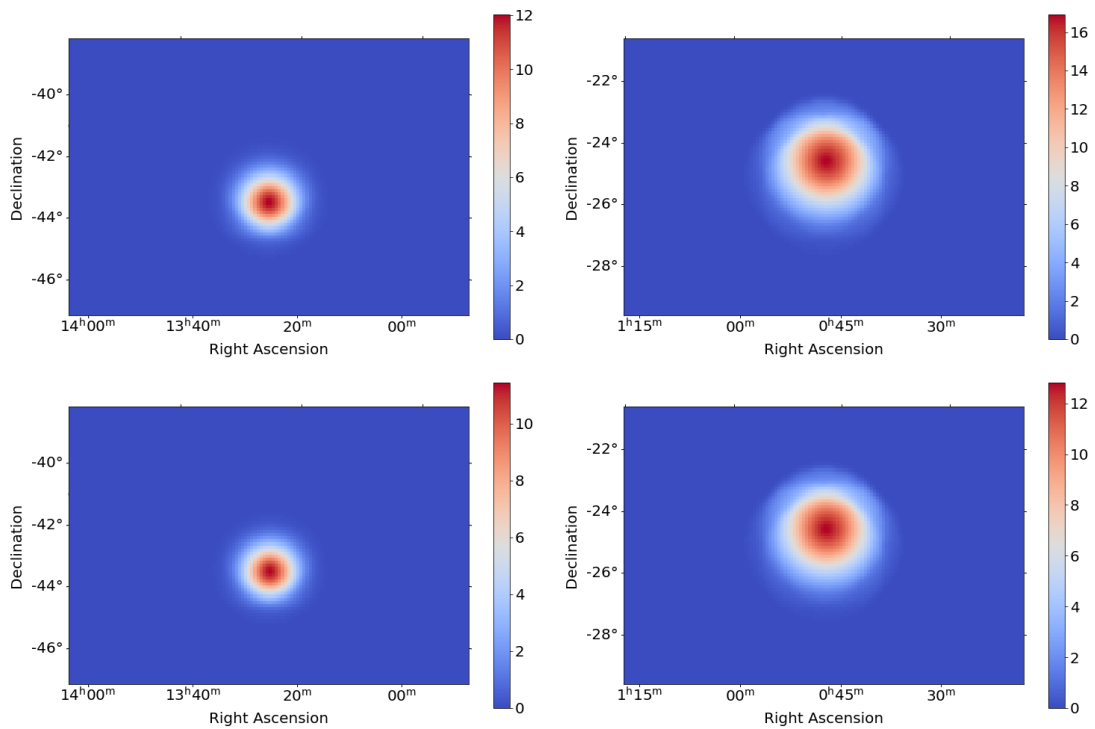


Figure 6.13: Map of counts in best-fit Gaussian. Top left: Cen A using *Method A*. Top right: NGC 253 using *Method A*. Bottom left: Cen A using *Method B*. Bottom right: NGC 253 using *Method B*. A side-by-side comparison of these plots and the residual maps after background subtraction shown in figure 6.7 can be found in appendix A.

methods, only the maps with the most and least significant Gaussian component are shown. The constraining of the amplitude to positive values in combination with the observed deficit is also the reason why the extension is much larger for the Gaussian component in the NGC 253 region of interest and almost as large as the maximum radial offset of the individual observations and why the fit background normalizations are so low. Indeed, the Gaussian fits part of the background and so hides the deficit instead of fitting a potential excess, reason for which the Gaussian was introduced into the fit. One could in principle try to solve this problematic behaviour by constraining parameters in the fit such as the extension of the Gaussian, so that it is not possible for it to fit the background instead of an excess, or by completely fixing the background normalizations to the output value from the run-wise simulations. However, as there is no hint for interstellar diffuse emission in the NGC 253 significance map and for regions of interest with a localized clear excess such a constraining is not necessary, this was also not done here. The main conclusion from this is that it is possible that the Gaussian fits the background instead of an excess which might lead to a big part of the counts being in the background model and also to a quite strong improvement in TS. However, the potential presence of this problem can easily be spotted by the big extension of the Gaussian compared to the size of the region of interest and the strong reduction of the overall fit background normalization.

The remaining residuals after the fit of the Gaussian and of the overall background normalization are shown in figure 6.14, again only for the two most extreme cases due to the similarity of the maps. As expected, the residuals are lower after the addition of a Gaussian to the fit and so adding further degrees of freedom, but the effect is comparatively small.

## 6.3 Analysis results

This section concentrates on the datasets in which an actual search for extended emission was performed. It first discusses the LMC and then the SMC.

### 6.3.1 LMC

The counts map obtained for the LMC on the dataset described previously is shown in figure 6.15. As expected, it follows very much the exposure maps, even though the low exposure region can barely be seen due to a different scaling. The exception to this is the brightest source in the LMC, N 157B which stands out on the counts map as much more counts are recorded from its direction than would be expected from a background-only contribution. The fainter sources 30 Dor C,

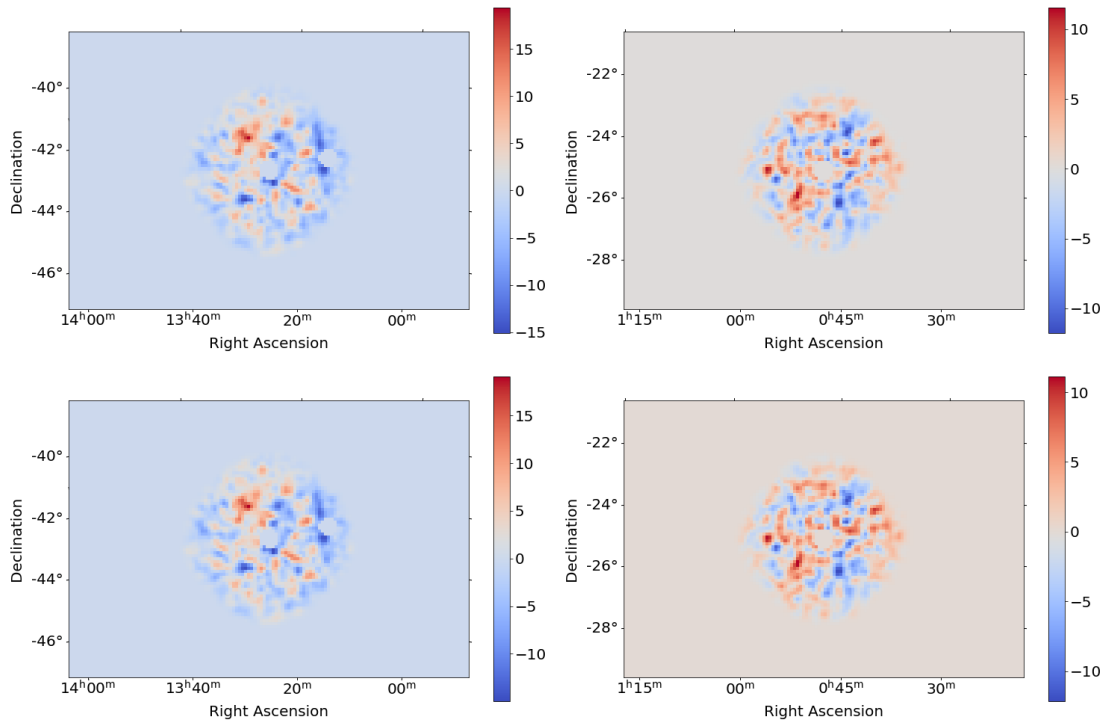


Figure 6.14: Residual maps after fit of one Gaussian component and of the overall background normalization with masked sources. The colour scale indicates the number of counts in each bin. Top left: Cen A using *Method A*. Top right: NGC 253 using *Method A*. Bottom left: Cen A using *Method B*. Bottom right: Cen A using *Method B*.

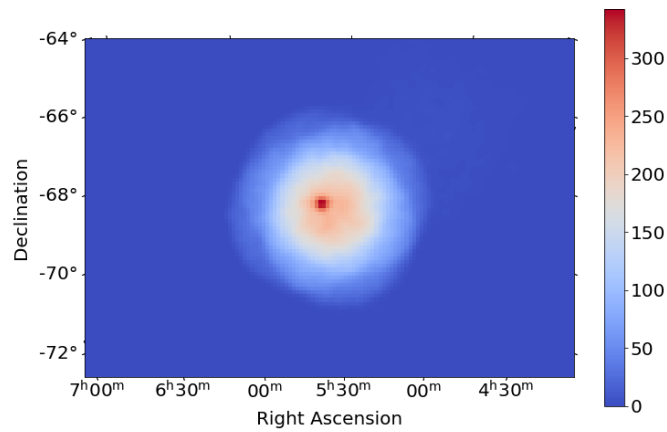


Figure 6.15: Counts map of LMC. The colour scale indicates the number of counts in each bin.

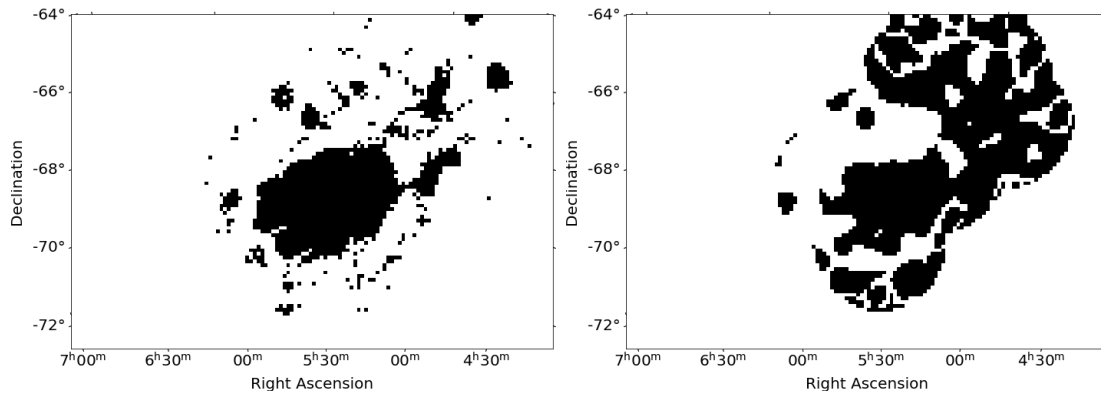


Figure 6.16: Exclusion regions defined in the different background subtraction procedures for LMC. Left: *Method C*. Right: *Method D*.

N 132D and LMC P3, which are also partly in lower exposure regions cannot be seen by eye on this counts map.

Then, I applied the four different background subtraction procedures described in section 5.6 summarized in table 5.1. The exclusion masks used to fit the background normalizations for *Method C* and *D* can be seen in figure 6.16. In contrast to Cen A and NGC 253, both exclusion masks cover a larger part of the region of interest. However, none of the fields of view is entirely covered and there are enough events left in each run to fit the individual background normalizations. Whereas for *Method C*, the exclusion region covers a similar part of the region of interest than for Cen A and NGC 253, it covers a much bigger part of the region of interest for *Method D* for LMC than for the other two sources. This indicates that there are more counts left per exposure after background subtraction for LMC, which is either due to a higher systematics level (which was already comparatively very high for NGC 253 as discussed before) or a signal beside background. This is discussed in more detail in the remainder of this subsection including all the analysis results.

The residual maps after this background subtraction are shown in figure 6.17. As before, only two maps are shown due to the similarity of all the maps. Again, most of the counts which can be seen on the Counts maps in figure 6.15, can be attributed to the background model as the range of the colour scale (indicating the difference in the number of counts from different parts of the region of interest) is reduced by an order of magnitude. However, this time there is a region where the residuals tend to positive values and they are mostly negative in the remainder of the region of interest (as expected as the total should sum up to approximately 0), which constitutes a first indication for an excess. These positive values are mostly concentrated around the central source N 157B and extending towards N 132D.

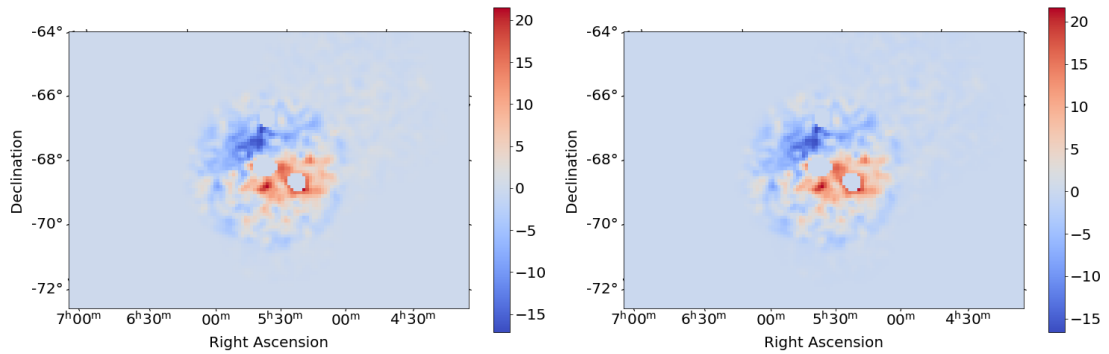


Figure 6.17: Residual maps after background subtraction with masked sources for LMC. The colour scale indicates the number of counts in each bin. Left: *Method A*. Right: *Method B*.

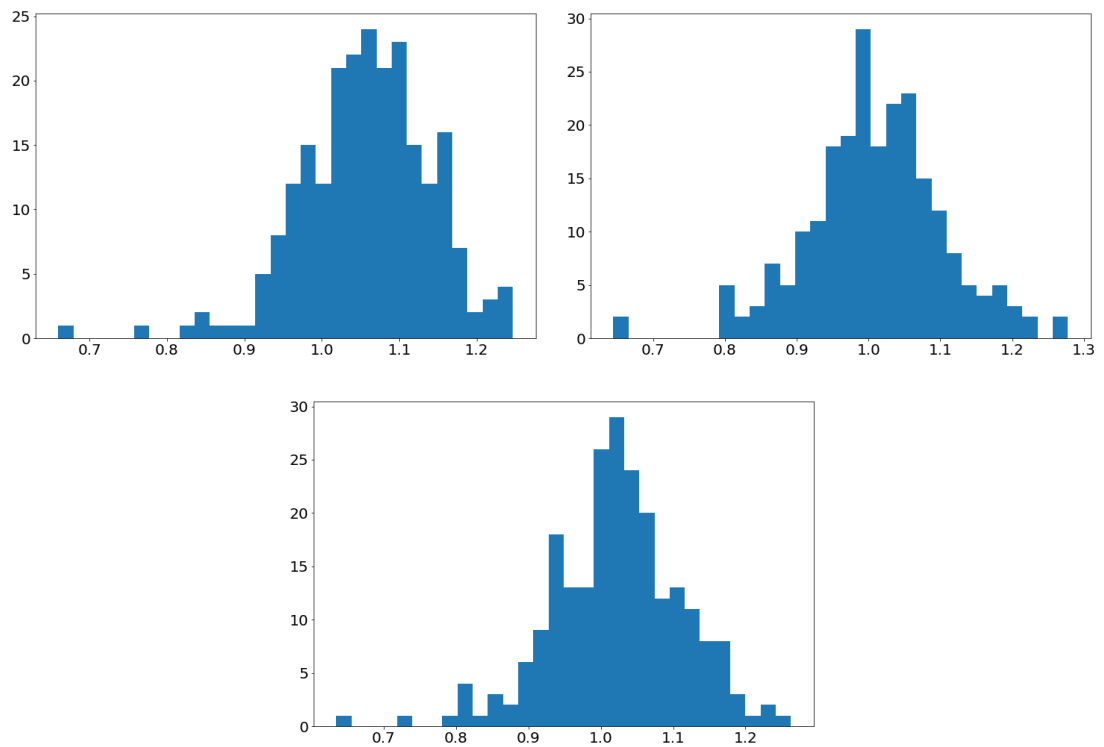


Figure 6.18: Fit background normalizations of LMC. Top left: *Method B*. Top right: *Method C*. Bottom: *Method D*.

There are even more indications for this excess when looking at the fit background normalizations. Indeed, for *Method A*, the overall fit background normalization was 1.06. The fit background normalization of the individual runs are shown in figure 6.18 for *Method B*, *C* and *D*. Fitting a Gaussian to these background distributions leads to a Gaussian with an average value of 1.06 and a standard deviation of 0.08 for *Method B*, with an average value of 1.01 and a standard deviation of 0.10 for *Method C* and with an average value of 1.02 and a standard deviation of 0.09 for *Method D*. Unlike for the systematic studies discussed previously, the average fit normalization value using exclusion regions (i.e., *Method C* and *D*) is much closer to 1 (i.e., the normalization predicted by the run-wise simulations) than to the average one obtained from *Method B*. This indicates that the background level is correctly reproduced outside the exclusion regions and that the underlying excess is probably to an additional, extended component. In addition, there seems to be barely any excess in the non-masked part of the region of interest as the fit background normalizations when using *Method C* and *D* are much closer to 1. The excess instead goes as for *Method A* in the overall fit background normalization as this fit is done over the entire region of interest (except for the masked sources). This leads to an overall background normalization of 1.05 using *Method C* and of 1.04 when using *Method D*. This is to be compared to the obtained 1.00 when using *Method B* (as was expected as the fit goes in this case exactly over the same region over which the individual normalizations have been determined), showing that indeed almost the entire excess gets masked by the exclusion regions. Looking at the shape of the distributions, they look quite Gaussian around the respective central values even though there are again some outliers with lower normalizations. This is especially the case when using *Method B*, however this is due to not all runs having the same pointing directions and so some of the runs not covering the excess and so expected to contribute to a Gaussian with an average around 1 whereas the runs covering the excess are expected to contribute to a Gaussian with a higher average. The standard deviations of the three distributions are very similar and similar to the values obtained for Cen A and NGC 253.

Let me now come to the analysis results using the four background subtraction methods. The significance maps after this background subtraction computed in the same way as before are shown in figure 6.19. Here, unlike for the residual maps shown before, the overall background normalization has not yet been adjusted, and one can see a strong excess. Contrary to Cen A or NGC 253, the difference in the significance maps of the different methods can immediately be seen. First of all, the scales are different: The significance map of *Method B* goes from  $-6$  to  $7$  sigma whereas the one for *Method A* goes from  $-3$  to  $11$  and the other two methods are again between these two extremes. This was already seen in the background

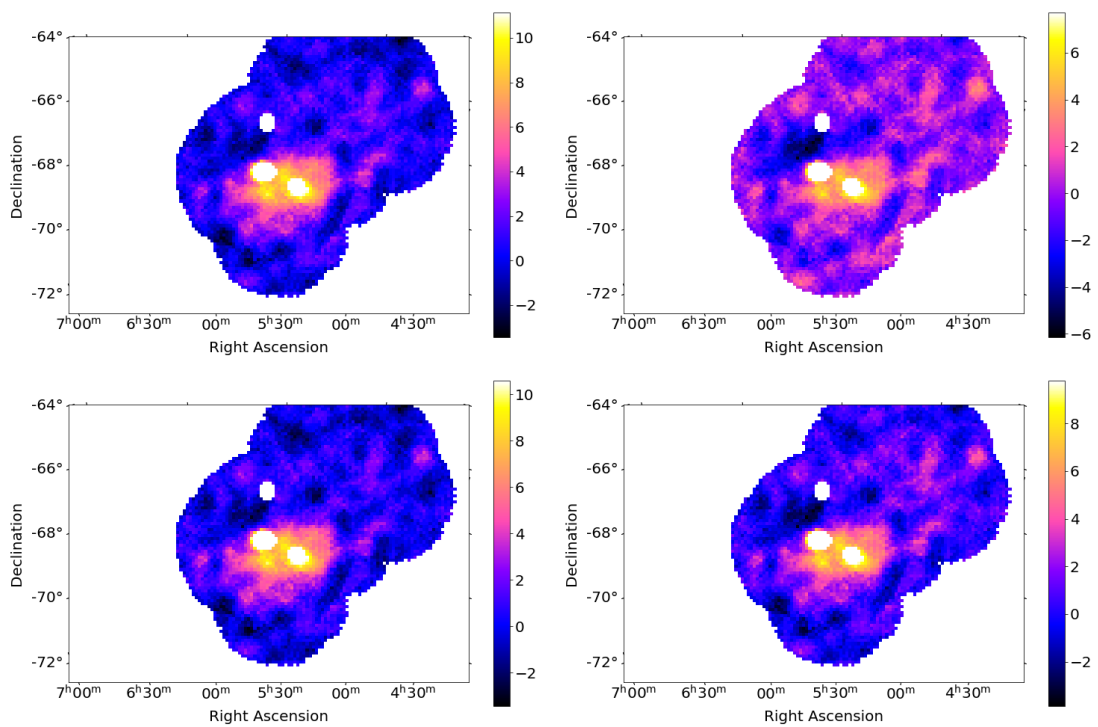


Figure 6.19: Li & Ma significance map of LMC using a top-hat convolution kernel with a size of 3 pixels (each pixel having a side length of  $0.1^\circ$ ) after background subtraction with masked sources. Top left: *Method A*. Top right: *Method B*. Bottom left: *Method C*. Bottom right: *Method D*.

normalizations discussed before and can be explained by any excess leading to an overestimation of the background normalizations when fitting these background normalizations over a region containing this excess. This is also the reason for the holes in the significance which appear for *Method B* and for the much flatter map over the whole region of interest as the background normalizations are just overestimated in the pointing directions containing the excess and so making the excess less significant compared to statistical or systematic variations. The other three maps look much more similar, even though the scales are different. The map obtained using *Method A* shows the highest significances. However, as shown before on Cen A and NGC 253 when looking at the significance distributions, using *Method A* might lead to a small systematic under- or overestimation of the background normalizations which is minimized when using *Method D*. This might be the case here as the significances are slightly higher for *Method A* than for *Method D* and between these both cases for *Method C*. However, this difference might also be due to the exclusion region being too small and the cut too loose. Nevertheless, all four methods deliver a significance map which shows a strong excess which very similar observed morphologies.

The significance maps for the four sources LMC, SMC (which is discussed in the following subsection), Cen A and NGC 253 fitting the background normalizations using *Method D* can be seen on the same scale in figure 6.20 to illustrate how much stronger the excess in the LMC is compared to the small non-physical deficits and excesses seen on Cen A and NGC 253. *Method D* has been chosen for this comparison as it is not impacted by the overestimation of the background normalization leading to holes in the significance map as *Method B*, it is less impacted by potential systematic uncertainties in the background normalization obtained from the run-wise simulations as *Method A* (as could be seen on the Cen A and NGC 253 dataset) and is less impacted by different exposures as *Method C*. It so seems to be the most robust method for extended excesses (as the one seen for LMC) as long as the exclusion regions do not cover so much of the field of view that there are no events left for determining the background normalizations. It will so be used throughout this thesis when only results of one method are shown. However, it is still worth to compare the analysis results of all four methods to spot any potentially unwanted behaviour (such as very different morphologies in the significant map).

The distribution of the significances in the different pixels for the different methods is shown in figure 6.21. It is clearly visible that these distributions do not follow a Gaussian, but have a long tail towards positive values up to almost 10 sigma or more (except for the distribution from *Method B*) displacing the average significance towards positive values and leading to a higher standard deviation. As expected from the best-fit overall background normalizations (discussed earlier

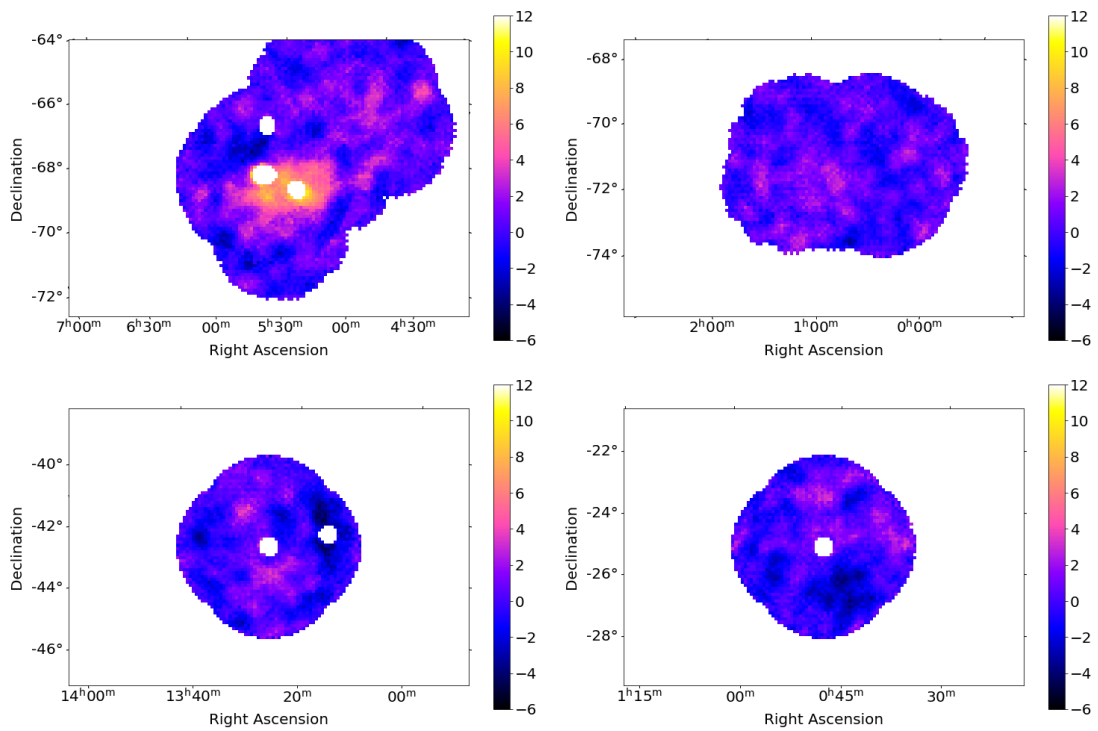


Figure 6.20: Li & Ma significance map using a top-hat convolution kernel with a size of 3 pixels after background subtraction using *Method D*. Top left: LMC. Top right: SMC. Bottom left: Cen A. Bottom right: NGC 253

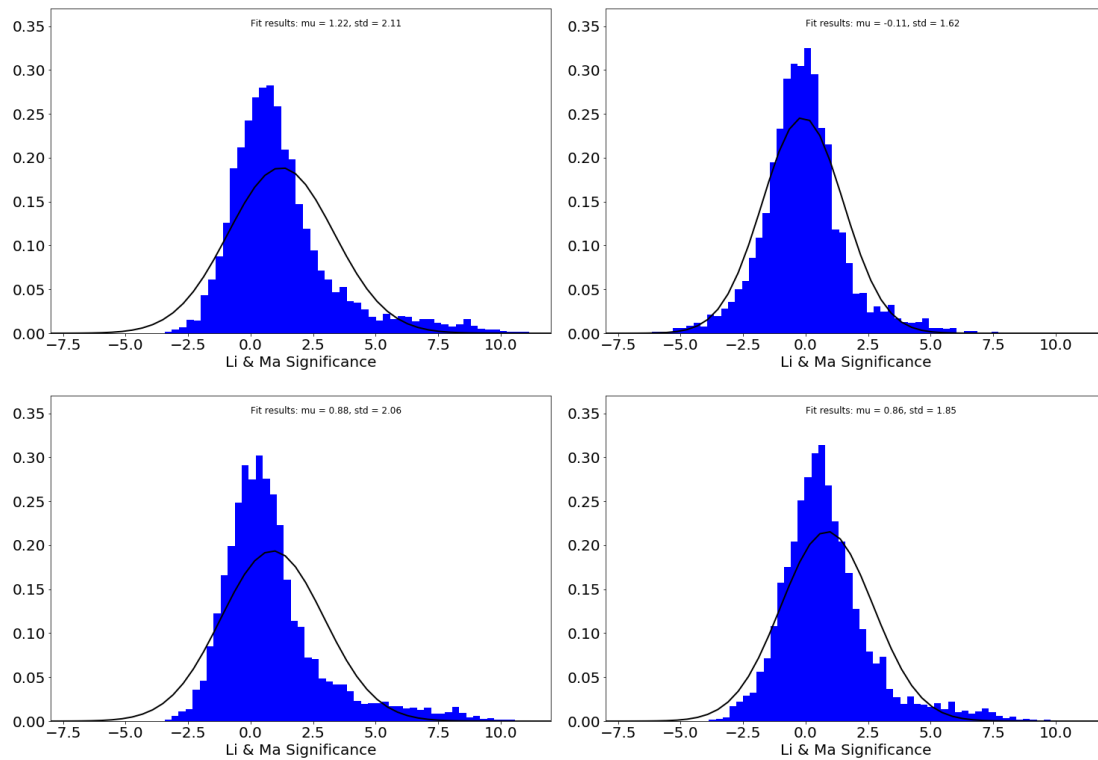


Figure 6.21: Li & Ma significance distribution of LMC over the entire region of interest (except for the masked sources). Top left: *Method A*. Top right: *Method B*. Bottom left: *Method C*. Bottom right: *Method D*. As can be seen by the fit, the distributions do not agree well with a Gaussian.

in the paragraph discussing figure 6.18), the average significance is the highest for *Method A*, than for *Method C* and afterwards for *Method D*. For the significance distribution obtained for *Method B*, the significance distribution reaches as expected only much lower values going up to 7.5 sigma. However, there still clearly is a non-Gaussian tail indicating an excess.

After having discussed numerous indications for an excess, this paragraph discusses the overall "systematics" level using the method described in section 6.2. However, as there are indications for an excess present in the region over which this "systematics" level is determined, it is here rather the level of non-statistical variations as it includes any potential signal. This was not the case for Cen A and NGC 253 as the basic assumption for this systematic study was that there is no signal (outside of the masked sources). For this reason, I call the systematics level from now on level of non-statistical variations, even though I still determine it in the same way. This paragraph compares the overall level of statistical variations to the one obtained on Cen A and NGC 253 and the expected level from the systematics studies. The obtained level of non-statistical variations was between 3.6% and 3.8% for all background subtraction methods. This is much higher than the 1.1% for Cen A or the 2.1% to 2.4% for NGC 253 and also much higher than the systematics level found in the systematics studies. This is a strong indication for the excess not being just due to systematics as the evaluation of the level of non-statistical variations leads to a much higher level than the systematics level seen in other regions of interest, but indeed a physical excess. This all the more, since the systematics level expected from the run-wise background models is not expected to depend on field of view conditions such as night sky background.

Before coming to the fit of a Gaussian component to this excess, I present one more validation check. Indeed, the data on the LMC presented in this study has been taken at very different pointing positions. If the excess is physical each pointing position should contribute to this excess at the same sky position. For this reason, the dataset has been subdivided in four individual regions and each run has been attributed to one of these regions depending on its pointing position:

- The first subset contains all the runs with a right ascension of  $85^\circ$  or more, 45 runs in total.
- The second subset contains all the runs with a right ascension of  $83^\circ$  or more and less than  $85^\circ$  and a declination of  $-69.5^\circ$  or more, 41 runs in total.
- The third subset contains all the runs with a right ascension of  $83^\circ$  or more and less than  $85^\circ$  and a declination of less than  $-69.5^\circ$ , 76 runs in total.
- The fourth subset contains all the runs with a right ascension of less than  $83^\circ$ , 68 runs in total.

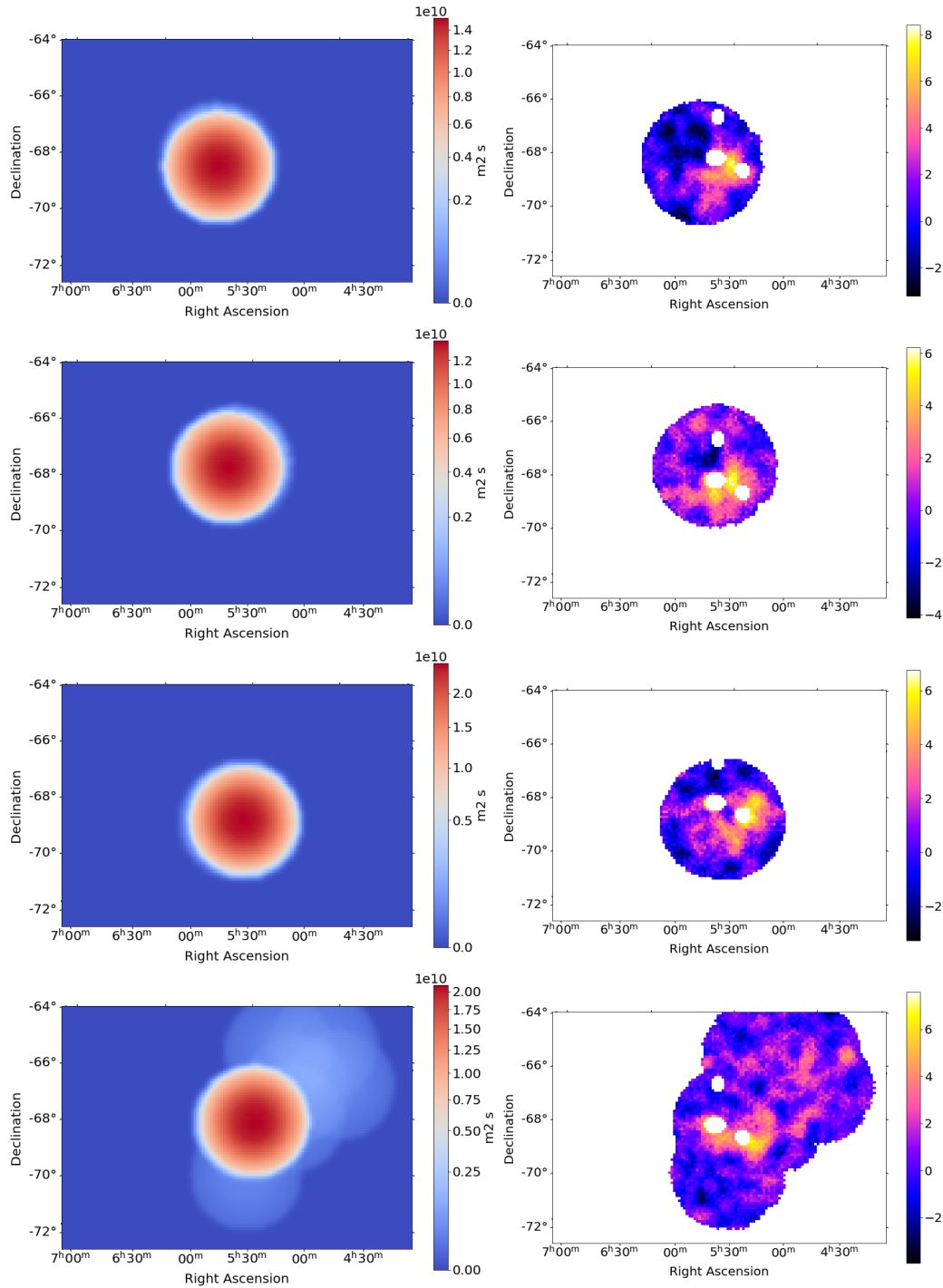


Figure 6.22: Subdivision of the LMC dataset in different sub-datasets according to the pointing position. Left: Exposure map. Right: Li & Ma significance map (computed as before using *Method D*). Top: The 45 runs with  $RA \geq 85^\circ$ . 2<sup>nd</sup> line: The 41 runs with  $83^\circ \leq RA < 85^\circ$  and  $DEC \geq -69.5^\circ$ . 3<sup>rd</sup> line: The 76 runs with  $83^\circ \leq RA < 85^\circ$  and  $DEC < -69.5^\circ$ . 4<sup>th</sup> line: The 68 runs with  $RA < 83^\circ$ . The main differences between the different exposure maps is that the exposure is shifted in the region of interest. The four sub-datasets are completely independent as can be seen from their definition.

The exposure maps and Li & Ma significance maps (derived using *Method D*) of all these individual sub-datasets can be seen in figure 6.22. Even though the region in which the excess is seen is at very different positions in the camera, one sees an excess in this region for all four fields of view. This constitutes an additional confirmation that the excess is robust and not only due to camera field of view systematics.

However, one can also see that the morphology of the excess looks slightly different on the different maps. This is on the one hand due to the different exposure. Among other the exposure is very low at right ascensions below the mask covering N 132D for the first two cases, and so it is impossible to see the excess which is seen there for the latter two cases. But on the other hand, part of it might also be due to statistical variations and systematic uncertainties. Among other, the maximum significance is higher for the first case than for the third and fourth case even though the exposure in the region of the excess is higher for these two cases which might be well explained by these uncertainties.

This difference in apparent morphology due to exposure also illustrates how the exposure limits the analysis results. Indeed, whereas on the two upper plots the exposure prevents us from seeing any potential excess right of N 132D which there are indications for on the two bottom maps, on the two bottom plots the excess also seems to extend to the edge of the exposure region (neglecting the very low exposure region on the bottom plot). This means that the edge of the significant excess I see is not necessarily because the physical emission component only extends to this region, but might also be due to lack of exposure at lower right ascension. This might be resolved by homogenising the exposure over a bigger region in future analysis as is be discussed in chapter 7.

After having discussed these individual regions, let me come to the addition of a Gaussian component to the fit to do a very basic characterization of the excess. As there is no energy information in the background models the spectrum was again fixed with a power-law with photon index 2, leading to four free parameters: the two position coordinates, the extension and the amplitude of the Gaussian component. However, as before the amplitude prediction computed this way is very unreliable and for this reason not quoted here but the one computed using a forward folding method is discussed later on.

The resulting Gaussian parameters, the fit overall background normalizations (when adding the Gaussian component to the fit), the difference in the TS value and statistical significance when adding a Gaussian component to the fit compared to the fit without a Gaussian component and the ratio of the counts in the fit Gaussian component compared to the total counts in the whole region of interest are shown in table 6.5 for the four configurations. Again, the position and extension of the Gaussian agree very well, independently of the background subtraction

Source <i>Method</i>	LMC			
	<i>A</i>	<i>B</i>	<i>C</i>	<i>D</i>
Fit overall background normalization	1.01	0.96	1.00	1.00
Fit parameters of Gaussian				
Right ascension [°]	81.42	81.64	81.81	81.49
Declination [°]	-69.83	-69.81	-69.87	-69.77
Extension [°]	0.9939	0.9778	1.019	0.8925
$\Delta$ TS w.r.t. fit without Gaussian	203.95	196.22	204.44	170.60
Statistical significance of Gaussian	$14.1\sigma$	$13.8\sigma$	$14.1\sigma$	$12.9\sigma$
Ratio of total counts in Gaussian [%]	3.98	3.96	4.27	3.27

Table 6.5: Fit overall background normalization, fit Gaussian parameters, improvement in TS and statistical significance with respect to the fit without a Gaussian component and ratio of total counts in the Gaussian component after adding a Gaussian component to the fit for the four configurations for LMC.

method, even though the differences are as expected a bit larger than for Cen A and NGC 253, and so the four methods lead to similar morphological results. For the fit overall background normalization, the difference in TS and the ratio of counts in the Gaussian, the differences are larger again. For the ratio of the counts in the Gaussian the values are between 3.27 and 4.27, with the lowest and the highest ratio obtained by the two methods fitting the background normalizations using exclusion regions (i.e., *Method D* and *C* respectively), which is very different from what was seen for Cen A and NGC 253. The same tendency is seen for the TS differences. Looking at the overall background normalizations, they are 1.00 when using the background normalization fitting method with exclusion regions (*Method C* and *D*) showing that the Gaussian accounts for the excess in the exclusion regions (unmasked for the fit of the Gaussian component and the overall background) so that no adaptation of the overall background normalization is necessary. For *Method A*, the overall fit background is 1.01 which is an indication for a slight overestimation of the background normalizations which was also seen in some cases in the systematic studies. For *Method B*, the overall fit background normalization is 0.96, showing that the contribution of the Gaussian component has been fit by background normalizations in the first step using this method. So, summarising the results from the four methods, all four methods lead to a Gaussian at an approximate right ascension of  $81.5^\circ$  and declination of  $-69.8^\circ$  with an approximate extension of  $1^\circ$ , a ratio of counts compared to the total number of counts in the region of interest between 3.27 and 4.27 and a change in TS between 170 and 205. Using that four degrees of freedom are added when adding the Gaussian component, this is equivalent to a statistical significance between  $12\sigma$

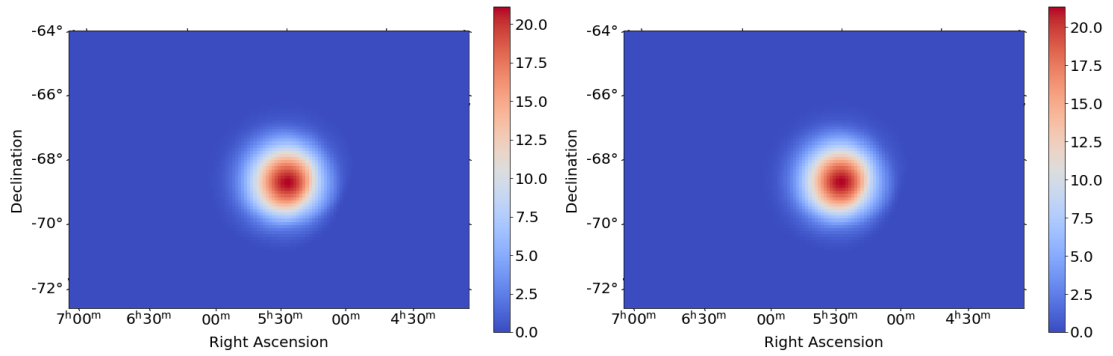


Figure 6.23: Map of counts in best-fit Gaussian component for LMC. Left: *Method A*. Right: *Method B*. A side-by-side comparison of these plots and the residual maps after background subtraction shown in figure 6.17 can be found in appendix A.

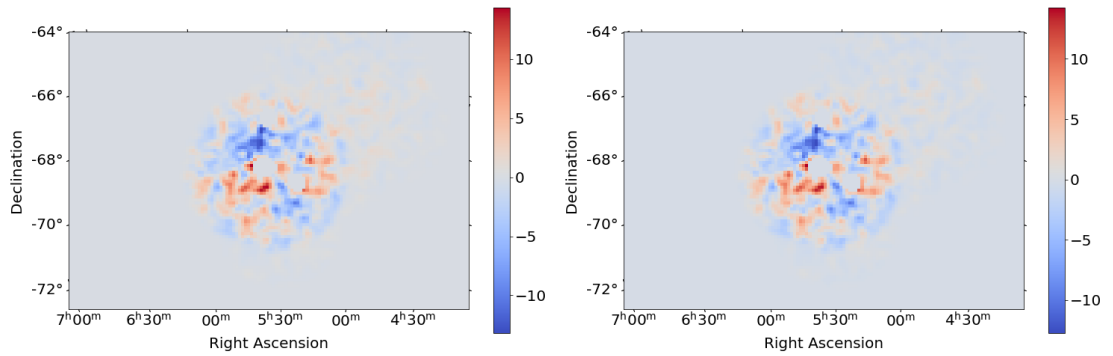


Figure 6.24: Residual maps of LMC after fit of one Gaussian component and the overall background normalization with masked sources. The colour scale indicates the number of counts in each bin. Left: *Method A*. Right: *Method B*.

and  $15\sigma$ . However, beside the statistical uncertainties, there are the systematic uncertainties which need to be taken into account which led to significances of up to  $8\sigma$  on the NGC 253 region of interest when adding a Gaussian component.

The counts in the best-fit Gaussian are shown in the maps in figure 6.23. One can see again how well the position and extension of the best-fit component agree for the different background subtractions (illustrated here for two of them) and that unlike for NGC 253, the best-fit Gaussian does not extend over the entire region of interest and so is not fitting the large-scale background instead of a more localized excess.

The remaining residuals after the subtraction of the fit Gaussian and the overall background normalization are shown in figure 6.24, again only for the two most extreme cases due to the similarity of the maps. This time, the residuals are much

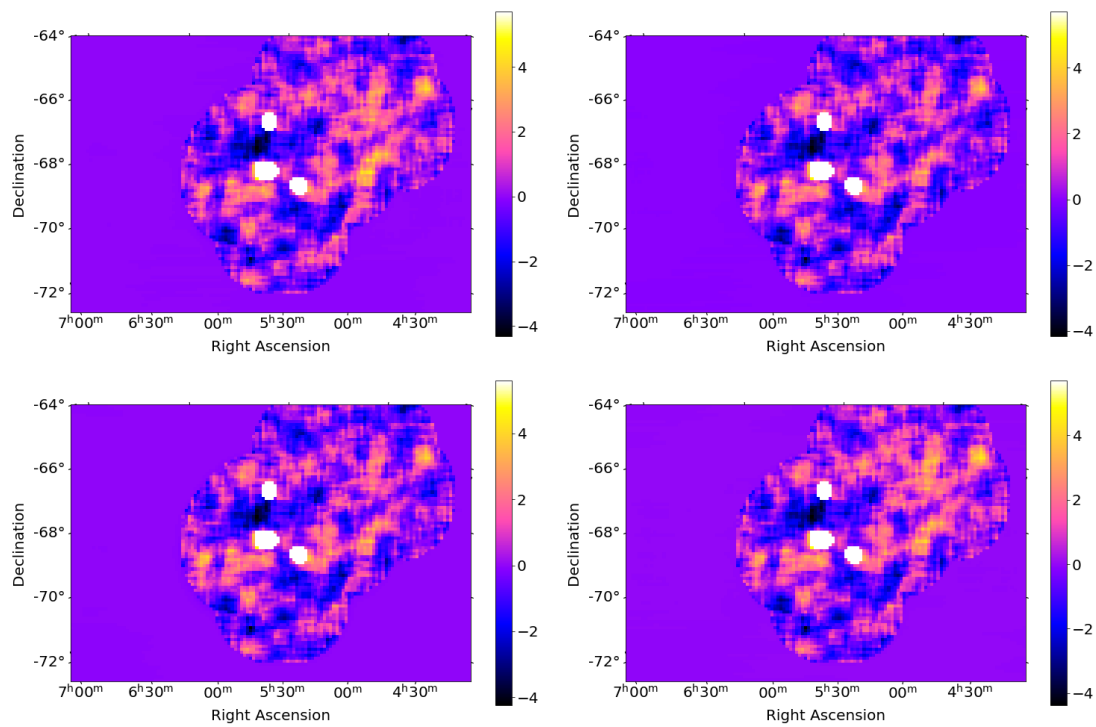


Figure 6.25: Li & Ma significance map of LMC after fit of one Gaussian component and the overall background normalization. Top left: *Method A*. Top right: *Method B*. Bottom left: *Method C*. Bottom right: *Method D*.

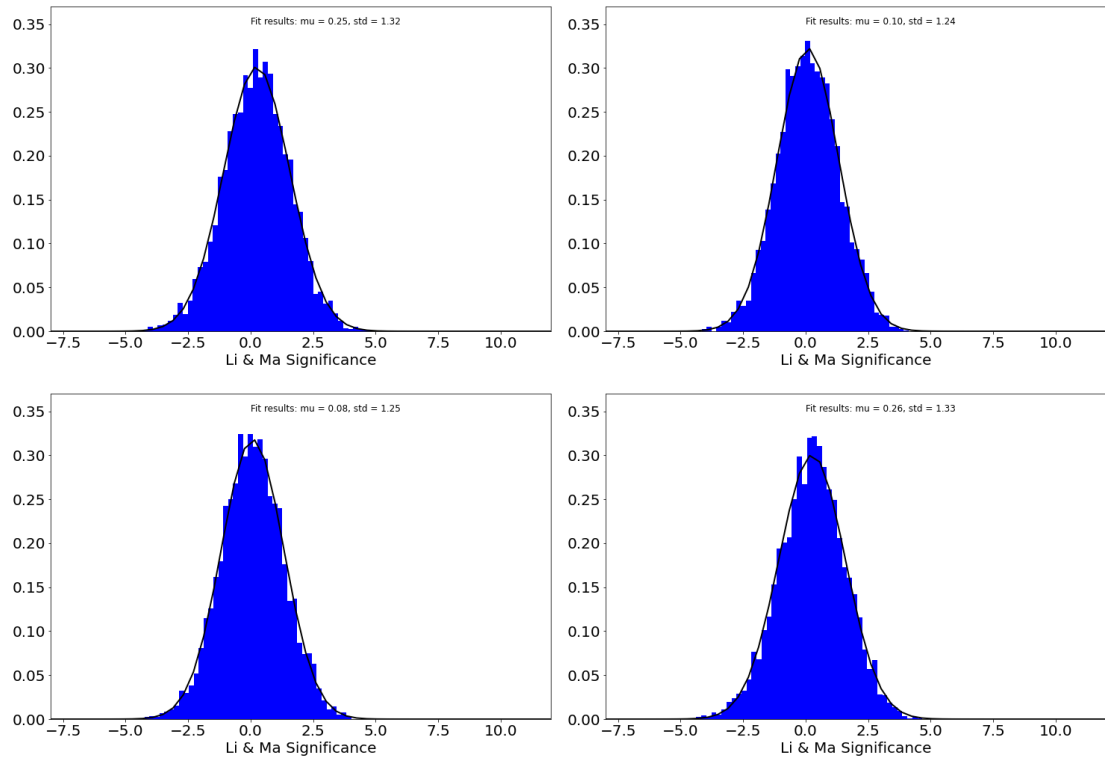


Figure 6.26: Li & Ma significance distribution of LMC over the entire region of interest (except for the masked sources) after fit of one Gaussian component and the overall background normalization. Top left: *Method A*. Top right: *Method B*. Bottom left: *Method C*. Bottom right: *Method D*.

lower than before the addition of the Gaussian and the region with the excess is not present anymore showing that it has been effectively reproduced by the Gaussian component. This finding is confirmed by looking at the Li & Ma significance maps after the subtraction of the Gaussian which are shown in figure 6.25 for the four background subtraction methods. The region where the significant excess has been seen before is not sticking out anymore and there is no indication for any significant excess anymore. The significance range has been reduced and the maps are much flatter than before. This is further confirmed by the significance distribution on figure 6.26, which are much narrower than without the Gaussian and have now similar or even slightly smaller widths than for Cen A and NGC 253. There is though a low exposure region at low right ascension which seems to be slightly brighter. However, this is well in agreement with systematic or even statistical uncertainties especially after the subtraction of a Gaussian. So, the Gaussian is describing the excess well enough so that no significant excess is left after its subtraction. In addition, the remaining significance maps agree very well for the four background subtraction methods.

As there is no a priori reason for the excess to be symmetric and it looks more extended in right ascension than in declination on the significance maps before the subtraction of the Gaussian component in figure 6.19, I performed the same fit with an asymmetric Gaussian component to see whether it performs better (using the same spectrum as for the symmetric Gaussian component). The resulting best-fit parameters, the fit overall background normalization, the difference in TS value and statistical significance when using an asymmetric Gaussian component compared to the fit with a symmetric Gaussian component and to the fit without any Gaussian component and the ratio of counts in the asymmetric Gaussian component compared to the total number of counts in the whole region of interest are shown in table 6.6 for the four background subtraction methods. The declination and lengths of the major axes agree really well again, however the found best-fit right ascensions show now larger differences, but the values agree still within  $1^\circ$ . The best-fit eccentricity is between 0.89 and 0.93 for the four background subtraction methods, showing that the best-fit asymmetric Gaussian component is very asymmetric. The orientation with respect to the right ascension axis is about  $70^\circ$  and so the asymmetric Gaussian component is as expected rather more extended in right ascension which might also explain the higher variation of the best-fit position in this direction. The use of an asymmetric Gaussian component instead of a symmetric Gaussian component barely changes the overall fit background normalizations. It however leads again to a reduction of TS between 46 and 53. This is, however, a smaller reduction of TS than was seen for NGC 253 in the systematics study, which means that the preference of the asymmetric Gaussian component compared to the symmetric one might be due to systematic uncertainties. The use

Source <i>Method</i>	LMC			
	<i>A</i>	<i>B</i>	<i>C</i>	<i>D</i>
Fit overall background normalization	1.01	0.96	1.00	1.00
Fit parameters of asymmetric Gaussian				
Right ascension [°]	80.28	81.26	81.39	80.74
Declination [°]	-69.55	-69.65	-69.69	-69.58
Semi-major axis [°]	1.926	1.545	1.697	1.697
Semi-minor axis (derived) [°]	0.741	0.703	0.737	0.670
Eccentricity	0.9230	0.8904	0.9009	0.9188
Orientation w.r.t. right ascension axis [°]	-69.38	-72.44	-72.05	-71.04
$\Delta$ TS w.r.t. fit				
with symmetric Gaussian	52.36	46.08	52.33	49.63
without Gaussian	256.31	242.30	256.77	220.23
Statistical significance of asymmetric Gaussian				
w.r.t. symmetric Gaussian	$7.0\sigma$	$6.6\sigma$	$7.0\sigma$	$6.9\sigma$
w.r.t. without Gaussian	$15.8\sigma$	$15.3\sigma$	$15.8\sigma$	$14.6\sigma$
Ratio of total counts in asymmetric Gaussian [%]	4.57	4.26	4.67	3.92

Table 6.6: Fit overall background normalization, fit parameters, improvement in TS and statistical significance with respect to the fit with a symmetric Gaussian component and with respect to the fit without a Gaussian component and ratio of total counts in the asymmetric Gaussian component after adding an asymmetric Gaussian component to the fit for the four configurations for LMC.

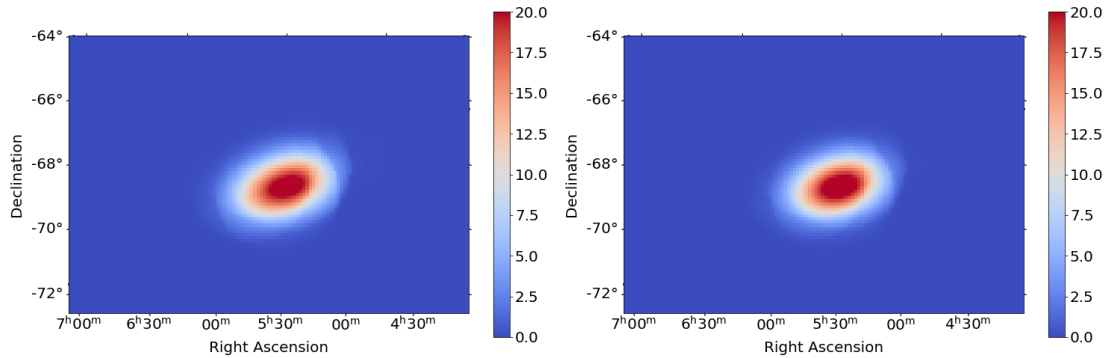


Figure 6.27: Map of counts in best-fit asymmetric Gaussian for LMC. Left: *Method A*. Right: *Method B*. A side-by-side comparison of these plots and the residual maps after background subtraction shown in figure 6.17 can be found in appendix A.

of an asymmetric Gaussian component also increases the ratio of the counts in the fit model for all the background subtraction methods which is now between 3.92 and 4.67. The lowest and the highest ratio are again obtained for the two different background subtraction methods using exclusion regions.

In comparison to the results obtained using a symmetric Gaussian component, the asymmetric Gaussian component leads to a lower right ascension (about  $81^\circ$  compared to  $81.5^\circ$ ), a slightly larger declination ( $-69.6^\circ$  compared to  $-69.8^\circ$ ) and a larger extension (about  $1.7^\circ$  major axis and  $0.7^\circ$  minor axis compared to  $1^\circ$ ). However, due to the high eccentricity of the best-fit asymmetric Gaussian component, such differences are to be expected.

The counts in the best-fit asymmetric Gaussian component are shown in the maps in figure 6.27. One can see again how well the parameters agree for the different background subtractions (illustrated for two of them on the figure). It is also visible how asymmetric the Gaussian component is. Even though the nominal extension of the Gaussian component is now larger, it is clearly visible that the Gaussian component does not extend over almost the entire field of view, unlike for NGC 253.

The Li & Ma significance maps after the subtraction of the asymmetric Gaussian component are shown in figure 6.28. Again, the significance maps for the four background subtraction methods are very similar. Around the region where the asymmetric Gaussian component has been fit, the maps are even flatter than for the fit of the symmetric Gaussian component. Indeed, the holes in the significance map are less deep and the positive significances are even lower in this region. The significance distributions on figure 6.29 are even narrower than for the fit of the Gaussian and clearly narrower than for Cen A and NGC 253. This makes some of the regions far away from the asymmetric Gaussian component

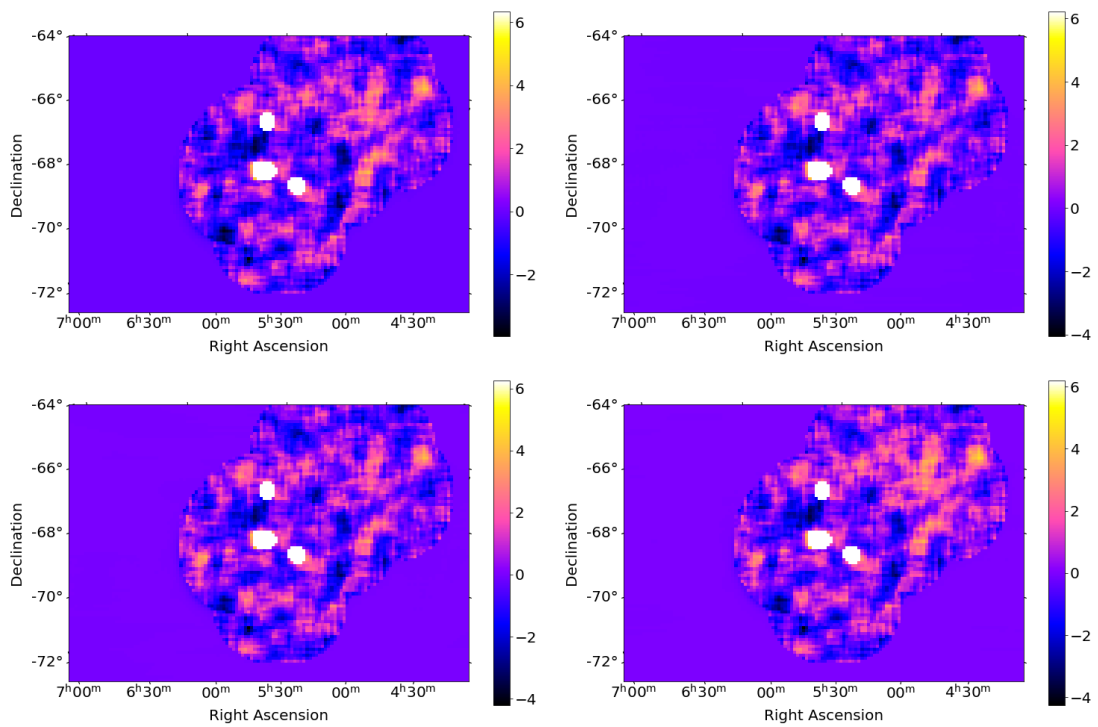


Figure 6.28: Li & Ma significance map of LMC after fit of an asymmetric Gaussian component and the overall background normalization. Top left: *Method A*. Top right: *Method B*. Bottom left: *Method C*. Bottom right: *Method D*.

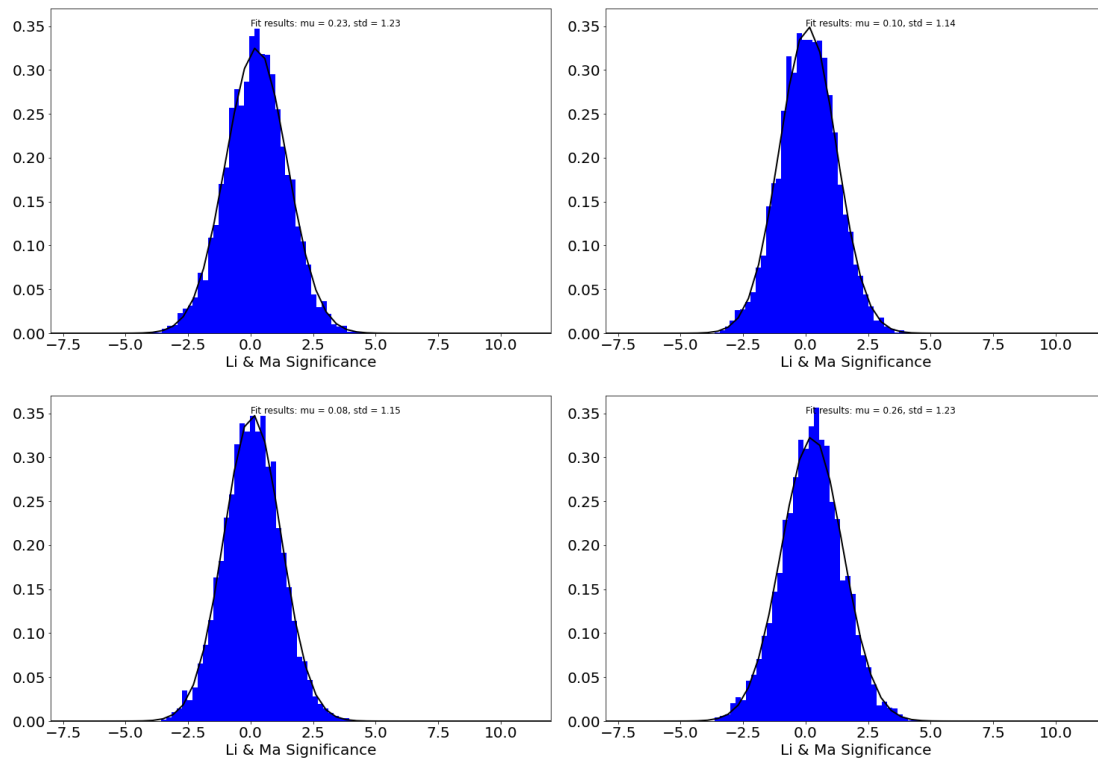


Figure 6.29: Li & Ma significance distribution of LMC over the entire region of interest (except for the masked sources) after fit of an asymmetric Gaussian component and the overall background normalization. Top left: *Method A*. Top right: *Method B*. Bottom left: *Method C*. Bottom right: *Method D*.

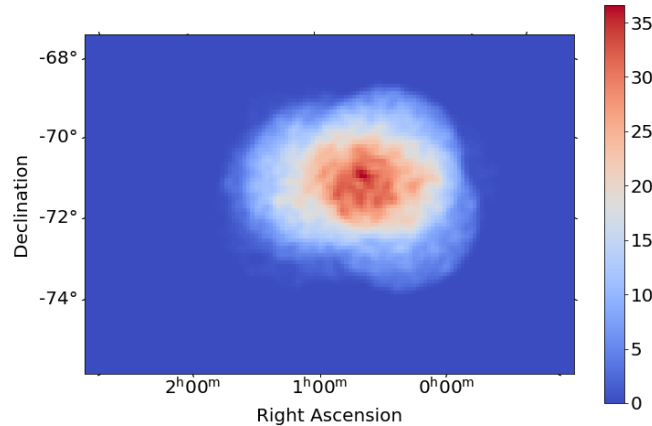


Figure 6.30: Counts map of SMC. The colour scale indicates the number of counts in each bin.

stick more out, in particular the one at low right ascension and high declination. Indeed, there are higher significances in this region now than in the region close to the fit component. Locally even 6 sigma are reached, which is a larger excess than the deficit seen in the NGC 253 region of interest, which was observed with much deeper exposure. However, here the overall background normalizations are fit including the asymmetric Gaussian component which could in principle lead to a small underestimation of the counts in the background. In addition, the comparatively high significances are in a very low exposure region, with only very few runs contributing, meaning that potentially non-optimal observation conditions which were not noticed during the run selection could have a very big impact in these positions. For this reason, the exposure in this study in this region is not high enough to discern whether any of this high significance regions shows indications for a physical excess. However, this shows that it is worth reinvestigating the LMC with a more homogeneous exposure, one of the legacy projects discussed within H.E.S.S.

### 6.3.2 SMC

The counts map obtained for the SMC on the dataset described previously is shown in figure 6.30. It also follows very much the exposure maps and there is no indication for a point-like source, as expected as no point-like source has been detected so far with H.E.S.S. with a much larger dataset. The map for SMC is also noisier which is due to the much smaller dataset compared to the other three sources.

I again applied the four different background subtraction procedures. The

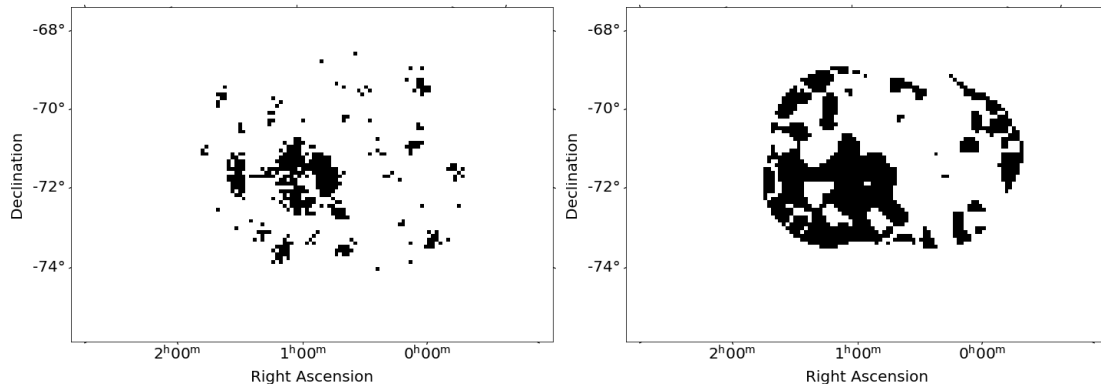


Figure 6.31: Exclusion regions defined in the different background subtraction procedures for SMC. Left: *Method A*. Right: *Method B*.

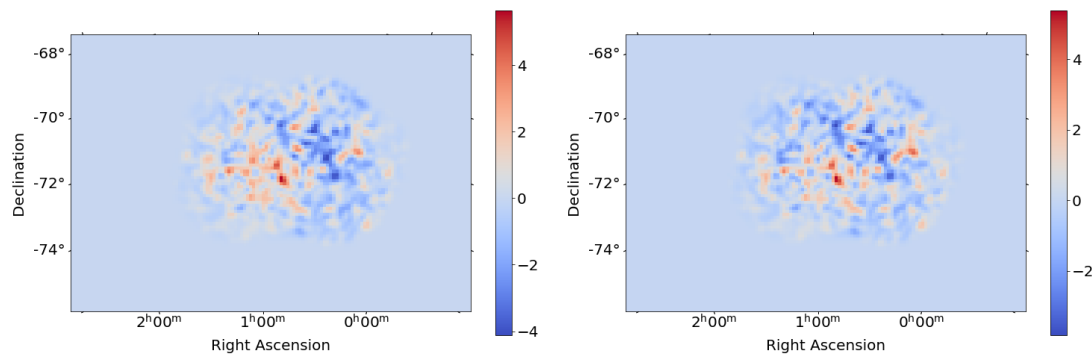


Figure 6.32: Residual maps after background subtraction for SMC. The colour scale indicates the number of counts in each bin. Left: *Method A*. Right: *Method B*.

exclusion masks for the *Method C* and *D* are shown in figure 6.31. This time, the exclusion masks cover a smaller fraction of the region of interest than for LMC and unlike for Cen A and NGC 253, it *Method D* which covers a larger fraction of the region of interest. This is also due to the lower exposure as the statistical variations in the residuals over background map are reduced with exposure whereas they stay the same in the significance map.

The residual maps after this background subtraction are shown in figure 6.32. Most of the counts which can be seen on the counts map in figure 6.30, can again be attributed to the background model as the range of the colour scale (indicating the difference in the number of counts from different parts of the region of interest) is reduced by an order of magnitude. The residuals are much flatter than for the LMC and similarly flat than for Cen A and NGC 253. There seems to be a small excess towards the left, but it is impossible to say whether it is significant only

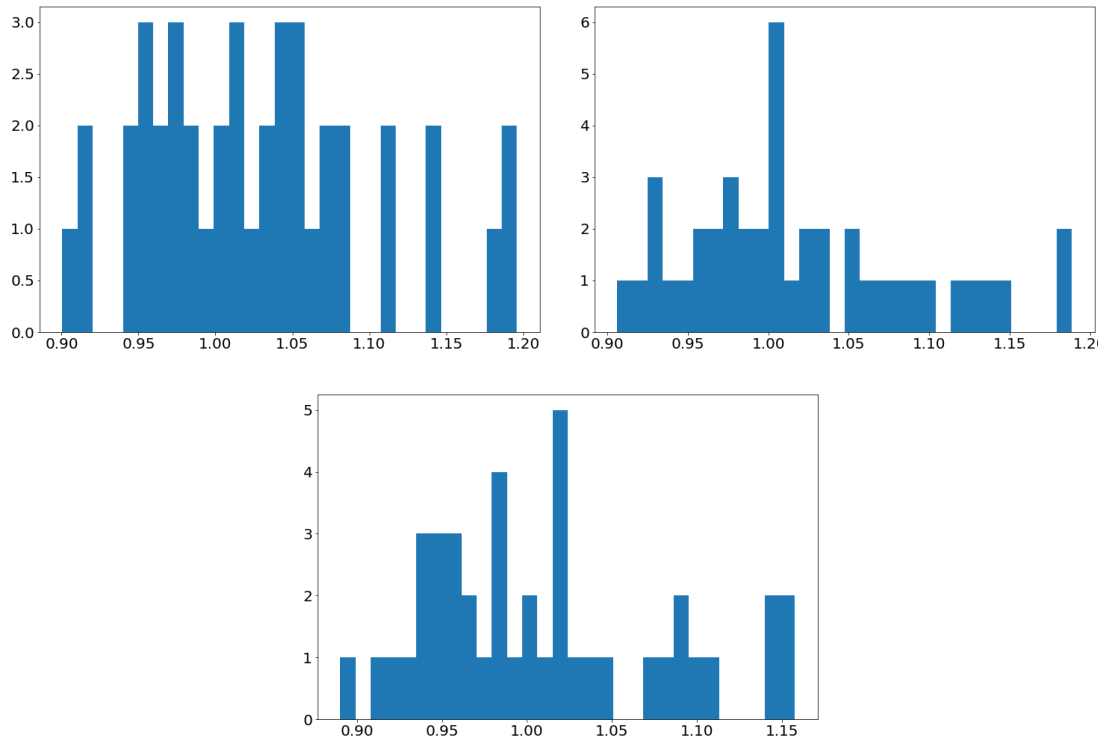


Figure 6.33: Fit background normalizations of SMC. Top left: *Method B*. Top right: *Method C*. Bottom: *Method D*.

from the residuals. However, before discussing any possible excess on a more suitable map, such as the significance map, let me first come to the background normalizations. The overall fit background normalization in *Method A* was 1.03, which is slightly further from 1 than what was seen for Cen A and NGC 253, but definitely lower than the one of LMC. However, this small difference compared to the systematic studies could also be explained by the lower exposure. The fit background normalizations of the individual runs for *Method B*, *C* and *D* are shown in figure 6.33. They look much noisier, due to the much lower number of runs in the SMC dataset. Fitting a Gaussian to these distributions leads to a Gaussian with average value 1.03, 1.02 and 1.01 for *Method B*, *C* and *D* respectively and a standard deviation of 0.07 for all the three methods. Unlike for LMC the fit background normalizations are much closer to each other and to 1 again as it was the case for Cen A and NGC 253. The standard deviation, which is the same for all three methods, again has a similar size than for the three other sources. This is an indication that the background model reproduces the data well, without the need for an extended component.

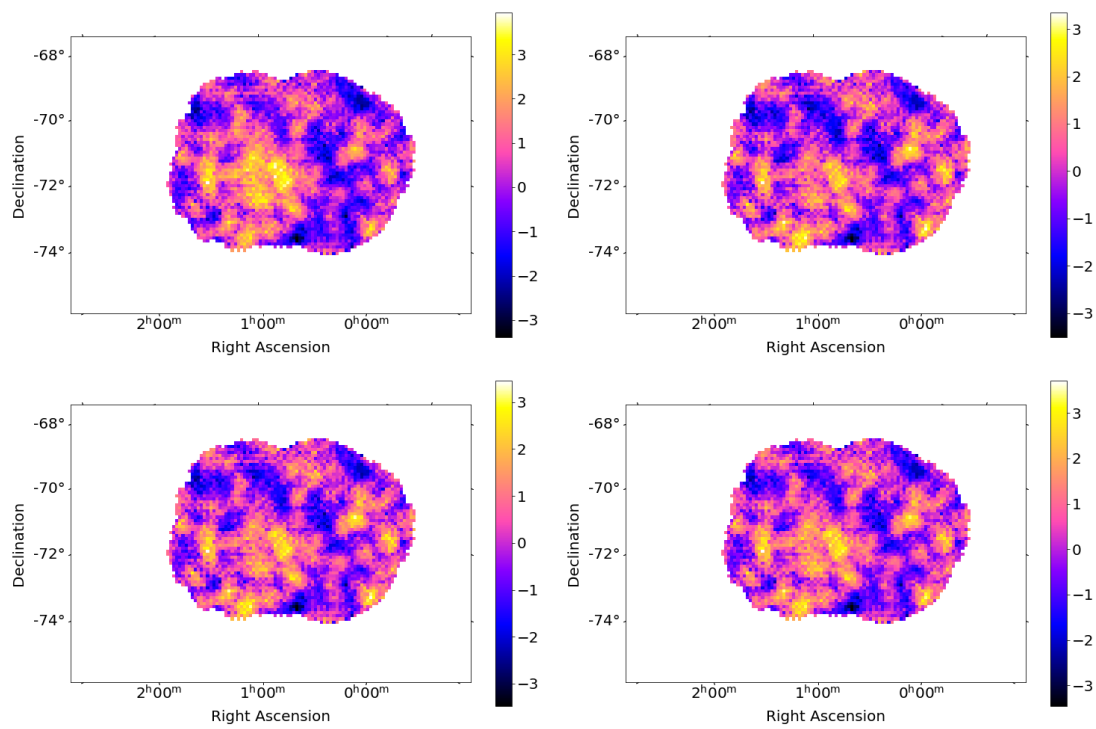


Figure 6.34: Li & Ma significance map of SMC using a top-hat convolution kernel with a size of 3 pixels (each pixel having a side length of  $0.1^\circ$ ) after background subtraction. Top left: *Method A*. Top right: *Method B*. Bottom left: *Method C*. Bottom right: *Method D*.

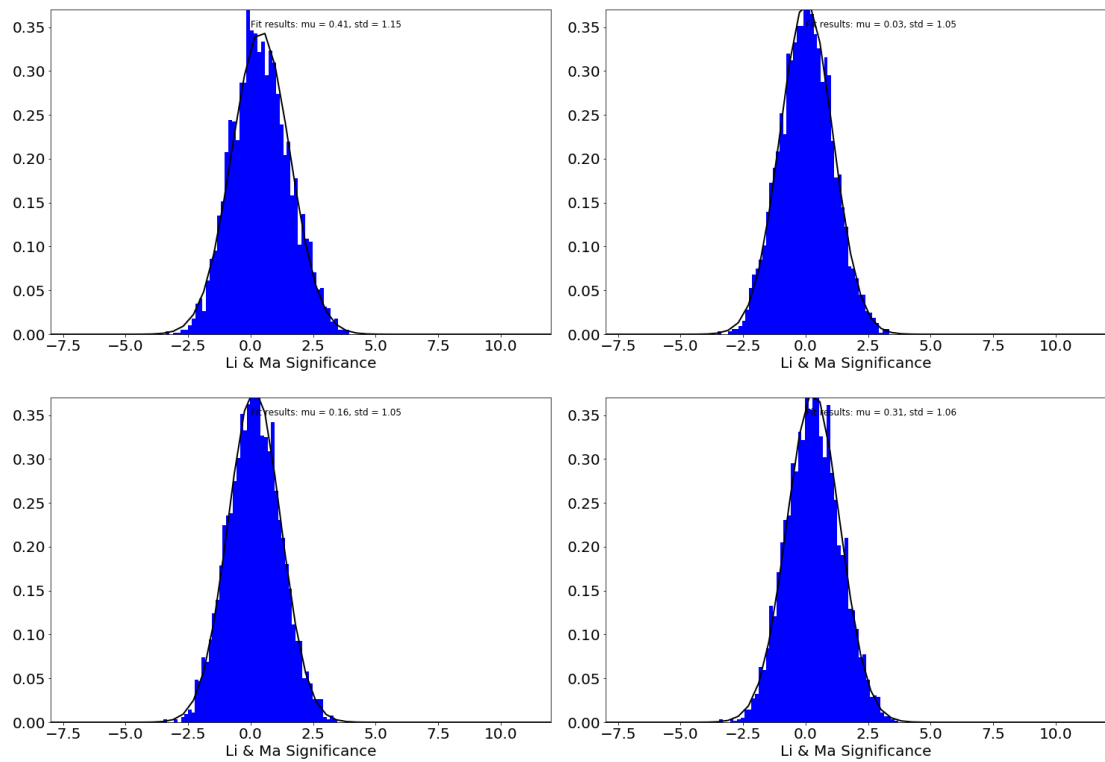


Figure 6.35: Li & Ma significance distribution of SMC over the entire region of interest. Top left: *Method A*. Top right: *Method B*. Bottom left: *Method C*. Bottom right: *Method D*.

The significance maps for the four different background subtraction methods computed in the same way as before are shown in figure 6.34. The significance maps look very similar for the four methods and are all rather flat, even though again the map obtained with *Method A* is a bit less flat. There is no sign for any excess above statistical variations. The significance maps are also very centred on 0 showing no hint for an overall under- or overestimation of the background normalizations as was seen for Cen A and NGC 253, for much deeper exposure datasets however. These findings are confirmed by the significance distributions in the different pixels for the different models shown in figure 6.35. They are very Gaussian with a mean between 0.03 and 0.41 which is much closer to 0 than the means seen for Cen A and NGC 253 and even the more compared to the one seen for LMC and a standard deviation very close to 1 being 1.15 for *Method A* and even closer to 1 for the other methods with values between 1.05 and 1.06. This shows that there is no hint for any excess (or deficit) in this comparatively small dataset. Both the means and the standard deviation are much closer to the expected value than for the three other sources which is partly probably also due to the comparatively very low exposure. Comparing the individual distributions for SMC, one can see again the typical behaviour that the mean is the furthest away from 0 for *Method A* and the closest to 0 for *Method B*.

The overall level of non-statistical variations for SMC was evaluated using the method described in the systematics study section (6.2). The level of non-statistical variations is 3.4% for *Method A*, 3.5% for *Method B*, 2.8% for *Method C* and 2.9% for *Method D*. The difference between the different methods is higher this time than for the other three sources and the level of non-statistical seems to be higher for *Method A* and *B* than for *Method C* and *D*. This might on the one hand be due to the background normalizations not being adjusted as well to the data especially when using *Method A*, but on the other hand also due to the lower exposure which leads to more noisy counts and residual maps and might make the resulting estimated level of non-statistical variations more dependent on the exact configuration and choice of the 5000 regions. Additionally, the level of non-statistical variations is much higher than for Cen A (1.1%) and NGC 253 (2.1% to 2.4%) and almost reaching the level of LMC (3.6% to 3.8%). This either means that SMC is a region of interest with a particular high systematics level or that it is not an empty region of interest that there is physical emission in the region of interest. The latter is well possible since as discussed previously, interstellar diffuse emission or emission from unresolved sources might well occur in the SMC and so emission would not be unexpected, and this emission might lead to an apparent higher level of non-statistical variations before being clearly visible in the significance maps, especially for such low exposure as considered here. The first would mean that the systematics level on SMC is higher than expected

Source <i>Method</i>	SMC			
	<i>A</i>	<i>B</i>	<i>C</i>	<i>D</i>
Fit overall background normalization	0.99	0.99	1.00	1.00
Fit parameters of Gaussian				
Right ascension [°]	16.23	13.76	14.02	15.15
Declination [°]	-73.17	-73.23	-73.22	-73.29
Extension [°]	1.145	0.7156	0.7419	0.9193
$\Delta$ TS w. r. t. fit without Gaussian	44.20	14.04	14.87	18.97
Statistical significance of Gaussian	$6.3\sigma$	$3.1\sigma$	$3.2\sigma$	$3.8\sigma$
Ratio of total counts in Gaussian [%]	3.22	1.22	1.30	1.72

Table 6.7: Fit overall background normalization, fit Gaussian parameters, improvement in TS and statistical significance with respect to the fit without a Gaussian component and ratio of total counts in the Gaussian component after adding a Gaussian component to the fit for the four configurations for SMC.

and might constitute a first hint for a higher systematics level at higher zenith angle, and so the LMC level of non-statistical variations not being so much above the expected maximum systematics level anymore. However, as it is completely unclear whether there is any physical excess in the SMC region of interest such a conclusion would be premature and further studies with deeper exposure are necessary. It might as well be that this is the first indication for extended emission in the SMC.

For consistency with the analysis of the other regions of interest, I now discuss the addition of a Gaussian component even though no significant excess has been seen. The resulting Gaussian parameters, the fit overall background normalizations, the difference in TS and statistical significance when adding a Gaussian component to the fit compared to the fit without Gaussian component and the ratio of the counts in the fit Gaussian component compared to the total counts in the whole region of interest are shown in table 6.7 for the four different background subtraction methods. This time the fit positions are fluctuating more and also the extensions are quite different. Especially the right ascensions varies between  $13.8^\circ$  and  $16.2^\circ$  and so span a range of  $2.4^\circ$ . The declinations agree more being all between  $-73.3^\circ$  and  $-73.1^\circ$ . The extensions show again more variations being between  $0.7^\circ$  and  $1.2^\circ$ . The reason for this very big difference between the best-fit parameters for the different background subtraction methods will become clearer when looking at the counts in the best-fit Gaussian component and will be discussed when looking at these maps. The fit overall background normalizations are very close to 1 for the four methods. This means that the difference in the average background normalizations (1.00 for *Method A* and 1.03 for *Method B*)

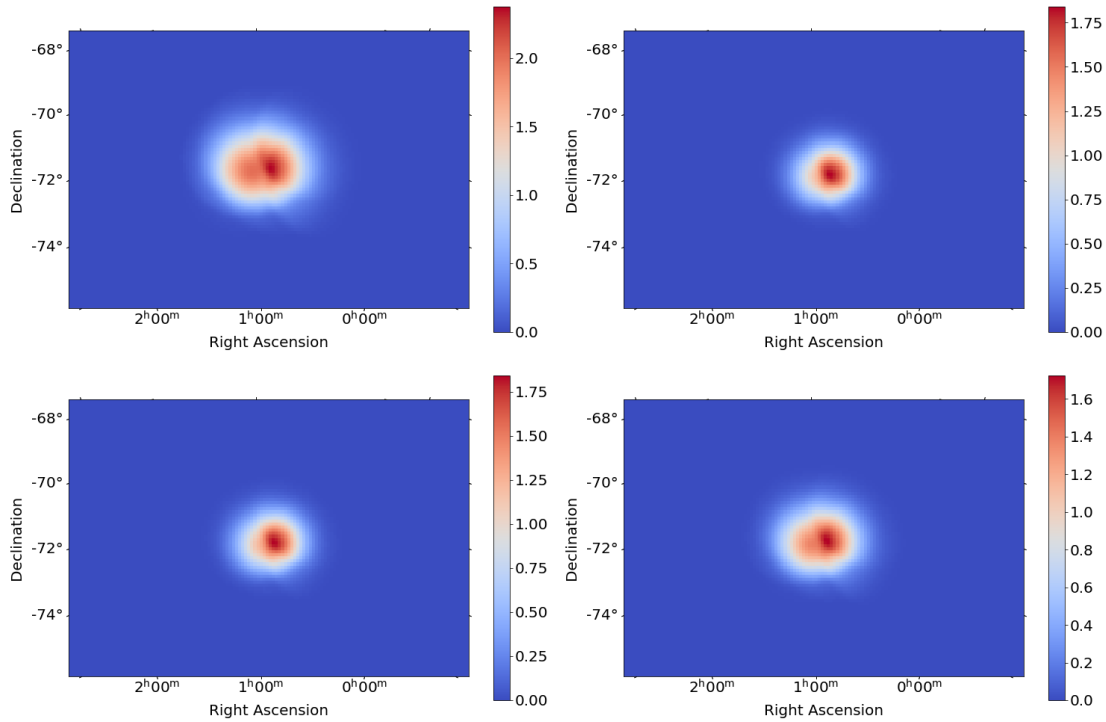


Figure 6.36: Map of counts in best-fit Gaussian for SMC. Top left: *Method A*. Top right: *Method B*. Bottom left: *Method C*. Bottom right: *Method D*. A side-by-side comparison of these plots (*Method A* and *B*) and the residual maps after background subtraction shown in figure 6.32 can be found in appendix A.

after fitting the background normalizations of the individual runs in the different methods are this time not equilibrated by the overall background normalizations, unlike for the regions of interest previously considered. However, the difference is small due to the difference in the average background normalizations only being small. Looking at the TS values and the ratio of counts in the Gaussians, the differences are this time really large between *Method A* and *B*. Indeed, the TS value is 44 and the ratio of counts 3.22 for *Method A* compared to between 14 and 19 and between 1.22 and 1.72 for the other three methods. A similar behaviour was seen for Cen A and NGC 253 even though not as extreme and could be explained by there already being a readjustment before the Gaussian fit when fitting the normalizations which partially removes potential excesses. However, this behaviour was not observed in the LMC region of interest, which could be because there the Gaussian fits a physical excess, whereas in the other three regions of interest the excess could be due to systematics.

The counts in the best-fit Gaussian component are shown in figure 6.36, this

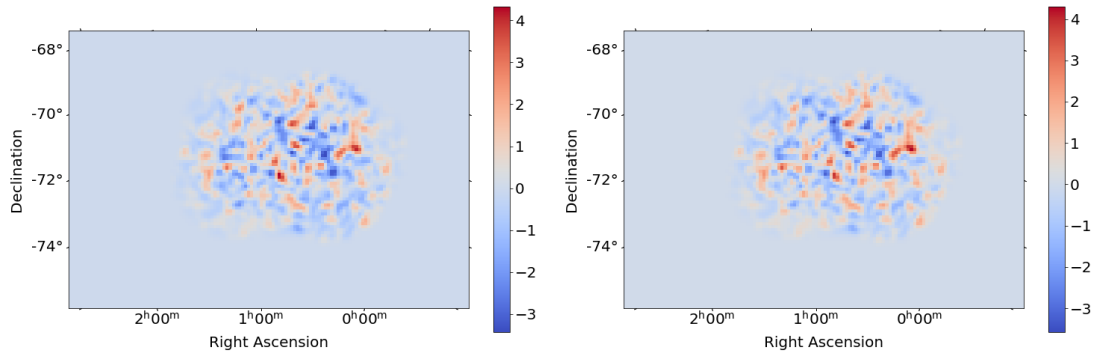


Figure 6.37: Residual maps of SMC after fit of one Gaussian component and the overall background normalization with masked sources. The colour scale indicates the number of counts in each bin. Left: *Method A*. Right: *Method B*.

time for all four background subtraction methods. These Gaussian components do not look Gaussian at all, unlike what was seen for the other three regions of interest. This is due to looking at the Gaussians in count space. Indeed, the Gaussian is the assumption for the source morphology and how this Gaussian is observed in counts space depends on the exposure on the individual parts of the Gaussian. However, the very inhomogeneous exposure on the SMC (which was shown in figure 6.4) leads to the original Gaussian distributions to be deformed to the counts map seen here. The Gaussians look very bright in the central region with high exposure and have some asymmetric contributions in lower exposure regions. This also explains the very different best-fit right ascensions and extensions seen for the different background subtraction methods. Looking at the extension of the Gaussians, they are much smaller than for NGC 253 and so the Gaussians do not extend over the entire region of excess and fit part of the background due to an overall too low background normalization over the whole region of interest. So, they describe a local component, which could however be due to systematics due to the comparatively low overall TS value.

The remaining residuals after the fit of the Gaussian component and the overall background normalization can be seen in figure 6.37. The maps look again very similar for the four background subtraction methods. The residuals are reduced compared to the fit without a Gaussian component, but not as much as for the other regions of interest given them being already very flat in the fit without Gaussian component.

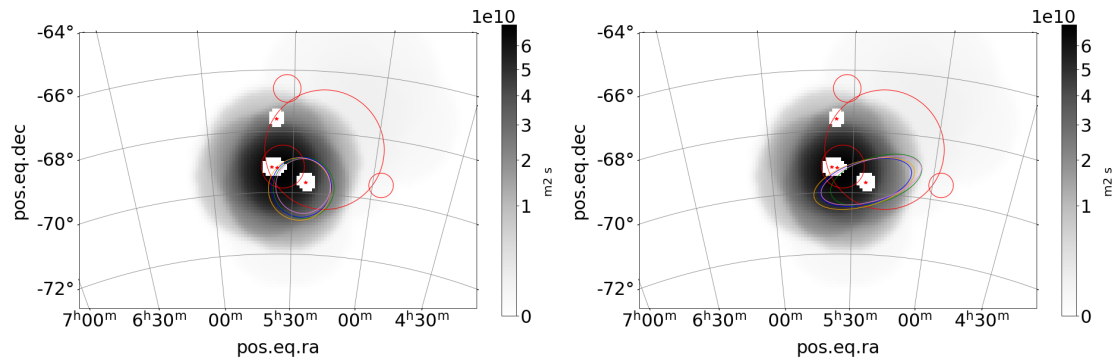


Figure 6.38: Best-fit components for LMC overlaid on the exposure map with masked sources. Red stars: Known H.E.S.S. sources. Red circles: *Fermi* components discussed in section 5.2 obtained with the analytic model. Green component: Best-fit component from *Method A*. Blue component: Best-fit component from *Method B*. Orange component: Best-fit component *Method C*. Violet component: Best-fit component from *Method D*. Left: Fitting a symmetric Gaussian component to the excess. Right: Fitting an asymmetric Gaussian component to the excess.

## 6.4 Physical interpretation of the excess seen in the Large Magellanic Cloud

After having discussed the four datasets and the results of the analysis on them, it turns out that the only dataset in which significant emission, beside the one from the known sources, can be seen is the Large Magellanic Cloud dataset. For this reason, the results obtained from this dataset are discussed in more detail in this section in order to get from a significant excess in a given region to a more physical interpretation by interpreting its position and going from counts space to flux space.

### 6.4.1 Position

First of all, I start by discussing the position of the observed excess. Figure 6.38 shows again the exposure in the LMC dataset used in this study. However, this time the best-fit Gaussian *Fermi*-LAT components obtained with their analytic model as discussed in section 5.2 are overlaid. It is immediately visible that the exposure used in this analysis is very inhomogeneous across LMC. This is due to most observations having been taken close to the known H.E.S.S. sources. Indeed, most of the exposure is acquired in the lower left part of the map, leading to a strong difference in exposure at the positions of the different *Fermi*-LAT components. The exposure is very low at the positions of the component G4 (at low right

ascension) and of component G3 (at high declination). And also, parts of the large G1 component are at low exposure. G2 on the other hand is right at the centre of the exposure, however a big part of it is covered by the masks on N 157B and 30 Dor C, which might reduce the sensitivity of my analysis to a component at this position. Due to very different exposure, the sensitivity at the positions of the different components varies a lot. Especially for the large component G1, it would be possible to see only part of it with H.E.S.S. However, beside this difference in sensitivity, H.E.S.S. is of course also sensitive to higher energies than *Fermi*-LAT, and so the morphology and components can also be expected to be intrinsically different.

In addition to the *Fermi*-LAT Gaussian components and the known H.E.S.S. sources, the best-fit components found in the previous section are also overlaid, once for the fit of a symmetric Gaussian component and once for the fit of an asymmetric Gaussian component. This shows once more how well the morphology of the components obtained with the different background subtraction methods agree with each other. However, it also shows where the components lie with respect to the acquired exposure. The components do not lie at the centre of the exposure, but more displaced towards South-West. They extend towards very low exposure regions, even more for the fit of the asymmetric Gaussian component. This opens the question, raised already earlier, whether the edge of the high significance region I see is really the edge of the physical emission or whether it is just limited by very low exposure region. This question cannot be answered here, one would need more data to cover the missing parts of LMC. For now, one needs to take into account that the excess seen in this analysis might only be a part of the physical component present in LMC.

The same *Fermi*-LAT and best-fit components are shown in figure 6.39 above an optical sky map. Whereas the *Fermi*-LAT components cover the whole LMC, the H.E.S.S. component seems to be more limited to a smaller region of the LMC. As discussed before, this is among other due to the limited exposure in this analysis. However, one can see that the H.E.S.S. component is spatially coincident with the brightest part of LMC. This correlation can already be seen when fitting the symmetric Gaussian component, but it is even more the case when fitting the asymmetric Gaussian component.

This correlation with the brightest region of LMC leads to the question if there is any correlation with night sky background. The night sky background seen by H.E.S.S. can be estimated from the pedestal width [101]. The higher the night sky background the wider the observation pedestals due to the statistical fluctuation of the light seen from the night sky background. The night sky background rate  $f_{NSB}$  can then be estimated with the following formula:

$$f_{NSB} = \sqrt{RMS_P^2 - RMS_0^2 - \sigma_{\gamma_e}^2/\tau}, \quad (6.8)$$

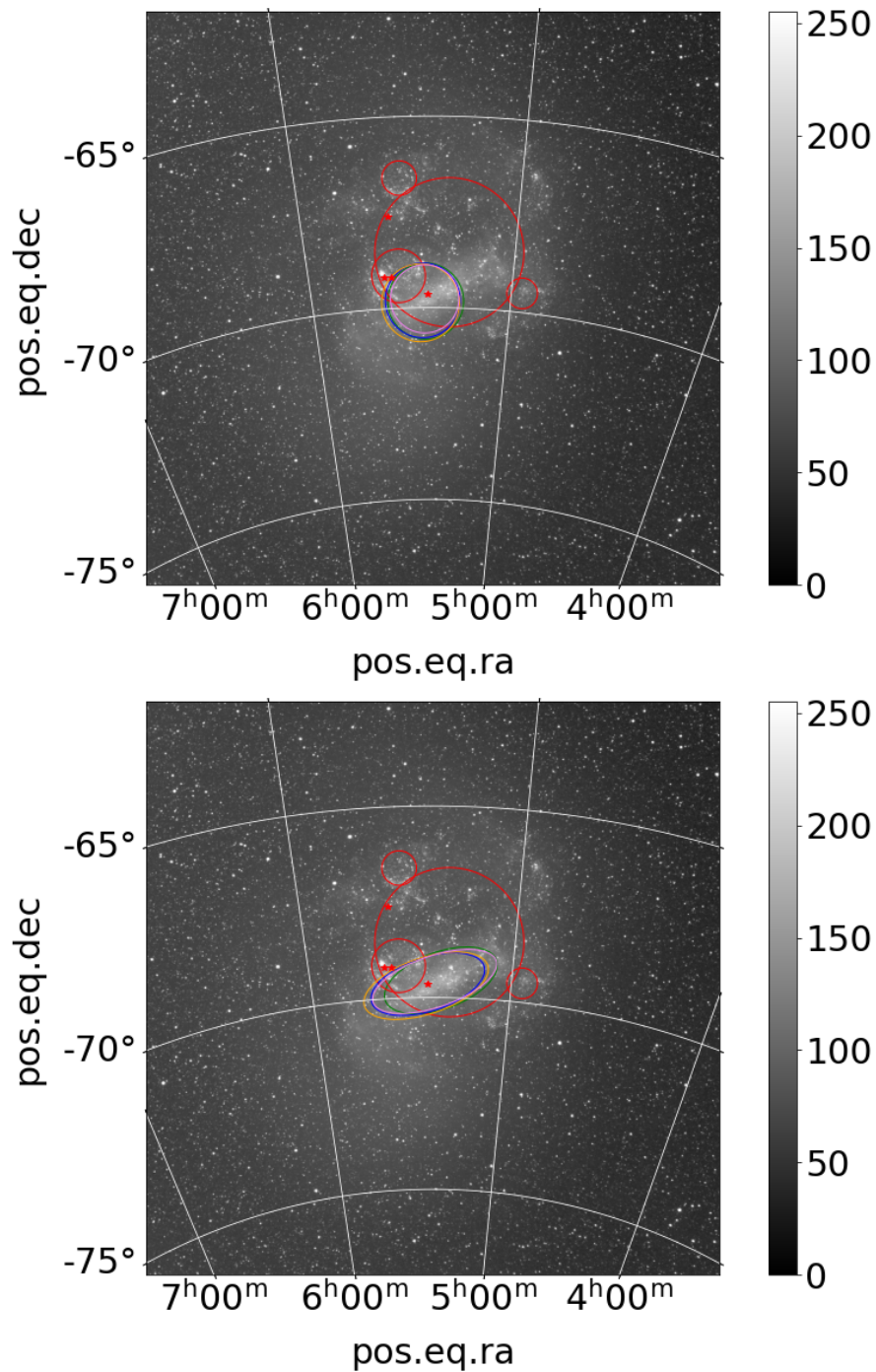


Figure 6.39: Best-fit components for LMC over optical sky map. Red stars: Known H.E.S.S. sources. Red circles: *Fermi* components discussed in section 5.2 obtained with the analytic model. Green component: Best-fit component from *Method A*. Blue component: Best-fit component from *Method B*. Orange component: Best-fit component *Method C*. Violet component: Best-fit component from *Method D*. Top: Fitting a symmetric Gaussian component to the excess. Bottom: Fitting an asymmetric Gaussian component to the excess. Retrieved from [164].

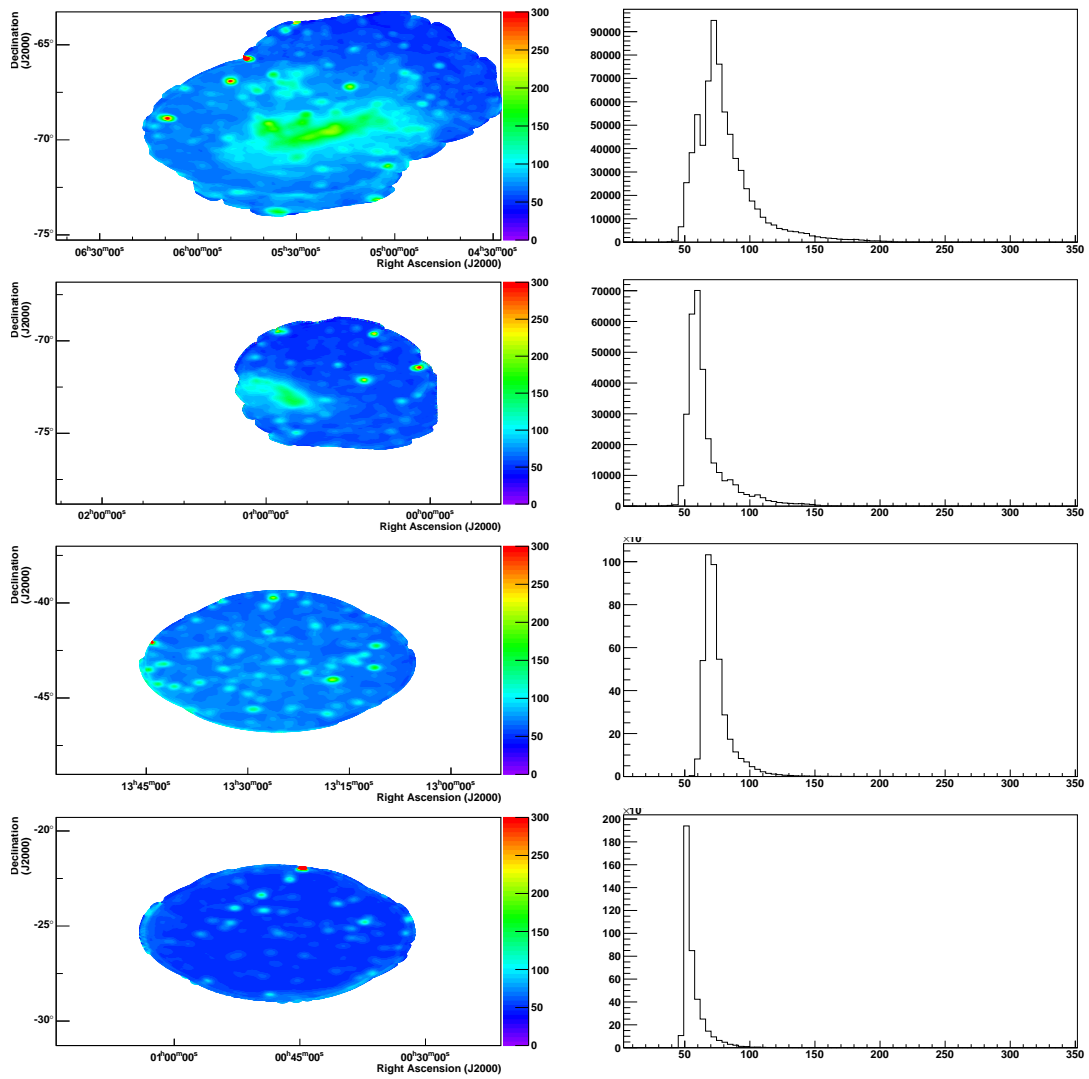


Figure 6.40: Night sky background maps (left) and night sky background in pixels (right) for LMC, SMC, Cen A and NGC 253 (from top to bottom).

where  $RMS_P$  is the width of the observation pedestal,  $RMS_0$  the width of the electronic pedestal determined with closed camera lid in the shelter as described in subsection 2.3.1,  $\sigma_{\gamma e}$  the width of the single electron peak and  $\tau$  the readout window. Figure 6.40 shows the night sky background maps for the four analysed sources as estimated from the high gain pedestal width and its distribution over pixels. LMC and SMC indeed show extended brighter regions compared to Cen A and NGC 253, where there are only localized bright spots corresponding to stars. In addition, the brighter region in LMC coincides with the seen excess. However, for SMC there is a similar high night sky background region where no excess can be seen. In addition, the high night sky background region in LMC reaches values of about 200 MHz, which is not particularly high as in the galactic plane night sky backgrounds up to 300 MHz are frequently reached [113] and as discussed in section 5.5, the night sky background is taken into account in the run-wise simulations and almost no correlation between night sky background and the background normalization could be found in the systematics study.

The brightest region of the LMC is also the region the most crowded with stars and optical emissions, and so a region with high activity. This is also indicated by the presence of already four gamma-ray sources in or very close to this region (N 157B, 30 Dor C, N 132D and PSR J0540-6919). So, it is not completely unexpected that the cosmic-ray density might correlate with this region as cosmic-ray sources often also produce gamma rays or photons in other energy bands. So, in the following, I discuss other possible correlations of the seen excess with other features of the LMC.

As mentioned earlier, interstellar diffuse emission is expected to be of either hadronic or leptonic origin and a full leptonic origin of the components seen by *Fermi*-LAT is difficult to accommodate with the absence of emission in other spectral bands and the absence of a strong interstellar radiation field necessary for Inverse Compton scattering. Hadronic diffuse emission though would not be expected to be so much correlated with the light distribution inside a galaxy, but rather with the gas distribution as hadronic diffuse emission is produced by the interaction of cosmic rays with interstellar gas. For this reason, a neutral hydrogen gas column density map of the LMC is shown in figure 6.41. This gas map has been constructed from observation of the 21 cm emission line of neutral atomic hydrogen in the radio band. It combines data from two radio experiments, namely data from the multibeam receiver of the Parkes telescope in Australia, which is sensitive to large scale structures, published in [165] and data from the Australia Telescope Compact Array (ATCA) using the aperture synthesis technique, which is sensitive to small structures, published in [166] in order to achieve an optimal sensitivity to both small and large scales. These two datasets have then been merged in [167] using a Fourier-plane technique to get the map shown on the figure.

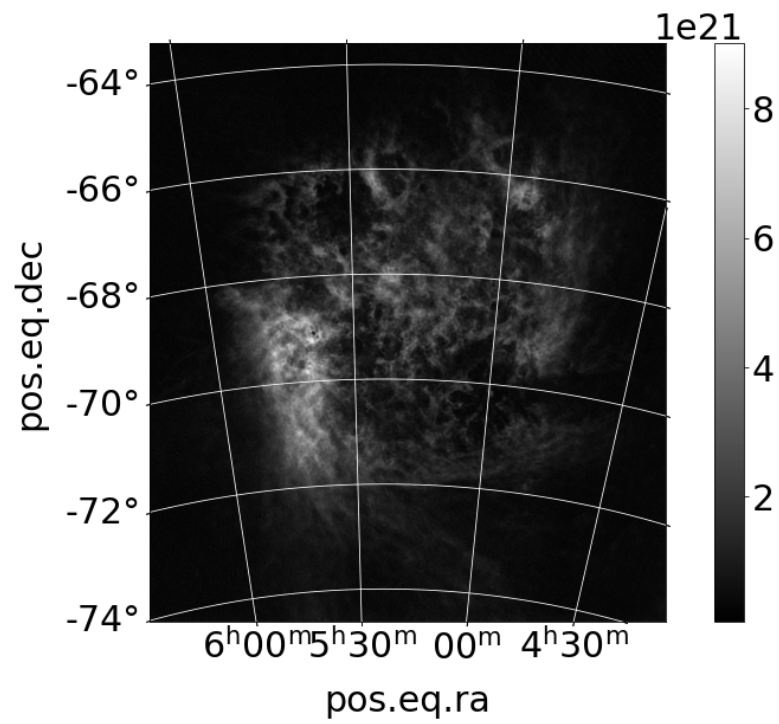


Figure 6.41: Neutral hydrogen column gas density map of LMC obtained in a combination [167] of Parkes [165] and ATCA [166] measurements of the 21 cm emission line of hydrogen.

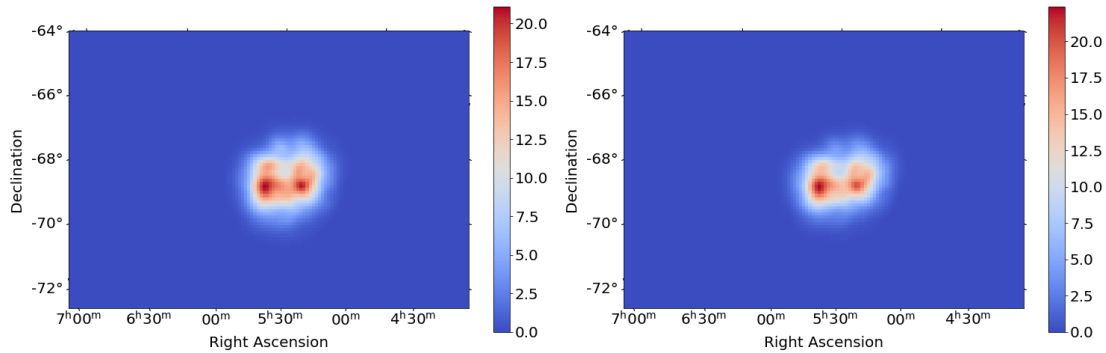


Figure 6.42: Counts map of the best-fit emissivity component using *Method D*. Left: Gaussian multiplied with neutral hydrogen column gas density map. Right: Asymmetric Gaussian multiplied with neutral hydrogen column gas density map.

This gas map is also part of the *Fermi*-LAT emissivity model presented earlier in section 5.2. Indeed, the gas map used to build-up the *Fermi*-LAT emissivity model was a combination of a gas map from three different hydrogen species, the atomic hydrogen, the molecular hydrogen and the ionized hydrogen. For the atomic hydrogen, which makes up the major part of the gas in the LMC, they use the same gas map as I show in figure 6.41 which encompasses the major part of the gas in the LMC.

In the following, I follow a similar procedure as *Fermi*-LAT in their emissivity model and convolve the gas map with a Gaussian (or an asymmetric Gaussian) by multiplying the component with the gas column density in each pixel and then fit this multiplied model to the observed LMC data. I still assume that the multiplied component represents the emission morphology and thus fold this component with the IRFs and the exposure. Under the assumption that the neutral hydrogen gas distribution traces the total gas distribution and that interstellar diffuse emission is produced in the interaction of this gas with the cosmic rays, the parameters of the best-fit model then directly describe the emissivity, i.e., the gamma-ray emission rate per hydrogen atom per unit energy per solid angle [129], from a given direction on the sky and so give a direct handle to the cosmic ray distribution in the LMC. This however neglects inhomogeneities in the gas and cosmic ray distribution over the line of sight.

The resulting counts maps for the fit of such an emissivity component are shown in figure 6.42, on the left for a symmetric Gaussian base model and on the right for an asymmetric one. Here only the results from *Method D* are considered, as it is not impacted by the overestimation of the background normalizations as *Method B* and also not fully relying on the background normalizations from the run-wise simulations and their systematic uncertainties as *Method A*. From the figure, it is

Source <i>Method</i> Gaussian spatial model	LMC	
	<i>D</i>	
	Symmetric	Asym.
Fit overall background normalization	1.00	1.00
Fit parameters of model		
Right ascension [°]	80.96	80.72
Declination [°]	-69.82	-69.74
Extension / Semi-major axis [°]	0.7634	0.8613
Semi-minor axis (derived) [°]	/	0.6624
Eccentricity	/	0.6392
Orientation with respect to right ascension axis [°]	/	-77.71
$\Delta$ TS w.r.t. non-multiplied model	27.10	-16.18
Corresponding statistical significance	$5.2\sigma$	$4.0\sigma$ worse
$\Delta$ TS w.r.t. fit without any extended component	197.70	204.05
Corresponding statistical significance	$13.9\sigma$	$14.0\sigma$
Comparison to $\Delta$ TS of non-multiplied model w.r.t. fit without any extended component	170.60	220.23
Corresponding statistical significance	$12.9\sigma$	$14.6\sigma$
Ratio of total counts in model [%]	3.17	3.03

Table 6.8: Fit results for the Gaussian and the asymmetric Gaussian multiplied with the gas map: Fit overall background normalization, fit parameters, improvement or degradation in TS and statistical significance with respect to the fit with the non-multiplied Gaussian (or asymmetric Gaussian) and the fit without an extended model and ratio of total counts in the model. In addition, the improvement in TS when adding a simpler geometric component to the background-only fit which was already indicated in table 6.5 and 6.6 is indicated for comparison.

immediately visible that, as expected, the shape is much more irregular than for the fit of a simpler geometric model. The difference in the counts map for using a symmetric and an asymmetric Gaussian base model is also much less significant than previously, as the Gaussian model has already gotten an extended shape through its multiplication with the gas map. The actual fit overall background normalization, parameters of the best-fit model, improvement or degradation of TS and statistical significance with respect to the simpler geometric model not multiplied with the gas map and the background-only fit and ratio of counts in the model are shown in table 6.8. Comparing the best-fit parameters to the parameters found earlier when not multiplying with the gas map the best-fit position of the Gaussian emissivity component is much closer to the value found for the asymmetric Gaussian and the eccentricity for the asymmetric Gaussian is much lower. This is due to the Gaussian component gaining some asymmetry when multiplying it with the gas map leading to the Gaussian emissivity component fit being closer to the asymmetric Gaussian fit and the additional asymmetry needed for the asymmetric Gaussian emissivity component being less. This lower eccentricity for the asymmetric Gaussian emissivity component also has a direct impact on the semi-major axis whose value is now much closer to the one of the semi-minor axis. Comparing the TS value of the emissivity component with the one of the simple component, one sees that there is a strong improvement of TS by 27.10 for the Gaussian component when going to the emissivity model whereas there is a degradation by 16.18 for the asymmetric Gaussian component. This is due to the difference in TS between the symmetric and asymmetric component fit being only 14.35 when multiplying them with the gas map compared to 49.63 when not multiplying them. So, multiplying with the gas map leads the symmetric Gaussian to get an asymmetric shape and improves the fit, but deteriorates the fit for the asymmetric Gaussian. The difference in TS with respect to a background-only model is (as mentioned earlier) summarized in table 6.8.

Given the contradictory results for the symmetric and asymmetric Gaussian, it is difficult to draw a conclusion on how well the interstellar diffuse emission is correlated with the gas. On one side the gas map leads to the correct asymmetric shape of the emission, on the other side it does not seem able to reproduce the smaller structures better than a purely geometric model and a similar asymmetry is also seen in the optical map of LMC and could so be a general feature not only present in the gas map. In addition, the change in the TS value is not larger than the change in TS found in the systematics studies, as was already the case for the symmetric and asymmetric geometric Gaussian component. So, the preference for any of the four models is not above the current systematics level of the used run-wise simulation-based background subtraction.

The best-fit emissivity component is centred close to N 132D (which has a

position of  $(81.26^\circ, -69.64^\circ)$  [168], however as discussed earlier it is possible that due to the very inhomogeneous exposure only part of the component is visible in this analysis and that the component extends over a much larger part of LMC. For this reason and also because the best-fit component is in a very crowded region, it is hardly possible to identify the cosmic ray source(s) injecting the cosmic rays producing the interstellar diffuse emission. This all the more, as I only identified one extended component in this analysis which prevents a statistical analysis of the presence of a certain source type in the components which has been tried in the *Fermi*-LAT analysis.

However as discussed, it is not at all certain that the observed emission is of hadronic origin. Indeed, the emission or part of it could well be of leptonic origin. However, for the same reasons as before, it is difficult to find the source of injection of these leptons. Moreover, leptonic interstellar diffuse emission is expected to be more concentrated around the sources of leptons due to radiative losses and so less correlated with the radiation field or gas density on larger scales. For that reason, an emissivity approach as for the hadronic component does not make so much sense as one would expect the emission to be more sensitive to the local variation of the lepton density.

A completely different possibility would be that the extended emission seen with H.E.S.S. is not originating from genuine interstellar diffuse emission, but due to unresolved sources. However, unresolved sources are much more difficult to model than a single Gaussian component as each unresolved source introduces at least three new parameters. For this reason a rough estimate for the number of necessary sources was made from the 68 % containment radius of a single point source. This 68 % containment radius is less than  $0.1^\circ$  compared to an extension of  $0.89^\circ$  for the best-fit Gaussian leads to the necessity of about 80 point-like sources to cover the whole area of the Gaussian within its 1-sigma contour with point-like sources assuming they only significantly contribute within their 68 % containment radius. However, this first approximation neglects the contribution of point-like sources outside of their 68 % containment radius, emission from the known sources inside the Gaussian (N 132D, N 157B and 30 Dor C) which have even more significant emission outside their 68 % containment radius and for N 132D are even inside the Gaussian, and that the Gaussian is only a best fit and so parts of it might not have a significant signal. Nevertheless, it shows that at least a two-digit number of sources is needed to describe the observed excess with point-like sources. Considering extended unresolved sources would reduce the number of needed sources, however this was not investigated further as it would make the modelling even harder and it is also not possible to distinguish interstellar diffuse emission from unresolved sources and so to decide on which extension to set the boundary from the modelling alone.

In conclusion of this discussion on the spatial position of the seen excess and its potential origin, the very inhomogeneous exposure of the H.E.S.S. dataset used in this analysis and the systematic uncertainties of the method, make it impossible to conclude whether the observed excess is more likely to be of hadronic origin, leptonic origin, due to unresolved sources or a combination of multiple of these contributions. This said, the extension of the excess seems to make at least a two-digit number of point-like sources, or extended sources, necessary to describe it solely by unresolved sources. For the same reasons, any the spatial correlation with sources injecting cosmic rays could also not been determined.

## 6.4.2 Flux

### Forward folding method

I tried to compute the fluxes in the component using a forward folding method. Indeed, as discussed earlier in section 5.5, there is no energy information in the background models, and for this reason the spectral shape (including the photon index) cannot be determined. For this reason, I first assume a spectral shape for the best-fit spatial component, here power-law spectra with different photon indices. Then, for each individual run, using the energy dependent point spread function, a three-dimensional exposure map with 20 energy bins between 250 GeV and 25 TeV on a logarithmic scale and a three-dimensional energy dispersion map with the same energy binning, I compute the expected total number of counts in the best-fit component for a given spectral model normalization. Afterwards, I add the number of predicted counts over all the runs in the analysis. This leads to a prediction of the expected number of counts for the given flux and the best-fit spatial model. Scaling the flux normalization by the ratio of the predicted counts by the counts in the best-fit model, leads then to a prediction of the flux in the best-fit model under the assumed spectral model (Rule of three). I obtain an estimation of the uncertainty on this flux from the uncertainty on the amplitude obtained from the fit.

### Cross Check on known sources

After having shown that there is no indication for extended emission in the Cen A or NGC 253 region of interest, these regions are well suited to check if the flux determination method allows to reconstruct fluxes of point sources correctly. Indeed, if there is no extended emission, there is no risk of confusing flux from the extended emission with flux from the source. In addition, it is easy to unmask Cen A, 1ES 1312-423 and NGC 253 with leaving the other known H.E.S.S. sources masked, which would not be possible for the overlapping sources N 157B and 30

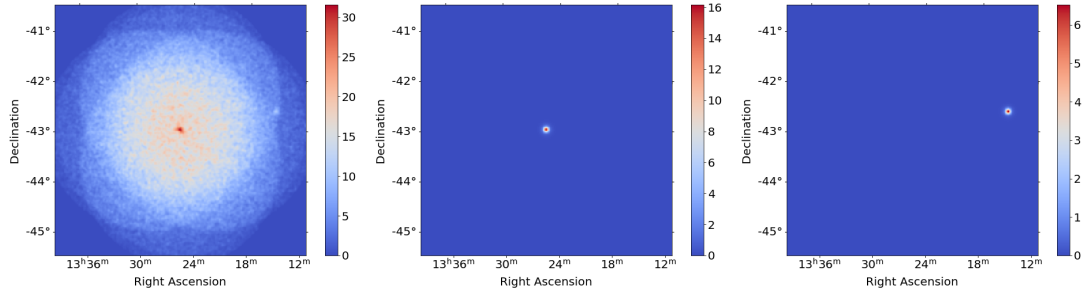


Figure 6.43: Left: Counts map of the Cen A region used for the fit and spectral determination of Cen A and 1ES 1312-423. Centre: Best-fit model of Cen A. Right: Best-fit model of 1ES 1312-423. The colour scale indicates the number of counts in each bin.

Dor C. Cen A, 1ES 1312-423 and NGC 253 are so natural test beds for the spectral determination method. As all of these sources are point sources, it is not necessary to use such an extended sky map for the fit of the point-like source. This allowed me to go to a less extended sky map with finer binning ( $0.02^\circ$ ) for the second part of the analysis and so to better take into account the extension of the H.E.S.S. PSF in the sky map. For this comparison, I use *Method D* again. For the fit of the background normalizations, I still use the same extended sky map with a  $0.1^\circ$  binning.

The sky map used for the determination of the best-fit component and the spectrum of Cen A is shown on the left of figure 6.43. Except for the smaller extension skymap in the second fit, the procedure is exactly the same as the one used for the detection of extended emission earlier. Instead of a Gaussian model, I used a point-like model for sources with three free parameters, namely the two position coordinates and the amplitude. For the fit of Cen A, I masked 1ES 1312-423 again. This led to the best-fit component shown on the centre of figure 6.43. The best-fit right ascension was  $201.370^\circ$  and the best-fit declination  $-43.006^\circ$ , which is in excellent agreement with the latest published H.E.S.S. values of  $201.376^\circ$  and  $-43.004^\circ$  [161]. Then, I forward-folded the power-law spectrum with a photon index of 2.52 and a flux normalization of  $1.49 \times 10^{-13} \text{ cm}^{-2} \text{ s}^{-1} \text{ TeV}^{-1}$  at 1 TeV of Cen A as found in [169] with the instrument response functions to get an expected number of counts of 306.66 compared to 431.46 counts in the best-fit point-like model. This means that the flux of Cen A is overestimated by 41% using this forward-folding method. From the fit results, the relative uncertainty on the amplitude of the best-fit component is about 9%, meaning that the systematic discrepancy of 41% indicates that there are systematic uncertainties above the statistical uncertainty. These systematic uncertainties are discussed in more detail after having discussed the results for the other sources. These results for all the

	Relative uncertainty on the amplitude from the best-fit component	Overestimation of flux
Cen A	9 %	41 %
1ES 1312-423	13 %	31 %
NGC 253	13 %	18 %
N 157B	15 %	14 %
N 132D	14 %	21 %

Table 6.9: Table summarizing the relative uncertainty from the best-fit component and the systematic overestimation of the flux for the different point sources on which the forward folding method has been tested.

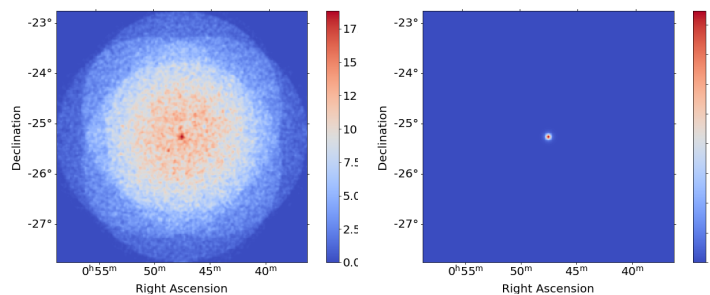


Figure 6.44: Left: Counts map of the NGC 253 region used for the fit and spectral determination of NGC 253. Right: Best-fit model of NGC 253.

considered sources are summarized in table 6.9.

I followed the same procedure for 1ES 1312-423 on the same region of interest, this time with Cen A masked. This led to the best-fit component shown on the right of figure 6.43. The best-fit right ascension was  $198.776^\circ$  and the best-fit declination  $-42.617^\circ$ , which agrees within uncertainties with the values published by H.E.S.S. in [170] of  $198.744^\circ$  and  $-42.597^\circ$ . Then again, I forward-folded the power-law spectrum with a photon index of 2.85 and a flux normalization of  $1.89 \times 10^{-13} \text{ cm}^{-2} \text{ s}^{-1} \text{ TeV}^{-1}$  at 1 TeV of 1ES 1312-423 as found in [170] with the instrument response functions. This led to an expected number of counts of 128.53 compared to 168.04 counts in the best-fit point-like model. This means that the flux of 1ES 1312-423 is overestimated by 31 % using this forward-folding method. From the fit results, the relative uncertainty on the amplitude of the best-fit component is about 13 %, and so the discrepancy is again much bigger than the statistical uncertainty.

The sky map of the NGC 253 region used for the determination of the best-fit component and the spectrum is shown on the left of figure 6.44. Then, I followed again the same procedure as for Cen A and 1ES 1312-423, this time with no

masked source as NGC 253 is the only known gamma-ray source in the region of interest, to get the best-fit counts map shown on the right of figure 6.44. The best-fit right ascension was  $11.887^\circ$  and the best-fit declination was  $-25.290^\circ$ , which is in excellent agreement with the latest values published by H.E.S.S. in [52] of  $11.886^\circ$  and  $-25.290^\circ$ . I forward-folded the power-law spectrum with a photon index of 2.39 and a flux normalization of  $1.34 \times 10^{-13} \text{ cm}^{-2} \text{ s}^{-1} \text{ TeV}^{-1}$  at 1 TeV of NGC 253 as found in [52] with the instrument response functions. This led to an expected number of counts of 190.66 compared to 225.84 counts in the best-fit point-like model. This means that the flux of NGC 253 is overestimated too using this forward-folding method, namely by 18%. From the fit results, the relative uncertainty on the amplitude of the best-fit component is 13% and so the discrepancy is again bigger than the statistical uncertainty, even though not so much as in the Cen A region of interest.

As mentioned earlier in this subsection, the situation is much more complicated in the LMC as there is expected to be interstellar diffuse emission and source confusion between N 157B and 30 Dor C. This might lead to wrongly attribute part of the flux to a wrong source and so to higher uncertainties. Nevertheless, keeping only N 132D and LMC P3 masked and introducing a Gaussian model for the extended emission and two point-like models for N 157B and 30 Dor C, and using the same forward-folding procedure than before, leads to an over-estimation by 14% of the flux of N 157B. From the fit results, the relative uncertainty on the amplitude of the best-fit component is about 15%. Keeping N 157B, 30 Dor C and LMC P3 masked and introducing a Gaussian model for the interstellar diffuse emission, and using the same forward-folding procedure than before, leads to an over-estimation by 21% of the flux of N 132D. From the fit results the relative uncertainty here is about 14%.

So there seems to be a general tendency to over-estimate the flux using the previously described forward-folding method as summarized again in table 6.9. A similar behaviour has been seen in other run-wise analyses too, even when using a different flux reconstruction method. This was traced back to a mismatch between the effective areas obtained with classical Monte-Carlo simulations and run-wise Monte-Carlo simulations of about 20% whose origin is currently<sup>2</sup> unclear and under investigation. From the obtained fluxes for the known point sources, it seems that this analysis is indeed impacted by this problem and so that the reconstructed fluxes are systematically over-estimated.

However, beside this issue, I am here trying to assess the flux from one energy

---

<sup>2</sup>Currently here means at the time of finalizing the first version of this thesis manuscript in October 2021. In the meantime, this issue has been further investigated and the mismatch has been reduced to less than 10% [171]. The mismatch was mainly due to a double counting of dead time in run-wise simulations. These recent new findings could unfortunately not be incorporated in this thesis anymore.

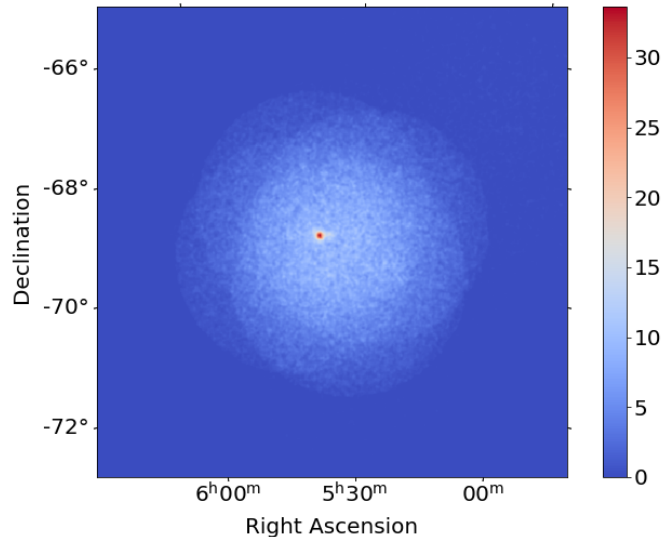


Figure 6.45: Counts map of LMC used for the flux determinations.

bin. This assumes that the run-wise simulations correctly describe the energy dependence of the real background events with high accuracy and also that the energy dependence of the instrument response functions are known very accurately. Small differences can here have huge impacts as an inaccurate description in a small energy range propagates to the whole energy range as there is no record at which energies events have been recorded. For this reason, the creation of energy-dependent background models from run-wise simulations is necessary to get more reliable flux values and also an entire energy spectrum instead of the flux normalization. This would also allow to test different spectral hypotheses, discuss the photon indices and make more meaningful spectral comparisons with experiments in other energy ranges such as *Fermi-LAT* as i discussed in chapter 7. This means that there might be additional systematic uncertainties beside the 20 % uncertainty seen in other analyses, as is already indicated by the Cen A result where the over-estimation is more than this 20 %.

### Results for Gaussian and asymmetric Gaussian component in LMC

I used this forward-folding method to estimate the fluxes in the best-fit components on the LMC extended emission obtained from *Method D*. For consistency reason with the point source cross-check, I did this again with a finer binning of the sky map of  $0.02^\circ$ , however using this time a sky map extended enough to encompass the whole exposure. This sky map is shown in figure 6.45 and performing the fit based on this counts map with new binning only slightly changed the values of the best-fit

Photon index	Differential flux at 1 TeV and its uncertainty [ $10^{-12} \text{ cm}^{-2} \text{ s}^{-1} \text{ TeV}^{-1}$ ]	
	Best-fit Gaussian	Best-fit asymmetric Gaussian
2.0	$13.1 \pm 2.1$	$19.6 \pm 3.4$
2.2	$14.5 \pm 2.3$	$21.8 \pm 3.8$
2.4	$15.8 \pm 2.5$	$23.6 \pm 4.1$
2.6	$16.7 \pm 2.7$	$25.0 \pm 4.3$
2.8	$17.3 \pm 2.8$	$25.9 \pm 4.5$

Table 6.10: Differential flux at 1 TeV in the best-fit component assuming a power-law spectrum for different photon index assumptions: 2.0, 2.2, 2.4, 2.6 and 2.8. The first column indicates the assumed photon index, the second column the differential flux for the best-fit symmetric Gaussian component and its statistical uncertainty obtained from the relative uncertainty of the best-fit uncertainty and the third column the differential flux for the best-fit asymmetric Gaussian component and its statistical uncertainty obtained from the relative uncertainty of the best-fit uncertainty. All values are given for the background subtraction using the background normalizations from *Method D*.

parameters for the different components. For the two different parametrizations of the best-fit component, i.e., the symmetric Gaussian and the asymmetric Gaussian, I performed the forward-folding for different photon indices for the assumed power-law spectrum as the photon index of the extended component is unknown. I used indices of 2.0, 2.2, 2.4, 2.6 and 2.8 even though interstellar diffuse emission would be rather expected to be at the low end of this photon index range as mentioned before, as there are point sources having such high photon indices.

The reconstructed differential fluxes at 1 TeV for the different photon index assumptions and their statistical uncertainties are shown for the two spatial models in table 6.10. In addition, the right of figure 6.46 shows how the spectra reconstructed from these differential fluxes would look like (using the photon indices input in the forward-folding procedure) whereas the left shows the best-fit spatial component from which these spectra are derived. It can be seen that the reconstructed flux takes very similar values for the different models in the H.E.S.S. sensitive range (as is expected) and that the spectra almost cross in one single point a bit below 1.4 TeV which is quite in the centre of the sensitive range of this analysis whereas as expected the extrapolation to lower energies depends more on the assumed photon index. From the table, one can see that the reconstructed fluxes are of the order of magnitude of  $10 \times 10^{-12} \text{ cm}^{-2} \text{ s}^{-1} \text{ TeV}^{-1}$  and so higher by an order of magnitude or more than the fluxes of the point sources in the LMC, even than the one of N 157B which has a flux of  $1.3 \times 10^{-12} \text{ cm}^{-2} \text{ s}^{-1} \text{ TeV}^{-1}$  [53]. However, N 157B is a point source with respect to the H.E.S.S. point spread function and

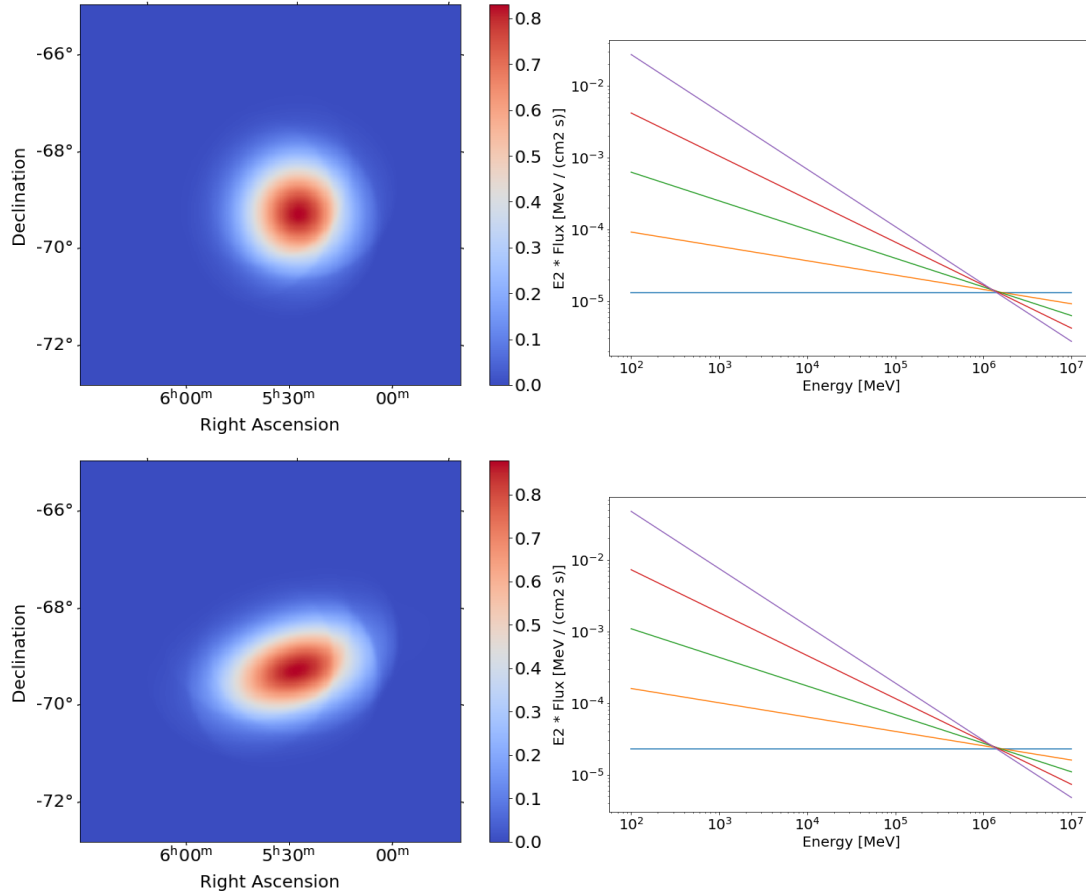


Figure 6.46: Top left: Counts map of the best-fit Gaussian component on the LMC extended emission. Top right: Differential spectrum constructed from the computed differential flux in the best-fit Gaussian component using the power-law spectral model input in the forward-folding procedure. Bottom left: Counts map of the best-fit asymmetric Gaussian component on the LMC extended emission. Bottom right: Differential spectrum constructed from the computed differential flux in the best-fit asymmetric Gaussian component using the power-law spectral model input in the forward-folding procedure. The different colours on the right plots indicate the different photon indices used in the forward-folded models (from bottom to top left of the crossing): Blue: 2.0. Orange: 2.2. Green: 2.4. Red: 2.6. Violet: 2.8.

Source <i>Method</i>	LMC			
	<i>D</i>			
Overall background normalization	Free	1.05	1.02	0.95
Fit parameters of Gaussian				
Right ascension [°]	81.57	80.71	81.34	81.46
Declination [°]	-69.77	-69.65	-69.72	-69.83
Extension [°]	0.9180	0.5295	0.7463	1.6937

Table 6.11: Fit Gaussian parameters under different assumptions for the overall background normalizations: Free overall background normalization and background normalizations scaled by 1.05, 1.02 and 0.95.

so its flux at source position reaches a much higher value than is reached locally in the extended component. The differential flux at 1 TeV also increases with the assumed photon index, which is due to the almost crossing at 1.4 TeV (mentioned before). The relative statistical uncertainty, as obtained from the uncertainty on the best-fit amplitude of the Gaussian and the asymmetric Gaussian component in the second fit (during which the (asymmetric) Gaussian component and the overall background normalization is fit), is 16% for the symmetric Gaussian component and 17% for the asymmetric Gaussian component. So, the statistical uncertainty is lower than the systematic uncertainties previously found in the reconstruction of the spectra of the point-like sources.

### Influence of background normalizations

However, any uncertainty coming from the background models has a much higher impact on extended sources than on point-like sources as the number of background counts increases with region size. This increased systematic uncertainty is not included in the systematic uncertainties found in the reconstruction of the spectra of the point-like sources. For this reason, I performed a study of the dependence of the flux on the background normalization. I adjusted the background normalizations of the individual runs as before. However, in the second step where up to now I adjusted the model together with the overall background normalization on the stacked dataset, leading to fit values for the overall background normalization very close to 1, I now fix the background normalization to 0.95, 1.02 and 1.05. This allows me to study the behaviour of the fit under this different background normalizations.

The values of the parameters of the best-fit symmetric and asymmetric Gaussian component under this different background normalization assumptions are shown in table 6.11 and table 6.12. In these tables, column 2 (free overall background normalization) corresponds to the fit as performed up to now, using *Method*

Source <i>Method</i>	LMC			
	<i>D</i>			
Overall background normalizations	Free	1.05	1.02	0.95
Parameters of asymmetric Gaussian				
Right ascension [°]	80.85	80.60	80.84	78.21
Declination [°]	-69.58	-69.61	-69.60	-68.97
Semi-major axis [°]	1.7196	0.9657	1.3003	4.0109
Semi-minor axis (derived) [°]	0.6887	0.3845	0.5264	1.1675
Eccentricity	0.9163	0.9173	0.9144	0.9567
Orientation w.r.t. right ascension axis [°]	-70.58	-79.85	-74.45	-59.61

Table 6.12: Fit asymmetric Gaussian parameters under different assumptions for the overall background normalizations: Free overall background normalization and background normalizations scaled by 1.05, 1.02 and 0.95.

$D$  as for the results presented in table 6.10. The slight difference between the values of the parameters in these tables and tables 6.5 and 6.6 is due to the different binning of the sky map for the determination of the flux ( $0.02^\circ$  - used in this subsection 6.4.2) in order to be consistent with the determination of the flux of the point sources and the sky map used earlier ( $0.1^\circ$  - used in the rest of the thesis). The other columns show the best-fit parameters for the different background normalization assumptions. The most striking difference is the extension which increases as the normalization decreases. This was to be expected as the higher the background normalization, the bigger the part of the (physical or non-physical) excess that is cut away by the background subtraction and the lower the background normalization, the more of the background going into the (asymmetric) Gaussian. The best-fit positions of the components agree rather well, even though they are not fully consistent within the uncertainties obtained from the fit. The best-fit asymmetric Gaussian for the overall background normalization being 0.95 is the one exception to this. This is most likely due to this component fitting a big part of the region of interest and so rather fitting the background, as it was the case for NGC 253. The eccentricity and the orientation also agree rather well for the asymmetric Gaussians except for the same exception. This shows that the positions and orientations of the best-fit components are rather stable against a change of the background normalizations.

The reconstructed fluxes using the forward-folding method for the same four overall background normalizations are shown in table 6.13. One can immediately see that the reconstructed flux strongly depends on the background normalization. Indeed, for the systematic uncertainty of less than 5% on the average background normalization for a given field of view (obtained from the best-fit normalization

Bkg Norm	Photon index	Differential flux at 1 TeV and its uncertainty [ $10^{-12} \text{ cm}^{-2} \text{ s}^{-1} \text{ TeV}^{-1}$ ]	
		Best-fit Gaussian	Best-fit asymmetric Gaussian
Free	2.0	$13.1 \pm 2.1$	$19.6 \pm 3.4$
	2.2	$14.5 \pm 2.3$	$21.8 \pm 3.8$
	2.4	$15.8 \pm 2.5$	$23.6 \pm 4.1$
	2.6	$16.7 \pm 2.7$	$25.0 \pm 4.3$
	2.8	$17.3 \pm 2.8$	$25.9 \pm 4.5$
Fixed to 1.05	2.0	$3.0 \pm 0.5$	$4.0 \pm 0.7$
	2.2	$3.3 \pm 0.5$	$4.4 \pm 0.7$
	2.4	$3.6 \pm 0.6$	$4.8 \pm 0.8$
	2.6	$3.8 \pm 0.6$	$5.1 \pm 0.9$
	2.8	$4.0 \pm 0.7$	$5.2 \pm 0.9$
Fixed to 1.02	2.0	$7.6 \pm 0.8$	$9.7 \pm 1.2$
	2.2	$8.5 \pm 0.9$	$10.8 \pm 1.3$
	2.4	$9.2 \pm 0.9$	$11.7 \pm 1.5$
	2.6	$9.8 \pm 1.0$	$12.4 \pm 1.5$
	2.8	$10.1 \pm 1.0$	$12.8 \pm 1.6$
Fixed to 0.95	2.0	$53.7 \pm 7.6$	$93.4 \pm 4.2$
	2.2	$59.5 \pm 8.5$	$103.6 \pm 4.7$
	2.4	$64.3 \pm 9.1$	$111.9 \pm 5.0$
	2.6	$67.9 \pm 9.7$	$118.2 \pm 5.3$
	2.8	$70.3 \pm 10.0$	$122.3 \pm 5.5$

Table 6.13: Differential flux at 1 TeV in the best-fit component assuming a power-law spectrum for different photon index assumptions: 2.0, 2.2, 2.4, 2.6 and 2.8. The second column indicates the assumed photon index, the third column the differential flux for the best-fit symmetric Gaussian and its statistical uncertainty obtained from the relative uncertainty of the best-fit uncertainty and the fourth column the differential flux for the best-fit asymmetric Gaussian and its statistical uncertainty obtained from the relative uncertainty of the best-fit uncertainty. All values are given for the background subtraction using *Method D*. In addition to table 6.10, here results for different assumptions for the overall background normalization in the final fit of the (asymmetric) Gaussian component are shown: First it is left free in this final fit (as in the rest of the thesis), then it is set to 1.05, 1.02 and 0.95 times the normalization fit in the fit of the normalization of the individual runs in order to study the influence of the background normalization on the reconstructed flux.

<i>Fermi</i> component	E1 + E3	E2	E4	E0
Differential flux extrapolated to 1 TeV [ $10^{-12} \text{ cm}^{-2} \text{ s}^{-1} \text{ TeV}^{-1}$ ]	1.6	2.1	0.70	0.0002

Table 6.14: Extrapolation of the differential flux seen in the different components shown in figure 5.4 to 1 TeV using the best-fit spectra presented in *Fermi*-LAT LMC paper [140].

in section 5.5), this could lead to a difference of up to a factor 5 as follows from the table. However, this systematic uncertainty quantifies the difference between the best-fit background normalization on OFF-runs and the one obtained from the run-wise simulations and so strictly only applies to *Method A*. *Method D* which is considered here is used since it is less impacted by this systematic uncertainty. It is however hardly possible to quantify by how much, especially in the presence of a signal which might distort any assessment from OFF-runs a bit, as for *Method D* the background is fit to the data. However, even for an overall normalization which would only be off by 2% could lead to a difference of a factor of 2 in the reconstructed flux. For this reason, it becomes clear that the systematic uncertainty on the background normalization can have a strong impact on the flux reconstructed. This makes it necessary to further investigate this uncertainty and the flux reconstruction in future studies, as it seems currently not possible to reconstruct the flux reliably with this forward-folding method.

### Comparison with the *Fermi*-Lat fluxes

In order to compare the obtained fluxes with the best-fit *Fermi*-components which I discussed in section 5.2, I extrapolated the flux of the four *Fermi* components to 1 TeV assuming that the spectrum follows the best-fit spectral shape measured by *Fermi* up to this energy. I used the emissivity model, as the spectral parameters are only given for this model in the paper [140]. The obtained differential fluxes are shown in table 6.14. As can be seen, the extrapolated flux from the *Fermi* components is almost an order of magnitude lower than the computed H.E.S.S. fluxes using the forward-folding method. This is illustrated again on figure 6.47. However, as discussed previously the systematic uncertainty on the H.E.S.S. flux is very high. The uncertainty in the background normalization might reduce the discrepancy to a factor of 2. Adding to this the systematic uncertainties derived on the point sources and the statistical uncertainties might explain the discrepancy. A 5% systematic uncertainty on the overall background normalization would though be higher as expected. This might be an indication for additional systematic uncertainties in the method not spotted yet. This shows how big the uncertainties

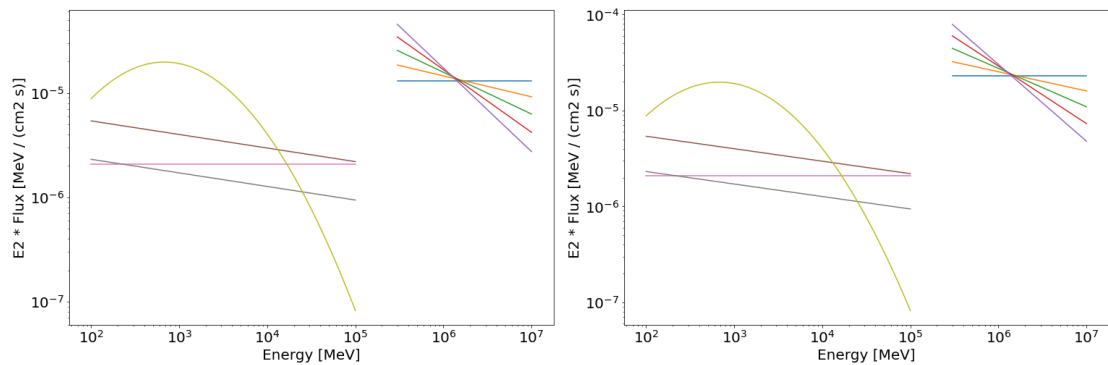


Figure 6.47: Spectrum constructed from the computed differential flux in the best-fit component using the power-law spectral model input in the forward-folding procedure in the H.E.S.S. sensitive range (on the right of the figures) compared to the spectrum measured by *Fermi*-LAT for the four components found in their diffuse analysis using the emissivity model [140] (on the left of the figures). Left: Spectrum of the best-fit Gaussian component (for H.E.S.S.). Right: Spectrum of the best-fit asymmetric Gaussian component (for H.E.S.S.). The different colours for the H.E.S.S. components indicate again the different photon indices used in the forward-folding procedure and is the same as for the previous plot. For the spectra of the Fermi components, the spectrum of the E0 component (as shown in figure 5.4) is shown by the curved yellow line, the component being the combination of the E1 and E3 Gaussian by the brown (top straight) line, the E2 component by the pink (horizontal straight) line and the E4 component by the gray (bottom straight) line.

on the H.E.S.S. flux in the observed extended component are and that reducing them will be one of the major tasks of future analyses.

## 6.5 Conclusion

In this part of my thesis, I presented a novel method to search for extended emission. This method is based on run-wise simulations in which the considered dataset is simulated on a run-by-run basis. I used this run-wise simulations to generate instrument response functions and a background model. These instruments response functions and background model are completely independent of the data taken on the considered field of view while still taking into account the observation conditions. The background model was subtracted from the recorded data in order to be left with a potential signal. I determined the systematics of this method at deep exposure on a Centaurus A and an NGC 253 dataset. Finally, I applied this method to the search for interstellar diffuse emission on the LMC and the SMC.

This novel method left to the emergence of an extended component in the LMC, whereas the SMC dataset was in agreement with pure background. This might also be due to the low statistics in the SMC analysis compared to the three other datasets. However, the level of non-statistical variations was higher in SMC than for Cen A, NGC 253 and studies on OFF-fields performed at lower exposure. Even though this is only a slight hint for the presence of a signal beyond statistical variations, this shows that it might be worth to come back to the SMC with a deeper exposure dataset to confirm the putative presence of a signal.

The extended component emerging in the LMC is in contrast very robust against a change in the procedure of determination of the background normalizations of the individual runs. It is above the level of systematics determined in the study of OFF-runs and confirmed on the Cen A and NGC 253 dataset. This shows that this extended component is of physical origin. It so constitutes the first detection of potential interstellar diffuse emission inside a galaxy with an Imaging Atmospheric Cherenkov Telescope. I described the shape of this extended component by adjusting it with a symmetric Gaussian component and an asymmetric Gaussian component. This showed that it is centred close to N 132D and that it has an extension of at least  $0.9^\circ$ .

In order to find a potential correlation of the emission with structures in the LMC, I considered different models: first a symmetric and asymmetric Gaussian emission model to test a potential asymmetry and later on these models were multiplied with the atomic neutral hydrogen gas density (i.e. the component was multiplied with the gas column density in each pixel). I introduced this model as hadronic interstellar diffuse emission is expected to be produced by the interaction of cosmic rays with gas. Multiplying the model with the gas distribution so gives

a direct handle on the cosmic ray distribution if the emission is of hadronic origin. The model performing the best was the asymmetric Gaussian, which would be an indication for the emission to be asymmetric and not so well correlated with the gas density. However, the increase in performance of this model compared to the three other models is not above systematic uncertainties, and so the question whether the observed excess is correlated to the gas distribution in the LMC is still open. This means that the systematic uncertainties of this analysis do not allow me to characterize the morphology of the excess further.

Moreover, the systematic uncertainties and the very inhomogeneous exposure also lead to the central position of the physical excess being unknown. Indeed, it is possible that the observed excess is only part of a larger emission component in the LMC. This makes a potential correlation study with possible emission sources incomplete as one does not know if one accounts for all the emission. For this reason, it is not clear whether the observed emission is of hadronic or leptonic origin or if it comes from unresolved sources or if it is a combination of the three as discussed in more detail in section 6.4.1.

As a part of this study, I also tried to determine the flux of the observed emission. However, it turned out that the systematic uncertainties of the used forward-folding method are so high that it is impossible to get any meaningful value.

This leaves us with the first detection of potential interstellar diffuse emission with an Imaging Atmospheric Cherenkov Telescope. The systematic and statistical uncertainties are currently too high to determine the morphology or the flux of the observed excess. This extended emission observed in the LMC is a first demonstration of what is possible with Imaging Atmospheric Cherenkov Telescopes using a background model and instrument response functions completely independent of the data taken on the considered field of view while still taking into account the observation conditions. A refinement of the method and a full use of the dataset at hand will make deep morphological and spectral studies possible and allow the search for extended emission in other regions in the sky as will be discussed in the next chapter (7) which discusses the perspectives of this study.

# Chapter 7

## Perspectives

After giving an introduction into the field of gamma-ray astronomy and discussing the instrument used in this work, H.E.S.S., I discussed a novel calibration method for optical efficiencies and the search for interstellar diffuse emission in this thesis. For the optical efficiency calibration, I first of all optimised the current muon-based optical efficiency calibration method at large zenith angles by introducing a cut based on the goodness of the muon ring fit to the observed muon ring. This led to the disappearance of a zenith angle dependence in the muon optical efficiencies I noticed earlier, but does not have a significant impact on the average muon efficiency used in H.E.S.S. analyses due to the low number of high zenith angle runs taken with H.E.S.S.

After having sorted out this problem with the muon-based optical efficiencies, I considered a novel UAV-based relative optical efficiency calibration method. To do this, a first-generation prototype LED-based light source was mounted on a UAV which was positioned inside the field of view of the four HESS-I telescopes. It illuminated all of them with a pulsed light source whose pulses were recorded. The telescopes were then inter-calibrated based on the total amount of light they recorded. Beside inter-calibration, I showed that it is possible to use the UAV data to verify the pointing correction and the time-stamping of H.E.S.S.

Planned future campaigns will allow us to ameliorate the uncertainties (which are now at few percentage level) through a better understanding of systematic uncertainties and improvements to the UAV prototype and potentially go beyond a simple verification for the pointing corrections. They will also allow us to test the use of the UAV in further calibration tasks, such as doing a full-multiwavelength inter-calibration and possibly absolute optical efficiency calibration by characterising the properties of the light source better or to monitor the atmospheric transparency by mounting meteorological devices on the UAV.

One of the aims of these future campaigns is to reduce the systematic uncertainties of this novel calibration method enough to make it competitive for the

optical efficiency calibration of future Imaging Atmospheric Arrays such as CTA. The goal of this is also to allow an easy multi-wavelength optical efficiency calibration which is not achievable with the muon-based method, however needed to reach the requirements to achieve the planned sensitivity, energy and angular resolution of CTA. A UAV-based multi-wavelength calibration is one possibility for filling this hole in the traditional optical efficiency calibration and can so help to reach the requirements to fulfil the science projects of CTA.

One of the three central themes investigated in these science projects is "Understanding the Origin and Role of Relativistic Cosmic Particles" [87]. In order to increase this understanding, two galaxies will be observed as key science projects within CTA: Our Milky Way and the Large Magellanic Cloud. The idea is not only to study the origin of cosmic rays in sources which might also produce gamma rays, but also to study their propagation within these galaxies. This propagation can be best studied through the interaction of these cosmic rays with gas, radiation or magnetic fields. In these interactions gamma-rays can be produced which can be observed with CTA.

However, gamma-rays can be observed with any Imaging Atmospheric Cherenkov Telescope and it is so not necessary to wait for the advent of CTA to search for this gamma-ray interstellar diffuse emission. In this thesis, I discussed the first detection of potential interstellar diffuse emission with an Imaging Atmospheric Cherenkov Telescope. I obtained this detection of an emission component with an extension of at least  $0.9^\circ$  in the Large Magellanic Cloud using a novel run-wise simulation-based analysis method. This allowed me not to be impacted by any potential very extended excess in the background subtraction as the instrument response function and background model generated from these run-wise simulations are completely independent of the data taken on the considered field of view while still taking into account the observation conditions.

For this first detection of an extended emission component in the Large Magellanic Cloud, further studies of the morphology and the spectrum were limited by the statistical and systematic uncertainties. Both of these uncertainties are expected to be greatly reduced in future. On the statistical side, only 14% of the available LMC runs taken with H.E.S.S. are considered in this analysis. This is on the one hand due to only using one camera configuration in order to reduce systematic uncertainties. In the future when the systematic uncertainties will be well understood, one can extend this method to the other configurations after adapting the zenith angle and radial corrections and re-estimating the systematic uncertainties for all the configurations. This would lead to a big gain in statistics as only 29% of the available LMC data has been taken with the currently considered camera configuration. On the other hand, strict selection cuts are currently used in order to reduce systematic uncertainties. It might be possible to loosen

some of them and increase statistics even more, even though some of the data will remain completely unusable (among other due to very bad weather conditions or technical failures impacting multiple telescopes) and so it will never be possible to use all the runs. In addition to this already available data, one of the proposed projects of the H.E.S.S. legacy program is the study of the cosmic ray population in the LMC. A part of this project is to increase the H.E.S.S. exposure to 50 hours everywhere in the LMC by increasing the exposure at the edges of the LMC (as more than 100 hours of exposure are already available in its central parts around the *Fermi* component G2). This will fully resolve the problem with the inhomogeneous exposure encountered in this work leading to possibly only parts of a physical emission component being visible and allow deeper morphological studies, at least from the statistical side and the discovery of further potential diffuse components in the LMC. In addition, to the search for interstellar diffuse emission this higher exposure will also allow to put further constraints on point-like sources or lead to the discovery of new point-like source.

On the systematic side, energy dependent run-wise background models are currently under development. This will allow to go from a simple flux determination to a full spectral study. This leads to a completely new handle on the systematic uncertainties in the flux computation and will hopefully allow us to improve them and so to get more reliable fluxes. This energy dependent background models, the increase of the number of camera configurations and the further investigation of the run-wise background analysis method will also increase our knowledge of systematic uncertainties and help us to reduce them. This will among other possibly reduce the systematic uncertainties on the prediction of the background normalization from the run-wise simulations and so increase the performance of *Method A*. This might lead to a reliable analysis method fully independent of the data taken on the field of view to be investigated. This would not only allow us to do a full morphological and spectral study of the extended emission observed in the LMC, but also to re-apply this method to other fields of view.

SMC could be revisited with higher statistics and better understood systematic uncertainties to understand whether the observed higher level of statistical variations is due to a higher systematic level or to a physical excess.

However beyond these two targets discussed in this thesis, these first results and the discussed perspectives show the potential of Imaging Atmospheric Cherenkov Telescopes in the study of extended emission using novel analysis methods. Indeed, up to very recently H.E.S.S. and other Cherenkov telescopes mostly detected point-like sources or sources with a small extension, and the study of extended emission at gamma-ray energies was mostly performed with *Fermi*-LAT. In the last years, first studies of more extended sources were completed with H.E.S.S. (and other Imaging Atmospheric Cherenkov Telescopes), among other a study on Geminga [154]

using the field-of-view background and ON-OFF background method, showing that H.E.S.S. is capable of detecting very extended sources. However, in this Geminga analysis, the real cut-off of the emission could not be determined due to the extension of the emission, and so a run-wise approach could also improve our knowledge on this source. This shows the potential of Cherenkov telescopes to detect extended emission using different non-standard (at least in the detection of point-like sources) methods and so to complement the view *Fermi*-LAT has on extended structures at higher energies and finer resolution of substructures.

This view is and will be complemented by newer even higher energy instruments such as HAWC and LHAASO, instruments which were discussed in section 1.5.3. Both of these instruments are well suited to detect extended sources and are sensitive to even higher energies than H.E.S.S. They have detected numerous extended sources, and together with *Fermi*-LAT and Cherenkov Telescopes, these sources can be studied from the MeV range to the PeV range in gamma-rays.

One prime target for such studies is our Galaxy, the Milky Way. Diffuse gamma-ray emission at GeV energies originating from it has already been detected with the SAS-2 satellite in the 1970s [172]. The gamma-ray emission in the MeV and GeV energy range has later on be studied in detail with other satellite instruments, most recently with *Fermi*-LAT [129]. This not only let to the detection of the expected interstellar diffuse emission from the Galactic plane and of emission from some point-like sources or small extended sources, but later on also to the detection of two huge bubble-like structures extending  $50^\circ$  above and below the Galactic centre [173] called the *Fermi* bubbles. Their origin is still unclear. Beside *Fermi*-LAT, first detections of gamma-ray interstellar diffuse emission from the Galactic plane have recently been reported by HAWC [174, 175] and LHAASO [176]. These detections can be expected to be refined and further characterised over the next years through increased statistics and reduced systematics or better modelling to disentangle interstellar diffuse emission from unresolved sources. Galactic interstellar diffuse emission is so a very active field of research and there have been other efforts beside the ones mentioned here. H.E.S.S. also has published lower limits on galactic interstellar diffuse emission as discussed in section 5.2. The reason for the publication of lower limits was due to using a background subtraction method based on a background determination within the field of view. Ongoing work on galactic interstellar diffuse emission within the H.E.S.S. collaboration using the run-wise simulation-based method described in this thesis, is expected to resolve this issue and allow a proper characterization of galactic interstellar diffuse emission at TeV energies with H.E.S.S. and characterise its morphology and spectrum. The characterization of such extended emission will show the real capabilities of this run-wise simulation-based background subtraction method.

Going back to LMC and SMC, ample observation results from *Fermi*-LAT are available with which a multi-wavelength picture can be built after a successful characterization of their extended emission with H.E.S.S. However, the Magellanic Clouds are only visible from the Southern hemisphere and can so not be observed with any Northern hemisphere instrument such as HAWC and LHAASO. For data of the Magellanic Clouds taken at higher energies, one has to wait for the advent of SWGO (discussed in section 1.5.3) which will have an optimal location for their observation and will complement *Fermi*-LAT and H.E.S.S. results.

As mentioned earlier, beyond the three major Imaging Atmospheric Cherenkov Telescope arrays currently in operation, a much larger one is currently under construction, CTA. It is foreseen to increase the sensitivity by one order of magnitude and to reach an unprecedented energy and angular resolution, and is so even better suited to characterize interstellar diffuse emission than H.E.S.S., and this on the Northern and Southern hemisphere given its two locations. The observation of LMC and the galactic plane are two of its proposed key science projects. The increased sensitivity, energy and angular resolution will permit to study the fine structure of extended emission in even more detail and so further increase our knowledge about interstellar diffuse emission. To do so CTA will be able to build on the H.E.S.S. results and especially use the analysis method developed to detect very extended emission. Indeed, even though the CTA telescopes have a larger field of view than the ones of H.E.S.S., one might still be confronted to emission which extends over the whole field of view. This then leads to the need for a background subtraction method taking this in to account in order not to end up with a lower limit. In addition to this, CTA will be constituted of many more telescopes than all current Imaging Atmospheric Telescope Arrays and it is foreseen that it uses different pointing strategies. This leads to an extreme increase in possible array configurations and makes it hardly possible to produce individual Monte Carlo simulations for each individual configuration separately a priori. The use of run-wise simulations for less common array configurations could be a solution for this.



# Appendix A

## Side-by-side comparison of residual maps and best-fit Gaussians

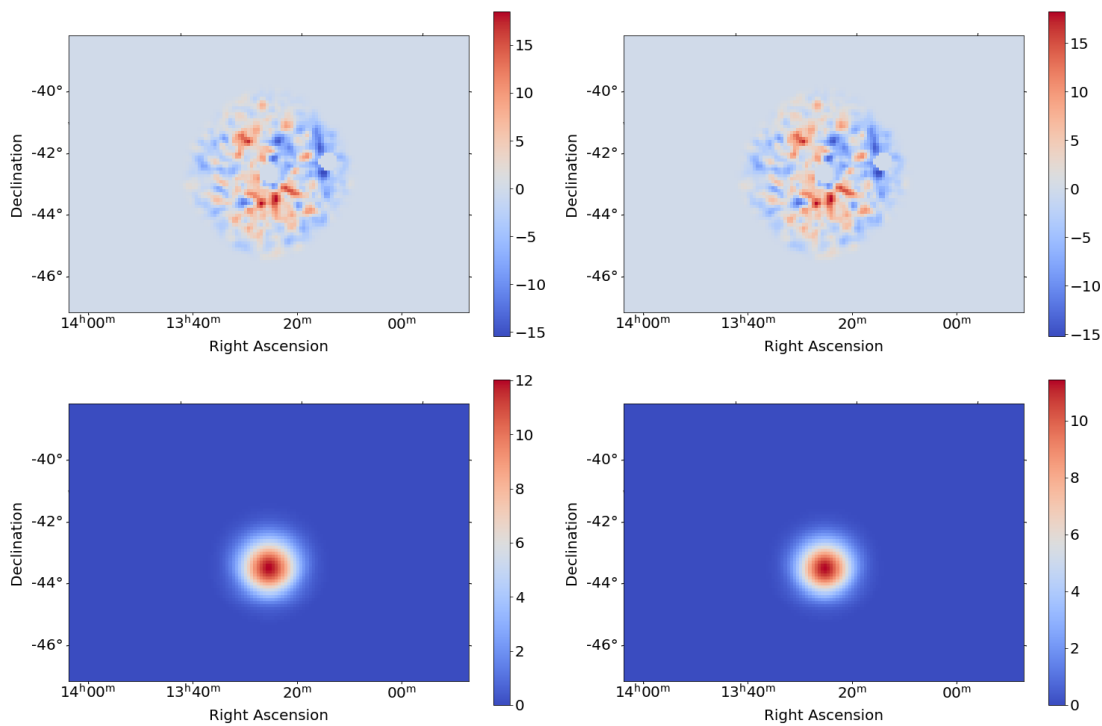


Figure A.1: Top: Residual maps after background subtraction with masked sources for Cen A. The colour scale indicates the number of counts in each bin. Bottom: Map of counts in best-fit Gaussian for Cen A. Left: *Method A*. Right: *Method B*.

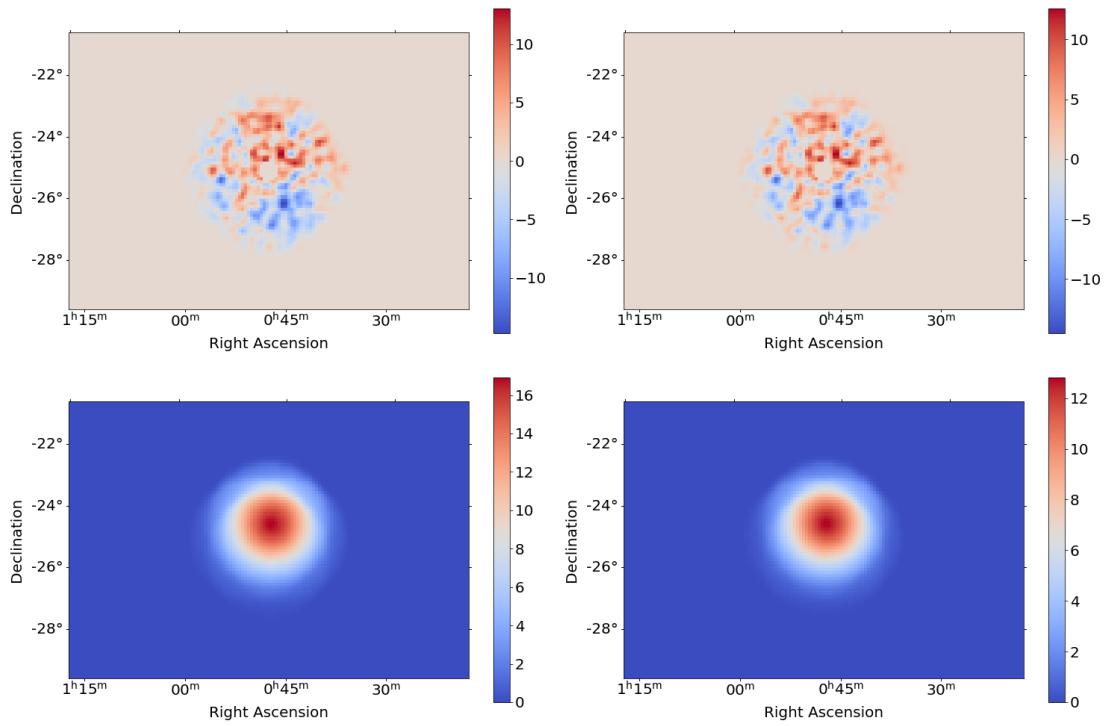


Figure A.2: Top: Residual maps after background subtraction with masked sources for NGC 253. The colour scale indicates the number of counts in each bin. Bottom: Map of counts in best-fit Gaussian for NGC 253. Left: *Method A*. Right: *Method B*.

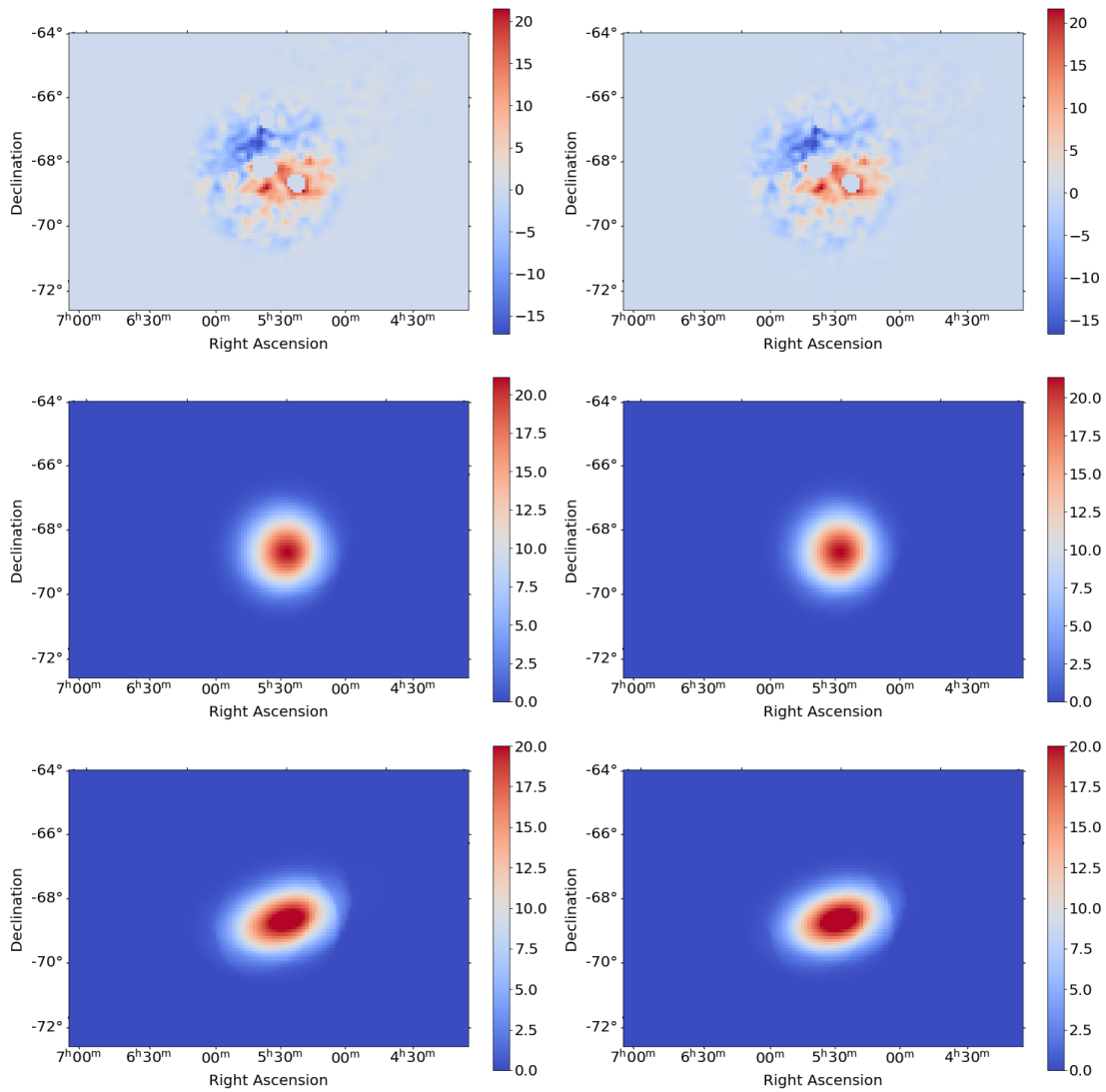


Figure A.3: Top: Residual maps after background subtraction with masked sources for LMC. The colour scale indicates the number of counts in each bin. Centre: Map of counts in best-fit Gaussian component for LMC. Bottom: Map of counts in best-fit asymmetric Gaussian for LMC. Left: *Method A*. Right: *Method B*.

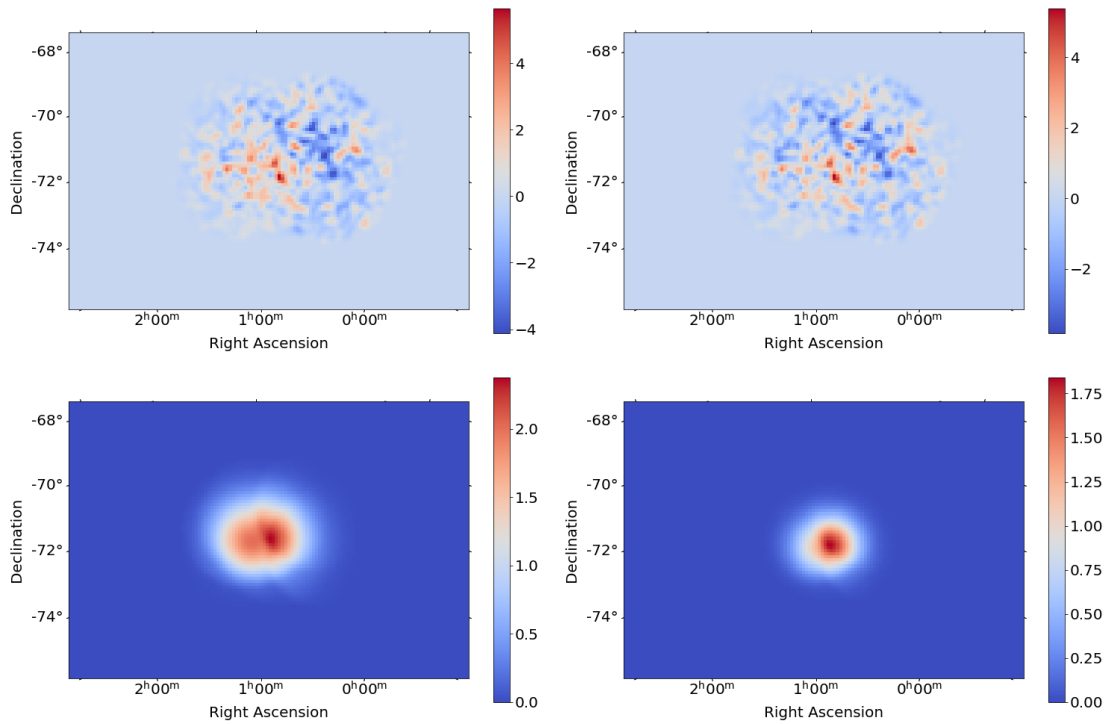


Figure A.4: Top: Residual maps after background subtraction for SMC. The colour scale indicates the number of counts in each bin. Bottom: Map of counts in best-fit Gaussian for SMC. Left: *Method A*. Right: *Method B*.

# Appendix B

## LMC results for standard analysis

This appendix shortly discusses the results of a standard ring background analysis of the LMC of the same data used in this thesis in order to detect the extended emission with the novel run-wise simulation-based background subtraction method. I performed this standard analysis using the same runlist and the same semi-analytic model reconstruction for the selection and reconstruction of gamma-like events discussed in section 2.4.3 as for the main analysis. For the ring background analysis, I use standard parameters for point-like sources such as a standard over-sampling radius of  $0.1^\circ$ . The use of non-standard parameters might lead to an increase of sensitivity of the ring background subtraction method towards a very extended excess, however I did not perform an optimization of the parameters as this was not the goal of this work and I wish to show a comparison with a standard method.

The significance map obtained with this ring background method is shown in comparison to the significance map obtained earlier with *Method D* in figure B.1. As can be seen beside the excess from the point-like sources (and especially N 157B) which are not masked in the ring background subtraction method, there is no indication for any excess using the standard ring background subtraction method. This shows that the novel run-wise simulation-based analysis method is much more sensitive to such extended excesses than standard analysis methods. However, other non-standard analysis methods or the use of non-standard parameters in standard analysis methods might also increase the performance.

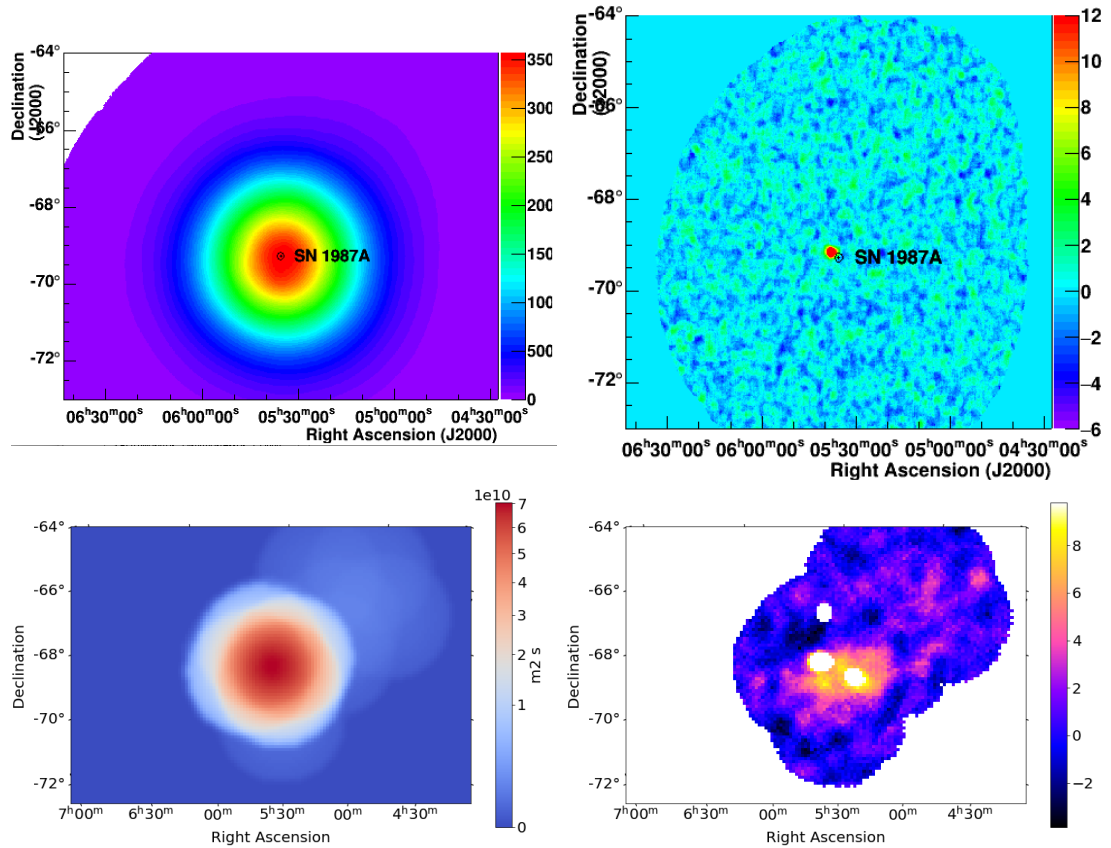


Figure B.1: Comparison of results obtained for LMC using novel run-wise background subtraction method to standard ring background analysis method. Top left: Gamma-like sky acceptance map. Top right: Li & Ma significance map for the ring background method. Bottom left: Exposure map of LMC. Bottom right: Li & Ma significance map after background subtraction with masked using the novel run-wise simulation-based background subtraction method and *Method D* for the background subtraction.

# Acknowledgments

I want to thank all the numerous people without whom this thesis project would not have been possible. Unfortunately, the number of people who helped me to get forward with this thesis is too large to cite them all in person here and there are also many people helping me behind the scenes without me necessarily knowing who provided or sometimes even without me realising that someone provided help to me. My apologies go to all these people who I cannot cite in person, especially since all these contributions, as minor as they might have been, were in their sum crucial for the success of this thesis project, and so I am very thankful for these contributions.

I want to thank Mathieu de Naurois who had scientifically speaking the biggest impact on my thesis as he taught me almost everything I know about doing research and always tried to help me, no matter what I needed help with. I especially want to thank him, since the boundary conditions of this thesis preparation were most likely also not what he expected with having two long lockdowns where he needed to take care of his children and the lab and he still found time to discuss my little issues with me and to push me to get forward with my thesis. He also managed to create great opportunities for me by getting to present at almost all H.E.S.S. collaboration meetings, at a summer school and even at ICRC. He let me be part of his enormous knowledge and I think I can truly say with that with most other supervisors my thesis would not have ended as successful.

Then I want to thank Anthony Brown who came up with this fantastic idea of doing a drone calibration which constitutes the first part of my thesis and pushed a lot to get this done. Without him I would never have managed to have such a great contribution at ICRC and write such a great paper. I also want to thank Alison Mitchell and Vincent Marandon who helped me to sort out the muon calibration, which was supposed to be well understood, and without whom I would never have managed to do a comparison with the results of the muon calibration, and Jean-Philippe Lenain who helped me to understand the issues I had with the H.E.S.S. simulations and to adapt the simulations to the drone calibration tasks and put a lot of effort in this even though he is already taking care of the H.E.S.S. simulations which is for sure more than a full-time job.

For the diffuse emission part of this thesis, I would like to thank Markus Holler, who allowed me to use the analysis software he developed for the use on the Milky Way and helped me to adapt it on the LMC. He was always available to answer my questions about the analysis and taught me a lot about political issues in science and how deal with them. I also want to thank the other member of the diffuse emission task, namely Romed, Sebastian, Kathrin, Olaf, Constantin, Ralf, Julia and all the people having worked previously on this which I never met, for their help and their contributions to the software.

I would like to thank my jury members, and especially my rapporteurs Isabelle Grenier and Oscar Blanch-Bigas for so carefully proof-reading my manuscript and helping me a lot to improve the manuscript to its current state. I also wish to thank Isabelle for taking the time to discuss all her comments in detail with me. Then, I am also thankful to both of them and my other jury members, the president of the jury Régis Terrier, Nukri Komin, Pierrick Martin, Gernot Maier and Anthony Brown for accepting to be part of my jury, for their feedback on my work and all their very thoughtful questions and the subsequent discussion. I also thank them for coming in person to my defence in these trying times or, in the case of Gernot Maier who unfortunately could not join in person, for still joining remotely and doing the necessary preparations for this.

Then, I am very grateful to Albert Jahncke, who unfortunately does not have the chance to accept any thanks anymore. He introduced me to the H.E.S.S. array and taught me everything I know about its operation during our shift in Namibia. He also was very welcoming towards us and made everything to make our stay at the H.E.S.S. site as pleasant as possible and even prepared one of his famous BBQs for us. I will always keep him in good memories for everything he did for me.

I also want to thank the other members of the local crew, Frikkie, Volker and Toni which also did everything for us to have a nice stay and also introduced us to parts of the H.E.S.S. system and helped us operate the telescopes.

Then, I wish to thank Gosia Curylo who shared the Namibian H.E.S.S. adventure with me and without whom my stay at the H.E.S.S. site would have been much less pleasant. I think together, we managed to operate the H.E.S.S. array quite smoothly even though it was just upgraded with a new camera. Here, I also want to seize the occasion to thank Felix Werner who was always available on call when we had some trouble with this camera even though it was mostly night time in Europe. However, with Gosia I also had a great time in the rarer quieter times where everything went smoothly thanks to her great movie taste and her showing me how to operate the smaller optical telescope and I also want to thank her for that.

Coming back to Paris again, I want to thank the other members of the as-

trogamma group of LLR, Rémi, Steve, Deirdre, Gérard, Denis and Philippe. I not only had very fruitful discussions with them in my or their office, during our weekly group meetings, but also during lunch breaks. They always encouraged me with my work and helped me with everything I asked them for. They proofread numerous of my contributions and listened to presentations I planned to give, and so undoubtedly improved them.

Then, I would like to thank Émilie who accepted to be my god mother in this lab, and out of whose offer to help I probably did not make enough, since there often seemed more urgent things to do than discussing with her. I also want to apologize for somehow having rejected this offer like that.

I also wish to thank Ecole Polytechnique for offering me the funding for this PhD, after so many other funding applications failed and without which this thesis could not have happened. I also want to thank their administrative staff as well as the administrative and technical staff of the laboratory, among which Sylvaine, Thu, Mélanie, Alimata and Laetitia, but many more people behind the scenes, which made mostly everything of my PhD going smooth and tried everything to smooth things where they were not going smooth. Without this help, I would most likely sometimes just have given up on administrative stuff.

My thanks also go to Cyril and Sami who were Postdocs when I started my PhDs. They helped me a lot to get involved in astrogamma, the group and the H.E.S.S. collaboration in the beginning. They also always tried to answer my question about physics and the H.E.S.S. software. Beside that we also spent a nice time together inside and outside the lab.

I am very thankful to Janeth who beared sharing an office with me during two whole years. She did not only scientifically supported me wherever she could, but also has become a great friend over the years. Without her my PhD would for sure not have been as fun and I would probably already have felt lonely before the start of the pandemics. I want to specially thank her for introducing me to Peruvian food and drinks and showing me new fun board games

I also want to thank Hazal who was supposed to share the office with me for a semester after Janeth left, which unfortunately turned to only three weeks in the end due to Covid. Even though her short physical stay inside the lab, she has become a great friend and we had many enjoyable moments together. I would like to thank her for all the fruitful and interesting discussions we had, not only on physics topics. She is always encouraging me and inspiring me to try to do better.

I wish to thank Halim and Judit with whom I shared my office at the end of my PhD for their help and support in this very intense phase. I want to thank them for all the very fruitful discussions on physics as well as on non-physics topics, which unfortunately fall a bit short due to my focus on my thesis. I also thank them to create small breakout moments from my thesis which reduced my stress

a lot such as by introducing me to the Lebanese way to party.

I would also like to thank Christian who shared the office with me at the beginning of my PhD to help me to get involved in astrogamma and LLR and for all the nice coffee breaks.

My thanks also go to Christelle who was the only PhD having started around the same time in H.E.S.S. than me in the Paris area. I would like to thank her for discussing our somehow common experience within the collaboration, our common successes and issues, and for always trying to help me.

I would also like to thank her as well as Lucia, Monica, Gabriel and Michelle for making me feel welcome inside the H.E.S.S. collaboration, introducing me to H.E.S.S. meetings and always trying to help me to progress. Beside that, I would also like to thank them for all the fun we had together at the collaboration meetings.

Thanks also to all the other PhD students of the lab, and especially to Jonas, Chiara, Jonas, Duje, Alberto and Guillaume who made my stay at the LLR a nice through our numerous lunches at the lab together, but also outside the lab through our numerous picnics, BBQs, parties, trips and Limoncello preparing and tasting together.

I also want to thank Nina and all the other people I met in the summer school in Cargese for making this summer school as pleasant and enjoyable as it was.

And then I also want to thank my family, my mother, my father, my brother and my sister, but also my grand parents for always encouraging and supporting me on my path and being always there when I did not know what to do. They have given me beside Hazal and Janeth the strength to go towards the end of this thesis and to continue when I doubted myself. There are no words to describe my gratefulness for everything they did for me.

After having thanked all the people who made the progress in thesis project possible during the last a bit more than three years, I also would like to thank all the people who gave me the opportunity to get so far before starting my thesis adventure. Indeed, one does not get born with the abilities to start a thesis project. For this reason, I would like to thank all the people who contributed to my education be it at Ecole Polytechnique in Palaiseau, at ETH in Zurich, in Lycée Michel-Rodange in Luxembourg or in my kindergarten and primary school in Bridel. I also want to thank all the friends I made in these different education steps but also outside of school, among other in my girl- and boyscouting group in Bridel for all the encouragement, support and friendship they gave me in these more than 27 years. Without them I would never have managed to even get to start writing this thesis.

# Bibliography

- [1] W. Herschel, *Investigation of the Powers of the Prismatic Colours to Heat and Illuminate Objects; With Remarks, That Prove the Different Refrangibility of Radiant Heat. To Which is Added, an Inquiry into the Method of Viewing the Sun Advantageously, with Telescopes of Large Apertures and High Magnifying Powers*, The Royal Society Publishing, vol. 90, p. 255, March 27, 1800
- [2] W. L. Kraushaar et al., *High-Energy Cosmic Gamma-Ray Observations from the OSO-3 Satellite*, The Astrophysical Journal, vol. 177, p. 431, October 15, 1972
- [3] E. Buckingham, *On the deduction of Wien's displacement law*, Bulletin of the Bureau Standards, February 28, 1912
- [4] NASA, as cited in J. De Pasquale et al., *High Energy Vision: Processing X-rays* [Online], July 28, 2015, [https://www.researchgate.net/publication/282270380\\_High\\_Energy\\_Vision\\_Processing\\_X-rays](https://www.researchgate.net/publication/282270380_High_Energy_Vision_Processing_X-rays)
- [5] C. T. R. Wilson, *On an Expansion Apparatus for making Visible the Tracks of Ionising Particles in Gases and some Results obtained by its Use*, The Royal Society Publishing, vol. 87, p. 227, June 13, 1912
- [6] V. F. Hess, *Über den Ursprung der durchdringenden Strahlung*, Physikalische Zeitschrift vol. 14, p. 610, June 5, 1913
- [7] C. D. Anderson, *The Positive Electron*, Physical Review, vol. 43, p. 491, March 15, 1933
- [8] S. H. Neddermeyer and C. D. Anderson, *Note on the Nature of Cosmic-Ray Particles*, Physical Review, vol. 51, p. 884, March 30, 1937
- [9] H. Blewett, *The Cosmotron - A Review*, Review of Scientific Instruments, vol. 24, p. 725, December 29, 2004
- [10] J. A. Prins, *Latitude Effect of Cosmic Radiation*, Nature, vol. 132, p. 781, November 18, 1933

- [11] T. H. Johnson, *The East-West Asymmetry of the Cosmic Radiation in High Latitudes and the Excess of Positive Mesotrons*, vol. 59, p. 11, January 1, 1941
- [12] M. Nagano, *Search for the end of the energy spectrum of primary cosmic rays*, New Journal of Physics, vol. 11, June 30, 2009
- [13] L. J. Gleeson and W. I. Axford, *Solar Modulation of Galactic Cosmic Rays*, The Astrophysical Journal, vol. 154, p. 1011, December 1968
- [14] G. Matthiae, *The cosmic ray energy spectrum as measured using the Pierre Auger Observatory*, New Journal of Physics, vol. 12, July 9, 2010
- [15] S. Thoudam et al., *Cosmic-ray energy spectrum and composition up to the ankle: the case for a second Galactic component*, Astronomy & Astrophysics, vol. 595, p. A33, October 25, 2016
- [16] P. Mertsch, *Rapporteur Talk: Cosmic Ray Direct*, 37th International Cosmic Ray Conference, 2021
- [17] A. Aab et al., *Observation of a large-scale anisotropy in the arrival directions of cosmic rays above  $8 \times 10^{18}$  eV*, Science, vol. 357, p. 1266, September 22, 2017
- [18] P. Sreekumar et al., *Constraints on the cosmic rays in the Small Magellanic Cloud*, Physical Review Letters, vol. 70, p. 127, January 11, 1993
- [19] K. Greisen, *End to the cosmic-ray spectrum?*, Physical Review Letters, vol. 16, p. 748, April 25, 1966
- [20] CERN, *Cosmic rays: particles from outer space*, [online] <https://home.cern/science/physics/cosmic-rays-particles-outer-space>, retrieved October 16, 2021
- [21] E. Fermi, *On the Origin of the Cosmic Radiation*, Physical Review Letters, vol. 75, p. 1169, April 15, 1949
- [22] A. R. Bell, *The acceleration of cosmic rays in shock fronts - I*, Monthly Notices of the Royal astronomical Society, vol. 182, p. 147, January 1978
- [23] C. L. Mader et al., *LASL Shock Hugoniot Data*, Los Alamos Series on dynamic material properties, 1980
- [24] A. Marcowith et al., *The microphysics of collisionless shock waves*, Reports on Progress in Physics, vol. 79, p. 046901, 2016

- [25] A. M. Hillas, *The origin of ultra-high-energy cosmic rays*, Annual Review of Astronomy and Astrophysics, vol. 22, p. 425, September, 1984
- [26] M. G. Baring, *Diffuse Shock Acceleration: The Fermi mechanism*, 32nd Rencontres de Moriond, January, 1997
- [27] L. O. Drury, *Particle Acceleration in Shocks*, Astrophysics and Space Science, vol. 233, p. 251, 1995
- [28] Toru Tanimori, *Cangaroo results on southern sky TeV gamma ray sources*, 31st SLAC Summer Institute on Particle Physics: Cosmic Connection to Particle Physics, 2003
- [29] O. Klein and A. Nishina, *Über die Streuung von Strahlung durch freie Elektronen nach der neuen relativistischen Quantendynamik von Dirac*, Zeitschrift für Physik, vol. 52, p. 853, 1929
- [30] R. Buschaer and G. Benford, *General theory of coherent curvature radiation*, Monthly Notices of the Royal Astronomical Society, vol. 177, p. 109, October 1976
- [31] S. R. Kelner et al., *Synchrotron-to-curvature transition regime of radiation of charged particles in a dipole magnetic field*, The Astronomical Journal, vol. 149, p. 33, January 5, 2015
- [32] V. Weidemann and D. Koester, *The upper mass limit for white dwarf progenitors and the initial-final mass relation for low and intermediate stars*, Astronomy and Astrophysics, vol. 121, p. 77, May, 1983
- [33] S. Chandrasekhar, *On stars, their evolution and their stability*, Nobel lecture, December 8, 1983
- [34] S. P. Reynolds, *Supernova Remnants at High Energy*, Annual Review of Astronomy and Astrophysics, vol. 46.1, p. 89, 2008
- [35] J. A. Johnson et al., *The origin of the elements: a century of progress*, Philosophical transactions of the royal society A, vol. 378, August 17, 2020
- [36] J. A. Johnson, *The origin of the solar elements*, [online], <https://blog.sdss.org/author/jajohnson51/> , January 9, 2017, figure as described in [35]
- [37] W. Hillebrandt and J. C. Niemeyer, *Type Ia Supernova Explosion Models*, Annual Review of Astronomy and Astrophysics, vol. 38, p. 191, September, 2000

- [38] E. A. Helder et al., *Observational signatures of particle acceleration in supernova remnants*, Space Science Reviews, vol. 137, p. 369, August 31, 2012
- [39] J. Hester and A. Loll, *The Crab Nebula*, [online] [https://www.nasa.gov/multimedia/imagegallery/image\\_feature\\_1604.html](https://www.nasa.gov/multimedia/imagegallery/image_feature_1604.html), March 2, 2010
- [40] R. Nemiroff and J. Bonnell, *Light from Cygnus A*, [online] <https://apod.nasa.gov/apod/ap150124.html>, January 24, 2015
- [41] V. S. Beskin, *Radio pulsars: already fifty years!*, Physics-Uspekhi, vol. 61 p. 353, 2018
- [42] B. M. Gaensler and P. O. Slane, *The Evolution and Structure of Pulsar Wind Nebulae*, Annual Review of Astronomy and Astrophysics, vol. 44, p. 17, September 22, 2006
- [43] G. Duchêne and A. Kraus, *Stellar Multiplicity*, Annual Review of Astronomy and Astrophysics, vol. 51, p. 269, August, 2013
- [44] H. Abdalla et al., *Detection of variable VHE  $\gamma$ -ray emission from the extragalactic  $\gamma$ -ray binary LMC P3*, Astronomy and Astrophysics, vol. 610, p. L17, January 2018
- [45] R. Blandford et al., *Relativistic Jets in Active Galactic Nuclei*, Annual Review of Astronomy and Astrophysics, vol. 57, p. 467, August 2019
- [46] A. Einstein, *Zur Elektrodynamik bewegter Körper*, Annalen der Physik, vol. 322, p. 891, 1905
- [47] P. Mészáros, *Gamma ray bursts*, Reports on Progress in Physics, vol. 69, p. 2259, 2006
- [48] B. Zhang and P. Mészáros, *Gamma ray bursts: progress, problems & prospects*, International Journal of Modern Physics A, vol. 19, p. 2385, 2004
- [49] R. W. Klebesadel et al., *Observations of gamma ray bursts of cosmic origin*, The Astrophysical Journal, vol. 182, p. L85, June 1, 1973
- [50] H. Abdalla et al., *A very-high-energy component deep in the  $\gamma$ -ray burst afterglow*, Nature, vol. 575, p. 464, November 20, 2019
- [51] L. Mohrmann et al., *The young massive stellar cluster Westerlund 1 in  $\gamma$  rays as seen with H.E.S.S.*, 37th International Cosmic Ray Conference, 2021

- [52] A. Abramowski et al., *Spectral analysis and interpretation of the gamma-ray emission from the starburst galaxy NGC 253*, The Astrophysical Journal, vol. 757, p. 158, 2012
- [53] A. Abramowski et al., *The exceptionally powerful TEV  $\gamma$ -ray emitters in the Large Magellanic Cloud*, Science, vol. 347, p. 406, January 2015
- [54] S. J. Wagner, *Detection of VHE gamma ray emission from the recurrent nova RS Ophiuchi with H.E.S.S.*, The Astronomer's Telegram, num. 14844, August 10, 2021
- [55] D. J. Thompson et al., *SAS-2 High-energy gamma ray observations of the Vela pulsar*, The Astrophysical Journal, vol. 200, p. L79, September 1, 1975
- [56] D. J. Thompson et al., *SAS-2 Gamma ray observations of PSR 17467-46*, Astrophysical Letter, vol. 17, p. 173, May 26, 1976
- [57] G. F. Bignami et al., *The COS-B experiment for gamma-ray astronomy*, Space Science Instrumentation, vol. 1, p. 145, 1975
- [58] D. J. Thompson et al., *Calibration of the energetic gamma ray experiment telescope (EGRET) for the Compton Gamma-Ray Observatory*, Astrophysical Journal Supplement, vol. 86, p. 629, June 1993
- [59] C. Winkler et al., *The INTEGRAL mission*, Astronomy & Astrophysics, vol. 411, p. L1, November 17, 2003
- [60] W. B. Atwood et al., *The Large Area Telescope on the Fermi gamma ray space telescope mission*, The Astrophysical Journal, vol. 697, p. 1071, June 1, 2009
- [61] G. T. Zatsepin and A. E. Chudakov, *Method of finding local sources of high-energy photons*, Journal of Experimental and Theoretical Physics, vol. 14, p. 469, February 1962
- [62] T. C. Weekes, *Observation of TeV gamma rays from the Crab Nebula using the atmospheric Cerenkov imaging technique*, The Astrophysical Journal, vol. 342, p. 379 July 1, 1989
- [63] G. Puelhofer, *The Technical Performance of the HEGRA System of Imaging Air Cherenkov Telescopes*, Astroparticle Physics, vol. 20, p. 267, December 2003
- [64] M. Tavani et al., *The AGILE Mission*, Astronomy & Astroparticle, vol. 502, p. 995, January 30, 2009

- [65] N. Gehrels et al., *The Swift Gamma-Ray Burst Mission*, The Astrophysical Journal, vol. 611, p. 558, 2004
- [66] Agenzia Spaziale Italiana - Space Science Data Centre *Fermi LAT instrument*, [online] <https://fermi.ssdsc.asi.it/> , retrieved October 16, 2021
- [67] K. Bernlöhner, *Development of gamma ray air showers*, [online] <https://www.mpi-hd.mpg.de/hfm/CosmicRay/Showers.html> , 1999
- [68] J. Matthews, *A Heitler model of extensive air showers*, Astroparticle Physics vol. 22, p. 387, January 2005
- [69] P. A. Zyla, *The Review of Particle Physics (2018)*, Physical Review D98, p. 452, 2018
- [70] P. A. Zyla, *The Review of Particle Physics (2018)*, Physical Review D98, p. 134, 2018
- [71] A. De Angelis and M. J. Martins Pimenta, *Introduction to Particle and Astroparticle Physics*, Springer, September 5, 2015
- [72] M. de Naurois, *L'astronomie  $\gamma$  de très haute énergie. Ouverture d'une nouvelle fenêtre astronomique sur l'Univers non thermique.*, Mémoire d'Habilitation à diriger des Recherches de l'Université Paris VI, March 13, 2012
- [73] P. A. Čerenkov, *Radiation of particles moving at a velocity exceeding that of light, and some of the possibilities for their use in experimental physics*, Nobel Lecture, December 11, 1958
- [74] A. Horvath, *Cherenkov radiation*, [online] <https://commons.wikimedia.org/wiki/File:Cherenkov.svg> , March 16, 2006
- [75] J. V. Jelley and N. A. Porter, *Čerenkov Radiation from the Night Sky, and its Application to  $\gamma$ -Ray Astronomy*, Quarterly Journal of the Royal Astronomical Society, vol. 4, p. 275, September 1963
- [76] F. A. Aharonian et al., *The potential of ground based arrays of imaging Cherenkov telescopes. I. Determination of shower parameters*, Astroparticle Physics, vol. 6, p. 343, 1997
- [77] D. López, *MAGIC telescopes*, [online] <https://www.uab.cat/web/newsroom/news-detail/x-1345668003610.html?noticiaid=1345777026944> , retrieved 2020
- [78] VERITAS, *VERITAS and building*, [online] <https://veritas.sao.arizona.edu/> , retrieved October 16, 2021

- [79] S. Klepser, *HESS II gamma ray experiment five telescope array*, [online] <https://astrogamma.se/h-e-s-s/>, retrieved October 16, 2021
- [80] J. Aleksić et al., *The major upgrade of the MAGIC telescopes, Part I: The hardware improvements and the commissioning of the system*, *Astroparticle Physics*, vol. 72, p. 61, January 1, 2016
- [81] N. Park et al., *Performance of the VERITAS experiment*, The 34th International Cosmic Ray Conference, July 30 - August 6, 2015
- [82] H. Abdalla et al., *The H.E.S.S. Galactic plane survey*, *Astronomy & Astrophysics*, vol. 612, p. 61, April 2018
- [83] D. Horns, *H.E.S.S.: Status and future plan*, 2nd Workshop on TeV Particle Astrophysics, 2016
- [84] H. Abdalla et al., *First ground-based measurements of sub-20 GeV to 100 GeV  $\gamma$ -rays from the Vela pulsar with H.E.S.S. II*, *Astronomy & Astrophysics*, vol. 620, p. A66, December 2018
- [85] Cherenkov Telescope Array Observatory gGmbH, *CTA technology*, [online] [https://www.cta-observatory.org/wp-content/uploads/2019/12/CTA-Specifications\\_v08\\_formatted.pdf](https://www.cta-observatory.org/wp-content/uploads/2019/12/CTA-Specifications_v08_formatted.pdf), December 2019
- [86] G. Pareschi et al., *The mini-array of SST-2M telescopes, precursors for the Cherenkov Telescope Array*, *Journal of Physics: Conference Series*, vol. 718, p. 052028, 2016
- [87] B. S. Acharya et al., *Science with the Cherenkov Telescope Array*, World Scientific, 2019
- [88] J. Goodman, *The HAWC Observatory*, [online] <https://www.hawc-observatory.org/>, November 2016
- [89] A. U. Abeysekara et al., *Sensitivity of the High Altitude Water Cherenkov Detector to Sources of Multi-TeV Gamma Rays*, *Astroparticle Physics*, vol. 50-52, p. 26, December 2013
- [90] P. Huentemeyer et al., *The Southern Wide-Field Gamma-Ray Observatory (SWGRO): A Next-Generation Ground-Based Survey Instrument*, *Bulletin of the AAS*, vol. 51, p. 7, 2019
- [91] C. Li and B. Ma, *LHAASO discovery of highest-energy photons towards new physics*, *Science Bulletin*, vol. 66, p. 2254, July 28, 2021

- [92] J. A. Hinton, *The Status of the H.E.S.S. Project*, New Astronomy Reviews, vol. 48, p. 331, 2004
- [93] W. Hofmann, *H.E.S.S. Project Chronology*, [online] <https://www.mpi-hd.mpg.de/hfm/HESS/pages/about/chronology/>, retrieved October 16, 2021
- [94] P. Hofverberg et al., *Commissioning and initial performance of the H.E.S.S. II drive system*, The 33rd International Cosmic Ray Conference, 2013
- [95] J. M. Davies and E. S. Cotton, *Design of the quartermaster solar furnace*, Solar Energy, vol. 1, p. 16, 1957
- [96] K. Bernlöhner et al., *The optical system of the H.E.S.S. imaging atmospheric Cherenkov telescopes. Part I: layout and components of the system*, Astroparticle Physics, vol. 20, p. 111, November 2003
- [97] M. de Naurois and D. Mazin, *Ground-based detectors in very-high-energy gamma ray astronomy*, Comptes Rendus Physique, vol. 16, p. 610, 2015
- [98] Satellite photo from Bing Maps (<https://www.bing.com/maps>), retrieved September 21, 2021
- [99] The H.E.S.S. collaboration, *High Energy Stereoscopic System*, [online] <https://www.mpi-hd.mpg.de/hfm/HESS/pages/about/>, retrieved October 16, 2021
- [100] The H.E.S.S. collaboration, *Characteristics of the H.E.S.S. telescopes*, [online] [https://www.mpi-hd.mpg.de/hfm/HESS/pages/about/HESS\\_I\\_II/](https://www.mpi-hd.mpg.de/hfm/HESS/pages/about/HESS_I_II/), retrieved October 16, 2021
- [101] F. Aharonian et al., *Calibration of cameras of the H.E.S.S. detector*, Astroparticle Physics, vol. 22, p. 109, June 30, 2004
- [102] S. Bonnefoy et al., *Performance of the upgraded H.E.S.S. cameras*, The 35th International Cosmic Ray Conference, July 10 - July 20, 2017
- [103] J. Bolmont et al., *The camera of the fifth H.E.S.S. telescope. Part I: System description*, Nuclear Instruments and Methods in Physics Research Section A: Accelerators, Spectrometers, Detectors and Associated Equipment, vol. 761, p. 46, October 11, 2014
- [104] G. Julien, *Premiers résultats de l'expérience HESS et étude du potentiel de détection de matière noire supersymétrique*, Ph.D. thesis, Université Pierre et Marie Curie - Paris VI, 2003

- [105] K. Bernlöhr, *Impact of atmospheric parameters on the atmospheric Cherenkov technique*, Astroparticle Physics, vol. 12, p. 255, 2000
- [106] S. Funk et al., *The trigger system of the H.E.S.S. telescope array*, Astroparticle Physics, vol. 22, p. 285, 2004
- [107] R. Chalme-Calvet et al., *Muon efficiency of the H.E.S.S. telescope*, Atmo-HEAD Workshop 2013
- [108] M. Gaug et al., *Using muon rings for the calibration of the Cherenkov Telescope Array: A systematic review of the method and its potential accuracy*, The Astrophysical Journal Supplement Series, vol. 243, p. 11, 2019
- [109] S. Gillessen, *Arcsecond Level Pointing Of The H.E.S.S Telescopes*, The 28th International Cosmic Ray Conference, July 31 - August 7, 2003
- [110] F. Aharonian et al., *Observations of the Crab Nebula with H.E.S.S.*, Astronomy and Astrophysics, vol. 457, p. 899, October 2006
- [111] A. M. Hillas, *Cherenkov light images of EAS produced by primary gamma rays and by nuclei*, 19th International Cosmic Ray Conference, August 1985
- [112] F. Dubois et al., *A multivariate analysis approach for the imaging atmospheric Cherenkov telescope system H.E.S.S.*, Astroparticle Physics, vol. 32, p. 73, July 2009
- [113] M. de Naurois and L. Rolland, *A high performance likelihood reconstruction of gamma rays for Imaging Atmospheric Cherenkov Telescopes*, Astroparticle Physics, vol. 32, p. 231, July 2009
- [114] K. Levenberg, *A Method for the Solution of Certain Problems in Least Squares*, Quarterly of Applied Mathematics, vol. 2, p. 164, July 1944
- [115] D. W. Marquardt, *An Algorithm for Least-Squares Estimation of Nonlinear Parameters*, Journal of the Society for Industrial and Applied Mathematics, vol. 11, p. 431, June, 1963
- [116] D. Berge et al., *Background Modelling in Very-High-Energy  $\gamma$ -ray Astronomy*, Astronomy and Astrophysics, vol. 466, p. 1219, April 24, 2007
- [117] G. P. Rowell, *A new template background estimate for source searching in TeV gamma ray astronomy*, Astronomy & Astrophysics, vol. 410, p.389, October 4, 2003

- [118] T. Li and Y. Ma, *Analysis methods for results in gamma ray astronomy*, The Astrophysical Journal, vol. 272, p. 317, September 1, 1983
- [119] F. Piron et al., *Temporal and spectral gamma ray properties of Mkn 241 above 250 GeV from CAT observations between 1996 and 2000*, Astronomy and Astrophysics, vol. 374, p. 895, August 3, 2001
- [120] M. Holler et al., *Photon Reconstruction for H.E.S.S. Using a Semi-Analytical Shower Model*, The 34th International Cosmic Ray Conference, July 30 - August 6, 2015
- [121] M. Gaug et al., *Calibration of the Cherenkov Telescope Array*, The 34th International Cosmic Ray Conference, July 30 - August 6, 2015
- [122] J. Bäuml et al., *Measurement of the Optical Properties of the Auger Fluorescence Telescope*, The 33rd International Cosmic Ray Conference, 2013
- [123] A. M. Brown, *On the prospects of cross-calibrating the Cherenkov Telescope Array with an airborne calibration platform*, Astroparticle Physics, vol. 96, p. 69, October 14, 2017
- [124] Satellite photo from Google Maps (<https://www.google.com/maps>), retrieved September 21, 2021
- [125] R. Cornils et al., *The optical system of the H.E.S.S. imaging atmospheric Cherenkov telescopes. Part II: mirror alignment and point spread function*, Astroparticle Physics, vol. 20, p. 119, November 2003
- [126] S. Gillessen, *Sub-Bogenminuten-genaue Positionen von TeV-Quellen mit H.E.S.S.*, Ph.D. thesis, Ruprecht-Karls-Universität Heidelberg, 2004
- [127] A. M. W. Mitchell et al., *Cross-calibration of telescope optical throughput efficiencies using reconstructed shower energies for the Cherenkov Telescope Array*, Astroparticle Physics, vol. 75, p. 1, 2016
- [128] G. Ponti et al., *An X-ray chimney extending hundred of parsecs above and below the Galactic Centre*, Nature, vol. 567, p. 347, March 13, 2019
- [129] M. Ackermann et al., *Fermi-LAT observations of the diffuse  $\gamma$ -ray emission: implications for cosmic rays and the interstellar medium*, The Astrophysical Journal, vol. 750, p. 35, April 2012
- [130] A. Abramowski et al., *Diffuse Galactic gamma ray emission with H.E.S.S.*, Physical Review D, vol. 90, p. 12, 2014

- [131] D. L. Bertsch et al., *Diffuse gamma ray emission in the galactic plane from cosmic-ray, matter and photon interaction*, The Astrophysical Journal, vol. 416, p. 587, September 28, 1993
- [132] S. C. O. Glover and M.-M. Mac Low, *On the relationship between molecular hydrogen and carbon monoxide abundances in molecular clouds*, Monthly Notices of the Royal Astronomical Society, vol. 412, p. 337, March 14, 2011
- [133] U. Lisinfeld and H. J. Völk, *On the radio spectral index of galaxies*, Astronomy and Astrophysics, vol. 354, p. 423, 2000
- [134] N. Ben Bekhti et al., *HIP4I: A full-sky HI survey based on EBHIS and GASS*, Astronomy and Astrophysics, vol. 594, p. 15, October 20, 2016
- [135] ESA/Planck Collaboration, *All-sky images of molecular gas seen by Planck*, [online] <https://sci.esa.int/web/planck/-/50011-all-sky-image-of-molecular-gas-seen-by-planck> , February 12, 2012
- [136] D. P. Finkbeiner, *A full-sky H $\alpha$  template for microwave foreground prediction*, The Astrophysical Journal Supplement Series, vol. 146, p. 407, June 2003
- [137] G. Pietrzyński et al., *A distance to the Large Magellanic Cloud that is precise to one per cent*, Nature, vol. 567, p. 200, March 13, 2019
- [138] S. Brunier, *Magellanic Clouds - Irregular Dwarf Galaxies*, [online] [https://upload.wikimedia.org/wikipedia/commons/4/41/Magellanic\\_Clouds\\_%E2%80%95\\_Irregular\\_Dwarf\\_Galaxies.jpg](https://upload.wikimedia.org/wikipedia/commons/4/41/Magellanic_Clouds_%E2%80%95_Irregular_Dwarf_Galaxies.jpg) , August 27, 2009
- [139] J. Harris and D. Zaritsky, *The star formation history of the Large Magellanic Cloud*, The Astronomical Journal, vol. 138, p. 1243, September 22, 2009
- [140] M. Ackermann et al., *Deep view of the Large Magellanic Cloud with six years of Fermi-LAT observations*, Astronomy and Astrophysics, vol. 586, p. A71, September 2015
- [141] R. H. D. Corbet et al., *A luminous gamma ray binary in the Large Magellanic Cloud*, The Astrophysical Journal, vol. 829, p. 105, September 27, 2016
- [142] M. Ackermann et al., *An extremely bright gamma ray pulsar in the Large Magellanic Cloud*, Science, vol. 350, p. 801, November 13, 2015
- [143] A. A. Abdo et al., *Observations of the Large Magellanic Cloud with Fermi*, Astronomy & Astrophysics, vol. 512, p. 15, March 18, 2010

- [144] J. P. Ridley et al., *Eight new radio pulsars in the Large Magellanic Cloud*, Monthly Notices of the Royal Astronomical Society, vol. 433, p. 138, July 21, 2013
- [145] M. Yew et al., *New optically identified supernova remnants in the Large Magellanic Cloud*, Monthly Notices of the Royal Astronomical Society, vol. 500, p. 2336, November 2, 2020
- [146] S. D. Points et al., *Large-scale diffuse X-ray emission from the Large Magellanic Cloud*, The Astrophysical Journal Supplement Series, vol. 136, p. 99, September 2001
- [147] P. Maggi et al., *The population of X-ray supernova remnants in the Large Magellanic Cloud*, Astronomy and Astrophysics, vol. 585, p. 53, January 2016
- [148] R. C. Smith et al., *The UM/CTIO Magellanic Cloud Emission-line Survey*, Publications Astronomical Society of Australia, vol. 15, p. 163, 1998
- [149] Q. Wang and D. J. Helfand, *LMC-2 as the Blowout of a Hot Superbubble*, The Astrophysical Journal, vol. 379, p. 327, September 1991
- [150] S. D. Points et al., *The supergiant shell LMC 2. I. The kinematics and physical structure*, The Astrophysical Journal, vol. 518, p. 298, June 10, 1999
- [151] A. Sinha et al., *Search for enhanced TeV gamma-ray emission from Giant Molecular Clouds using H.E.S.S.*, The 37th International Cosmic Ray Conference, July 12 - 13, 2021
- [152] D. Tiziani, *The first analysis of very-high-energy gamma rays from the Large Magellanic Cloud with a novel analysis technique*, Ph.D. thesis, Friedrich-Alexander-Universität Erlangen-Nürnberg, 2020
- [153] A. Jardin-Blicq et al., *A complementary view of the Galactic plane in TeV gamma rays by HAWC and H.E.S.S.*, The 36th International Cosmic Ray Conference, 2019
- [154] A. M. W. Mitchell et al., *Detection of extended TeV emission around the Geminga pulsar with H.E.S.S.*, The 37th International Cosmic Ray Conference, July 12 - 13, 2021
- [155] M. Holler et al., *A Run-Wise Simulation and Analysis Framework for Imaging Atmospheric Cherenkov Telescope Arrays*, Astroparticle Physics, vol. 123, p. 102491, December 2020

- [156] M. Holler et al., *Run-Wise Simulations for Imaging Atmospheric Cherenkov Telescope Arrays*, The 35th International Cosmic Ray Conference, July 10 - July 20, 2017
- [157] Markus Holler, private communication
- [158] Romed Rauth, private communication
- [159] V. A. Epanechnikov, *Non-parametric estimation of a multidimensional probability density*, *Teoriya Veroyatnostei i ee Primeneniya*, vol. 14, p. 156, 1969
- [160] F. Aharonian et al., *Discovery of very high energy gamma-ray emission from Centaurus A with H.E.S.S.*, *The Astrophysical Journal*, vol. 695, p. L40, March 19, 2009
- [161] H. Abdalla et al., *Resolving acceleration towards very high energies along the jet of Centaurus A*, *Nature*, vol. 582, p. 356, June 17, 2020
- [162] F. Acero et al., *Detection of gamma rays from a starburst galaxy*, *Science*, vol. 326, p. 1080, November 20, 2009
- [163] M. Holler, *Assessing Background Systematics in an Analysis Field of View*, H.E.S.S. Internal Note 21/01, February 2021
- [164] Data presented in A. Mellinger, *A color All-Sky Panorama Image of the Milky Way*, *Publications of the Astronomical Society of the Pacific*, vol. 121 p. 1190, November 2009, retrieved through NASA, *SkyView, The Internet's Virtual Telescope* on March 29, 2021
- [165] L. Staveley-Smith et al., *A new look at the large scale HI structure of the Large Magellanic Cloud*, *Monthly Notice of the Royal Astronomical Society*, vol. 339, p. 87, February 2003
- [166] S. Kim et al., *An HI Aperture Synthesis Model of the Large Magellanic Cloud*, *The Astrophysical Journal*, vol. 503, p. 674, August 1998
- [167] S. Kim et al., *A neutral hydrogen survey of the Large Magellanic Cloud: Aperture synthesis and multibeam data combined*, *The Astrophysical Journal Supplement Series*, vol. 148, p. 473, October 2003
- [168] H. Abdalla et al., *LMC N132D: A mature supernova remnant with a power-law gamma ray spectrum beyond 8 TeV*, *Astronomy & Astrophysics*, accepted July 2021

- [169] H. Abdalla et al., *The  $\gamma$ -ray spectrum of the core of Centaurus A as observed with H.E.S.S. and Fermi-LAT*, Astronomy & Astrophysics, vol. 619, p. 10, November 2018
- [170] A. Abramowski et al., *H.E.S.S. and Fermi-LAT discovery of  $\gamma$ -rays from the blazar 1ES 1312-423*, Monthly Notices of the Royal Astronomical Society, vol. 434, p. 1889, September 2013
- [171] Sebastian Panny, private communication
- [172] J. L. Puget and F. W. Stecker, *The distribution of cosmic rays in the galaxy and their dynamics as deduced from recent  $\gamma$ -ray observations*, The Astrophysical Journal, vol. 191, p. 323, July 15, 1974
- [173] M. Su et al., *Giant gamma-ray bubbles from Fermi-LAT: AGN activity or bipolar galactic wind?*, The Astrophysical Journal, vol. 724, p. 1044, November 10, 2010
- [174] A. Nayerhoda et al., *Gamma Ray Diffuse Emission from the Galactic Plane with HAWC Data*, The 36th International Cosmic Ray Conference, 2019
- [175] A. Nayerhoda et al., *Galactic Gamma-Ray Diffuse Emission at TeV energies with HAWC Data*, The 37th International Cosmic Ray Conference, July 12 - 13, 2021
- [176] S. Zhao et al., *Measurement of the diffuse gamma-ray emission from Galactic plane with LHAASO-KM2A*, The 37th International Cosmic Ray Conference, July 12 - 13, 2021







**Titre :** Inter-Calibration Aéroportée des Télescopes H.E.S.S. et Emission Gamma Diffuse Interstellaire de Très Haute Energie du Grand Nuage de Magellan

**Mots clés :** Astronomie gamma ; Technique Tcherenkov Atmosphérique ; Emission Diffuse ; Efficacités optiques ; Drone

**Résumé :** Le Système Stéréoscopique à Haute Energie H.E.S.S. en Namibie est l'un des trois grands réseaux de Télescopes à Imagerie Tcherenkov Atmosphérique (IACT) opérationnels. Ces réseaux sont conçus pour détecter indirectement des photons aux énergies les plus hautes couramment observables, appelés rayons gamma. Pour pouvoir mesurer précisément l'énergie des photons gamma, il est indispensable de calibrer les cinq télescopes de H.E.S.S. individuellement, mais aussi de les inter-calibrer.

La première partie de cette thèse propose une nouvelle méthode pour déterminer les efficacités optiques relatives des télescopes du réseau H.E.S.S. Celle-ci est basée sur un drone volant au-dessus du réseau et éclairant les télescopes avec une source de lumière pulsée. Cette méthode permet, contrairement à celle utilisée jusqu'alors, de mesurer la dépendance à la longueur d'onde des efficacités. En se basant sur les résultats d'une première campagne, cette thèse démontre que cette méthode permet d'inter-calibrer les télescopes de H.E.S.S. et, additionnellement, de vérifier l'horodatage et les corrections de pointé de

H.E.S.S., qui sont nécessaires car le pointé est imparfait à cause de la déformation du sol et de la structure du télescope sous son propre poids.

La seconde partie de cette thèse discute la recherche d'émission gamma diffuse interstellaire en provenance du Grand Nuage de Magellan. Il s'agit d'une galaxie naine qui, à l'instar de la Voie Lactée, contient non seulement des étoiles mais également des rayons cosmique (protons et électrons principalement) et de la matière interstellaire. Outre les sources astrophysiques, on attend également une émission diffuse interstellaire produite par les interactions de ces particules avec le gaz interstellaire et les champs de rayonnement. J'utilise une nouvelle méthode de soustraction de fond basée sur des simulations Monte Carlo observation-par-observation (simulations «run-wise») du fond attendu qui est soustrait des données observées. J'ajuste l'émission résiduelle sur les données en utilisant un maximum de vraisemblance. Ceci mène à l'émergence d'une composante d'émission étendue près de N 157B qui pourrait être due à l'émission diffuse, et constituer ainsi sa première détection avec un IACT.

**Title :** Airborne Inter-Calibration of H.E.S.S. Telescopes and Interstellar Diffuse Very-High-Energy Gamma-Ray Emission in the Large Magellanic Cloud

**Keywords :** Diffuse Emission ; Atmospheric Cherenkov Technique ; Gamma-ray astronomy ; Optical Efficiencies ; UAV

**Abstract :** The High Energy Stereoscopic System (H.E.S.S.) in Namibia is one of the three major Imaging Atmospheric Cherenkov Telescope (IACT) arrays currently in operation. As such, it is designed to indirectly detect photons at the highest energies currently observable, called gamma-rays. As the five telescopes of H.E.S.S. work together as an array, it is not only necessary to calibrate them individually, but also to inter-calibrate them.

The first part of this thesis proposes a novel method to determine the relative optical efficiencies of the telescopes of the H.E.S.S. array. It is based on an unmanned aerial vehicle positioned inside the field of view of all the telescopes on which a pulsed light source illuminating them is mounted. The method permits, unlike the one used so far, to monitor the wavelength dependent evolution of the efficiencies. Based on the results of a first campaign, this thesis shows that we are indeed able to inter-calibrate the H.E.S.S. telescopes and, in addition, to verify the time stamping and poin-

ting corrections of H.E.S.S., which are necessary as the pointing is imperfect due to the deformation of the ground and the telescope structure due to its weight.

The second part of this thesis is about the search for interstellar diffuse gamma-ray emission produced in the Large Magellanic Cloud. The LMC is a dwarf galaxy which, as the Milky Way, does not only contain stars, but also cosmic rays (mostly electrons and protons) and interstellar matter. Beside the astrophysical sources, one also expects diffuse interstellar emission produced by the interactions of these particles with the interstellar gas and the radiation fields. I use a novel background subtraction method based on a run-by-run Monte Carlo simulation ("run-wise" simulation) of the expected background which is subtracted from the observed data. I fit the residual emission to the data with a maximum likelihood. This leads to the emergence of an extended emission component near N 157B, which could be attributed to diffuse emission, and would so constitute its first detection with an IACT.